Planetary and Space Science

Editor-in-Chief: MILTON GREENBERG

Regional Editors:

D. R. BATES
A. I. LEBEDINSKY
S. K. MITRA
W. W. KELLOGG
D. F. MARTYN
M. NICOLET
F. L. WHIPPLE

Volume 6, 1961

ELECTROMAGNETIC EFFECTS OF RE-ENTRY

Selected Papers from the Symposium on

THE PLASMA SHEATH: ITS EFFECTS ON COMMUNICATION AND DETECTION

1959

PERGAMON PRESS, INC.

NEW YORK · OXFORD · LONDON · PARIS

CONTENTS

PAGE

SECTION A. THERMODYNAMIC AND ELECTRICAL PROPERTIES OF STOCK-IONIZED FLOW FIELDS

W. C. TAYLOR: **Analysis of Radio Signal Interference Effects due to Ionized Layer around a Re-entry Vehicle** - - - - - - - - - - - - - - - 1

H. W. RIDYARD: **Comparison of the Ionized Shock Layer about Two- and Three-Dimensional Blunt Shapes at Hypersonic Speeds** - - - - - - - - - - - - 10

I. P. SHKAROFSKY, M. P. BACHYNSKI and T. W. JOHNSTON: **Collision Frequency Associated with High Temperature Air and Scattering Cross-Sections of the Constituents** - - - 24

W. B. SISCO and J. M. FISKIN: **Basic Hypersonic Plasma Data of Equilibrium Air for Electromagnetic and other Requirements** - - - - - - - - - - - - 47

M. H. BORTNER: **The Effect of Errors in Rate Constants on Non-Equilibrium Shock Layer Electron Density Calculations** - - - - - - - - - - - - - 74

A. R. HOCHSTIM: **Electron Concentration in Closed Form for High Temperature Air and Air with Additives** - - - - - - - - - - - - - - - 79

S. C. LIN: **Rate of Ionization Behind Shock Waves in Air** - - - - - - - - 94

SECTION B. INTERACTION OF MICROWAVES AND IONIZED AIR

R. J. PAPA and W. P. ALLIS: **Waves in a Plasma in a Magnetic Field** - - - - - - 100

M. M. KLEIN, H. D. GREYBER, J. I. F. KING and K. A. BRUECKNER: **Interaction of a Non-Uniform Plasma with Microwave Radiation** - - - - - - - - - - 105

J. W. MARINI: **Radiation and Admittance of a Slotted-Sphere Antenna Surrounded by a Plasma Sheath** - - - - - - - - - - - - - - - - 116

C. L. DOLPH and H. WEIL: **On the change in Radar Cross-Section of a Spherical Satellite caused by a Plasma Sheath** - - - - - - - - - - - - - 123

L. PETERS, Jr., and R. B. GREEN: **Echo Area of a Plasma-Coated Sphere** - - - - 133

CONTENTS

PAGE

SECTION C. VOLTAGE BREAKDOWN OF ANTENNAS

W. E. SCHARFMAN and T. MORITA: **Power-Handling Capability of Antennas at High Altitude** - - - - - - - - - - - - - - - - 142

R. F. WHITMER and A. D. MACDONALD: **R.F. Antenna Breakdown Conditions in the Presence of the Plasma Sheath** - - - - - - - - - - - - - - - 149

P. P. KEENAN: **Microwave Breakdown of Antenna Radomes at High Altitudes** - - - 155

SECTION D. EXPERIMENTAL TECHNIQUES FOR EXPLORING THE INTERACTION OF MICROWAVE ENERGY WITH IONIZED FLOWFIELD

P. W. HUBER: **Experiments with Plasmas Produced by Alkali-Metal-Seeded Cyanogen-Oxygen Flames for Study of Electromagnetic Wave Propagation at the Langley Research Center** - 172

R. L. CHUAN: **Experimental Investigation of Electromagnetic Propagation through the Plasma Sheath in a Hypersonic Low Density Wind Tunnel** - - - - - - - - - 180

R. I. PRIMICH: **Microwave Techniques for Hypersonic Ballistic Ranges** - - - - - 186

C. J. MAIDEN and C. ST. PIERRE: **Some Measurements of the Physical Properties of the Plasma Sheath around Hypersonic Projectiles** - - - - - - - - - - - 196

K. M. BALDWIN, O. E. BASSET, E. I. HAWTHORNE and E. LANGBERG: **Telecommunications during Re-entry** - - - - - - - - - - - - - - - - 207

ABSTRACTS OF PAPERS PRESENTED AT THE SYMPOSIUM BUT NOT INCLUDED IN THIS VOLUME - - - - - - - - - - - - - - - 219

Planetary and Space Science

CUMULATIVE INDEXES

Volumes 6–8
1961

Editor-in-Chief: MILTON GREENBERG

Regional Editors:

D. R. BATES
W. W. KELLOGG
D. F. MARTYN
T. NAGATA
W. ORR ROBERTS
H. FRIEDMAN
A. I. LEBEDINSKY
S. K. MITRA
M. NICOLET
F. L. WHIPPLE

PERGAMON PRESS

NEW YORK · OXFORD · LONDON · PARIS

Subject Index

Absorption
- microwave radiation in a plasma, **6**, 105.
- radiowaves in ionosphere: **8**, 151.
- soft X-rays by aluminium: **8**, 169

Air, high temperature
- electron concentration in closed form: **6**, 79.
- collision frequency: **6**, 24.
- cross-sections for constituents: **6**, 24

Air, seeded: **6**, 79, 172.
Airglow, artificial, measurement of diffusion coefficient: **8**, 35.
Antennae
- ambipolar diffusion, effect on breakdown: **6**, 149
- power handling at high altitudes: **6**, 142
- radiation from slotted-sphere: **6**, 116
- radomes, microwave breakdown at high altitudes: **6**, 155.
- R.F. breakdown in presence of sheath: **6**, 149.

Arcing, at high altitudes: **7**, 11
Atmosphere of Earth
- abundance of N_2, **8**, 9.
- ARDC 1959 model, review: **7**, 454.
- model for downward transfer of energy: **7**, 434.
- thermal structure of ozonosphere from satellite measurements: **7**, 423.

Aurora
- circular symmetry in geomagnetic equatorial plane: **8**, 142.
- excitation of high altitude red arcs: **8**, 59.
- excitation of subvisual OI arcs at middle latitudes: **8**, 198.
- observations during I.G.Y. and I.G.C.: **8**, 125.
- observations in Alaska including high altitude red arcs: **8**, 49.
- precipitation of trapped particles: **8**, 13.
- transmission of UHF signals through: **7**, 272.

Book reviews
- *An introduction to celestial mechanics* by T. E. Sterne: **8**, 122.
- *Cosmic radio waves* by I. S. Shklovskii, trans. by R. B. Rodman and C. M. Varsavsky: **8**, 122.
- *Physics of the solar chromosphere* by Richard N. Thomas and R. Grant Athay: **8**, 122.

Carbon dioxide, in atmosphere of Venus: **8**, 23.
Collision frequencies, high temperature air: **6**, 24.
Communications, by satellites: **7**, 254.
Computers
- high speed memory element: **6**, 184.
- random failures in components: **7**, 242
- simulation of missiles: **7**, 179.

Cosmic rays, measurement on geophysical rockets: **8**, 165.

Diffusion
- ambipolar, effect on antenna breakdown: **6**, 149.
- coefficients, determined from sodium vapour trails: **8**, 35.

Electron concentration in high temperature air: **6**, 79.
Exosphere, model of ion distributions in: **8**, 71.

Guidance
application of dynamic programming: **7,** 176.
control of soft landings on the Moon: **7,** 70.
high precision stellar navigator: **7,** 57
homing: **7,** 125
inertial components to supplement astro-fixes: **7,** 19.
interplanetary and lunar vehicles: **7,** 64, 94.
miss distances for lunar and interplanetary trajectories: **7,** 125.
orbital transfer for satellites: **7,** 132.
orbits of space rockets in the direction of the Moon: **8,** 107.
problems in interplanetary space: **8,** 97.
reconnaissance missions to Venus and Mars: **7,** 40.
static inverter: **7,** 1.
trajectories for continuous propulsive thrust: **7,** 145.
vertical azimuth transfer system: **7,** 108.

Hydroxyl emission, nightglow: **8,** 197.
Hypersonics
collision frequencies in high temperature air: **6,** 24.
effect of errors in rate constants on calculated shock layer electron densities: **6,** 74.
electron concentration in closed form for high temperature air: **6,** 79.
ionized shock layer for blunt shapes: **6,** 10.
plasma data of equilibrium air: **6,** 47.
radio signal interference due to ionized layer: **6,** 1; **7,** 286.
rate of ionization behind shock waves: **6,** 94.

Ionization
non-equilibrium, in shock waves: **6,** 74.
rate behind shock waves in air: **6,** 94.
rate in lower atmosphere: **8,** 9.
Ionosphere
D-region, origin of: **8,** 200.
electron concentration: **8,** 183.
positive ion concentration from Sputnik III: **8,** 179
Ions, in exosphere: **8,** 71.

Kepler problem, equations of disturbed motion: **8,** 79.

Micrometeorites
flux measurement: **7,** 417.
on Sputnik III: **8,** 82.
Micro-organisms, viability in ultra-high vacuum: **8,** 30.
Microwaves
radiation, absorption in plasma: **6,** 105.
techniques for hypersonic ballistic ranges: **6,** 186.
Missiles
damping of structural bending: **7,** 26.
performance of static inverter: **7,** 1.
radar tracking: **7,** 81.
reliability: **7,** 208, 217, 230.
simulation by a digital computer: **7,** 179.
trajectory charts: **7,** 118.
Moon
expansion and contraction: **8,** 1.

linear array of small craters: **8,** 121
orbits of rockets: **8,** 107.
soft landings on: **7,** 70.

Nightglow, hydroxyl emission: **8,** 197.
Nitrogen, molecular, abundance in terrestrial atmosphere: **8,** 9.

Plasma
coated sphere, echo area: **6,** 133.
data of equilibrium air: **6,** 47.
from seeded cyanogen flame, propagation in: **6,** 172.
non-uniform, interaction with microwave radiation: **6,** 105.
propagation properties: **6,** 1.
sheath, on spherical satellite, radar cross-section: **6,** 123.
sheath, physical properties around projectiles: **6,** 196.
sheath, propagation through, in hypersonic low density wind tunnel: **6,** 180.
waves, attenuation of: **6,** 1.
waves, in a magnetic field: **6,** 100.
WKB approximation in: **6,** 105.

Radiation, solar, rocket measurements: **8,** 120.
Reconnaissance, mission to Venus and Mars: **7,** 40.
Re-entry
effects of impact: **7,** 386.
radiation from slotted-sphere antenna with plasma sheath: **6,** 116.
radio signal interference due to ionized layer: **6,** 1; **7,** 286.
telecommunications during: **6,** 207.
R.F. fields, random, measurement using short electric and magnetic dipoles: **8,** 68.

Satellites
bi-elliptical transfer between coplanar circular orbits: **7,** 164.
communications by means of: **7,** 254.
determination of Earth's gravitational potential: **8,** 43.
effect of Earth's oblateness on rotational motion: **8,** 173.
Hohmann transfer: **7,** 132, 164.
illumination conditions and periods in shadow and sunlight: **8,** 159.
impact of meteoric particles on Sputnik III: **8,** 82.
orbital transfer: **7,** 132.
orbits derived from gravitational model of the Earth: **7,** 154.
orientation effects: **7,** 445.
path in normal gravitational field of the Earth: **8,** 86.
positive ion concentrations from Sputnik III: **8,** 173.
radar cross-section: **6,** 123.
Shock layer
blunt shapes: **6,** 10.
non-equilibrium ionization in: **6,** 74.
transmission of e.m. radiation through **6,** 1.
Sodium, vapour trails: **8,** 35.
Solar, radiation, rocket measurements: **8,** 120.
Space flight
bioastronautics research: **7,** 356.
closed cycle life support system: **7,** 370.
ecology problems: **7,** 345.
effects of impact: **7,** 386.
hypothetical orbital flight: **7,** 309,

man in space: **7,** 301.
micro-organisms: **8,** 30.
physiological effects: **7,** 378, 395.
space simulators: **7,** 324, 335.
Thermal impact: **7,** 427.
Tracking
generalized trajectory charts: **7,** 118.
high precision 200 million mile system: **7,** 94.
photographic satellite position determination: **7,** 76.
radar, for satellites and missiles: **7,** 81.

Van Allen radiation
composition of lower belt: **7,** 411.
longitudinal dependence: **8,** 13.
Velocity, corrections for space vehicle: **7,** 40.
Venus, CO_2 content of atmosphere: **8,** 23.

Waves, plasma, in magnetic field: **6,** 100.
Whistlers, dispersions for an ionospheric model: **8,** 71.
W.K.B. approximation, in a plasma: **6,** 105.

Author Index

(B signifies book review and R research note)

Allis, W. P. **6,** 100
Altman, S. P. **7,** 132
Anderson, G. P. **7,** 242
Arthur, J. S. **7,** 81

Bachynski, M. P. **6,** 24
Baldwin, K. M. **6,** 207
Barker, C. L., Jnr. **7,** 335
Basset, O. E. **6,** 207
Battin, R. H. **7,** 40
Bellman, R. **7,** 176
Berkofsky, L. **7,** 434
Bock, C. D. **7,** 57
Bowring, J. I. R. **7,** 309
Bracha, V. J. **7,** 208
Brady, J. S. **7,** 301
Brechner, V. O. **7,** 378
Brown, R. Hanbury, **8,** 123 (B)
Brueckner, K. A. **6,** 105
Brueschke, E. E. **8,** 30

Champion, K. S. W. **7,** 454
Chuan, R. L. **6,** 180
Cohen, A. D. **7,** 118
Cohen, H. A. **7,** 417
Cook, G. E. **8,** 122 (B)
Crooks, J. W. **7,** 94
Cutler, C. C. **7,** 254

Darlington, S. **7,** 70
Deehr, C. S. **8,** 49
Dieter, N. H. **7,** 76
Dolph, C. L. **6,** 123
Dreyfus, S. **7,** 176

Ebert, B. P. **7,** 309
Emmerich, C. L. **7,** 108
Epstein, A. H. **7,** 179

Fielder, G. **8,** 1
Fiskin, J. M. **6,** 47
Freed, L. E. **7,** 26

Ghosh, S. N. **8,** 9
Green, R. B. **6,** 133
Greyber, H. D. **6,** 105
Gringauz, K. I. **8,** 183

Hawthorne, E. I. **6,** 207
Henry, J. C. **7,** 81
Hibbs, A. R. **8,** 121 (R)
Hochstim, A. R. **6,** 79
Hoelker, R. F. **7,** 164
Holly, F. E. **7,** 411
Huber, P. W. **6,** 172
Hughes, J. V. **7,** 145
Hugill, J. **8,** 68
Hultqvist, B. **8,** 142

Ingalls, R. P. **7,** 272
Inn, E. C. Y. **8,** 201 (R)
Istomin, V. G. **8,** 179

James, J. C. **7,** 272
Johnson, R. G. **7,** 411
Johnston, T. W. **6,** 24

Kalaba, R. **7,** 176
Kaplan, L. D. **8,** 23
Karmiol, E. D. **7,** 230
Keenan, P. P. **6,** 155
King, J. I. F. **6,** 105; **7,** 423
Kislik, K. D. **8,** 86
Kizner, W. **7,** 125
Klein, M. M. **6,** 105
Konikoff, J. J. **7,** 370
Kornhauser, M. **7,** 386
Krasovskii, V. I. **8,** 125, 197 (R)

Langberg, E. **6,** 207
Laning, J. H. **7,** 40
Lawton, R. W. **7,** 386
Lin, S. C. **6,** 94
Lipow, M. **7,** 217
Lloyd, D. K. **7,** 217
Loughnan, C. J. **8,** 13
Lur'e, A. I. **8,** 79
Luton, W. B. **7,** 324

Macdonald, A. D. **6,** 149
McNally, D. **8,** 122 (B)
Maiden, C. J. **6,** 196
Marini, J. W. **6,** 116
Michaels, J. E. **7,** 427
Miczaika, G. R. **7,** 76
Miller, K. L. **7,** 26
Minzner, R. A. **7,** 454
Morita, T. **6,** 142
Mundo, C. J. **7,** 19

Nauman, R. J. **7,** 445
Nazarova, T. N. **8,** 82
Nelson, J. R. **7,** 345
Nomicos, G. N. **7,** 145

Papa, R. J. **6,** 100
Patterson, T. N. L. **8,** 71
Peters, L. **6,** 133
Peterson, L. E. **7,** 242
Peterson, N. W. **7,** 179
Pettengill, G. H. **7,** 81
Pittman, C. W. **7,** 64
Pogrund, R. S. **7,** 395
Pond, H. L. **7,** 454
Pounds, K. A. **8,** 120 (R)
Primich, R. I. **6,** 186
Quinn, F. B. **7,** 378

Raushenbakh, B. V. **8,** 97
Rees, J. A. **8,** 35
Rees, M. H. **8,** 49, 59, 198 (R)
Ridyard, H. W. **6,** 10
Rudakov, V. A. **8,** 183

St. Pierre, C. **6,** 196
Sarychev, V. A. **8,** 173
Savet, P. H. **7,** 154
Scharfman, W. E. **6,** 142
Schroeder, W. **7,** 64
Sebring, P. B. **7,** 81
Sedov, L. I. **8,** 107
Shafer Yu. G. **8,** 165
Shapiro, R. **7,** 434
Sharma, K. D. **8,** 9
Shkarovskii, I. P. **6,** 24
Silber, R. **7,** 164
Sisco, W. B. **6,** 47
Smith, D. E. **8,** 43
Spink, B. R. **7,** 11
Steffe, W. **7,** 1
Stone, M. L. **7,** 272
Suess, R. H. **8,** 30

Taylor, W. C. **6,** 1; **7,** 286
Thompson, A. B. **7,** 324
Tokar, E. N. **8,** 97

Wal, L. Van Der **7,** 356
Wanlass, C. L. **7,** 184
Wanlass, S. D. **7,** 184
Weil, H. **6,** 123
Whitehead, J. D. **8,** 151
Whitmer, R. F. **6,** 149
Willard, M. **8,** 30
Wisnieff, R. E. **7,** 108

Yarygin, A. V. **8,** 165
Yatsunskii, I. M. **8,** 159
Youtcheff, J. S. **7,** 230

Planetary and Space Science

VOLUME 6

ELECTROMAGNETIC EFFECTS OF RE-ENTRY

Selected Papers from the Symposium on

THE PLASMA SHEATH: ITS EFFECTS ON
COMMUNICATION AND DETECTION
1959

Edited by

WALTER ROTMAN
and
GERALD MELTZ

AIR FORCE CAMBRIDGE RESEARCH LABORATORIES
L. G. HANSCOM FIELD, BEDFORD, MASS.

PREFACE

A collection of papers selected from among those delivered at the first Plasma Sheath Symposium comprises the contents of this volume. The three-day meeting, which examined radio-wave propagation in a shock-ionized medium and several other related topics, convened at Boston, Massachusetts, on December 7, 8 and 9, 1959, under the auspices of the Electromagnetic Radiation Laboratory of the Air Force Cambridge Research Laboratory.

A perusal of the contents will reveal that the term *plasma sheath* is used to describe a phenomenon altogether different from the space-charge boundary between a plasma and its container. In contrast to Langmuir's original meaning we define the term to be the contiguous envelope of ionized gas that forms about a body as it enters the earth's atmosphere at hypersonic velocities. It is apparent, since the two concepts are not synonymous, that the normal usage will not result in ambiguity.

Both the plasma sheath and the consequent ionized wake markedly affect re-entry communications, telemetry, reconnaissance and detection. Heretofore, telemetry records have furnished the principal experimental evidence of these interactions. An examination of this data clearly shows that the transmission of radio signals can be prohibitively impaired by shock layer attenuation. Fortunately it has been possible to record the telemetry information and retransmit it when the ionization decreases or store it in a recoverable capsule to be retrieved after impact. However, vehicles which must continuously transmit and receive information during re-entry cannot effect so simple a solution. In this instance one is compelled to use frequencies which are well in excess of the plasma frequency, a nominal upper limit for attenuation. Thus the range of usable operating frequencies is bounded below by plasma absorption (a frequency of the order of 10 kMc/s) and above by ordinary atmospheric attenuation and component limitations. In addition to the attenuation, spurious modulation resulting from nonlinear interactions may further restrict the coherent transmission or reception of data.

Apart from any other considerations, these few illustrate the pragmatic importance attached to a study of the electromagnetic interaction phenomena associated with atmospheric re-entry. A glance at the Table of Contents will indicate the wide scope of this subject and, hence, the manifold influence of the plasma sheath. Accordingly, it is of interest to note that the numerous problems which have been posed or suggested by an advancing space technology possess a common characteristic feature: each spans many diverse scientific disciplines. Indeed, a tacit realization of this fact, together with a desire to stimulate the interchange of information between researchers in aerodynamics, electronics and plasma physics provided the primary motivation for the organization of the Symposium.

Collectively, the material included in this volume stresses a comprehensive grasp of the many engineering ramifications of the plasma sheath—electromagnetic interaction. It is our hope that the contents will contribute to a synoptic understanding of the overall problem in addition to correlating past and present investigations and highlighting areas which require future study. In the interest of completeness we have included the abstracts of all the papers on the agenda; moreover, those which do not appear in full have been collected as a separate set and published as an A.F.C.R.L. technical documentary report.

This volume is organized into four major sections. The first seven papers (Section A) examine

the thermodynamic and electrical properties of shock-ionized flow fields. Section B deals with the propagation characteristics of plasmas and the reflective properties of plasma-coated objects. Voltage breakdown, an associated problem, is discussed in Section C. The final Section examines a number of experimental techniques for exploring the interaction of the plasma sheath and radiowaves.

We wish to express our sincere thanks to the many people who had a share in the work of planning, organizing, and conducting the symposium. Mr. R. F. TURNER who tirelessly worked to organize and conduct the Symposium in a stimulating and engaging fashion deserves the major credit for its success. The numerous clerical details were competently handled by Miss Alice Cahill of the Electromagnetic Radiation Laboratory.

WALTER ROTMAN
GERALD MELTZ

PLANETARY AND SPACE SCIENCE

Notice to Subscribers

Volume 6 and 7 are being issued as complete volumes containing selected papers on Electromagnetic Effects of Re-entry from the Symposium "*The Plasma Sheath: Its Effects on Communication and Detection*" and the proceedings of the Fourth AFBMD/STL Symposium "*Advances in Ballistic Missiles and Space Technology*." The current issues of the Journal are continuing as parts of Vol. 5.

SECTION A

THERMODYNAMIC AND ELECTRICAL PROPERTIES OF SHOCK-IONIZED FLOW FIELDS

ANALYSIS OF RADIO SIGNAL INTERFERENCE EFFECTS DUE TO IONIZED LAYER AROUND A RE-ENTRY VEHICLE

W. C. TAYLOR

Electromagnetics, Lockheed Aircraft Corporation Missiles and Space Division, Sunnyvale, California

Abstract—The theoretical section of this paper discusses the electromagnetic properties of the ionized shock layer about a missile re-entering the atmosphere; a treatment is then given of the problem of predicting the transmission, through the shock layer, of electromagnetic waves originating on the vehicle. The major portion of this section is given to outlining the important quantitative aspects for calculating the extent of the attenuation problem.

Theoretical curves are given which allow rapid prediction of the attenuation effects due to air ionization once temperature and density are specified in the shock layer. If other sources of free electrons are significant, e.g. ablation products, separate determination of the density distribution must be made. Specific results are given on certain Polaris configurations and trajectories as computed using this method; these predictions are based upon two specific transmitter frequencies. Although the method utilizes the Lorentz theory and the plane wave-plane homogeneous sheet assumption is made, the resulting estimates are shown to agree satisfactorily with signal strength records of actual re-entry tests. A quantitative discussion is given concerning the approximations inherent with the use of the Lorentz theory of conductivity in view of "strong fields" near a transmitter and the velocity dependence of collision cross-sections. A portion is given to possible solutions of the transmission problem suggested by the parameters available in various ranges of temperature and density; particular attention is given to transmitter frequency and position of the antenna. A method is demonstrated for extrapolating the results of a minimum of predictions for a given combination of radiator and re-entry body to include predictions for a wide range of altitudes and velocities.

INTRODUCTION

In the course of re-entry propagation studies, it becomes necessary to investigate the problem from several aspects. This is largely true because of the diverse phenomena involved and because of the infancy of our abilities to analyse and cope with the resulting problems. This paper is devoted to several points of interest which we have discovered in arriving at predictions for a given missile–radiator-trajectory combination, and to presenting some pertinent results of these predictions. Available parameters for lessening the ionization difficulties are discussed.

PROPAGATION PROPERTIES OF PLASMA

The specific properties of a weakly ionized gas which affect the propagation of an electromagnetic wave are semi-quantitatively summarized by a combination of the simple Lorentz conductivity theory with the usual expressions for the plane-wave propagation constants; by applying these principles, α, the attenuation

constant, and β, the phase constant, can be expressed by

$$\alpha = \omega\sqrt{\left\{\frac{\mu\varepsilon}{2}\left[\sqrt{\left(1+\frac{\sigma^2}{\omega^2\varepsilon^2}\right)}-1\right]\right\}}$$
$$= \frac{\omega}{\sqrt{(2)}c}\sqrt{\left\{-\varepsilon_r+\sqrt{\left[\varepsilon_r^2+\frac{\nu^2}{\omega^2}(1-\varepsilon_r)^2\right]}\right\}} \quad (1)$$

and

$$\beta = \omega\sqrt{\left\{\frac{\mu\varepsilon}{2}\left[\sqrt{\left(1+\frac{\sigma^2}{\omega^2\varepsilon^2}\right)}+1\right]\right\}}$$
$$= \frac{\omega}{\sqrt{(2)}c}\sqrt{\left\{+\varepsilon_r+\sqrt{\left[\varepsilon_r^2+\frac{\nu^2}{\omega^2}(1-\varepsilon_r)^2\right]}\right\}} \quad (2)$$

In the above expressions, ω, μ, ϵ and σ have their usual meanings, c is the velocity of light, ν is the mean electron collision frequency, and

$$\varepsilon_r = 1 - \frac{\omega_p^2}{\nu^2+\omega^2}$$

where ω_p is the usual "plasma frequency" or "critical frequency". Equations (1) and (2) possess the advantage that α and β are always real and positive when the positive root signs are used in this form. Now these two equations, which implicitly give α and β as functions of the three "frequency" variables, hardly lend themselves for simple summary of propagation properties; however, if one normalizes α and β by one of these variables, the right-hand expressions become functions of only two (dimensionless) parameters; the result can be represented by a more easily visualized surface, from which a physical interpretation can be inferred. In particular, if one normalizes by ω_p, equation (1) becomes

$$\frac{\alpha}{\omega_p} = \frac{Y}{\sqrt{(2)}c}\left\{-\left(1-\frac{1}{Y^2+V^2}\right)\right.$$
$$\left.+\left[\left\{1-\frac{1}{Y^2+V^2}\right)^2+\frac{V^2}{Y^2(Y^2+V^2)^2}\right]^{1/2}\right\}^{1/2}$$

where $Y = \dfrac{\omega}{\omega_p}$ and $V = \dfrac{\nu}{\omega_p}$

The corresponding surface is approximately indicated in Fig. 1a by contour lines of constant α/ω_p; the dashed lines, and the dark line along $\omega/\omega_p = 1$, divide the surface into four important regions of interest, all of which are encountered in re-entry plasmas.* In Region I, attenuation decreases with increasing ω but increases with increasing collision frequency. Region II is characterized by an essentially constant (α/ω_p), independent of both ω and ν; in fact, the "plateau" of this region is analytically described by $\omega_p > \omega > \nu$, giving from equation (1),

$$\alpha \approx \frac{\omega_p}{c} \quad (3)$$

Region III exhibits a slow variation of (α/ω_p) just opposite to Region I, i.e. (α/ω_p) increases for increasing ω but decreases for increasing ν. Finally, Region IV shows (α/ω_p) independent of ω and varying inversely with ν. The most interesting aspect of the surface is the extreme slope at $\omega/\omega_p \approx 1$ where $\nu/\omega_p < 1$, giving rise to the term "critical frequency." It is due to this behaviour that an increase in ω can effectively solve the transmission problem in higher altitudes (where $\nu/\omega_p < 1$) if ω can exceed ω_p. In lower altitudes, where ν^2 may exceed ω_p^2 even though ionization is still high, the attenuation can be reduced if $\omega^2 \gg \nu^2$. The behavior in Region III is the basis for the proposal in some extreme cases to reduce ω in order to reduce attenuation; obviously such a measure cannot make as drastic a reduction for a given change in ω as can an increase in ω which takes conditions from Region II to I, but it may be the only recourse for some instances. Ideally, it might be desirable to place a low-frequency transmitter near the stagnation point where electron densities are a maximum and a high-frequency transmitter in the position where electron densities are a minimum. When the latter signal is cut off, the low-frequency transmitter has the best chance of transmission, the high ω_p taking it far to the left in Region III. More quantitative inspection shows that a ratio

* A pictorial representation of the attenuation and phase constants in a lossy plasma are shown in Figs. 1b and 2a. The level lines in Figs. 1a and 2a correspond respectively to these surfaces. For convenience, all variables are represented on a logarithmic scale.

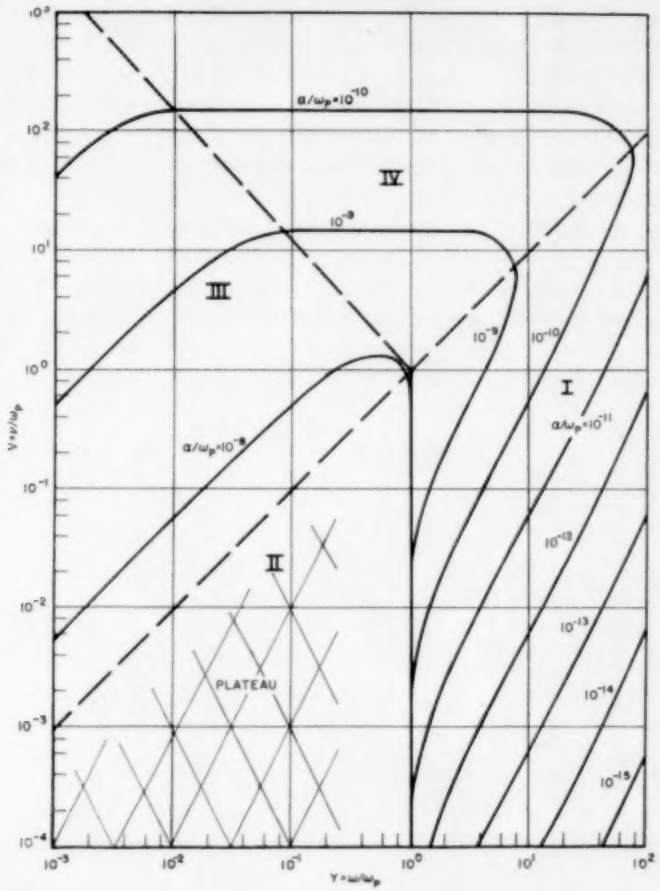

Fig. 1a. Normalized attenuation constant as a function of normalized collision frequency and wave frequency.

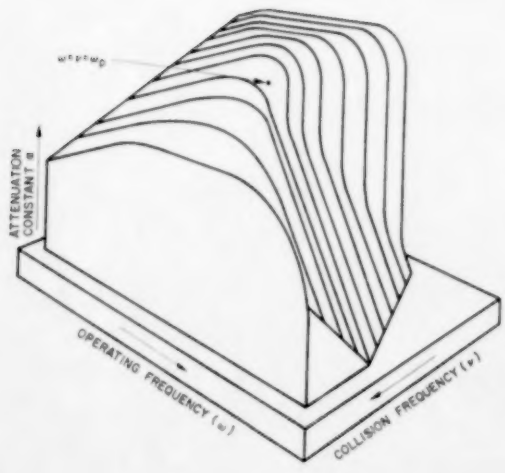

Fig. 1b. Pictorial representation of attenuation constant in a lossy plasma.

as great as 10^3 between the ω's may be required for the low frequency to be advantageous.

The qualitative variation of α with ω_p as well as with ω and ν can be deduced from Fig. 1a. Going from upper right to lower left along any straight line of unity slope (along which $\omega/\nu =$ constant but ω_p increases), it is seen that α/ω_p will always increase or remain constant, which means that α itself will increase rapidly and monotonically with ω_p in all cases. It is for this reason that electron density and, hence, temperature is always quite significant in the determination of plasma-wave interaction.

Fig. 2a was produced from a similar expression for β. Except near the transition zones, Region I is characterized by β/ω_p varying linearly with ω/ω_p, but independent of ν/ω_p; this corresponds to a constant value of β, which is, in fact, the free-space phase constant, $\beta_0 = 2\pi/\lambda_0$. Region II indicates rapid variation in β/ω_p with both co-ordinates, and the most important feature is a deep minimum where ω/ω_p is slightly less than unity. From this "trough", β/ω_p will rise rapidly with any change in ω/ω_p, this variation being linear for decreasing ω/ω_p and quite abrupt at the "critical" zone.

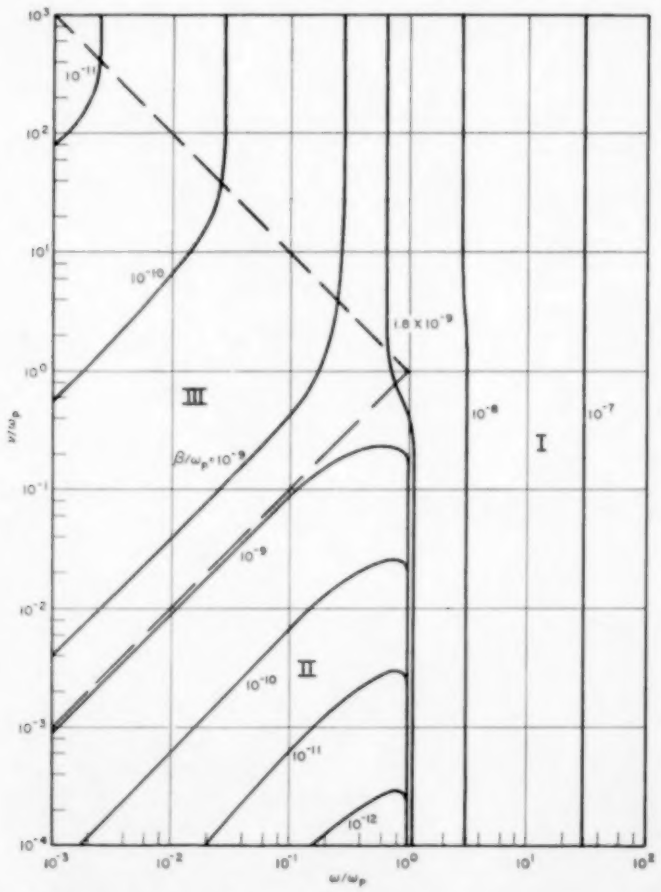

Fig. 2a. Normalized phase constant as a function of normalized collision frequency and wave frequency.

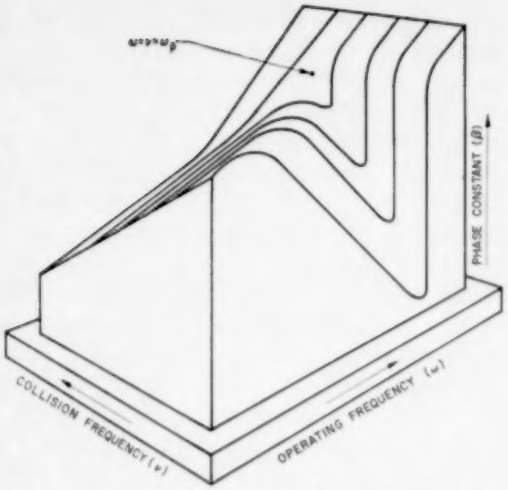

Fig. 2b. Pictorial representation of phase constant in a lossy plasma.

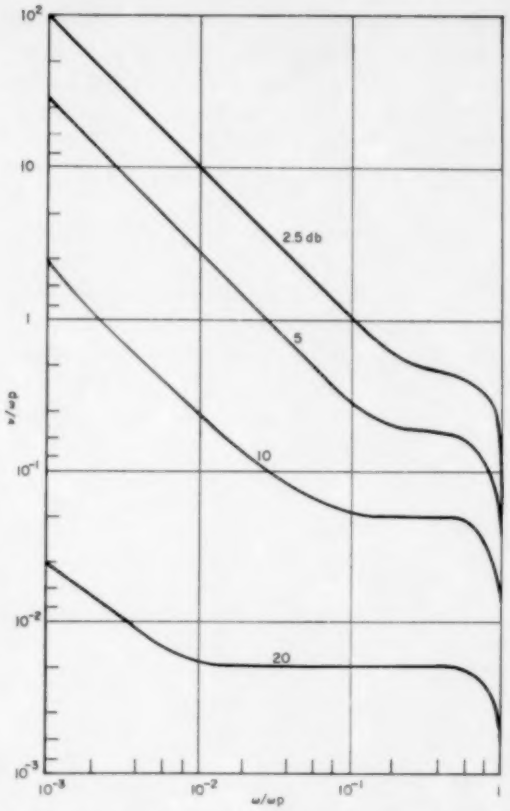

Fig. 3. Boundary attenuation vs. ν/ω_p and ω/ω_p.

The variation of ω in Regions II and III is important in the computation of the reflection co-efficient or, more important to this study, the transmission into a semi-infinite plasma at a discrete boundary. Fig. 3 shows lines of constant transmission coefficient as a function of ω/ω_p and ν/ω_p. The lines are identified by the values of power (dB) effected by the mis-match at this boundary. Note that no attenuation due to propagation over a finite distance is taken into account here.

The Lorentz conductivity theory requires the approximation that the energy imparted to an electron by the electric field (per cycle) is small compared with the thermal energy of the electron. For the case of a 200 Mc/s signal in air at 3000°K, this requires that the maximum field strength, E, not exceed about 0·1 V/cm. The principal effect of stronger fields, disregarding inelastic collisions, is to increase the collision frequency. Hence the usefulness of Figs. 1–3 is not impaired so long as ν is correctly evaluated. Sisco and Fiskin[1] show that for the conditions above and a mean free path of 0·15 cm, an increase of E by a factor of 10, will increase ν by a factor of about 3. The magnitude of the error involved in neglecting these effects is seen to vary widely, depending upon the radiator and its frequency as well as density and pressure. In the case when attenuation is high, the region of space where the above approximation might be poor is expected to be confined to a relatively thin layer near the antenna.

A limiting case for increase of E occurs with r.f. breakdown conditions, which, depending upon particle density and frequency of the radiator, are often met with common transmitters on ballistic missiles during both exit and re-entry. If electron densities due to thermal ionization are below the critical concentration (such that $\omega_p < \omega$), the breakdown losses will usually exceed those determined in the preceding

analysis. However, for $\omega_p > \omega$, the conditions which effect transmission losses in breakdown already exist to the degree that further ionization by the electric field will likely be masked in effect.

ANALYSIS AND PREDICTION OF TOTAL ATTENUATION

The propagation properties of a plasma have been shown to vary all the way from those of highly conducting materials to those of lossy dielectrics and free space. In the case of a plasma where the negative term of the permittivity can play a role more important than the real conductivity, it seems appropriate to define a good propagating medium as one with $\beta^2 \gg \alpha^2$ and a poor one with $\alpha^2 \gtrsim \beta^2$. Due to the rapid variation of α and β in the region $\alpha \approx \beta$, there exists little middle ground in the plasmas between the cases of "good propagator" and "poor propagator". Illustrating this, Figs. 4 and 5 show, respectively, approximate high altitude ($\omega^2 \gg \nu^2$) and low altitude ($\omega^2 \ll \nu^2$) spatial distributions of α and β. These correspond to the computed or assumed temperature and density distributions found varying radially outward from a relatively blunt-nosed, cylindrical body with a velocity of approximately 16,000 ft/sec in both cases. These and other computations lead to a "plasma model" which is illustrated in Fig. 6, for an altitude of approximately 100,000 feet.

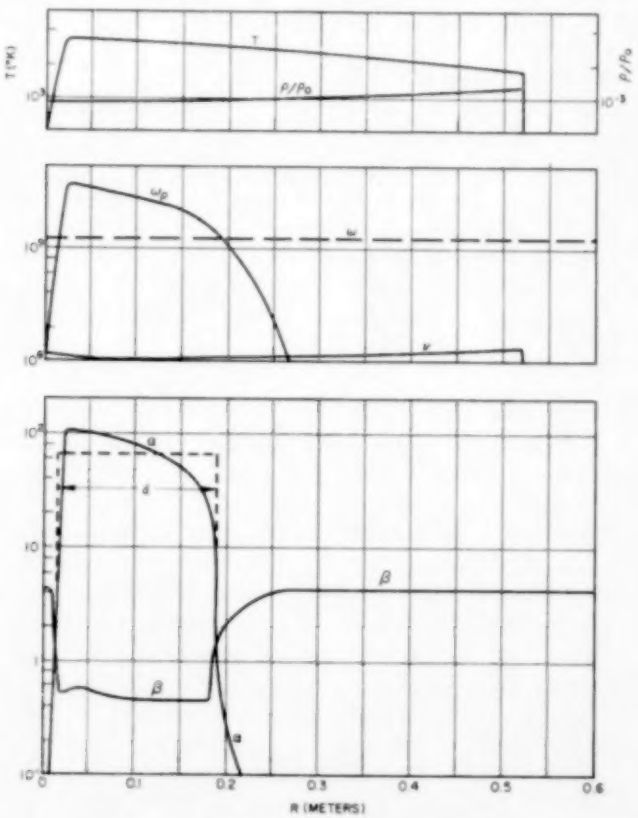

Fig. 4. Broadside profile of plasma properties (high altitude).

In the upper half, corresponding to a 200 Mc/s frequency, the ion sheath is pictured as having a core of metal-like ($\alpha \gg \beta$) propagation properties with varying α, β and thickness "d". This core is "coated" by a dielectric also with varying thickness and loss characteristics, and the thin boundary between core and coating corresponds to the region around $\alpha \approx \beta$. The "core" will extend as far as temperatures are high enough that $\omega_p/\omega > 1$. There seems little doubt that such a core does exist in an undetermined thickness in the shock layer since actual telemetered signals have experienced the great attenuation which would be predicted from this plasma model. It also seems likely that the rapid onset of the fade experienced in some cases corresponds to a quick transition in time into "cut-off" of the layer over the transmitting antenna.

The lower half of Fig. 6 applies to a frequency of 5000 Mc/s, and the model points up vividly the accrued benefits of the 25-fold frequency increase if one utilizes a rearward placement of the transmitting antenna; the altitude for which this figure is drawn, 100,000 ft, is representative of severe ionization for this combination of frequency, placement of radiator and velocity.

The simplest quantitative evaluation of the total attenuation is accomplished by considering the plasma as a flat sheet of infinite extent upon which a plane wave is (normally) incident. The thickness and propagation properties of this "equivalent sheet" are largely determined by

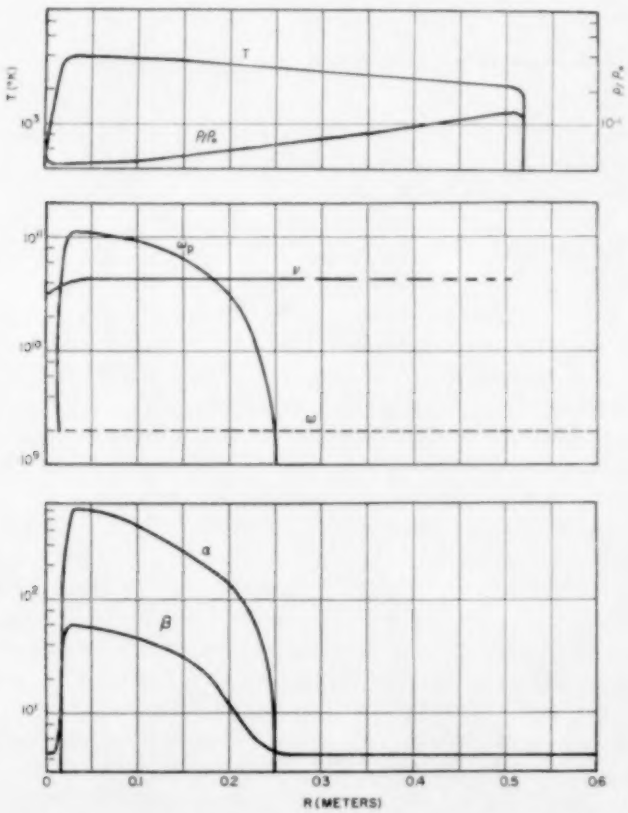

Fig. 5. Broadside profile of plasma properties (low altitude).

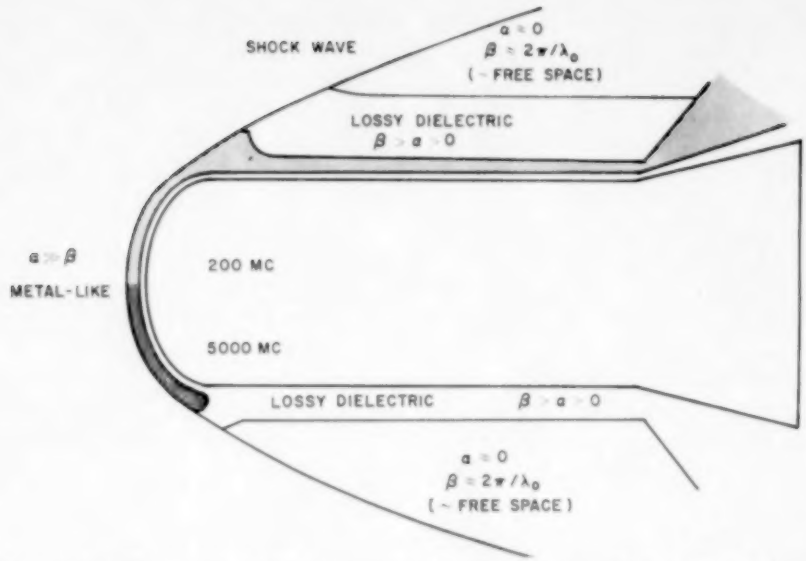

Fig. 6. Simplified plasma properties for two frequencies (altitude = 100,000 ft; velocity = 16,000 ft/sec).

those of the "metal-like" portion of the sheath since its effects are considerably more important than a dielectric coating, the only significant thickness of which is on the side of the sheath opposite the transmitter. The boundaries of this "sheet", located where $\alpha=\beta$, are considered discrete because α and β appear to change rapidly over a thickness which is very small compared with wavelengths considered here.

The radome-type problem of determining the power transmission co-efficient through the sheet is simplified because the extreme attenuation resulting from a single traversal through the sheet will make the effect of multiple reflections small enough to neglect because of the lack of precision available to this prediction procedure. The fraction of the originally incident power transmitted into space beyond the sheet is then computed as the product of the surface mis-match transmission co-efficients and the attenuation factor associated with propagation within the sheet, exp. $(-2\alpha d)$, where d is the thickness of the sheet determined by profiles of the type shown in Figs. 4 and 5. Expressed in decibels of power attenuation, the total attenuation is then estimated by

$$A(\text{dB}) \approx 2 \times 10 \log \frac{1}{|\tau|^2} + 8{\cdot}7 \int_0^d \alpha \, dl \qquad (4)$$

where $|\tau|^2$ is the surface transmission coefficient; the factor 2 is used since there are two boundaries and $|\tau|^2$ is approximately the same for both in the simple broadside model discussed here. The integration in equation (4) is performed numerically to a precision commensurate with that of the profile determination.

Assuming the axis of the vehicle is always parallel to its velocity vector, the above procedure can be applied to a particular antenna location and a particular frequency, and attenuation computed over a wide range of both altitude and velocity; when this information is compiled on a velocity-altitude grid, the results seem generally sensible and useful for interpreting trends even if the quantitative results seem unreliable. The most advantageous presentation we have found for such a compilation is

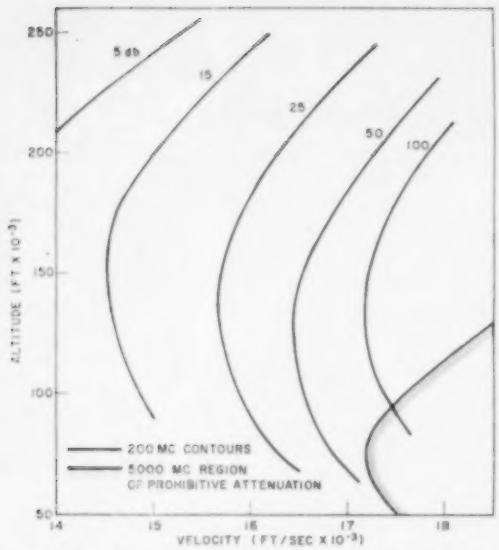

Fig. 7. Predicted attenuation vs. altitude and velocity (broadside radiation).

illustrated in Fig. 7. Here, contour lines of total predicted attenuation are drawn as applying to a 200 Mc/s signal radiated from what appears to be the most favourable region shown in Fig. 6; i.e. that on the rear position of the cylinder. The history of attenuation for a flight can be determined from the intersections of the attenuation contours and the altitude–velocity contour of the flight.

The character of disruption and re-acquisition of a higher frequency signal, such as 5 kMc/s, is expected to be much more abrupt. This can be expected since the higher frequency is successful in suppressing attenuating effects only until the cut-off condition is reached. Once this is the case, however, the specific attenuation is essentially independent of frequency as indicated by equation (3), and can be considered as essentially prohibitive of communication since ω_p will be quite high. Hence the prediction of attenuation of a signal of this frequency or higher reduces to determining the altitude–velocity region where this condition ($\omega_p/\omega > 1$) exists over the antenna. Fig. 7 indicates such a region for the rear-cylinder location. Fortunately, it is reasonable in many cases for the velocity–altitude locus of a particular missile trajectory to by-pass completely (on the high altitude side) this critical region by limiting W/C_DA of the missile, even though velocities are quite high.

CONCLUSIONS

In the preceding discussion, the following points have been presented:

1. Signals in the 200-Mc/s region, radiated from typical antenna locations, will experience significant attenuation during a portion of the trajectory when the peak re-entry velocity of a ballistic missile exceeds about 14,000 ft/sec. Fig. 7 shows approximate predictions for an antenna placed well behind the stagnation area of a cylindrical body.

2. An increase of frequency can increase, decrease or leave essentially unchanged the attenuating effect of the plasma on the signal, depending largely upon the electron concentration. Usually, for environments found over a cylindrical after-body of a missile, increasing the frequency will decrease the attenuation at least in time duration and, for sufficiently high frequencies, may reduce it to a negligibly low level. Fig. 7 shows the advantages of an increase from 200 Mc/s to 5 kMc/s for this antenna position.

3. For simple vehicle shapes, attenuation of a signal (200 Mc/s or greater in frequency) will decrease with the distance of the radiator from the stagnation point, since ionization intensity is less in regions where the vehicle surfaces are more parallel to direction of travel. Irregularities, such as flares, which produce internal shocks are exceptions.

4. Since peak attenuation comes at lower altitudes for higher frequencies, a comparatively rapid decrease of velocity during re-entry is favourable for successful telecommunications when signals in the kilomegacycle range or higher are used.

REFERENCE

1. W. B. Sisco and J. M. Fiskin, *Effect of Relatively Strong Fields on the Propagation of EM Waves Through a Hypersonically Produced Plasma*, Douglas Aircraft Company, LB-25642, Long Beach, Calif. (1958).

COMPARISON OF THE IONIZED SHOCK LAYER ABOUT TWO- AND THREE-DIMENSIONAL BLUNT SHAPES AT HYPERSONIC SPEEDS

H. W. RIDYARD
Aerodynamics Operation, Missile and Space Vehicle Department
General Electric Company, Philadelphia, Pennsylvania

Abstract—A comparative study of the ionized shock layer about simple two and three dimensional blunt shapes has been conducted at a Mach number of 15 and an altitude of 100,000 ft. Various shock layer profiles of the aerodynamic and thermodynamic flow quantities and electron densities are given for the inviscid and viscous regions of the flow. It is seen that the largest electron concentrations are present at the blunt nose of the configurations. Both the shock layer thicknesses and electron densities for the two dimensional bodies are greater than for the three dimensional bodies. The Gravalos numerical method was used to determine the inviscid flow results. The non-linearities in the variations of the resulting flow quantities makes it difficult to predict these results accurately by use of simple approximate methods.

INTRODUCTION

During that portion of the flight trajectory of a hypersonic vehicle which lies in the atmosphere, the kinetic energy of the vehicle will be transmitted to the surrounding air in the form of thermal energy. As long as the vehicle travels at supersonic speeds, the region affected will be enclosed within the bow shock wave. The shock wave may be considered as a surface that coincides with large discontinuities in the flow quantities which exist in the surrounding flow field. As flight speeds increase, the shock wave tends to wrap itself around the vehicle creating a region between the shock wave and the vehicle known to aerodynamicists as the shock layer. A typical arrangement of the shock layer is illustrated schematically in Fig. 1. The blunt-nosed body shown here is of general interest for re-entry purposes.

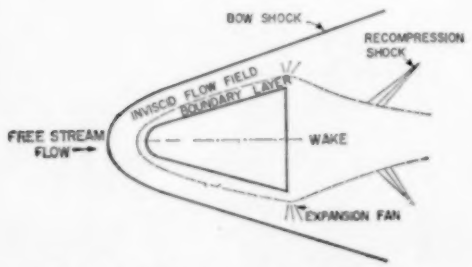

Fig. 1. Flowfield regions in shock layer.

The aerodynamic and thermodynamic structure of the shock layer is highly non-uniform; that is, large variations in temperature and pressure are present with maximum values occurring at the stagnation point or nose where the bow shock is normal to the flight direction. Aft of the stagnation region, the shock wave is oblique to the flight direction and here the temperature and pressure are considerably less than the stagnation values.

At sufficiently high shock layer temperatures the air may dissociate and ionize. Since the thermodynamic properties of the flow are non-uniform, the resulting electron concentrations, which are highly temperature dependent, will vary markedly from point to point. These non-uniformities which are present for a given flight condition will also vary with such factors as

flight velocity, altitude, vehicle configuration and attitude. It is not surprising therefore that the determination of the detailed structure of the shock layer or plasma sheath, if you will, becomes a complex problem in gas dynamics.

For the purpose of analysis the flow in the shock layer is usually divided into separate regions because of the noticeable differences in the character of the flow in these regions. For example, at high Reynolds number conditions viscous shear effects in the nose region are restricted to a relatively thin boundary layer near the surface while the main stream is primarily inviscid in nature. At low Reynolds numbers, of course, the boundary layer thickens and this distinction between the inviscid and viscous layers disappears.

Aft of the body the flow expands and a portion of the gas enters the wake region where the flow is highly turbulent. In this complex flow region mixing occurs across the boundaries and secondary shocks may be present due to the turning of the flow in the stream direction. Because of these complexities the flow in the wake region has not been included in the scope of this investigation. Therefore, let us restrict our attention to the flow over the forebody or nose of the vehicle. For this region numerical techniques have recently become available to determine the detailed structure of the shock layer.

The Aerodynamics Operation of the Missile and Space Vehicle Department of the General Electric Company under sponsorship of the Ballistic Missiles Division of the United States Air Force has been conducting an extensive study of blunt body flow fields using these techniques which will be reported in Ref. (1). It is the purpose of this paper to present a portion of the results from this analytical investigation for simple two and three dimensional blunt shapes. Profiles of the shapes considered are illustrated in Fig. 2. The bodies which were derived from these profiles were either two dimensional wedges of infinite span with

Fig. 2. Body shapes investigated.

cylindrical leading edges or sphere-cone bodies of revolution. For comparison purposes the nose diameters of these bodies were identical and the wedge and cone angles, respectively, for the two and three dimensional bodies (denoted by θ) were the same. The specific values of θ investigated were 0, 10, 20 and 30 degrees; however, the major portion of the results reported herein are for values of θ equal to 0 and 30 degrees.

The analysis was arbitrarily restricted to a region within about 2·5 nose diameters (D_N) from the stagnation point. In this region various shock layer profiles of the aerodynamic and thermodynamic quantities as well as electron densities were obtained and are presented for both the inviscid and viscous regions of the flow at a flight Mach number of 15 and an altitude of 100,000 ft.

METHODS OF ANALYSIS

Before proceeding with a description of the results, it would appear advisable to review the

general assumptions and specific methods employed in the analysis.

General Assumptions

Continuum fluid model

The gas dynamic analysis is based on a continuum fluid model. A continuum is defined here in terms of the ratio of the mean free path λ to some pertinent reference dimension such that λ divided by this reference dimension is much less than one for a continuum. A conservative reference dimension for the present analysis would be the shock detachment distance Δ at the stagnation point; hence, $(\lambda/\Delta) \ll 1$ for a continuum by definition.

Evaluating the mean free path at free stream conditions and assuming that a value of $(\lambda/\Delta) = 0{\cdot}1$ is consistent with our definition, it can be shown that a continuum exists up to an altitude of about 200,000–250,000 ft. If we evaluate the mean free path at the relatively higher density conditions of the shock layer, the continuum model may be assumed to be valid up to an altitude of almost 300,000 ft. The present investigation conducted at an altitude of 100,000 ft is well within these limits.

Equilibrium dissociation

A second general assumption is that local chemical and thermodynamic equilibrium exists in the shock layer. By this, it is meant that the chemical reaction rates involved in the dissociation–ionization processes are assumed to be so fast that an equilibrium chemical composition of the gas is present at each point in the shock layer.

Thin boundary layer

Finally, the conventional boundary layer assumption has been made that there exists a thin boundary layer at the surface of the body where viscous effects are important. Hence, the boundary layer is analysed separately from the remainder of the shock layer (that is, the inviscid region), except that the boundary layer analysis requires input conditions from the inviscid layer analysis.

The range of validity of this thin boundary layer assumption may be estimated by considering the "merged" boundary layer parameter δ/Δ; that is, the ratio of the boundary layer thickness δ to the shock layer thickness Δ at the stagnation point. By use of Scala's results[2] for this merged flow parameter the thin boundary layer assumption for a nose diameter D_N of about 1 ft is valid up to about 140,000 ft for the three dimensional nose and up to about 170,000 ft for the two dimensional nose. Once again the present analysis is well within these limits. As a matter of fact, the thin boundary layer assumption should be valid at the present flight conditions for a nose on the order of an inch in diameter.

Inviscid Flow Methods

Two general approaches were considered in analysing the inviscid portion of the flow field. The first of these involved the numerical solution of the entire flow field by use of the method developed by Gravalos *et al.*[3] The second approach involved the application of several approximate methods including supersonic cone and wedge theory,[4] modified Newtonian impact theory,[5] and the blast wave analogy[6] for comparison with the numerical solutions.

Gravalos numerical method

The Gravalos method[3] entails the solution of the equations of motion for the steady flow of a compressible, inviscid, non-heat conducting gas in chemical equilibrium at hypersonic speeds. The pertinent equations of motion are of the elliptic type in the subsonic region behind the detached shock and are of the hyperbolic type in the remainder of the flow which is supersonic. Since conventional numerical methods for the elliptic equations are unstable, an iterative scheme was developed to determine the flow in the transonic region of the shock layer. The solution in this region is used to determine a starting boundary for the downstream supersonic

region which is computed by the method of characteristics.

To date some twenty transonic solutions have been obtained at various trajectory conditions over a Mach number range from 3·5 to 22 at altitudes up to 250,000 ft. These solutions have been obtained mostly for spherical noses. Comparison of the results of a few of these solutions with experimental data are shown in Figs. 3 and 4.

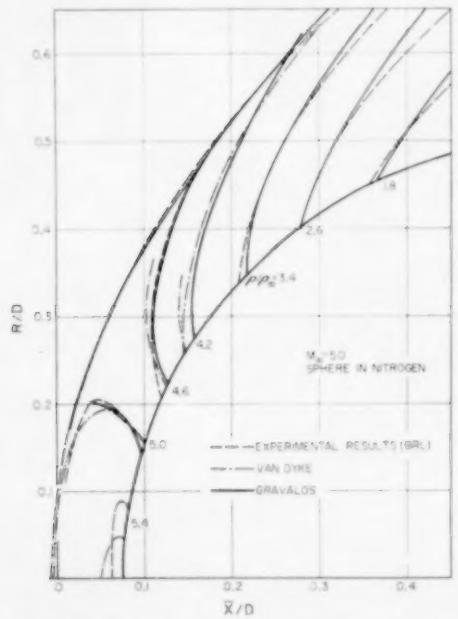

Fig. 3. Comparison of constant density lines in the flow field.

Fig. 3 shows a comparison of constant density lines and shock shapes in nitrogen flow at the nose of a sphere at Mach number 5 as determined by the Gravalos numerical method,[3] the Van Dyke numerical method,[7] and the BRL interferometry measurements of Ref.[8]. The agreement is good considering the difficulties involved in obtaining both the experimental and the theoretical results.

Fig. 4 presents a comparison of pressure distributions over the nose of the sphere and the cylinder considered in the present study. The non-dimensional pressure coefficient $C_p/C_{p\max}$ is plotted against the radial angle $\bar{\theta}$ measured in degrees from the stagnation point where $C_p/C_{p\max}$ is equal to one. Modified Newtonian theory is included with the present two and three dimensional numerical results which are compared to various experimental results obtained by Oliver,[9] Crawford and McCauley[10] and Bogdonoff and Vas.[11] Note that the open symbols refer to data for a sphere and the shaded symbols refer to data for a circular cylinder.

In general the agreement between the experimental and theoretical results is good. The numerical solutions seem to underestimate the experimental data somewhat; however, this discrepancy is probably a Mach number effect. Both experiment and theory indicate that the values of $C_p/C_{p\max}$ are higher for the two dimensional results as compared to the three dimensional results. The simple modified Newtonian theory cannot predict this difference; however, it does compare well with the experimental data except for large values of θ where it erroneously approaches free stream pressure $(C_p/C_{p\max} = 0)$ at $\theta = 90^\circ$.

Approximate methods

Most of the available simple, approximate methods predict only the conditions at the surface of a blunt body and not those in the midst of the surrounding flow field. These latter conditions can only be determined accurately by numerical solutions. This state of affairs is usually satisfactory for those engineers primarily interested in loads and heat transfer at the surface; however, it is not very satisfactory, for example, for the communications engineer. In deriving an approximate technique to evaluate shock layer electron concentrations, it would appear that a minimum goal would be to obtain methods to predict conditions at both the shock and the body and then to make some intelligent assumptions as to the distribution of electrons between these boundaries. The approximate

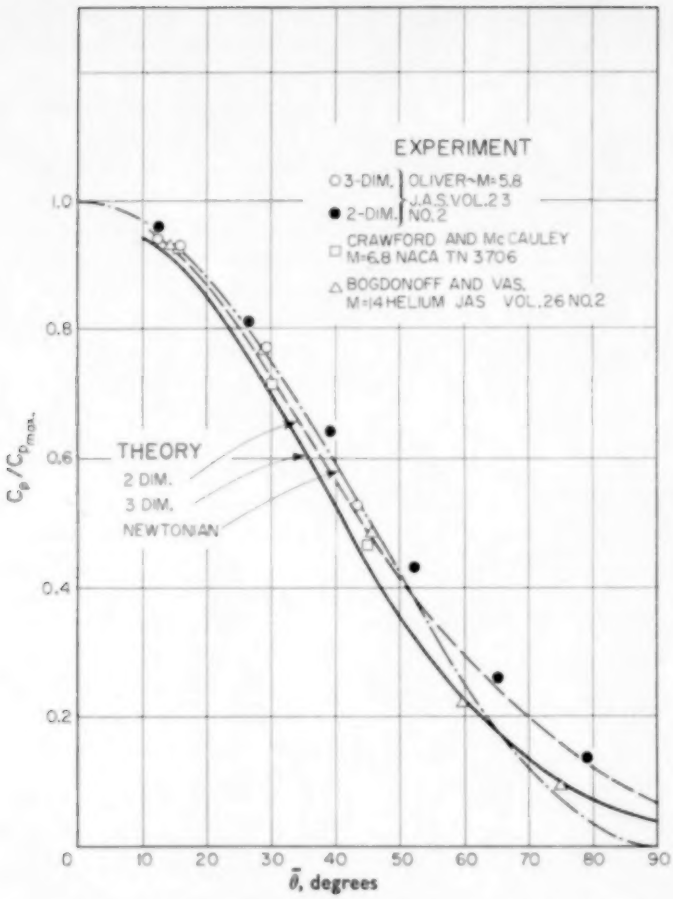

Fig. 4. Comparison of pressure distribution over the nose.

methods discussed herein were chosen with this idea in mind.

For the simple shapes considered in this paper, it is well known that modified Newtonian theory[5] illustrated in Fig. 4 provides good estimates of the pressure over cylindrical or spherical noses at least up to the sonic point on the body. Far downstream it would be expected that surface pressures would asymptotically approach the sharp wedge and pointed cone values of Ref. (4) at least for the higher body angles ($\theta=30°$). Consequently, these methods were investigated with some assurance of success.

For the case where $\theta=0$, that is, the hemisphere cylinder of revolution and the flat plate with the cylindrical leading edge, the blast wave theory as discussed by Lees and Kubota[6] was investigated. One of the advantages of this method is that it is useful for predicting shock shapes for blunt-nosed slender bodies as well as predicting surface pressures. However, it must be noted that the present application of blast wave theory is somewhat academic since it should not be expected to be very accurate in the region within two nose diameters of the stagnation point which is the range of interest selected for this study.

Viscous Flow Method

In order to evaluate the electron concentrations in the boundary layer, it was necessary to make certain assumptions concerning the character of the flow in this region. For conservative reasons the boundary layer was assumed to be turbulent, the wall temperature was taken to be 2000°R and the highly cooled, partially dissociated boundary layer analysis of Probstein *et al.*[12] was applied. One-seventh power non-dimensional velocity profiles were assumed, enthalpy distributions were found by use of the Crocco relation, and the state of the gas and the associated electron concentrations were determined assuming chemical equilibrium. The actual thickness of the boundary layer was found by use of the Kármán momentum integral relation of Ref. (12).

RESULTS AND DISCUSSION

Inviscid Flow Field

Shock shapes

The shock shapes from the application of the Gravalos numerical method are presented in Fig. 5(a) and (b) for the 0° and 30° body angles, respectively. It is evident from these figures that the shock layer thicknesses for the two dimensional solutions are greater than for the three dimensional solutions. However, in the immediate vicinity of the nose the shock shapes are identical for either body angle because the downstream effects of the body shape cannot be felt in this region. As a matter of fact for the zero degree body angle, the sections of the shock shapes shown which extend back about two nose diameters are determined completely by the circular portion of the nose. This result was arrived at by observing that the left-hand characteristic line emanating from the sphere-cylinder juncture (or cylinder-plate juncture) traverses the flow field and intersects the shock downstream from the $x/D_N = 2$ station. This is not however the case for the bodies with $\theta = 30°$ shown in Fig. 5(b) where it is seen that the shock shapes are deflected outward over the downstream portion of the flow field. Here also the shock angles are larger and the shock layers are thinner (more compressed) than for the $\theta = 0°$ case. Note the interesting inflection point in the three dimensional shock for the 30° cone angle body. This wavy shock shape has been observed a number of times in results from various experimental test facilities.

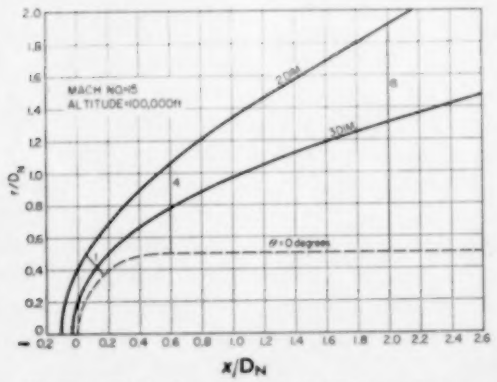

Fig. 5a. Shock shaperom is fnviscid theory 0 deg.

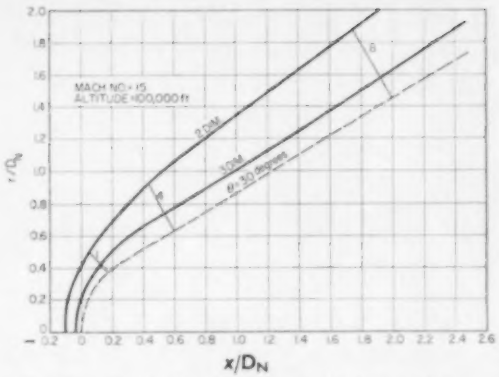

Fig. 5b. Shock shapes from inviscid theory 30 deg.

The blast wave theory predictions of these shock shapes were found to be rather poor as was expected and therefore, they are not included in the comparisons.

The remainder of the inviscid results are presented in the form of longitudinal and normal distributions of the various flow field quantities.

It should be noted that the normal distributions or shock layer profiles were taken from results along the lines indicated by the numbers 1, 4 and 8 in Fig. 5(a) and (b).

Longitudinal pressure and temperature distributions

Longitudinal pressure and temperature distributions along the body surface and at the shock wave are presented in Figs. 6 and 7. The downstream values of these quantities at the shock and at the body for either the two or three dimensional shapes are higher for the 30° body angle than for the 0° body angle, and the two dimensional values are in general higher than the three dimensional values as might have been expected.

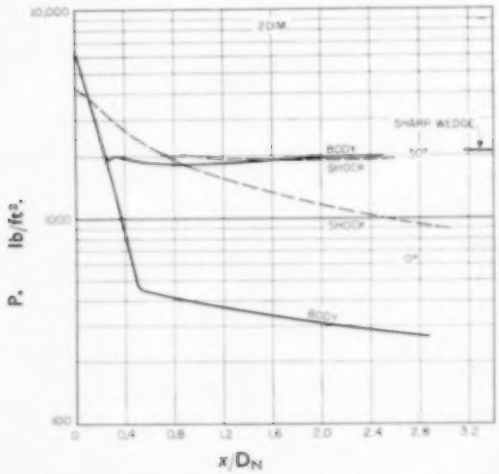

Fig. 6a. Longitudinal pressure distribution 2 dim.

A comparison of the values of the pressures shown in Fig. 6(a) and (b) indicates that for the 30° body angle the pressures at the shock are nearly equal to those at the body surface and are relatively constant over a considerable portion of the body. Furthermore these downstream pressures for $\theta=30°$ are predicted reasonably well for the two and three dimensional cases by the sharp wedge and pointed cone results of

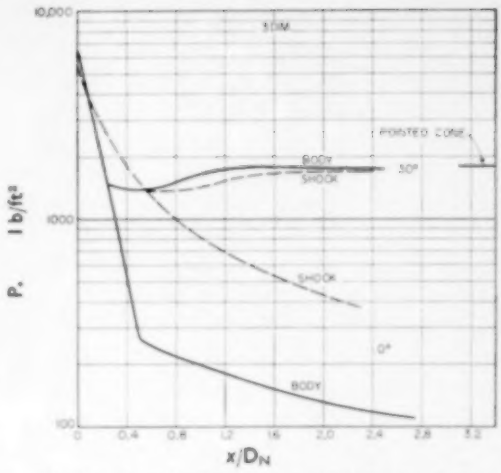

Fig. 6b. Longitudinal pressure distribution 3 dim.

Ref. (4). It will be of some interest to see if the normal distributions between the shock and the body values are bounded by these values. As noted previously in Fig. 4 the large variations in pressure over the circular nose portions of the bodies may be predicted by modified Newtonian theory.[5] It remains to be seen if a method can be developed to predict the gradual decrease in pressure over the aft portion of the bodies with the zero degree body angles. For this purpose the blast wave theory was applied, but it produced rather poor results at both the body and the shock. The possibility still remains, however, that the blast wave theory can be modified semi-empirically to coincide with the shock and body results for a large range of conditions; this approach is currently being pursued.

The longitudinal temperature distributions presented in Fig. 7(a) and (b) are quite similar to the pressure distributions. The temperatures decrease rapidly along the nose from the stagnation value of about 9000°R (or 5000°K) but remain relatively constant over the remainder of the body for both values of θ (0 and 30°). It is important to note, however, that the values of temperature at the shock are considerably lower than at the body so that large variations in electron density may be expected across the

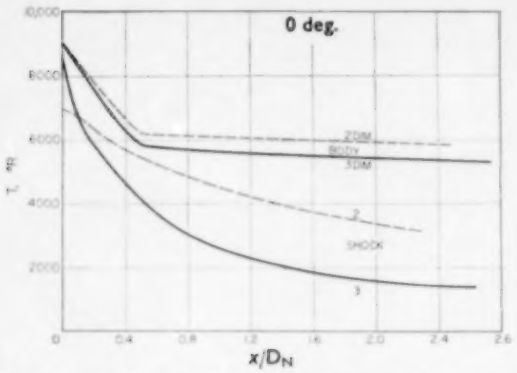

Fig. 7a. Longitudinal temperature distribution 0 deg.

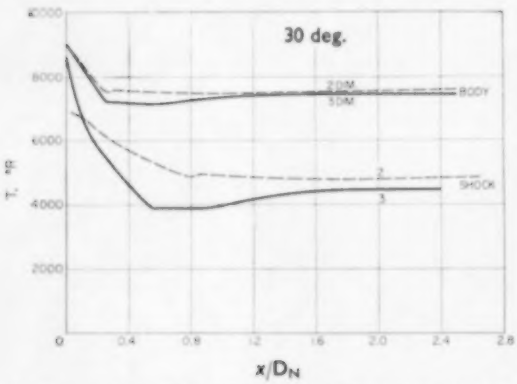

Fig. 7b. Longitudinal temperature distribution 30 deg.

shock layer for both the two and three dimensional shapes.

Variation of pressure with body angle

Since a few results are available for intermediate body angles (values of $\theta=10°$ and 20°), let us consider the variation of pressure with body angle presented in Fig. 8. These results are primarily for the three dimensional bodies and are shown for stations on the body and the shock at the extreme ends of the last shock layer normal, No. 8 (see Fig. 5). Note the non-linear variation of these results with body angle and the relatively close agreement between the shock and body values at angles above 15°. Note also the region of constant pressure at the shock for variations in body angle from 0 to about 10 or

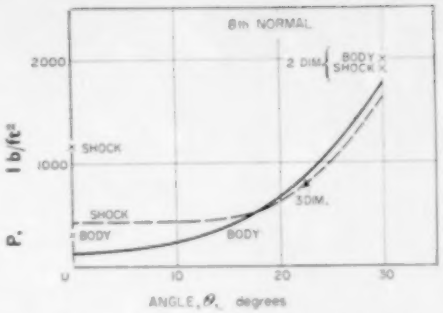

Fig. 8. Variation of pressure with body angle.

12°. This rather interesting result is caused by the fact discussed previously, that the shock pressure at normal No. 8 is not affected by changes in body angle which do not alter the body shape upstream of the region influenced by the appropriate left characteristic line joining the shock and the body at the points of interest.

As a result of these variations with body angle, shock layer electron concentrations may also be expected to vary non-linearly with body angle.

Shock layer profiles

Profiles of pressure P, temperature T, density ρ, velocity V, and electron density N_e are presented in Figs. 9–13 as a function of the non-dimensional distance y/Δ normal to the body surface. Note that Δ is the local shock detachment distance. The major trends of these results as affected by body angle and body station (or normal) for either the two or three dimensional shapes have already been inferred from the longitudinal distributions (Figs. 6 and 7). A few general comments with regard to the local variations across the shock layer are however in order.

There are significant non-linear variations of the flow quantities across the shock layer in the present results. In fact, there are several profiles which contain maximum or minimum values in the interior of the shock layer; see for example Figs. 10(a) or 11(b). The most nearly linear

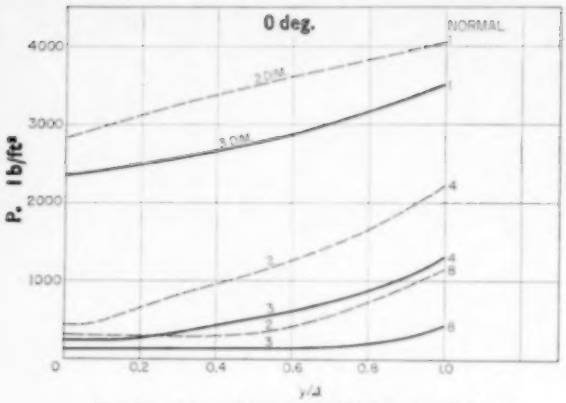

Fig. 9a. Normal pressure distribution 0 deg.

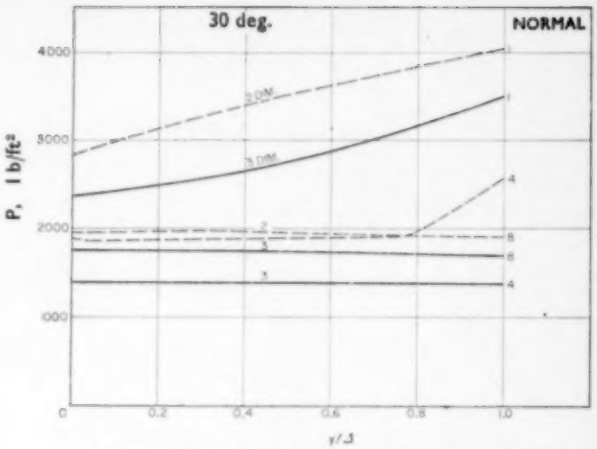

Fig. 9b. Normal pressure distribution 30 deg.

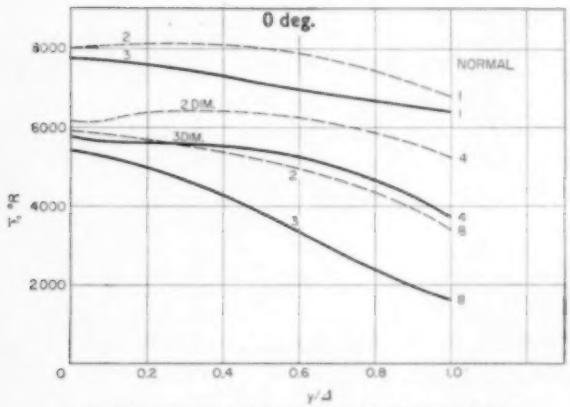

Fig. 10a. Normal temperature distribution 0 deg.

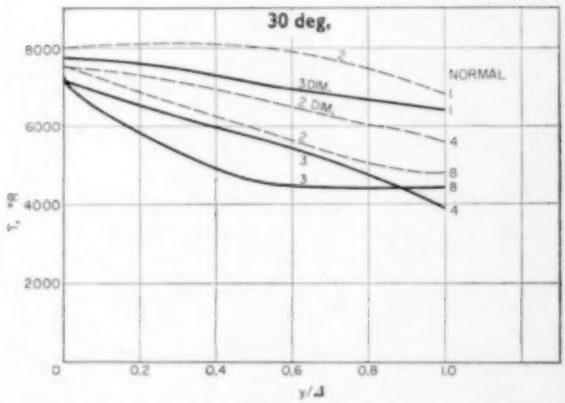

Fig. 10b. Normal temperature distribution 30 deg.

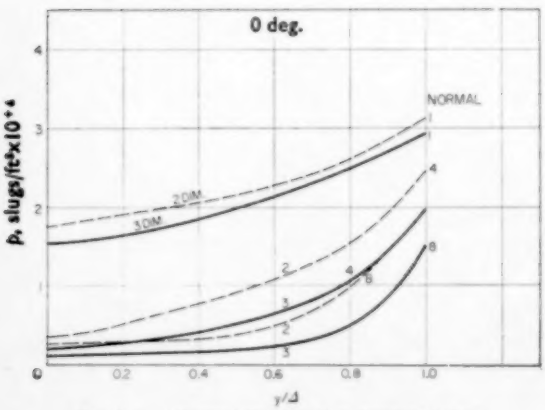

Fig. 11a. Normal density distribution 0 deg.

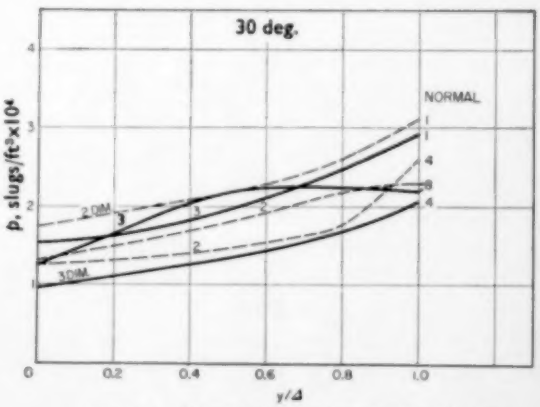

Fig. 11b. Normal density distribution 30 deg.

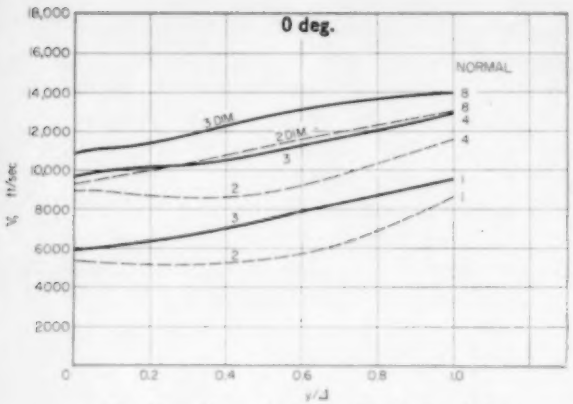

Fig. 12a. Normal velocity distribution 0 deg.

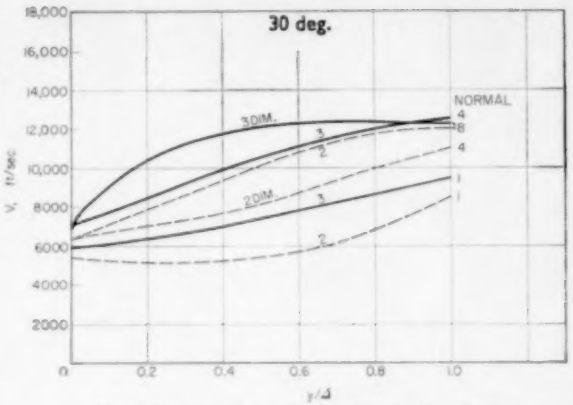

Fig. 12b. Normal velocity distribution 30 deg.

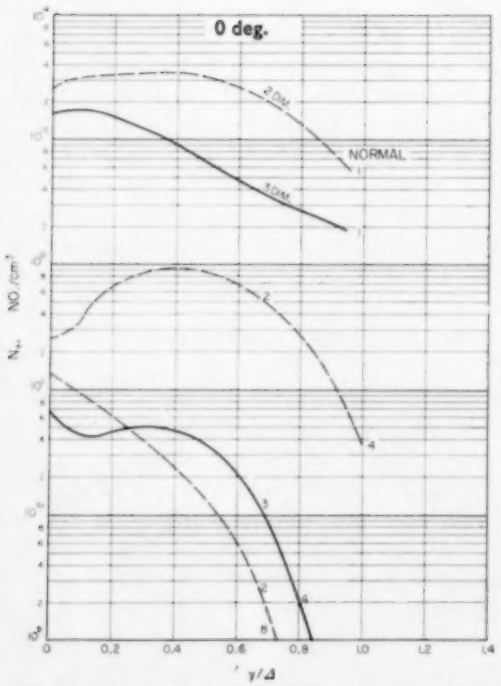

Fig. 13a. Normal electron density distribution 0 deg.

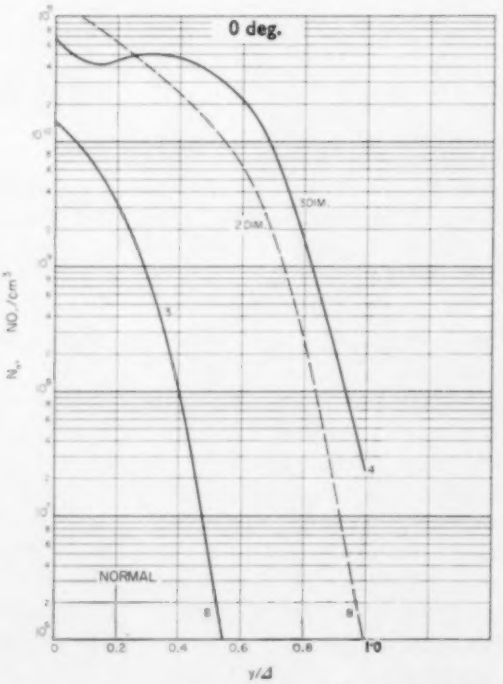

Fig. 13b. Normal electron density distribution 0 deg.

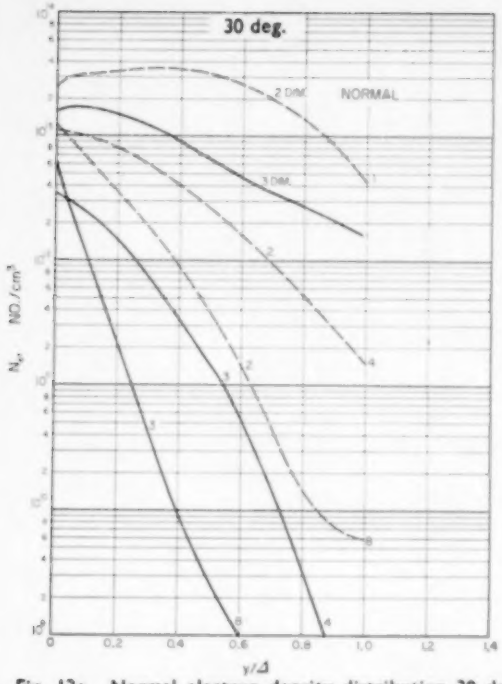

Fig. 13c. Normal electron density distribution 30 deg.

variations are shown in Fig. 9(a) which gives the pressure distributions for the larger body angle, $\theta=30°$. Even here, however, there is an unusual jog in the results for normal No. 4 in the two dimensional flow field.

The origin of this abrupt change in slope has been determined and its validity has been substantiated. This was done by tracing the left characteristic from the jog location to the body surface. It was observed that this characteristic emanated from the point of tangency of the leading edge cylinder and the wedge portions of the body contour. At this point there is a discontinuous change in the curvature of the body and in the slope of the longitudinal body pressure distribution (see Fig. 5). This change in slope is carried over into the flow field along the characteristic lines.

A particularly important consequence of the presence of non-linearities in the normal distributions or profiles arises from their affect on the search for an approximate method of predicting the shock layer structure. Thus, even if one could predict the conditions at the shock and the body by approximate methods in the region of interest here, one would be hard pressed to estimate the distribution between these limits.

Perhaps the most interesting quantity which is included in the shock layer profiles is the electron density N_e, shown in Fig. 13. These values were obtained from the Cornell Tables.[13] It should be noted that the highest value of N_e in the flow is that at the stagnation point ($N_{e_{stag}} \approx 1{\cdot}5 \times 10^{14}$). Fig. 13 shows that the electron densities for a given location are higher for the two dimensional shapes than for the three dimensional shapes. This result becomes of even greater significance when it is remembered that the two dimensional shock layer is considerably thicker than the three dimensional layer (Fig. 5).

The values of N_e for normal No. 1 (on the nose) vary by about an order of magnitude across the shock layer. For normal No. 8 the variation of N_e is about five orders of magnitude.

It must be pointed out that the values of electron density shown in Fig. 13 were determined from the inviscid flow solution and, therefore, near the body surface ($y/\Delta \to 0$) they are not physically correct. In this region the inviscid profiles should be modified to take into account the viscous boundary layer effect.

Viscous Flow Field

The boundary layer electron density profiles are presented in Fig. 14 and the boundary layer thicknesses are given in Fig. 15. The profiles are relatively constant over the boundary layer thickness at the rearward normals for the $\theta=0°$ bodies. Near the surface ($0<y/\delta<0{\cdot}1$) there is a sharp drop in electrons because the assumed wall temperature is so low (2000°R). For the $\theta=30°$ bodies the profiles are all relatively similar with about an order of magnitude variation in the magnitude of N_e over the boundary layer thickness.

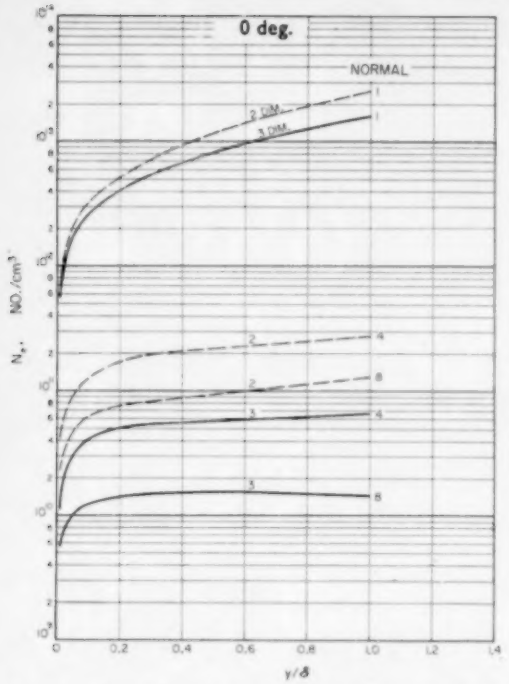

Fig. 14a. Boundary layer electron density profiles 0 deg.

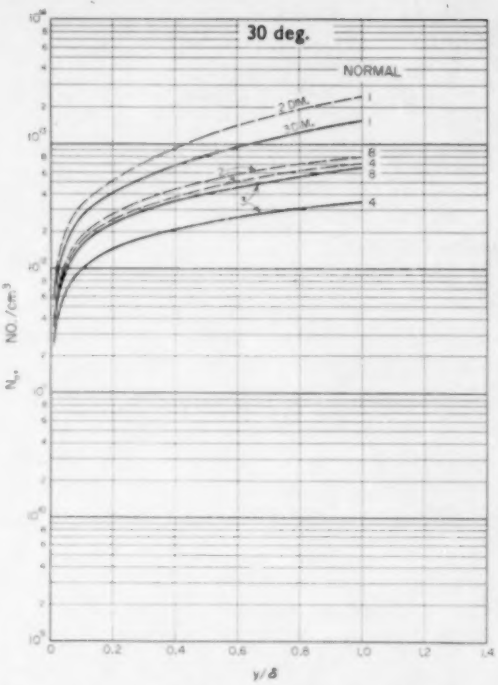

Fig. 14b. Boundary layer electron density profiles 30 deg.

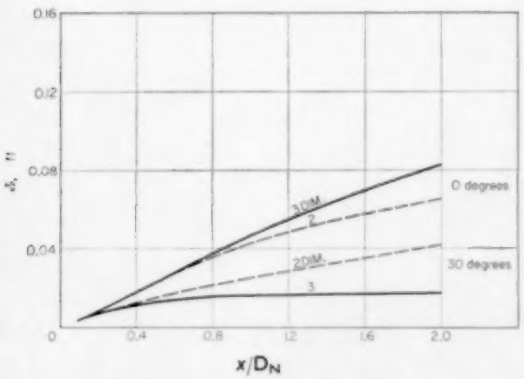

Fig. 15. Boundary layer thickness.

A simple comparison of the values of boundary layer thickness δ (Fig. 15) to the values of the shock layer thickness Δ (Fig. 5) indicates that $(\delta/\Delta) \approx 0{\cdot}1$ for all of the shapes studied. Hence, if the inviscid profiles are modified to include the boundary layer effects; these corrections will be restricted to a rather small region of the flow field. Because of this situation it was felt that the modification of the inviscid profiles was not warranted.

It must be emphasized that the present indication, that the boundary layer corrections are small, is by no means a general result. A similar study of two and three dimensional shock layers for other flight conditions could result in just the opposite effects. For example, if the investigation had been conducted at higher altitudes or higher wall temperatures, the boundary layer electron concentrations would probably have been much larger than those in the inviscid flow field. However, it is hoped that the present results have shed some light on both the qualitative and quantitative aspects of the structure of the plasma sheath.

CONCLUSIONS

A comparative study of the ionized shock layer about simple two and three dimensional

blunt shapes has been conducted at a Mach number of 15 and an altitude of 100,000 ft. A few of the more pertinent conclusions of this study are as follows:

1. The shock layer thicknesses and electron densities for the two dimensional bodies are considerably greater than those for the three dimensional bodies.

2. Body surface pressures predicted by the Gravalos numerical method for blunt-nosed bodies can also be predicted with reasonable accuracy by approximate methods over spherical or cylindrical noses by means of modified Newtonian theory, and over the wedge or conical portions of the contour by means of sharp wedge or pointed cone theory for large body angles ($\theta=30°$). For values of $\theta=0°$, the blast wave theory which is considered to be inaccurate close to the nose of a blunt body was applied as a matter of academic interest, and it gave poor agreement with the numerical results over a region 2·5 nose diameters in length. Blast wave theory predictions of the shock wave shapes were also in poor agreement with the numerical results.

3. Large variations in the thermodynamic quantities are present in both the longitudinal and normal cross sections of the shock layer; consequently, there are large variations in electron densities throughout the shock layer. In general, it is seen that the largest values of electron density are present at the blunt nose of the configuration.

4. The non-linear variations in the flow quantities would appear to make it difficult to derive simple methods for estimating the local shock layer structure.

5. In this analysis the boundary layer effects which were determined assuming turbulent flow and a wall temperature of 2000°R resulted in rather small corrections to the inviscid results.

SYMBOLS

D_N	nose diameter.
L	length.
x/D_N	non-dimensional distance along the centreline of the bodies.
r/D_N	non-dimensional distance from the centreline of the bodies.
$\bar{X}/D$, R/D	non-dimensional co-ordinates in Fig. 3.
δ	boundary layer thickness measured normal to surface.
Δ	shock layer thickness measured normal to surface.
y/δ	non-dimensional distance normal to surface for boundary layer analysis.
y/Δ	non-dimensional distance normal to surface for inviscid layer analysis.
$C_p/C_{p\,max}$	non-dimensional pressure coefficient.
M	Mach number.
N_e	electron density, No./c.c.
P	pressure, lb/ft².
ρ	density, lb sec²/ft⁴.
T	temperature, °R.
V	velocity, ft/sec.
θ	body angle measured with respect to centreline.
$\bar{\theta}$	complement of body angle, used in Fig. 4.

Subscripts refer to

∞	free stream.
max	stagnation value.
N	nose.
e	electrons.

REFERENCES

1. V. A. Langelo, S. L. Stamm and E. A. Brong, *Studies of the Flow Field in the Shock Layer about some Sphere–Cone Combination with Air in Chemical Equilibrium* (to be published).
2. S. M. Scala, *Amer. Rocket Soc. Jour.* **29**, 520 (1959).
3. F. G. Gravalos, I. H. Edelfelt and H. W. Emmons, *The Supersonic Flow About a Blunt Body of Revolution for Gases at Chemical Equilibrium*, Gen. Electr. MOSD, TIS No. R58SD245, (1958).
4. Ames Research Staff, *Equations, Tables and Charts for Compressible Flow*, NACA Rep. 1135 (1953).
5. J. A. Penland, *Aerodynamic Characteristics of a Circular Cylinder at Mach Number 6.86 and Angles of Attack up to 90°*, NACA TN 3861 (1957).
6. L. Lees and T. Kubota, *J. Aero. Sci.*, **24**, 195 (1957).
7. M. D. Van Dyke, and H. D. Gordon, *Supersonic Flow Past a Family of Blunt Axisymmetric Bodies*, NASA Rep. 1 (1959).

8. R. Sedney and G. D. Kahl, *Interferometric Study of the Hypersonic Blunt Body Problem*, Aberdeen Proving Ground, Maryland, B.R.L. Report 1100, April 1960.
9. R. E. Oliver, *J. Aero. Sci.* **23,** 177 (1956).
10. D. H. Crawford and W. D. McCauley, *Investigation of the Laminar Aerodynamic Heat-Transfer Characteristics of a Hemisphere-Cylinder in the Langley 11-in. Hypersonic Tunnel at a Mach Number of 6.8*, NACA Rep. 1313 (1957).
11. S. M. Bogdonoff, and I. E. Vas, *J. Aero. Sci.* **26,** 65 (1959).
12. R. F. Probstein, MacC. Adams and P. H. Rose, *Jet Propulsion*, **28,** 56 (1958).
13. J. C. Logan, Jr., and C. E. Treanor, *Tables of Thermodynamic Properties of Air from 3000° K to 10,000° K at Intervals of 100° K*, Cornell Aero. Lab., Buffalo, N.Y., Rep. No. BE-1007-3-A (Jan. 1957).

COLLISION FREQUENCY ASSOCIATED WITH HIGH TEMPERATURE AIR AND SCATTERING CROSS-SECTIONS OF THE CONSTITUENTS

I. P. SHKAROFSKY, M. P. BACHYNSKI and T. W. JOHNSTON
RCA Victor Company, Ltd., Research Laboratories, Montreal, Canada

Abstract—The plasma sheath acts as a lossy medium for electromagnetic waves, the loss being caused mainly by elastic collisions of electrons with the gas molecules, atoms and ions. In this paper, scattering cross-sections of electrons with neutral air particles are assembled from available experimental and theoretical data and are analysed. Those determinations which appear most reliable are chosen for calculating the variation of the collision cross-section with velocity for each component of air. Since the concentration of equilibrium constituents of air is dependent on temperature and density, the collision frequency, after summing over all neutral components, can be obtained as a function of three variables—temperature, density and electron velocity. One can also evaluate a collision frequency of electrons with ions as a function of these three variables. The total collision frequency is obtained by adding the collision frequency of electrons with neutral particles to the collision frequency of electrons with ions. The concept of a velocity-dependent collision frequency with ions is significant since it can be applied to partially ionized gases and to cases where a r.f. electric field exists.

The effective collision frequency can be obtained as a simple function of temperature and density by averaging over a Maxwellian distribution only in certain limiting cases, viz. very high or low ratios of r.f. to collision frequency. The limitations of various averaging techniques are discussed.

The above procedure is more exact than converting velocity to temperature directly through the relation 1 eV = 3/2 kT. Admittedly, the error in this direct conversion is within the spread of the various experimental results.

1. INTRODUCTION

In order to ascertain the interaction of an electromagnetic wave with hot plasmas, it is necessary to know the elastic scattering cross-sections for electron–atom and electron–ion collisions. For a plasma created in air, the situation is complicated by the number of possible different species (N_2, O_2, N, O, NO, A ions) which constitute the plasma. The electron interaction with each of these species is different and to obtain the plasma properties, each collision cross-section must be summed according to the number density of each species, and the sum must be averaged.

At present, considerable confusion exists over the values of the scattering cross-sections, the method of including ion effects, and the correct averaging techniques necessary to describe the actual physical situation. This work was undertaken in an attempt to resolve these difficulties, and hence arrive at correct values for the collision frequency of high temperature air, from which one can calculate the phase and attenuation parameters of an electromagnetic wave propagating in the plasma.

In evaluating the collision frequency, it is customary[1, 2] to employ the cross-sections assembled by Massey and Burhop[3] for electron interactions with neutral particles. Massey and Burhop give references for their data and claim that the cross-sections are averaged over a Maxwellian distribution. Upon investigating more carefully the original sources, it is at times difficult to relate the original data with those plotted in the text.

Another text by Healey and Reed[4] indicates that results derived from earlier d.c. experiments must be corrected due to errors in the averaging of quantities. In the initial experiments of Townsend and his students (1920–1925), who measured the motion of electrons in gases,[5] the correct integral form of the drift-velocity and diffusion-coefficient equations were unknown. Hence the values determined from their approximate relations are somewhat in error. Healey and Reed give correction factors which differ for Maxwellian and Druyvesteyn distributions in velocity.

In this paper, all available cross-sections measured or calculated for the major constituents of air, viz. N_2, O_2, NO, N, O, A, are assembled and the most reliable determination is chosen for NO, N, O and A. For N_2 and O_2 the accurate measurements by Nielsen and Bradbury[6] on drift velocity are combined with recent measurements by Crompton and Huxley[7] on ratio of drift velocity to diffusion coefficient, to provide reliable values for these two cross-sections. When necessary, the experimental values are corrected for (a) Maxwellian or (b) Druyvesteyn distribution in velocity. The recent data on N_2 and O_2 are also analysed by a more exact method employed for hydrogen by Bekefi and Brown.[8] This latter method gives the cross-section as a function of electron velocity, rather than a function of mean velocity. The advantage of evaluating the electron scattering cross-section as a function of velocity is that it can then be directly inserted into the integral form of the conductivity equation, and an accurate average can be obtained, as shown later.

For plasmas with a degree of ionization greater than about 1 per cent, electron interactions with the positive ions must be included. Here again, there is a multitude of incorrect approaches. The difficulty arises from the fact that the derivation of the conductivity equation for this case by Spitzer[9] applies only to a fully ionized gas and to d.c. This final result appears as an algebraic equation already integrated over electron velocity and depends on electron density and temperature. How can one use this result for a weakly ionized gas with an impressed r.f. field? Recent papers[11] tend to use the geometric mean of integrated conductivities for ions and for neutral particles. Clearly such an approach needs to be justified and can only be approximately correct. It seems most reasonable to derive a velocity-dependent collision frequency of electron encounters with ions and to add it to all the other collision frequencies for electron–neutral particle interaction. But how is this defined? The approach used in this paper for radio frequencies less than electron-ion collision frequency is to apply Spitzer and Harm's tabulated results[10] for the velocity-dependent integrand in their conductivity equation before it is integrated. Since velocity-dependent collision frequencies are used rather than integrated conductivities, the arbitrary nature of the calculation is removed.

Many approximate methods exist for averaging the velocity-dependent collision frequency over the velocity distribution. These various methods will be discussed, and rigorous equations for the two limiting cases of high and low radio frequencies compared with the total collision frequency will be derived.

2. THEORETICAL BASIS

In the absence of a d.c. magnetic field, the electronic conductivity σ of a plasma to a r.f. signal of angular frequency ω, due to neutral particle effects, is given by[11, 12]

$$\sigma = v_d ne/E = -\frac{4\pi e^2}{3m}\int_0^\infty \left[\frac{v^3(\nu - j\omega)}{\nu^2+\omega^2}\right]\frac{df_0}{dv}dv \qquad (1)$$

$$= \frac{4\pi e^2}{3m}\int_0^\infty f_0 \frac{d}{dv}\left[\frac{v^3(\nu - j\omega)}{\nu^2+\omega^2}\right]dv \qquad (1a)$$

where e, m, are the electronic charge and mass respectively,

n is the number of electrons per unit volume,

$j = \sqrt{-1}$,

v_d is the electron drift velocity,

E is the electric field (r.m.s. value if a.c., peak value if d.c.),
f_0 is the electron velocity distribution function,
v is the electron velocity, and
ν is the sum of collision frequencies of electrons with neutral particles for momentum transfer.

$$\nu = v\Sigma n_{pi}Q_{mi} \tag{2}$$

n_{pi} is the number of particles per unit volume of the i^{th} species and Q_{mi} is the electron collision cross-section for the i^{th} species for momentum transfer.

The free diffusion coefficient D of electrons in a plasma in the absence of any field is given by[11]

$$D = \frac{4\pi}{3n}\int_0^\infty f_0 \frac{v^4}{\nu} dv \tag{3}$$

The diffusion gives rise to an electron drift equal to the space gradient of $(-Dn)$ divided by n.

Finally the distribution function f_0 for energies below the ionization potential is of the form,[11, 8]

$$f_0 = A\exp -\left\{\int_0^v \left[kT_g + \frac{2e^2E^2}{3m\xi(\nu^2+\omega^2)}\right]^{-1} m\nu dv\right\} \tag{4}$$

where k is Boltzmann's constant,
ξ is the energy loss factor, a function of v,
T_g is the gas temperature,
A is a constant given by

$$n = \int_0^\infty f_0 4\pi v^2 dv.$$

In a shock front, the gas temperature is high. If any impressed field is sufficiently low in amplitude, the temperature term kT_g overweighs the electric field term in equation (4) and f_0 reduces to a Maxwellian distribution.

$$f_0 = A\exp(-mv^2/2kT_g) \tag{5}$$

On the other hand, in a gas discharge, the gas is usually near room temperature and the average electron energy resulting from the impressed field, is much larger than the average gas energy. In the electron energy range above 0·4 eV, the gas temperature is negligible and equation (4) yields

$$f_0 = A\exp\left\{-(3m^2/2e^2E^2)\int_0^v \xi(v^2+\omega^2)\nu dv\right\} \tag{6}$$

The average $\bar{\phi}$ of any quantity ϕ over the velocity distribution function is defined as

$$n\bar{\phi} = 4\pi\int_0^\infty \phi f_0 v^2 dv \tag{7}$$

The collision frequency and cross-section in the above equations are for momentum transfer. They are already averaged over angle of scattering θ as follows:

$$(\nu/n\nu)_i = Q_{mi} = \int_0^\pi 2\pi I_i(v,\theta)(1-\cos\theta)d\theta \tag{8}$$

where I_i is the differential scattering cross-section of gas i.

3. METHODS OF DETERMINING COLLISION CROSS-SECTION

(a) *Experimental*

(i) *Ramsauer method.* In the Ramsauer method of determining cross-section, the number of electrons lost from a beam as it passes through a gas is measured. In travelling a distance x, the number of electrons remaining divided by the initial number is

$$\exp(-n_iQ_i^0x)$$

where Q_i^0 is the scattering cross-section, not for momentum transfer, but averaged in the forward direction as

$$Q_i^0 = \int_0^\pi 2\pi I_i(v,\theta)\sin\theta\, d\theta \tag{9}$$

By measuring $I_i(v,\theta)$, either Q_i^0 or Q_{mi} can be determined by equations (8) and (9). Usually results derived by this method give Q_i^0.

For low electron velocities, equations (8) and (9) do not differ much. Since the beam is usually distributed in velocity the values determined are functions of average energy.

There are four other experimental methods for determining the collision cross-section for momentum transfer.

(ii) *Microwave method.*[13] With a high frequency electromagnetic wave, $\omega \gg \nu$, the ratio of the real to imaginary components of the conductivity is measured (cf. equation (1)). This method can provide the collision frequency for momentum transfer as a function of velocity for energies up to 0·3 eV. For higher energies, this technique has to be combined with one of the other methods;[8] unless ξ is independent of velocity, as in a monatomic gas.

(iii) *Crompton, Huxley–Nielsen, Bradbury method.*[6, 14] An electrical shutter method, developed by Nielsen and Bradbury,[6] is used to measure the drift velocity v_d (cf. equation (1)). This value is then combined with values of v_{dc}/D (cf. equations (1) and 2)) where v_{dc} is the d.c. value of v_d (with $\omega = 0$). This latter ratio is obtained by measuring diffusion perpendicular to a constant d.c. electric field with no magnetic field present. Townsend originated such measurements, and evaluated a coefficient known as the Townsend energy factor k_T, defined as

$$k_T = \frac{m\overline{v^2}/2}{3kT_g/2} = \frac{m\overline{v^2}}{3kT_g} \tag{10}$$

the ratio of electron to gas energy. He thought that k_T is equal to k_1 defined in equation (10a)

$$k_1 = \frac{e}{kT_g}\,\frac{DE}{v_{dc}} \tag{10a}$$

The statement that $k_T \simeq k_1$ is incorrect. In fact, the above equation has to be multiplied by the following dimensionless factor to obtain k_T. (Averages are defined in equation (7)).

$$\frac{k_T}{k_1} = \frac{\overline{\left(\frac{1}{v^2}\,\frac{d}{dv}\,\frac{v^3}{\nu}\right)}\,(\overline{v^2})}{\overline{(3v^2/\nu)}} \tag{10b}$$

Huxley,[14] besides indicating this correction, also modified the geometric set-up for measuring D/v_{dc}. Huxley combined his measurements of k_1 or DE/v_{dc} with Nielsen's to give the momentum transfer cross-section as a function of averaged electron energy, averaged either for a Maxwellian or Druyvesteyn distribution.

This was performed as follows: From equations (1) and (3) for a particular gas

$$\overline{\nu/Q} = \overline{(v^2/\nu)}n_p = 3n_pD = 3k_1v_{dc}/(eE/p) \tag{11}$$

with k_1 given by equation (10a).

$$k_1 = \frac{e}{kT_g}\,\frac{DE}{v_{dc}} = \frac{m}{kT_g}\,\frac{\overline{(v/Q)}}{\overline{\left(\frac{1}{v^2}\,\frac{d}{dv}\,\frac{v^2}{Q}\right)}} \tag{11a}$$

where $p = n_pkT_g$ is the gas pressure.

In their original papers, Huxley *et al.* found it convenient to calculate Q by the constant mean free path procedure. According to this procedure $Q(v)$ is replaced by $Q(\sqrt{\overline{v^2}})$ where $(\sqrt{\overline{v^2}})$ is the mean square velocity averaged over the velocity distribution. For a Maxwellian distribution, for example, this involves replacing v by $\sqrt{(3kT/m)}$. With this procedure, equations (11) and (11a) become

$$Q_m = \frac{\bar{\nu}}{\overline{\nu/Q_m}} = \frac{e}{3}\,\frac{kT_g}{m}\,\frac{1}{\sqrt{k_1}}\,\frac{E/p}{v_{dc}}\sqrt{(2\bar{v}\,\overline{v^{-1}})} \tag{12}$$

and

$$k_1 = \frac{m}{2kT_g}\,\frac{\bar{v}}{\overline{v^{-1}}} \tag{12a}$$

Thus measurements of k_1 or (DE/v_{dc}) and v_{dc} versus E/p are sufficient to give Q_m versus k_1. The constant in equation (12) depends on the velocity averages and hence on the distribution. Q_m is usually plotted versus $\overline{v^2}$ which is calculated from equations (10b) and (10), thus

$$\overline{v^2} = \left(\frac{3kT_g}{m}\right)k_T = \frac{3kT_g}{m}\left(\frac{2\overline{v^{-1}}\,\overline{v^2}}{3\bar{v}}\right)k_1 \tag{12b}$$

The value of $\overline{v^2}$ also depends on the distribution function.

It has recently been recognized that the calculation of Q_m need not rest on the above constant mean free path procedure. Under certain approximations,[8] one can obtain the cross-section directly as a function of velocity. This will now be indicated under conditions when equation (6) holds.

Assume that the collision frequency, ν, and energy loss factor, ξ, are functions of some power of velocity, thus:

$$\nu = \alpha v^h, \qquad \xi = \beta v^l \tag{13}$$

If equation (13) is substituted into equations (6), (1) and (3) for negligible ω, then it can be shown that

$$\frac{ED}{v_{dc}} = \frac{m}{e(3-h)} \frac{\Gamma[(5-h)/(l+2h+2)]}{\Gamma[(3-h)/(l+2h+2)]} \left[\frac{2(l+2h+2)}{3\beta}\left(\frac{eE}{m\alpha}\right)^2\right]^{2/(l+2h+2)} \tag{14}$$

$$v_{dc} = \frac{eE(3-h)}{3m\alpha} \frac{\Gamma[(3-h)/(l+2h+2)]}{\Gamma[3/(l+2h+2)]} \left[\frac{2(l+2h+2)}{3\beta}\left(\frac{eE}{m\alpha}\right)^2\right]^{-h/(l+2h+2)} \tag{15}$$

where Γ signifies a Gamma function.

Experimentally DE/v_d and v_d are measured versus E/p. The slopes of the log DE/v_d and log v_d versus E/p are sufficient to determine the constants h, l. Then from particular points, α and β can be found. Thus this method yields ν, and consequently Q, as a function of velocity.

A word of caution should be inserted. Equation (13) usually cannot approximate the dependence in the complete velocity range zero to infinity required in the integration of equations (1), (3). At best one can hope that the negative exponential in f_0 makes any contribution negligible above the velocity range of interest where equation (13) applies. Usually if h is a fraction less than one, this approximation holds. In any case, this procedure is more accurate than the constant mean free path procedure. The question arises whether the results of these procedures differ sufficiently to warrant the latter method, which is more tedious. At present, the values of the cross-sections are not known sufficiently well and the difference arising from the procedures, which is usually less than 1·1, is much smaller than the spread of cross-sections determined by various methods and authors. However, with new accurate determinations, it will be necessary to apply the more accurate method of deriving the cross-section.

(iv) *Townsend's method.* In this method, DE/v_d is determined as discussed in method (iii). The drift velocity is however obtained differently. A magnetic field is applied perpendicular to the electric field, and the deflection of the beam is measured. A complete discussion can be found in Refs. (4) and (14). Ref. (14) also points out how the original values given by Townsend and his students have to be corrected for a Maxwellian and Druyvesteyn distribution, according to the constant mean free path procedure.

(v) *Bailey's method.* The ratio of DE/v_d is found by diffusion perpendicular to a constant electric field by a set-up essentially similar to (iii) and (iv). The drift velocity is however obtained from the diffusion equation by measurements with the electric field parallel to the magnetic field. This method and corrections are also discussed extensively in Ref. (14).

(b) *Theoretical methods*

Theoretical cross-sections can be deduced from quantum mechanics. For nitrogen and oxygen molecules, the reader is referred to the paper by Fisk[15] for the method used. For atomic oxygen and nitrogen, calculations have been performed by several authors. For the low electron energies, any analysis based on the WBKJ approximation gives erroneous results. One should apply the Hartree–Fock potential including exchange and polarization potentials, and solve the Schroedinger wave equation including these potentials by expanding the solution in spherical harmonics. In initial attempts, with the Hartree–Fock potential,

exchange and polarization were neglected. Finally, it has been shown by Klein and Brueckner[16] that the calculated scattering cross-section can provide values of the photo-detachment cross-section. The latter can be compared with available experimental data. This provides a test for the accuracy of the scattering cross-section.

4. ELECTRON COLLISION FREQUENCIES

(a) *Collision frequency with neutral particles*

The cross-sections, determined by the above methods, can be applied to the calculation of the collision frequency of electrons with neutral particles in high temperature air (3000–12,000°K and higher if required). In this temperature range, the species of concern are those investigated in this paper, namely, N_2 O_2, NO, N, O and A. The concentration n_{pi} of each is given by Gilmore[17] as a function of temperature T_g and gas density ρ. By equation (2),

$$\nu(\rho,T_g,v) = v \sum_i n_{pi}(\rho,T_g)Q_{mi}(v) \qquad (2)$$

The collision frequency depends on concentration (or gas density and temperature) and on electron velocity, and has to be summed over all constituents.

(b) *Inclusion of ion effects for a partially ionized plasma*

Elastic scattering of electrons by positive ions contributes to the conductivity for degrees of ionization as low as 1 per cent. For a completely ionized gas, subject to an applied d.c. field of low amplitude, the conductivity is in m.k.s. units[9–11]

$$\sigma_{\text{ion}} = \gamma_E \frac{2m}{Z \ln \Lambda}\left(\frac{4\pi\varepsilon_0}{e}\right)^2\left(\frac{2kT}{\pi m}\right)^{3/2} \qquad (16)$$

where
$$\Lambda = \frac{4\pi\varepsilon_0 m v^2}{Ze^2}\sqrt{\left[\frac{\varepsilon_0 kT}{ne^2}\right]} \qquad (17)$$

$$\simeq \frac{3(4\pi\varepsilon_0 kT)}{2Ze^2\sqrt{[\pi n]}} \qquad (17a)$$

where ε_0 is permittivity of free space,

T is the electron temperature,
k is Boltzmann's constant,
Z is the charge on the ion (equal to one for a singly ionized gas),
γ_E is a factor which depends on Z. ($\gamma_E = 0{\cdot}582$ for $Z = 1$).

Equation (17a) is obtained from equation (17) by replacing mv^2 by $m\,\overline{v^2} = 3kT$.

For a partially ionized gas, most methods use the geometric mean for the total conductivity, viz.

$$1/\sigma_t = 1/\sigma + 1/\sigma_{\text{ion}} \qquad (18)$$

It will now be shown that this approximation is unnecessary. In the derivation of equation (16), Spitzer and Harm[10] write the following equations before integration over angle or velocity.

$$\sigma_{\text{ion}} = \iiint f^1(v)\frac{ev}{E}\cos\theta\, v^2 \sin\theta\, dv\, d\theta\, d\phi \qquad (19)$$

$$f^1(v) = f_0(v)\, D(x)\cos\theta \qquad (19a)$$

$$x = (mv^2/2kT)^{\frac{1}{2}}$$

$$f_0(v) = n\left(\frac{m}{2\pi kT}\right)^{3/2}\exp\left(-\frac{mv^2}{2kT}\right), \qquad (19b)$$

a Maxwellian distribution.

They also define a quantity A given by

$$A = \frac{mE(4\pi\,\varepsilon_0)^2}{2\pi\, e^3 n \ln\Lambda}\left(\frac{2kT}{m}\right) \qquad (19c)$$

Substituting equation (19a) and integrating only over the angles θ and ϕ in equation (19), one finds

$$\sigma_i = (4\pi\, e/3E)\int D\, f_0\, v^3\, dv \qquad (20)$$

$$= -\left(\frac{4\pi e^2}{3m}\right)\left(\frac{4\pi\varepsilon_0 m}{e^2}\right)^2\left(\frac{2kT}{m}\right)^{3/2}\frac{1}{4\pi n \ln\Lambda}\int_0^\infty \frac{D}{Ax}\frac{df_0}{dv}\, v^3 dv \qquad (20a)$$

The basic assumption in this analysis is that

collisions are binary events. The function D includes effects of electron–electron collisions. In Spitzer and Harm, the function D/A is tabulated for various x and Z for d.c. It can therefore be taken as a known function of velocity.

Compare now the equation for scattering by positive ions, equation (20a), with the equation for scattering by neutral particles, equation (1). This comparison must be made for $\omega = 0$, the situation where equation (20a) applies. Note the presence in equation (1) of the collision frequency for momentum transfer with neutral particles, as function of velocity. One can now define an equivalent expression to equation (20a) as the velocity-dependent collision frequency for momentum transfer with ions. That is, by analogy to equation (1), define ν_{ion} as

$$\sigma_{ion} = \frac{4\pi e^2}{3m} \int \frac{1}{\nu_{ion}} \frac{df_0}{dv} v^3 dv \qquad (20b)$$

From equations (20a) and (20b), one obtains,

$$\nu_{ion} = 4\pi n \left(\frac{e^2}{4\pi\varepsilon_0 m}\right)^2 \left(\frac{m}{2kT}\right)^{3/2} \frac{Ax}{D} \ln \Lambda \qquad (21)$$

One can also define a collision cross-section by

$$Q_{ion} = \frac{\nu_{ion}}{v n_{ion}} = 4\pi Z \left(\frac{e^2}{4\pi\varepsilon_0 m}\right)^2 \left(\frac{m}{2kT}\right)^2 \frac{A}{D} \ln \Lambda \qquad (21a)$$

Spitzer's tabulated values strictly apply to d.c. and probably to $\nu_{ion} > \omega$. For $\omega > \nu_{ion}$, Hwa[20] suggests neglecting electron-electron effects and letting (Ax/D) equal x^{-3}. Here the tabulated values are used in the calculations, since the results indicate that for temperatures less than 6000°K, the contribution of ν_{ion} to the total collision frequency is negligible and hence its exact form is insignificant, and for high temperatures, ν_{ion} is indeed greater than the radio frequency. This method is approximate. A different approach[21], valid for any ω/ν_{ion} ratio and any degree of ionization, is being evaluated. It is based on Landshoff's method[22] of expanding in Laguerre polynomials. One should also mention an analysis by Tchen[23] which indicates that an exact theory would have to account not only for electron–electron effects, but also for the non-Markovian process and for non-binary collisions.

Thus, approximately one can say this of ν_{ion}:

(1) It can be applied to a partially ionized gas by adding collision frequencies for neutral and ionized particles,

$$\nu_{total} = \nu_{ion} + \nu = v \sum_{neutral} n_{pi} Q_{mi} + v n_{ion} Q_{ion} = v \sum_{all} nQ \qquad (22)$$

(2) It can be applied to a.c. cases. The total collision frequency can be inserted in equation (1), and this equation can be evaluated for a radio frequency ω. This eliminates the d.c. restriction in Spitzer and Harm's analysis.

(c) Comparison with other work

After this method of analysis was derived, it was noticed that Sodha[18] has obtained a collision frequency with ions identical to equation (21). He applies it to a hydrogen gas for two cases—a completely ionized gas with a d.c. magnetic field and a d.c. electric field, and a partially ionized gas with only a d.c. electric field. No a.c. electric field cases are considered. Another paper is also of interest. In an analysis of run-away particles in thermonuclear fusion, Dreicer[19] derives an averaged velocity force equation, from which the following collision frequency for collisions of electrons with ions can be deduced.

$$\nu_{ion} = 4\pi n \left(\frac{e^2}{4\pi e_0 m}\right)^2 \left(\frac{m}{2kT}\right)^{3/2} \frac{\psi}{x} \ln \Lambda \qquad (23)$$

where $\psi(x)$ is plotted in Dreicer's paper. Equations (23) and (21) do not agree in numerical values. However, equation (23) is not applicable to this analysis, since it involves averaged velocities for x. That is, it has been derived from the momentum transport equation with the assumption of a displaced Maxwellian distribution.

Other works mentioned above are those in references 20 to 23.

5. RESULTS

All available cross-sections measured for the neutral constituents of air, i.e. N_2, O_2, NO, N, O and A (including the recent data of Crompton[7] for N_2, O_2), have been assembled and plotted in Figs. 1–6. The values were corrected by averaging over (a) Druyvesteyn or (b) Maxwellian distribution by the procedure of constant mean free path (cf. Section 3), and (c) the recent data for N_2, O_2 were analysed by the more exact method of equations (13–15). This latter method gives the cross-section as a function of electron velocity, rather than mean velocity. The assumptions, method used and basis of derivation of the various graphs are given in Tables 1 and 2. From all the available cross-sections for a given gas, the most reliable is chosen.

Table 1. Assumptions and Methods Used in the Various Determinations Given in Figs. 1, 2, 3 and 6

	Fig. 1(a), (b)	Fig. 2(a), (b)	Fig. 3	Fig. 6
Theoretical	11	1		
Experimental	1–10, 12–17	2–17	1–7	1–9
Q^0	1–4, 11	1–4		1–3
Q_m	5–10, 12–17	5–17	1–7	4–9
lev $= m\bar{v}^2/2$ (averaged)	1–10, 15, 16	2–16	1–7	1–5, 7–9
lev $= mv^2/2$ (unaveraged)	11–14, 17	1, 17		6
Ramsauer method	1–4	2–4		1–3
Townsend method	5–8	5–11	1–3, 7	4, 5, 7–9
Bailey method		12–14	4–6	
Huxley–Nielsen method	9, 10, 14–17	15–17		
Microwave method	12, 13			6
Original determination	1–5	2–5, 8, 12	1, 4	1–3, 5, 7
Corrected values subject to a Maxwellian distribution	6, 8(?) 9, 15	6, 9, 11(?), 13, 15	2, 5, 7(?)	4(?), 8
Subject to a Druyvesteyn distribution	7, 10, 16	7, 10, 14, 16	3, 6	9
Subject to a more correct distribution	12–14, 17	17		6

Table 2. Assumptions and Basis for Various Determinations Given in Figs. 4 and 5. All are Theoretical and the Energy is Given by $1\ \text{eV} = m\ v^2/2$

	Fig. 4	Fig. 5
WBKJ approximation		1
Numerical integration	1–3	2–5
Exchange and polarization included in analysis	2, 3	3–5
Results agree with experimental photo-detachment cross-sections of Branscomb	3	5

For N_2, seventeen variations of collision cross-section with electron energy are shown in Fig. 1(a) and (b). These differ markedly from one another but all lie within a factor of 3·5 for electron energies between 0·2 and 1·7 eV. For low energies up to 0·2 eV, the values of numbers 12 and 14 (which turn out to be identical, although determined by totally different techniques) are preferred; for intermediate energies up to 1·8 eV, the latest results of Huxley (number 17) are chosen. A comparison of 15, 16 and 17 is useful. The values for these three differ only within a factor of 1·08, so that the constant

mean free path approximation is better than one may suppose at first sight.

For O_2, seventeen curves of scattering cross-section electron energy are shown in Fig. 2(a) and (b). These differ within a factor of 2·8 between electron energies of 0·2 and 1·7 eV. The values of number 17 are adopted in spite of their somewhat different dependence from the others, because these results are recent and some of the difficulties in experimentation in O_2, such as attachment are recognized. Also they depend on the reliable values of Nielsen and Bradbury for the drift velocity. It is also of interest to note that the three values of numbers 15, 16 and 17 differ only within a factor of 1·07. Thus it seems adequate to use the simpler method of number 15 or 16 to approximate the method used in number 17.

For NO, seven experimental curves are plotted in Fig. 3. These curves differ within a factor of 2 near electron energies of 0·25 eV and less for higher energies. Due to lack of recent measurements, curve 6 is chosen, because a Druyvesteyn distribution represents approximately the condition in the above d.c. gas discharge experiment (with a low temperature gas). (Skinker and

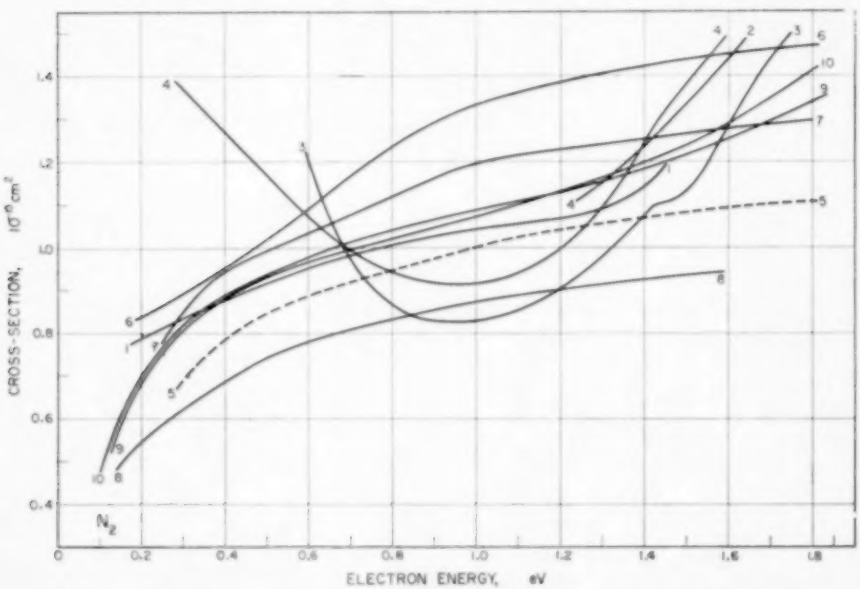

Fig. 1a. Various determinations of the collision cross-section of N_2 as a function of electron energy. Table I in the text indicates the assumption and the methods used in the various determinations. The numbers in the graphs refer to the following references:

1. C. RAMSAUER and R. KOLLATH, *Ann. Phys. Lpz.* **4,** 91 (1930).
2. E. BRUCHE, *Ann. Phys. Lpz.* **82,** 912 (1927).
3. C. E. NORMAND, *Phys. Rev.* **35,** 1217 (1930).
4. H. S. W. MASSEY and E. H. S. BURHOP, *Electronic and Ionic Impact Phenomena.* Oxford (1952). (Based on Ramsauer's method.)
5, 6, 7. J. S. TOWNSEND and V. A. BAILEY, *Phil. Mag.* **42,** 873 (1921). (Numbers refer respectively to original determination, and corrected values subject to a Maxwellian and Druyvesteyn distribution.)
8. H. S. W. MASSEY and E. H. S. BURHOP, *ibid.* (Based on Townsend's method.) Also L. LAMB and S. C. LIN, *J. Appl. Phys.* **28,** 754 (1957).
9, 10. R. W. CROMPTON, and D. J. SUTTON, *Proc. Roy. Soc.* A **215,** 467 (1952). (Subject to a Maxwellian and Druyvesteyn distribution respectively.) They use data of R. A. NIELSEN, *Phys. Rev.* **50,** 950 (1936).

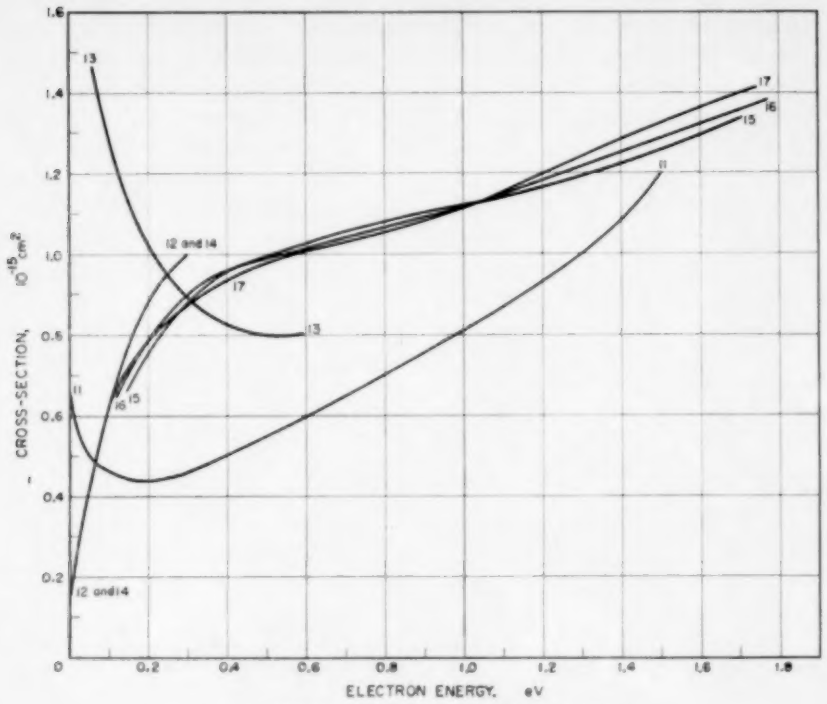

Fig. 1b. Continuation of Fig. 1a for N_2.

11. J. B. FISK, *Phys. Rev.* **49,** 167 (1936) (Theoretical.)
12. A. V. PHELPS et *al. Phys. Rev.* **84,** 559 (1951).
13. J. M. ANDERSON and L. GOLDSTEIN, *Phys. Rev.* **102,** 388 (1956).
14. L. G. H. HUXLEY, to be published.
15, 16, 17. R. W CROMPTON and L. G. H. HUXLEY, private communication. (Subject respectively to a Maxwellian, Druyvesteyn and a more correct distribution). They use data of R. A. NIELSEN, *Phys. Rev.* **50,** 950 (1936).

White's erroneous values in their table, are corrected in this analysis and in curves 1, 2 and 3.)

For atomic nitrogen, three theoretical evaluations are shown in Fig. 4. The values of curve 3 are assumed best, since, in addition to including polarization effects (neglected in curve 1), the photodetachment cross-section determined for curve 3 agrees better with experiment than curve 2 does.

For atomic oxygen, five theoretical estimates are given in Fig. 5. Those of curve 5 are preferred for the same reason as given for atomic nitrogen.

For argon, Fig. 6 indicates nine experimental determinations. The values of number 9 are chosen since this collision frequency is for momentum transfer and is based on the Druyvesteyn distribution.

The plots adopted for calculation of the properties of high temperature air are redrawn in Fig. 7.

The collision frequency of electrons with neutral particles is evaluated from the cross-sections in Fig. 7, and from the species concentration given by Gilmore[17] according to equation (2). The result depends on three variables, electron velocity, gas temperature and density. The electron collision frequency with ions is evaluated from equations (17) and (21) with the help of Gilmore's electron density values. The

two collision frequencies are then added according to equation (22). The calculations are shown in Figs. 8–12 for gas temperatures of 2,000, 4,000, 6,000, 8,000 and 12,000°K, and for gas densities with respect to atmospheric of 1, 10^{-1}, 10^{-2} and 10^{-3}, versus electron velocity in the 0·2–1·8 eV range. The solid curves represent ν_{total}. Whenever ν_{ion} and ν differ from ν_{total} within the energy ranges shown, this is also indicated. For each temperature there exists a value of the abscissa ($eV = mv^2/2e$) equal to the Maxwellian averaged energy ($\overline{mv^2}/2e$) for that temperature. This point is indicated by an arrow. The values in Figs. 8–12 are also presented in Table 3.

The following interesting points should be noted from Figs. 8–12:

(1) Electron interactions with neutral particles tend to cause the collision frequency to increase with electron energy while interactions with ions produce a collision frequency which decreases with energy. When the two are comparable (~6000–8000°K), the total or sum of the two is

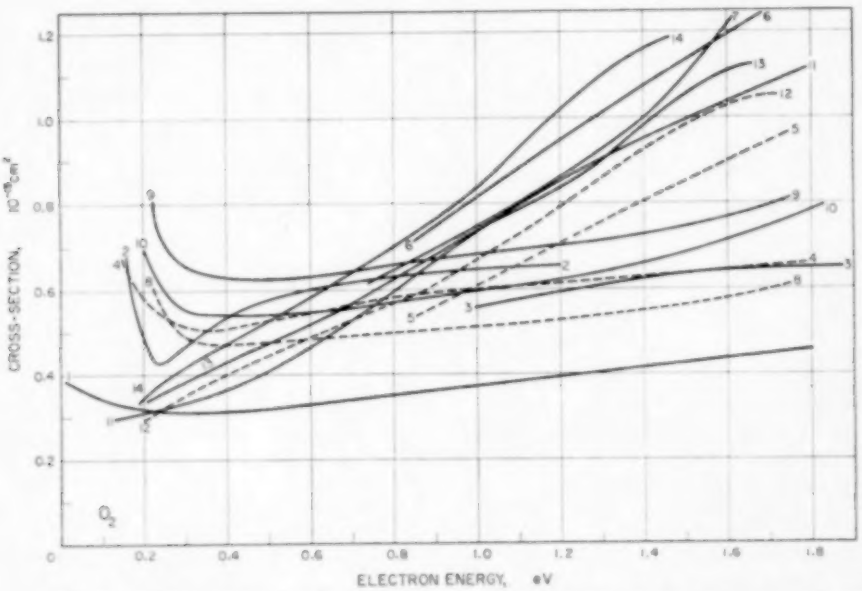

Fig. 2a. Various determination of the collision cross-section for O_2 as a function of electron energy. Table I in the text indicates the assumptions and the methods used in the various determinations. The numbers in the graphs refer to the following references:

1. J. B. FISK, *Phys. Rev.* **49**, 167 (1936). (Theoretical).
2. C. RAMSAUER and R. KOLLATH, *Ann. Phys. Lpz.* **4**, 91 (1930).
3. E. BRUCHE, *Ann. Phys. Lpz.* **82**, 912 (1927); **83**, 1065 (1927).
4. H. S. W. MASSEY and E. H. S. BURHOP, *ibid.* (Based on Ramsauer's method.)
5, 6, 7. J. S. TOWNSEND and V. A. BAILEY, *Phil. Mag.* **42**, 873 (1921). (Original determination and corrected values subject to a Maxwellian and Druyvesteyn distribution respectively.)
8, 9, 10. H. L. BROSE, *Phil. Mag.* **50**, 536 (1925). (Original determination and corrected values subject to a Maxwellian and Druyvesteyn distribution respectively.)
11. H. S. W. MASSEY and E. H. S. BURHOP, *ibid.* (Based on Townsend's method.) Also L. LAMB and S. C. LIN, *J. Appl. Phys.* **28**, 754 (1957).
12, 13, 14. R. H. HEALEY and C. B. KIRKPATRICK. See R. H. HEALEY and J. W. REED, *Behaviour of Slow Electrons in Gases*. Amalgamated Press, Sydney (1941). (Original determination and corrected values subject to a Maxwellian and Druyvesteyn distribution respectively.)

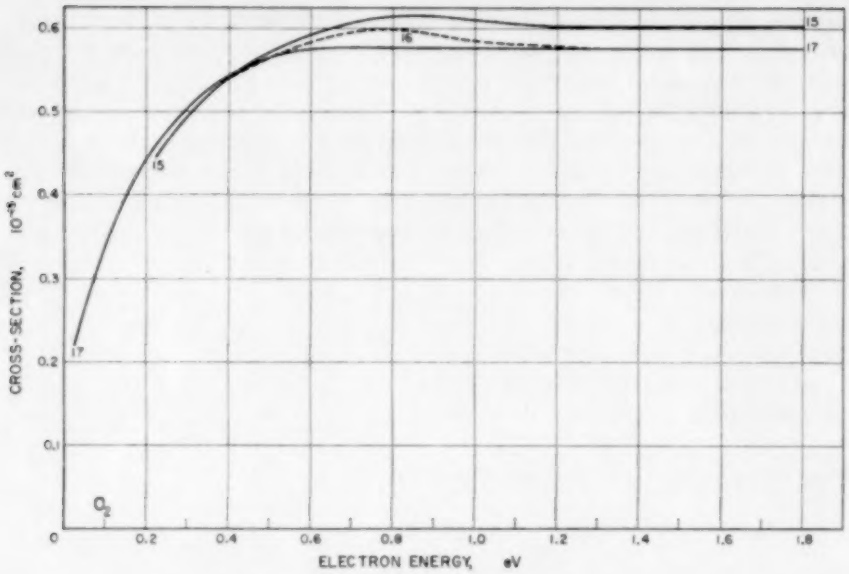

Fig. 2b. Continuation of Fig. 2a for O_2.

15, 16, 17. R. W. CROMPTON and J. G. H. HUXLEY, private communication. (Subject respectively to a Maxwellian, Druyvesteyn and a more correct distribution.) They use data of R. A. NIELSEN and N. E. BRADBURY, *Phys. Rev.* **51**, 69 (1937).

more or less constant with energy. This is significant since for such cases of constant collision frequency, the equations simplify greatly.

(2) The effect of ions first becomes perceptible at 4000°K for the lower densities (10^{-2} and below), and only for low energies.

(3) The effect of neutral particles becomes negligible at 12,000°K for the lower densities (10^{-2} and below) and at low energies.

(4) When the two effects become comparable at 6000 and 8000°K, calculations show that the ratio of electron to neutral particle density is about $0{\cdot}5 \times 10^{-2}$ or less than 1 per cent.

(5) For lower temperatures (3000 and 4000°K), the collision frequency increases with velocity by a factor of 5 in the range of interest and this dependence must be accounted for in equation (1). For high temperatures there is also a strong dependence on energy at the low energy end. This may, however, not be important, since the integration favours the region near the arrow in the graphs and in this region the variation with respect to velocity is less.

(6) For an angular radio frequency of 6×10^{10} c/s, the dividing line between $\omega > \nu_t$ and $\omega < \nu_t$ is near $\rho/\rho_0 = 5 \times 10^{-2}$ up to 6,000°K; it is near 10^{-2} for 8,000°K and is below 10^{-3} for 12,000°K so that for the latter case $\nu_t > \omega$.

Since these calculations are based on Spitzer's d.c. values for ν_{ion}, the graphs apply if ν_{ion} is negligible (6000°K or below) or if $\nu_{ion} > \omega$ (e.g. above 8000°K for X-band).

(7) As the temperature increases, the dependence of collision frequency on density decreases.

Although the collision frequencies shown were not averaged over velocity—this will be performed in subsequent work—the averaging procedures were investigated and are discussed in the next section.

6. AVERAGING PROCEDURES AND EFFECTIVE COLLISION FREQUENCY

The values obtainable from Figs. 8–12 can

be inserted into equation (1), and the integrand evaluated as function of four variables, ω, v, ρ and T. Numerical integration over velocity leaves only three variables, ω, ρ and T. Such a procedure, although possible, is laborious. Also, one may be able to approximate the variation of collision frequency with velocity by a simple empirical relation, which nevertheless may still be too difficult to evaluate directly from equation (1). Is there some simple method to use in the latter situation? It turns out that for either the high frequency case $\omega > \nu_t$ or the low frequency case $\nu_t > \omega$, such relations exist. For intermediate cases when $\omega \simeq \nu_t$ (which may be important in shock fronts, cf. Figs. 8–12), one can at best say that the value will not differ much from the spread in values between the two extremes. It need not however necessarily be equal to a value between the two extremes.

Recall that the average of any quantity ϕ is written as $\bar{\phi}$ and is given by equation (7). Thus equation (1a) can be written—remembering from equation (22) that $\nu_t = v\,\Sigma n\,Q$ is summed over neutral and ionized particles—as

$$\sigma_t = \frac{ne^2}{m}\overline{\left(\frac{1}{3v^2}\,\frac{d}{dv}\,\frac{v^3}{\nu_t + j\omega}\right)} \tag{24}$$

$$= \frac{ne^2}{m}\left[\frac{(1-\frac{v}{3}\,\frac{d}{dv})(\nu_t + j\omega)}{(\nu_t + j\omega)^2}\right] \tag{24a}$$

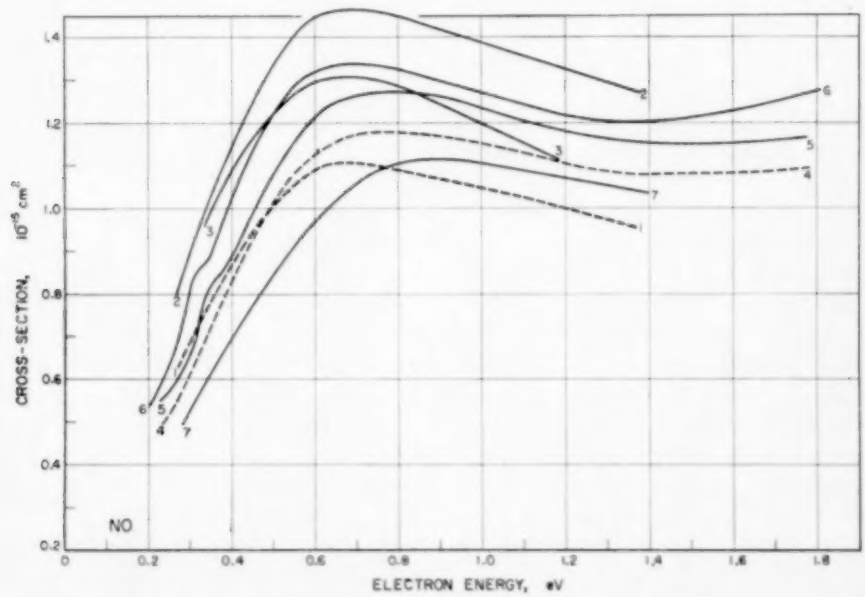

Fig. 3. Various determinations of the collision cross-section of NO as a function of electron energy. Table I in the text indicates the assumptions and the methods used in the various determinations. The numbers in the graphs refer to the following references:

1, 2, 3. M. F. SKINKER and J. V. WHITE, *Phil. Mag.* **46**, 630 (1923). (Original determination and corrected values subject to a Maxwellian and Druyvesteyn distribution, respectively.)

4, 5, 6. V. A. BAILEY and J. M. SOMERVILLE, *Phil. Mag.* **17**, 1169 (1934). (Original determination and corrected values subject to a Maxwellian and Druyvesteyn distribution, respectively.)

7. H. S. W. MASSEY and E. H. S. BURHOP, *ibid.* Also L. LAMB and S. C. LIN, *J. Appl. Phys.* **28**, 754 (1957).

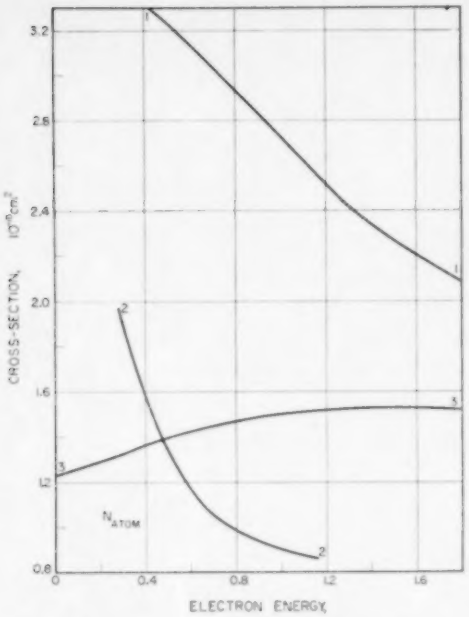

Fig. 4. Collision cross-section for atomic N as a function of electron energy according to the following theoretical determinations. Table 2 in the text indicates the assumptions and the basis.

1. L. B. ROBINSON, *Phys. Rev.* **105,** 922 (1957).
2. L. LAMB and S. C. LIN, *J. Appl. Phys.* **28,** 754 (1957).
3. M. M. KLEIN and K. A. BRUECKNER, *Phys. Rev.* **111,** 1115 (1958).

$$= \frac{ne^2}{m}\left[\frac{2}{3}\overline{\left(\frac{1}{\nu_t + j\omega}\right)} + \frac{j\omega - v^2\dfrac{d}{dv}(\nu_t/v)}{3(j\omega+\nu_t)^2}\right] \qquad (24b)$$

where the bars denote averages.

For a Maxwellian distribution (equation 5), one finds that

$$\frac{df_0}{f_0} = -\frac{m}{kT}vdv$$

so that equation (1) yields

$$\sigma_t = \frac{ne^2}{m}\frac{m}{3kT}\overline{\left(\frac{v^2}{\nu_t + j\omega}\right)} =$$

$$= \frac{ne^2}{m}\frac{1}{v^2}\overline{\left(\frac{v^2}{\nu_t + j\omega}\right)} \text{ (Maxwellian)} \qquad (25)$$

Particular Cases

(a) *Low frequencies or d.c.* ($\nu_t > \omega$)

Equations (24) and (25) reduce to

$$(\sigma_{dc})_t = \frac{ne^2}{m}\overline{\left(\frac{1}{3v^2}\frac{d}{dv}\frac{v^3}{\nu_t}\right)} = \frac{ne^2}{m}\left[\frac{2}{3}\overline{\frac{1}{\nu_t}} - \frac{\overline{v^2\dfrac{d}{dv}(\nu_t/v)}}{3\nu_t^2}\right] \qquad (26)$$

$$= \frac{ne^2}{m}\left(\frac{m}{3kT}\right)\overline{\left(\frac{v^2}{\nu_t}\right)} \quad \text{(Maxwellian distribution)} \qquad (26a)$$

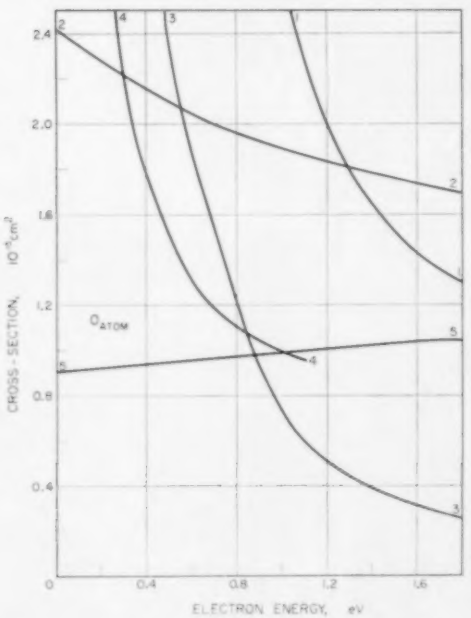

Fig. 5. Collision cross-section for atomic O as a function of electron energy according to the following theoretical determinations. Table 2 in the text indicates the assumptions and the basis.

1. S. K. MITRA *et al. Nature, Lond.* **145,** 1017 (1940).
2. T. YAMANOUCHI, *Prog. Theor. Phys.* **2,** 33 (1947). Also L. B. ROBINSON, *Phys. Rev.* **105,** 922 (1957).
3. P. HAMMERLING *et al. J. Appl. Phys.* **28,** 760 (1957).
4. L. LAMB and S. C. LIN, *J. Appl. Phys.* **28,** 754 (1957). (Same as third with different constants.)
5. M. M. KLEIN and K. A. BRUECKNER, *Phys. Rev.* **111,** 1115 (1958).

Define an equivalent collision frequency by the equation

$$\sigma_t = \frac{ne^2}{m(\nu_{eq} + j\omega)} \tag{27}$$

Equation (27) is the actual conductivity obtained from equation (24) when ν_t is a constant with respect to v. For low frequencies, we define an equivalent collision frequency

$$(\sigma_{dc})_t = ne^2/m\nu_{eq} \tag{28}$$

Equating equations (28) and (26), (26a), yields

$$\frac{1}{\nu_{eq}} = \overline{\left(\frac{1}{3v^2}\frac{d}{dv}\frac{v^3}{\nu_t}\right)} = \overline{\left(\frac{2}{3\nu_t}\right)} - \frac{\overline{v^2\frac{d}{dv}(\nu_t/v)}}{3\nu_t^2} \tag{29}$$

For a Maxwellian distribution this becomes:

$$\frac{1}{\nu_{eq}} = \frac{m}{3kT}\overline{\left(\frac{v^2}{\nu_t}\right)} = \frac{1}{\overline{v^2}}\overline{\left(\frac{v^2}{\nu_t}\right)} \text{ (Maxwellian)} \tag{29a}$$

Note that according to equation (29), $1/\nu_{eq}$ is not proportional to $\overline{1/\nu_t}$ as some authors[1] suppose. This proportionality holds only if

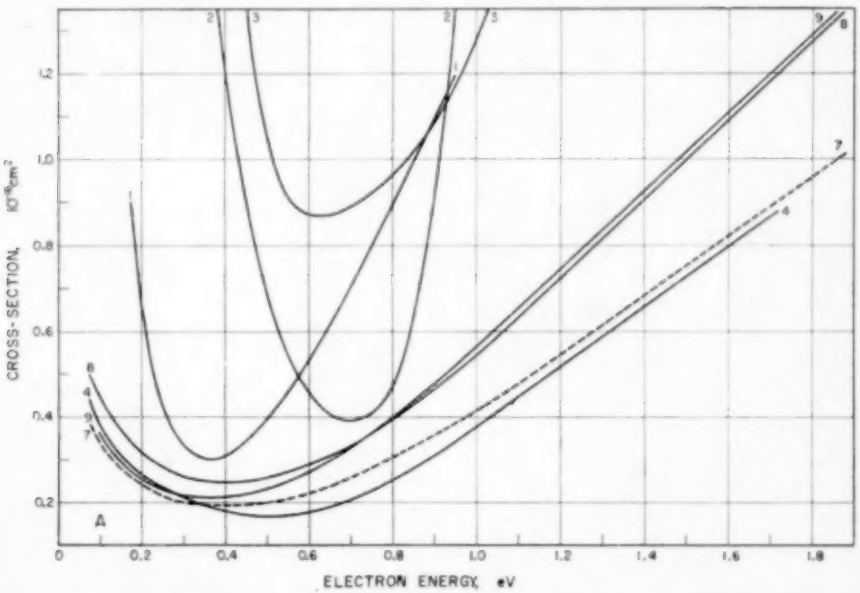

Fig. 6. Various determinations of the collision cross-section for A as a function of electron energy. Table I in the text indicates the assumptions and the methods used in the various determinations. The numbers on the graph refer to the following references:

1. C. RAMSAUER, *Ann. Phys., Lpz.* **64,** 513 (1921).
2. E. RUSCH, Phys. Z. **26,** 748 (1925).
3. C. E. NORMAND, *Phys. Rev.* **35,** 1217 (1930). Also H. S. W. MASSEY and E. H. S. BURHOP, *ibid.* (Based on Ramsauer's method.)
4. H. S. W. MASSEY and E. H. S. BURHOP, *ibid.* (Based on Townsend's method.) Also L. LAMB and S. C. LIN, *J. Appl. Phys.* **28,** 754 (1957). S. C. LIN *et al. J. Appl. Phys.* **26,** 95 (1955).
5. H. B. WAHLIN, *Phys. Rev.* **37,** 260 (1931). (Single point determined.)
6. A. V. PHELPS *et al. Phys. Rev.* **84,** 559 (1951). (Single point determined.)
7, 8, 9. J. S. TOWNSEND and V. A. BAILEY, *Phil. Mag.* **44,** 1033 (1922). (Original determination and corrected values subject to a Maxwellian and Druyvesteyn distribution, respectively.)

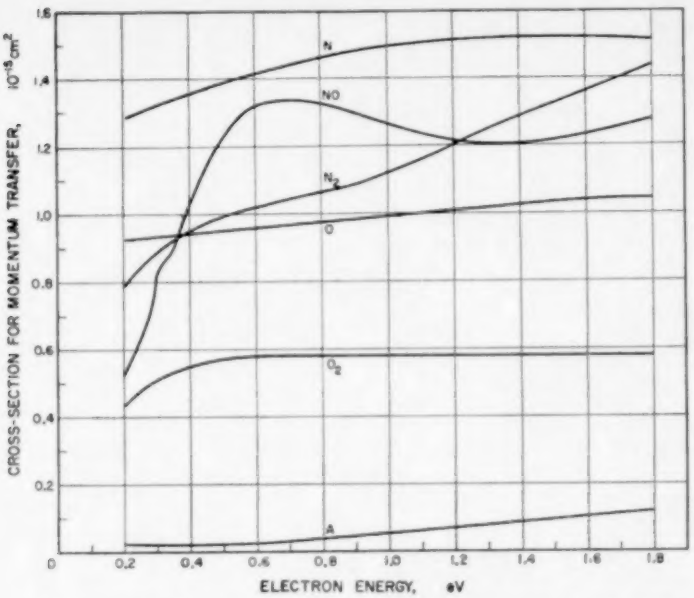

Fig. 7. Collision cross-sections for momentum transfer used in the determination of collision frequency. The values for the components of high temperature air were selected as follows:

N_2 R. W. CROMPTON and J. G. H. HUXLEY, private communication and determined with the correct distribution. They used data of R. A. NIELSEN, *Phys. Rev.* **50**, 950 (1936). (This curve is same as number 17 in Fig. 1b.)

O_2 R. W. CROMPTON and J. G. H. HUXLEY, private communication and determined with the correct distribution. They used data of R. A. NIELSEN and N. E. BRADBURY, *Phys. Rev.* **51**, 69 (1937). (This curve is same as number 17 in Fig. 2b.)

NO V. A. BAILEY and J. M. SOMERVILLE, *Phil. Mag.* **17**, 1169 (1934). Determined with a Druyvesteyn distribution. (Same as number 6 of Fig. 3.)

N M. M. KLEIN and K. A. BRUECKNER, *Phys. Rev.* **111**, 1115 (1958). (Same as number 3 of Fig. 4.)

O M. M. KLEIN and K. A. BRUECKNER, *ibid.* (Same as number 5 of Fig. 5.)

A J. S. TOWNSEND and V. A. BAILEY, *Phil. Mag.* **44**, 1033 (1922). Determined with a Druyvesteyn distribution. (Same as number 9 of Fig. 6.)

$\nu_i/v = \Sigma n Q$ can be assumed independent of velocity (v), in which case it is much simpler to write

$$1/\nu_{eq} \propto \overline{1/v}$$

An assumption used to simplify calculations, which also serves as an indication of typical values is the procedure of constant mean free path (cf. Section 3). This assumption effectively assumes the mean free path $= (1/n\ Q)$ or the collision cross-section to be independent of velocity. One transforms

$$Q(v) \to Q\sqrt{\overline{v^2}}$$

which for a Maxwellian distribution means $Q\ (T)$ is a function of temperature. According to this way of reasoning, equations (26) and (29) become

$$\sigma = \frac{2}{3}\frac{ne^2}{m}\frac{1}{\Sigma nQ}\overline{(1/v)} \text{ (Constant Mean Free Path)} \tag{30}$$

$$1/\nu_{eq} = \frac{2}{3\Sigma nQ}\overline{(1/v)} \text{ (Constant Mean Free Path)}$$

which for a Maxwellian distribution give

$$\sigma_t = \frac{ne^2}{m}\,\frac{8}{3\pi}\,\sqrt{\frac{\pi m}{8kT}}\,\frac{1}{\Sigma nQ} \quad \text{(constant mean free path and Maxwellian)} \tag{30a}$$

$$\nu_{eq} = \frac{3kT}{m}\,\frac{\Sigma nQ}{\bar{v}} = \quad \text{(constant mean free path and Maxwellian)}$$

$$= \frac{3\pi}{8}\,\sqrt{\frac{8kT}{\pi m}}\,\Sigma nQ \tag{30b}$$

(b) *High frequency* ($\omega \gg \nu_t$)

Expanding equations (24) and (25), yields

$$\sigma_t = \frac{ne^2}{jm\omega}\left[1 - \overline{\frac{1}{3v^2}\,\frac{d}{dv}\left(\frac{v^3\nu_t}{j\omega}\right)}\right] \tag{31}$$

$$= \frac{ne^2}{j\omega m}\left[1 - \frac{1}{\overline{v^2}}\left(\overline{\frac{v^2\nu_t}{j\omega}}\right)\right] \quad \text{(Maxwellian)} \tag{31a}$$

If one defines an equivalent high frequency collision frequency by

$$\sigma_t = \frac{ne^2}{m(\nu_{eq} + j\omega)} \quad \rightarrow \quad \frac{ne^2}{mj\omega}\left(1 - \frac{\nu_{eq}}{j\omega}\right)$$

for high frequency; then, by comparison,

$$\nu_{eq} = \overline{\frac{1}{3v^2}\,\frac{d}{dv}\,v^3\nu_t} \tag{32}$$

$$= \left[\frac{1}{\overline{v^2}}\,\overline{(v^2\nu_t)}\right] \quad \text{(Maxwellian)} \tag{32a}$$

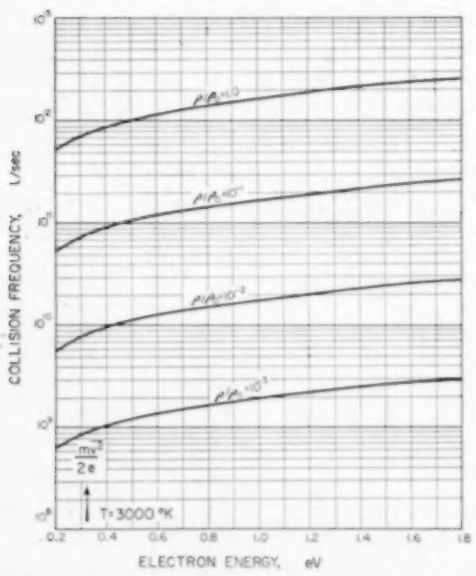

Fig. 8. Collision frequency of momentum transfer of air as a function of electron for 3000°K and various densities. Solid curve represents sum of collision frequencies of electrons with all neutral particles and singly ionized constituents. Dashed curve ——— represents contribution from collisions only with the neutral particles and cross curve + + + represents contribution from collisions only with the ions. The arrow indicates the energy equal to the mean energy for the particular temperature.

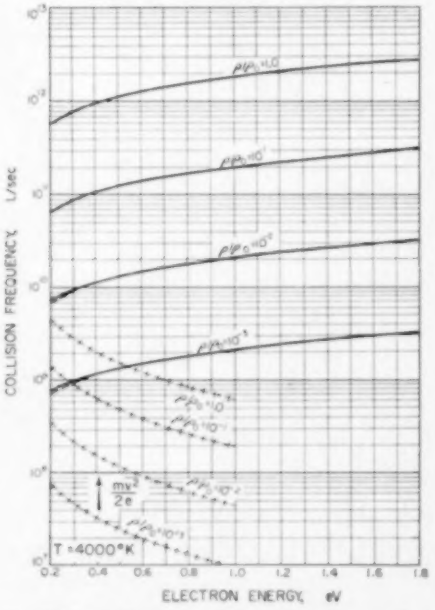

Fig. 9. Collision frequency for momentum transfer of air as a function of electron energy for 4000°K and various densities. Solid curve represents sum of collision frequencies of electrons with all neutral particles and singly ionized constituents. Dashed curve ——— represents contribution from collisions only with the neutral particles and crossed curve + + + represents contribution from collisions only with the ions. The arrow indicates the energy equal to the mean energy for the particular temperature.

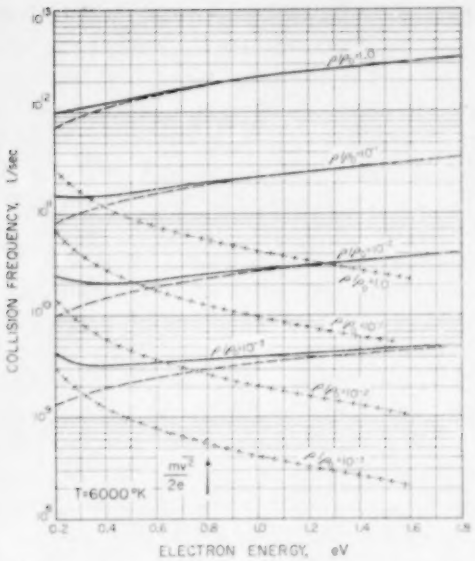

Fig. 10. Collision frequency for momentum transfer of air as a function of electron energy for 6000°K and various densities. Solid curve represents sum of collision frequencies of electrons with all neutral particles and singly ionized constituents. Dashed curve — — — represents contribution from collisions only with the neutral particles and crossed curve + + + represents contribution from collision only with the ions. The arrow indicates the energy equal to the mean energy for the particular temperature.

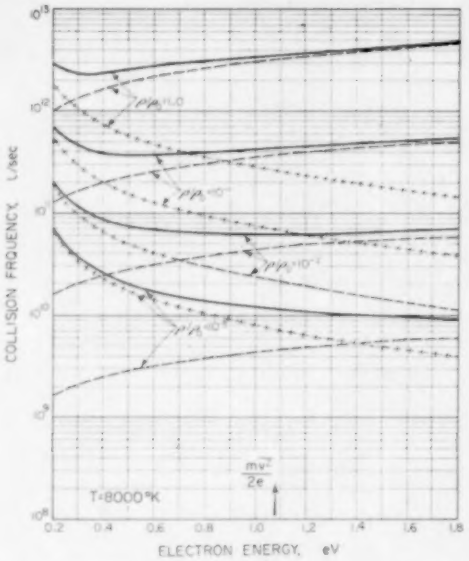

Fig. 11. Collision frequency for momentum transfer of air as a function of electron for 8000°K and various densities. Solid curve represents sum of collision frequencies of electrons with all neutral particles and singly ionized constituents. Dashed curve — — — represents contribution from collisions only with the neutral particles and crossed curve + + + represents contribution from collisions only with the ions. The arrow indicates the energy equal to the mean energy for the particular temperature.

If one now approximates by assuming the procedure of constant mean free path, then

$$\sigma_t = \frac{ne^2}{mj\omega}\left[1 - \frac{4}{3}\frac{\bar{v}}{j\omega}\,\Sigma\, nQ\right] \quad \text{(constant mean free path)} \tag{33}$$

$$\nu_{eq} = \left[\frac{4}{3}\,\bar{v}\,\Sigma\, nQ\right] \quad \text{(constant mean free path)} \tag{33a}$$

$$= \left[\frac{4}{3}\sqrt{\frac{8kT}{\pi m}}\,\Sigma\, nQ\right] \quad \text{(constant mean free path and Maxwellian)}$$

Equations (30a) and (33a) are commonly used. It is, however, obvious that these results are valid only for the approximations of high or low frequency, Maxwellian distribution and constant mean free path. It seems much more reasonable to use instead, for these two limits of high and low frequency, the equations (29) and (32). For a shock front, one can use equations (29a) and (32a).

The averages derived in Sections (a) and (b) are tabulated in Table 4.

(c) *Intermediate frequencies*

The correct method is to use the accurate equations (24) or (25) and integrate numerically over velocity. Any other method leads to complications.

For example, if we define an equivalent ν_{eq} as

$$\frac{1}{\nu_{eq}+j\omega} = \overline{\left(\frac{1}{3v^2}\,\frac{d}{dv}\,\frac{v^3}{\nu_t+j\omega}\right)} \tag{34}$$

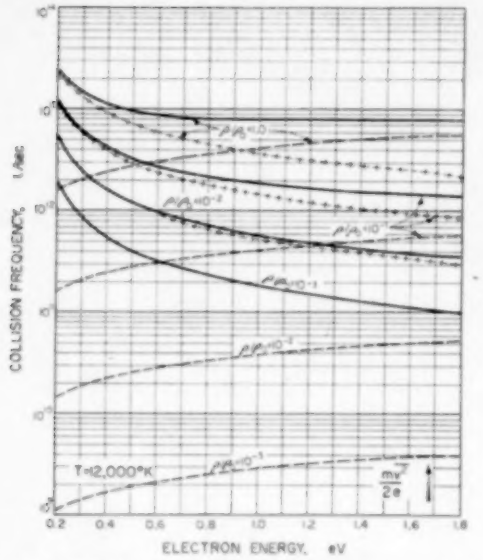

Fig. 12. Collision frequency for momentum transfer of air as a function of electron energy for 12,000°K and various densities. Solid curve represents sum of collision frequencies of electrons with all neutral particles and singly ionized constituents. Dashed curve — — — represents contribution from collisions only with the neutral particles and crossed curve + + + represents contribution from collisions only with the ions. The arrow indicates the energy equal to the mean energy for the particular temperature.

then two different values of ν_{eq} will be determined from the real and imaginary parts of the right hand side. It thus seems that the idea of an equivalent collision frequency or collision cross-section leads to a contradiction in the region where $\nu_t/\omega \simeq 1$, except when ν_t is a constant. As indicated above, ν_t does appear to be constant for high temperature air at intermediate temperatures near 6000° and 8000°K. Fortunately, usual microwave frequencies are of the order of ν_t here. The degree of approximation in using an equivalent collision frequency for lower temperatures has to be deduced. An indication is provided by letting $\nu_t \propto v^2$ (true for N_2 at low electron energies up to 0·12 eV). Then the ratio of equation (29a) and (32a) for high to low frequency cases can be calculated to be 5/3. For intermediate frequencies, the error can be assumed to be within this factor.

Plots of electromagnetic effects are usually represented[2] versus ν_t/ω or ν_t/ω_p. According to the above, such plots may seem to be open to question in the region near $\nu_t/\omega = 1$. In these studies, one can nevertheless define an equivalent ν_{eq} for high frequencies as

$$\nu_{eq} \equiv -j\omega\,\sigma_r/\sigma_i \qquad (35)$$

Table 3. Values of Collision Frequency

T = 3,000°K												
	$\rho/\rho_0 = 1$			$\rho/\rho_0 = 10^{-1}$			$\rho/\rho_0 = 10^{-2}$			$\rho/\rho_0 = 10^{-3}$		
	$n = 1{\cdot}948 \times 10^{11}$/cm³			$n = 7{\cdot}437 \times 10^{10}$			$n = 2{\cdot}279 \times 10^{10}$			$n = 6{\cdot}046 \times 10^{10}$		
eV	ν $\times 10^{11}$	ν_{ion} $\times 10^{7}$	ν_{total} $\times 10^{11}$	ν $\times 10^{10}$	ν_i $\times 10^{7}$	ν_t $\times 10^{10}$	ν $\times 10^{9}$	ν_i $\times 10^{6}$	ν_t $\times 10^{9}$	ν $\times 10^{8}$	ν_i $\times 10^{6}$	ν_t $\times 10^{8}$
0·2	5·10	3·95	5·10	5·24	1·61	5·24	5·64	5·29	5·65	6·38	1·51	6·38
0·3	7·09	2·47	7·09	7·26	1·00	7·26	7·72	3·28	7·72	8·56	0·935	8·57
0·4	8·84	1·78	8·84	9·03	0·718	9·03	9·54	2·35	9·54	10·48	0·669	10·48
0·5	10·35	1·35	10·35	10·56	0·544	10·56	11·12	1·78	11·12	12·1	0·506	12·1
0·6	11·7	1·04	11·7	11·9	0·421	11·9	12·6	1·37	12·6	13·7	0·390	13·7
0·7	12·9	0·820	12·9	13·2	0·330	13·2	13·8	1·08	13·8	15·1	0·305	15·1
0·8	14·0	0·655	14·0	14·3	0·264	14·3	15·0	0·859	15·0	16·3	0·243	16·3
1·0	16·2		16·2	16·6		16·6	17·4		17·4	19·0		19·0
1·2	18·9		18·9	19·3		19·3	20·2		20·2	22·0		22·0
1·4	21·7		21·7	22·1		22·1	23·2		23·2	25·1		25·1
1·6	24·3		24·3	24·8		24·8	25·9		25·9	28·1		28·1
1·8	27·0		27·0	27·5		27·5	28·7		28·7	31·0		31·0

Table 3. (Continued)

$T = 4{,}000°$K

	$\rho/\rho_0 = 1$			$\rho/\rho_0 = 10^{-1}$			$\rho/\rho_0 = 10^{-2}$			$\rho/\rho_0 = 10^{-3}$		
	$n = 3{\cdot}280\times10^{18}$			$n = 9{\cdot}257\times10^{17}$			$n = 1{\cdot}985\times10^{17}$			$n = 3{\cdot}692\times10^{16}$		
eV	ν $\times10^{11}$	ν_i $\times10^{9}$	ν_t $\times10^{11}$	ν $\times10^{10}$	ν_i $\times10^{9}$	ν_t $\times10^{10}$	ν $\times10^{9}$	ν_i $\times10^{8}$	ν_t $\times10^{9}$	ν $\times10^{8}$	ν_i $\times10^{7}$	ν_t $\times10^{8}$
0·2	5·64	4·49	5·68	6·37	1·43	6·51	6·95	3·48	7·30	7·18	7·32	7·91
0·3	7·79	2·69	7·82	8·60	0·848	8·69	9·23	2·05	9·44	9·48	4·28	9·91
0·4	9·62	1·96	9·64	10·57	0·616	10·63	11·23	1·48	11·37	11·47	3·08	11·78
0·5	11·38	1·54	11·39	12·3	0·481	12·3	13·0	1·15	13·1	13·2	2·39	13·5
0·6	12·9	1·25	12·9	13·9	0·389	13·9	14·6	0·929	14·7	14·9	1·92	15·1
0·7	14·2	1·03	14·2	15·3	0·320	15·3	16·1	0·762	16·2	16·4	1·57	16·5
0·8	15·4	0·855	15·4	16·6	0·265	16·6	17·4	0·631	17·5	17·7	1·30	17·9
1·0	17·8	0·603	17·9	19·2	0·186	19·2	20·2	0·442	20·3	20·6	0·908	20·7
1·2	20·5		20·6	22·2		22·2	23·4		23·4	23·8		23·9
1·4	23·4		23·5	25·3		25·3	26·7		26·7	27·2		27·2
1·6	26·2		26·2	28·2		28·2	29·7		29·7	30·3		30·3
1·8	29·0		29·0	31·2		31·2	32·8		32·8	33·4		33·4

Table 3. (Continued)

$T = 6{,}000°$K

	$\rho/\rho_0 = 1$			$\rho/\rho_0 = 10^{-1}$			$\rho/\rho_0 = 10^{-2}$			$\rho/\rho_0 = 10^{-3}$		
	$n = 3{\cdot}237\times10^{19}$			$n = 6{\cdot}207\times10^{18}$			$n = 1{\cdot}108\times10^{18}$			$n = 1{\cdot}980\times10^{17}$		
eV	ν $\times10^{11}$	ν_i $\times10^{11}$	ν_t $\times10^{10}$	ν $\times10^{10}$	ν_i $\times10^{10}$	ν_t $\times10^{10}$	ν $\times10^{9}$	ν_i $\times10^{9}$	ν_t $\times10^{9}$	ν $\times10^{8}$	ν_i $\times10^{9}$	ν_t $\times10^{9}$
0·2	7·07	2·69	9·76	7·93	6·62	14·5	9·58	14·54	24·1	1·29	3·08	4·38
0·3	9·43	1·60	11·03	10·36	3·83	14·2	12·37	8·26	20·6	1·64	1·73	3·37
0·4	11·51	1·128	12·64	12·5	2·66	15·2	14·8	5·67	20·5	1·95	1·177	3·12
0·5	13·3	0·894	14·2	14·4	2·08	16·5	17·0	4·41	21·4	2·23	0·911	3·14
0·6	15·0	0·743	15·8	16·2	1·72	17·9	19·1	3·61	22·7	2·50	0·743	3·24
0·7	16·5	0·636	17·2	17·8	1·46	19·3	21·0	3·06	24·0	2·74	0·627	3·37
0·8	17·9	0·553	18·5	19·3	1·263	20·6	22·7	2·63	25·4	2·97	0·538	3·51
1·0	20·7	0·430	21·2	22·4	0·974	23·3	26·2	2·02	28·2	3·41	0·411	3·82
1·2	23·9	0·338	24·2	25·7	0·762	26·5	29·8	1·57	31·4	3·82	0·312	4·13
1·4	27·1	0·270	27·4	29·1	0·605	29·7	33·4	1·24	34·6	4·20	0·251	4·45
1·6	30·2	0·218	30·4	32·2	0·487	32·7	36·6	0·998	37·6	4·55	0·201	4·75
1·8	33·2		33·3	35·3		35·6	39·7		40·4	4·87		5·01

Table 3. (Continued)

$T = 8{,}000$ K

	$\rho/\rho_0 = 1$			$\rho/\rho_0 = 10^{-1}$			$\rho/\rho_0 = 10^{-2}$			$\rho/\rho_0 = 10^{-3}$		
	$n = 2{\cdot}798 \times 10^{15}$			$n = 5{\cdot}939 \times 10^{15}$			$n = 1{\cdot}621 \times 10^{15}$			$n = 5{\cdot}030 \times 10^{14}$		
eV	$\nu \times 10^{12}$	$\nu_i \times 10^{12}$	$\nu_t \times 10^{12}$	$\nu \times 10^{11}$	$\nu_i \times 10^{11}$	$\nu_t \times 10^{11}$	$\nu \times 10^{11}$	$\nu_i \times 10^{11}$	$\nu_t \times 10^{11}$	$\nu \times 10^{10}$	$\nu_i \times 10^{10}$	$\nu_t \times 10^{10}$
0·2	1·04	1·83	2·87	1·31	5·38	6·69	0·161	1·813	1·97	0·168	6·59	6·76
0·3	1·39	1·003	2·40	1·66	2·82	4·48	0·203	0·927	1·130	0·211	3·32	3·53
0·4	1·68	0·724	2·41	1·97	1·98	3·95	0·240	0·642	0·882	0·249	2·28	2·53
0·5	2·01	0·555	2·56	2·26	1·49	3·75	0·274	0·480	0·754	0·285	1·69	1·98
0·6	2·27	0·462	2·73	2·53	1·23	3·76	0·307	0·391	0·698	0·318	1·37	1·69
0·7	2·49	0·398	2·89	2·78	1·046	3·82	0·336	0·332	0·668	0·349	1·16	1·51
0·8	2·69	0·350	3·04	3·01	0·913	3·92	0·364	0·288	0·653	0·378	1·004	1·38
1·0	3·07	0·282	3·35	3·45	0·727	4·17	0·416	0·228	0·644	0·432	0·789	1·22
1·2	3·45	0·233	3·68	3·86	0·595	4·46	0·462	0·186	0·647	0·478	0·641	1·12
1·4	3·83	0·195	4·03	4·25	0·495	4·74	0·503	0·154	0·657	0·520	0·529	1·049
1·6	4·20	0·164	4·37	4·59	0·414	5·01	0·540	0·128	0·668	0·557	0·440	0·997
1·8	4·57	0·139	4·71	4·91	0·349	5·26	0·572	0·108	0·680	0·589	0·369	0·958

Table 3. (Continued)

$T = 12{,}000$ K

	$\rho/\rho_0 = 1$			$\rho/\rho_0 = 10^{-1}$			$\rho/\rho_0 = 10^{-2}$			$\rho/\rho_0 = 10^{-3}$		
	$n = 6{\cdot}688 \times 10^{17}$			$n = 2{\cdot}081 \times 10^{17}$			$n = 6{\cdot}298 \times 10^{16}$			$n = 1{\cdot}736 \times 10^{16}$		
eV	$\nu \times 10^{12}$	$\nu_i \times 10^{12}$	$\nu_t \times 10^{12}$	$\nu \times 10^{12}$	$\nu_i \times 10^{12}$	$\nu_t \times 10^{12}$	$\nu \times 10^{11}$	$\nu_i \times 10^{11}$	$\nu_t \times 10^{11}$	$\nu \times 10^{10}$	$\nu_i \times 10^{11}$	$\nu_t \times 10^{11}$
0·2	1·61	23·57	25·19	0·163	12·33	12·49	0·150	54·6	54·7	0·114	20·37	20·38
0·3	2·03	12·74	14·76	0·205	5·98	6·18	0·189	24·7	24·8	0·144	8·78	8·80
0·4	2·40	8·94	11·33	0·242	3·95	4·20	0·222	15·7	15·9	0·169	5·47	5·48
0·5	2·74	7·03	9·77	0·277	3·00	3·27	0·254	11·62	11·87	0·194	3·97	3·99
0·6	3·06	6·02	9·09	0·309	2·50	3·81	0·284	9·54	9·82	0·216	3·22	3·24
0·7	3·36	5·11	8·47	0·339	2·08	2·42	0·312	7·84	8·15	0·237	2·62	2·65
0·8	3·64	4·55	8·19	0·367	1·83	2·19	0·338	6·80	7·14	0·257	2·26	2·28
1·0	4·16	3·77	7·93	0·419	1·48	1·90	0·385	5·44	5·82	0·293	1·78	1·81
1·2	4·61	3·23	7·84	0·464	1·25	1·71	0·427	4·54	4·97	0·325	1·48	1·51
1·4	5·02	2·84	7·86	0·505	1·084	1·59	0·464	3·91	4·37	0·353	1·26	1·30
1·6	5·38	2·51	7·90	0·540	0·952	1·49	0·497	3·41	3·90	0·378	1·10	1·13
1·8	5·70	2·24	7·95	0·572	0·843	1·41	0·526	3·00	3·53	0·400	0·962	1·00

Table 4. Averages

Quantity	Exact	Maxwellian Distribution	Constant Mean Free Path	Maxwellian Distribution and Constant MFP
$\frac{m\sigma_t}{ne^2} =$	$\overline{\frac{1}{3v^2}\frac{d}{dv}\left(\frac{v^3}{\nu_t + j\omega}\right)}$	$\frac{m}{3kT}\overline{\frac{v^2}{\nu_t + j\omega}}$	$\overline{\frac{2\nu_t + 3j\omega}{3(\nu_t + j\omega)^2}}$	See Ref. (12)
For $\nu_t > \omega$: $\frac{1}{\nu_{eq}} = \frac{m\sigma_t}{ne^2} =$	$\overline{\frac{1}{3v^2}\frac{d}{dv}\frac{v^3}{\nu_t}}$	$\frac{m}{3kT}\overline{\left(\frac{v^2}{\nu_t}\right)}$	$\frac{2}{3\Sigma n Q}\overline{\left(\frac{1}{v}\right)}$	$\frac{8}{3\pi}\sqrt{\left(\frac{\pi m}{8kT}\right)}\frac{1}{\Sigma n Q}$
For $\omega < \nu_t$: $\nu_{eq} = j\omega\left(1 + \frac{j\omega m\sigma_t}{ne^2}\right) =$	$\overline{\frac{1}{3v^2}\frac{d}{dv}v^3\nu_t}$	$\frac{m}{3kT}\overline{v^2\nu_t}$	$\frac{4}{3}\bar{v}\Sigma n Q$	$\frac{4}{3}\sqrt{\left(\frac{8kT}{\pi m}\right)}\Sigma n Q$

Note: $\bar{\phi} = \frac{1}{n}\int \phi f_0 4\pi v^2 dv$

where σ_i, σ_r are respectively the real and imaginary parts of the conductivity equation (1).

ν_{eq} in equation (35) has no physical significance in the range of $\nu_t > \omega$; it is just a definition useful in analysis. In the high frequency extreme, $\nu_t < \omega$, equation (35) reduces to equation (32). To show this, note that from equations (35) and (24)

$$\nu_{eq} = \frac{\overline{\left(\frac{1}{v^2}\frac{d}{dv}\frac{v^3\nu_t}{\nu_t^2+\omega^2}\right)}}{\overline{\left(\frac{1}{v^2}\frac{d}{dv}\frac{v^3\omega}{\nu_t^2+\omega^2}\right)}} \rightarrow \frac{\overline{\frac{1}{v^2}\frac{d}{dv}v^3\nu_t}}{3} \text{ for high } \omega,$$

so that in this limit, the equivalent collision frequency is equal to the high frequency one introduced in equation (32).

Note on Concentrations and Cross-Sections

The theory presented in this paper can be applied to calculate the properties of high temperature air subject to any revised determinations of one or more parameters in the analysis. Such determinations are under way in two fields. Hochstim at Convair has obtained more accurate values than Gilmore for the equilibrium concentrations of the species. Also analyses are under way at the University of Adelaide, AVCO, Westinghouse, Convair, among others, to obtain more accurately some cross-sections used here.

Acknowledgements—This work was done under contract to RCA Moorestown, Missile and Surface Radar Division.

REFERENCES

1. L. Lamb and S. C. Lin, *J. Appl. Phys.* **28,** 754 (1957).
2. M. P. Bachynski, T. W. Johnston and I. P. Shkarofsky, *Proc. Inst. Radio Engrs., N.Y.* **48,** 347 (1960).
3. H. S. W. Massey and E. H. S. Burhop, *Electronic and Ionic Impact Phenomena.* Oxford University Press (1952).
4. R. H. Healey and J. W. Reed, *The Behaviour of Slow Electrons in Gases.* Amalgamated Wireless Press, Sydney (1941).
5. J. S. Townsend, *Electrons in Gases.* Hutchinson, London (1947). Also *J. Franklin Soc.* **200,** 563 (1925).
6. R. A. Nielsen, *Phys. Rev.* **50,** 950 (1936). Also R. A. Nielsen and N. E. Bradbury, *Phys. Rev.* **51,** 69 (1937).
7. R. W. Crompton and L. G. H. Huxley, private communication.
8. G. Bekefi and S. C. Brown, *Phys. Rev.* **112,** 159 (1958).

9. L. SPITZER, *Physics of fully ionized gases*. Interscience Publishers, N.Y. (1956).
10. L. SPITZER and R. HARM, *Phys. Rev.* **89,** 977 (1953).
11. W. P. ALLIS, *Motion of ions and electrons* in *Handbuch der Physik*, Bd. 21, S. Springer, Berlin, (1956).
12. H. MARGENAU, *Phys. Rev.* **109,** 6 (1958).
13. A. V. PHELPS, O. T. FUNDINGSLAND and S. C. BROWN, *Phys. Rev.* **84,** 559 (1951).
14. L. H. G. HUXLEY and A. A. ZAAZOU, *Proc. Roy. Soc.* A **196,** 402 (1949).
15. J. B. FISK, *Phys. Rev.* **49,** 167 (1936).
16. M. M. KLEIN and K. A. BRUECKNER, *Phys. Rev.* **111,** 1115 (1958).
17. F. R. GILMORE, *Equilibrium composition and thermodynamic properties of air to 24000°K*, Rand Corp. Rep. RM–1543, (Aug. 1955).
18. M. S. SODHA, *Phys. Rev.* **113** 1163 (1959). Also M. S. SODHA and Y. P. VARSHNI, *Phys. Rev.* **111,** 1203 (1958).
19. H. DREICER, *Phys. Rev.* **115,** 238 (1959).
20. R. C. HWA, *Phys. Rev.* **110,** 307 (1958).
21. M. P. BACHYNSKI, T. W. JOHNSTON, and I. P. SHKAROFSKY, *Plasmas and the Electromagnetic Field*. McGraw Hill, New York (in press).
22. R. LANDSHOFF, *Phys. Rev.* **76,** 904 (1949).
23. C. M. TCHEN, *Phys. Rev.* **114,** 394 (1959).

BASIC HYPERSONIC PLASMA DATA OF EQUILIBRIUM AIR FOR ELECTROMAGNETIC AND OTHER REQUIREMENTS

W. B. SISCO and J. M. FISKIN

Douglas Aircraft Co., Long Beach, California

Abstract—Composition data necessary to determine the effects of hypersonically shocked air in equilibrium for the continuum flow regime on electromagnetic and other properties are presented in a simple systematic form. The data are presented in two sets of curves. The first set of data is useful when the temperature and density distribution behind a known shock front are available. In the second set, only the altitude and velocity are required to make reasonably accurate estimates of concentrations. Examples illustrating the use of the curves together with the assumptions and limitations involved are also included.

INTRODUCTION

Vehicles travelling in the earth's atmosphere at hypersonic speeds are surrounded by gaseous plasma sheaths of ionized, dissociated and chemically altered high temperature air. Particle concentrations in the sheath, in particular the electrons, determine the effects on electromagnetic and other operational characteristics. In general, these concentrations will modify, to some extent, the following electromagnetic properties: (1) antenna impedance, (2) propagation, (3) noise levels in the vehicle and distant electronic equipment, (4) scattering cross-section of vehicles and trails, (5) conductivity of the gas and (6) voltage breakdown characteristics. In addition, the elevated temperature and changed composition may radically modify the mechanical, thermodynamic and electrical properties of materials adjacent to the sheath. If a physical or chemical modification of the shocked gas is attempted, details of the composition also will be required.

In order to ascertain the degree of the modifications of the above properties, the composition of the high temperature air and its distribution around the vehicle at various altitudes and velocities are required. The computation of the concentrations necessitates a broad application of aerothermodynamics, statistical mechanics, physical chemistry and quantum theory. As a result, they are somewhat detailed, lengthy and complex. For the many design, analytical and proposal engineers who are closely or occasionally concerned with ion sheath problems, the effort required to understand the methods involved and actually compute one point of a vehicular trajectory is unduly long and laborious.

This report attempts to present a compact graphical synthesis of computations of these concentrations completed by the authors,[1] their associates[2, 3] and others.[4] The theoretical basis and methods of computing are contained in previous papers.[1, 5] The material is arranged to cover a wide range of aerothermodynamic conditions for convenient use by electrical and electronic engineers.

The data given in this report are arranged in two elementary forms. One set is to be used when the aerothermodynamic data are completely known, and the other when only the altitude and velocity are known. Illustrative examples demonstrating the use of both forms of information together with the assumptions and limitations involved are included.

COMPLETE AEROTHERMODYNAMIC DATA

If complete aerothermodynamic data, i.e. the

temperature and pressure or density distributions from the vehicle surface to the shock front, are given, then Figs. 1–11 yield the required concentrations. The aerothermodynamic data inputs herein are functions of altitude, velocity and vehicle configuration. The resulting curves give the number densities of e^-, N_2, O_2, NO, N, O, N^+, O^+, N^{++} and O^{++} as functions of temperature (T°K) for various density ratios (ρ/ρ_0), where ρ is the shocked air density and ρ_0 is the density at standard temperature and pressure (273·16°K and $1{\cdot}01325 \times 10^6$ dynes/cm^2). Use of

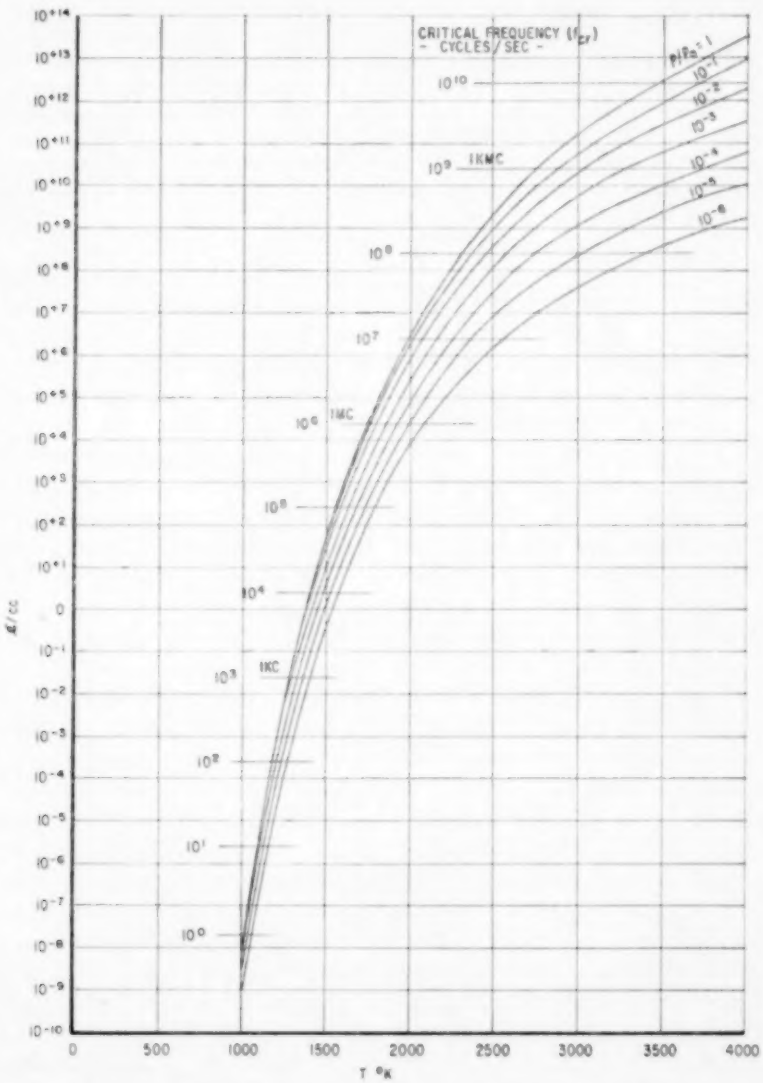

Fig. 1. Functional dependence of electron concentration on temperature and density ratio in air (0–4000°K).

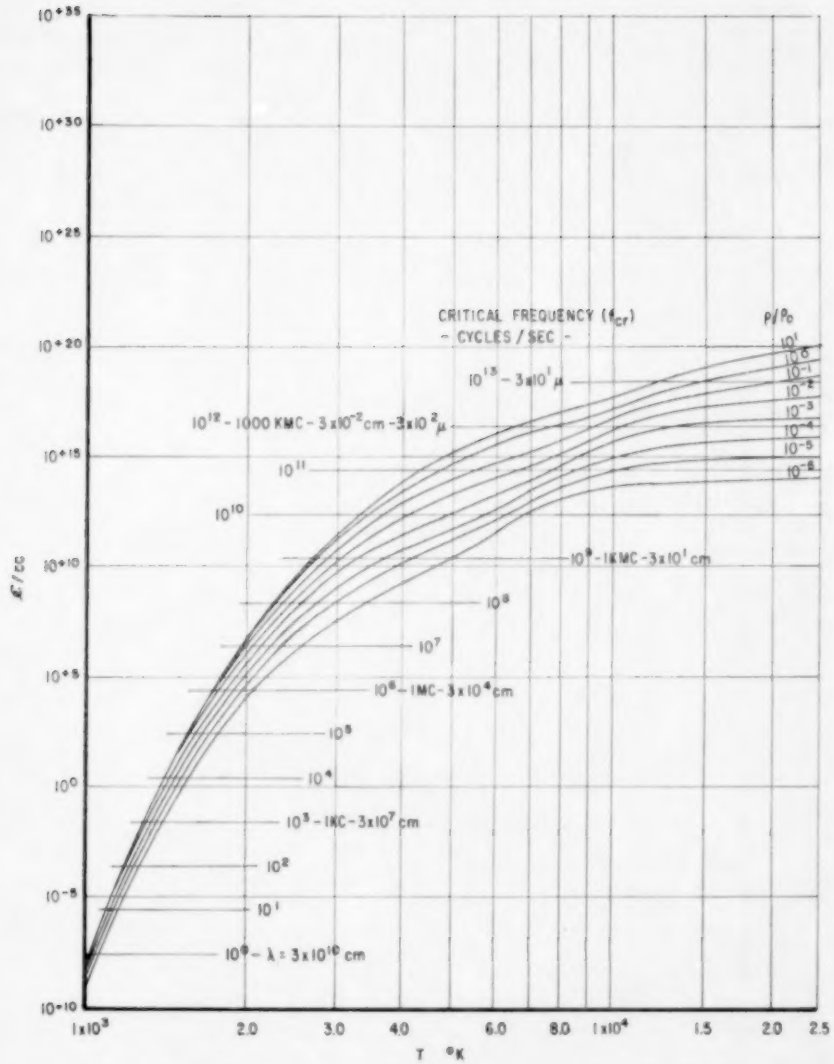

Fig. 2. Functional dependence of electron concentration on temperature and density ratio in air (1000–25,000°K).

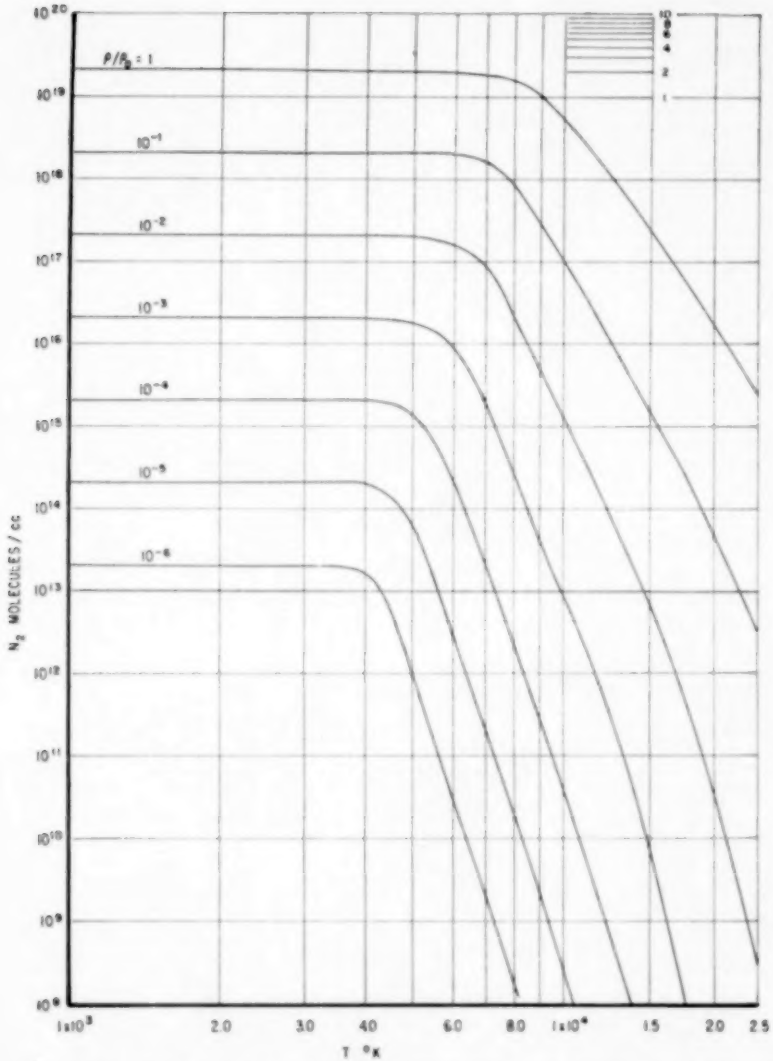

Fig. 3. Functional dependence of nitrogen molecule concentration on temperature and density ratio in air.

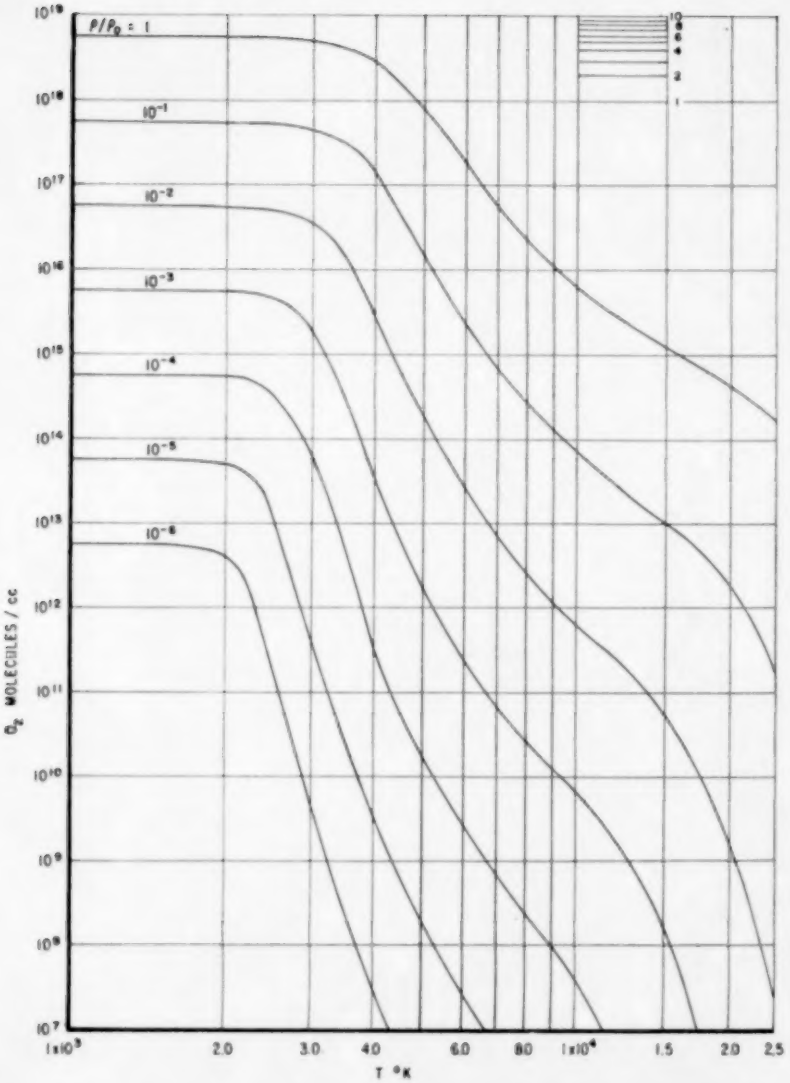

Fig. 4. Functional dependence of oxygen molecule concentration on temperature and density ratio in air.

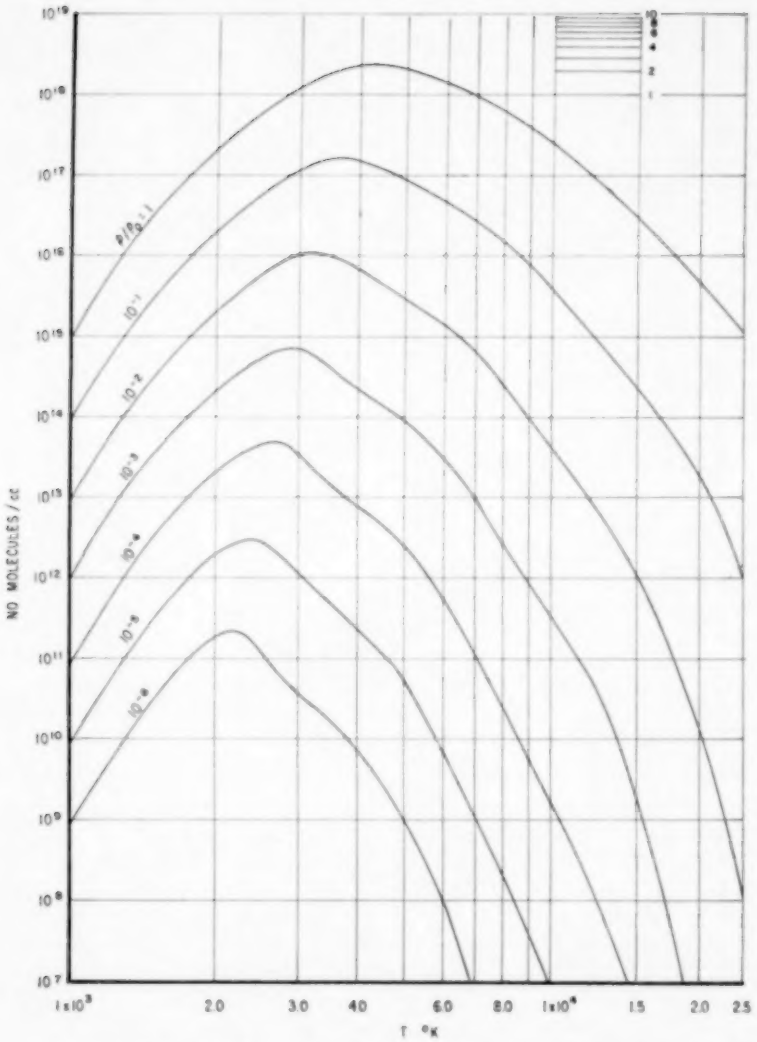

Fig. 5. Functional dependence of nitric oxide concentration on temperature and density ratio in air.

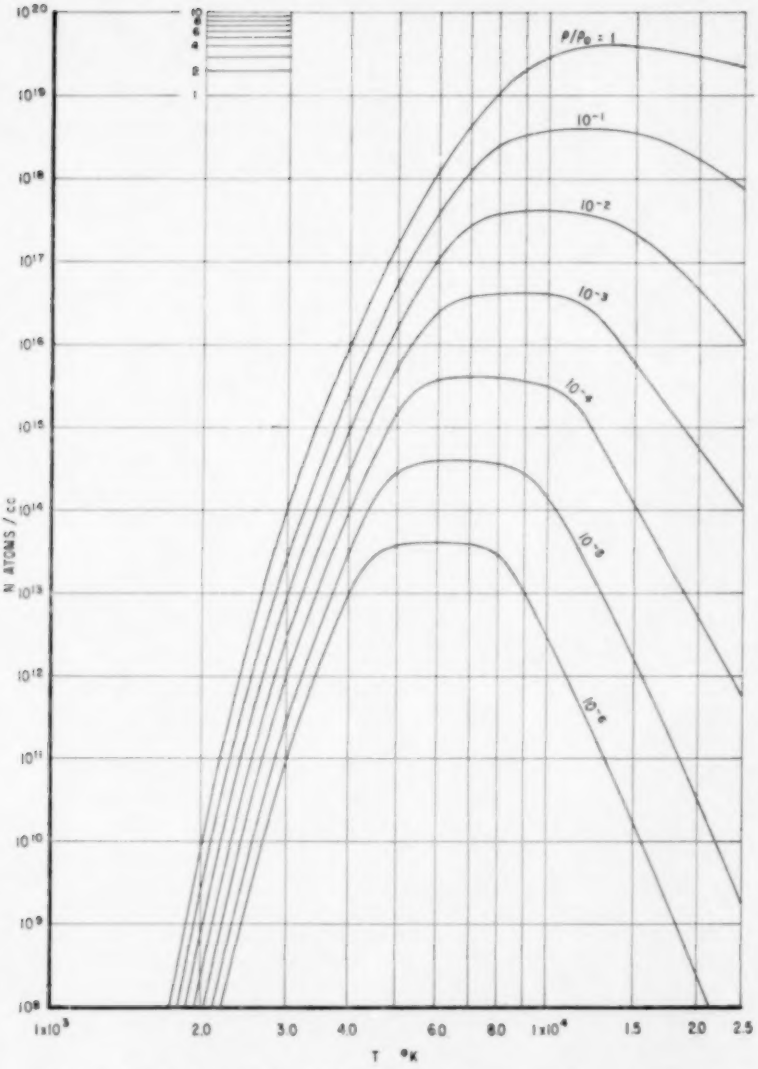

Fig. 6. Functional dependence of nitrogen atom concentration on temperature and density ratio in air.

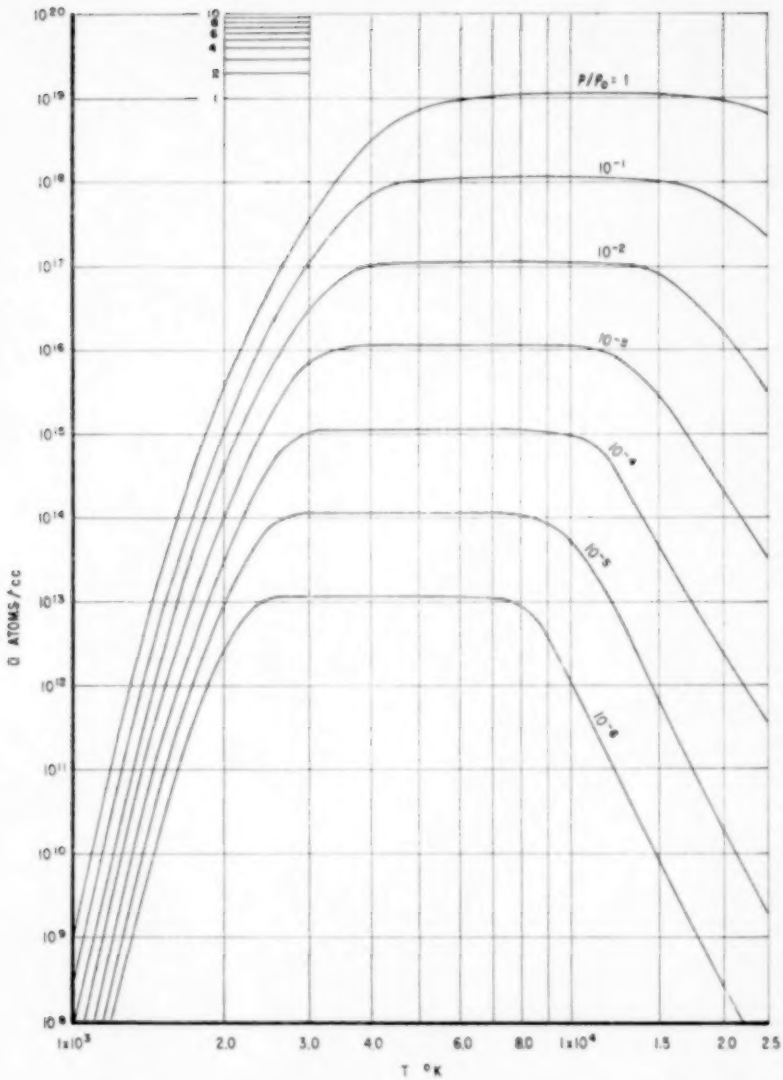

Fig. 7. Functional dependence of oxygen atom concentration on temperature and density ratio in air.

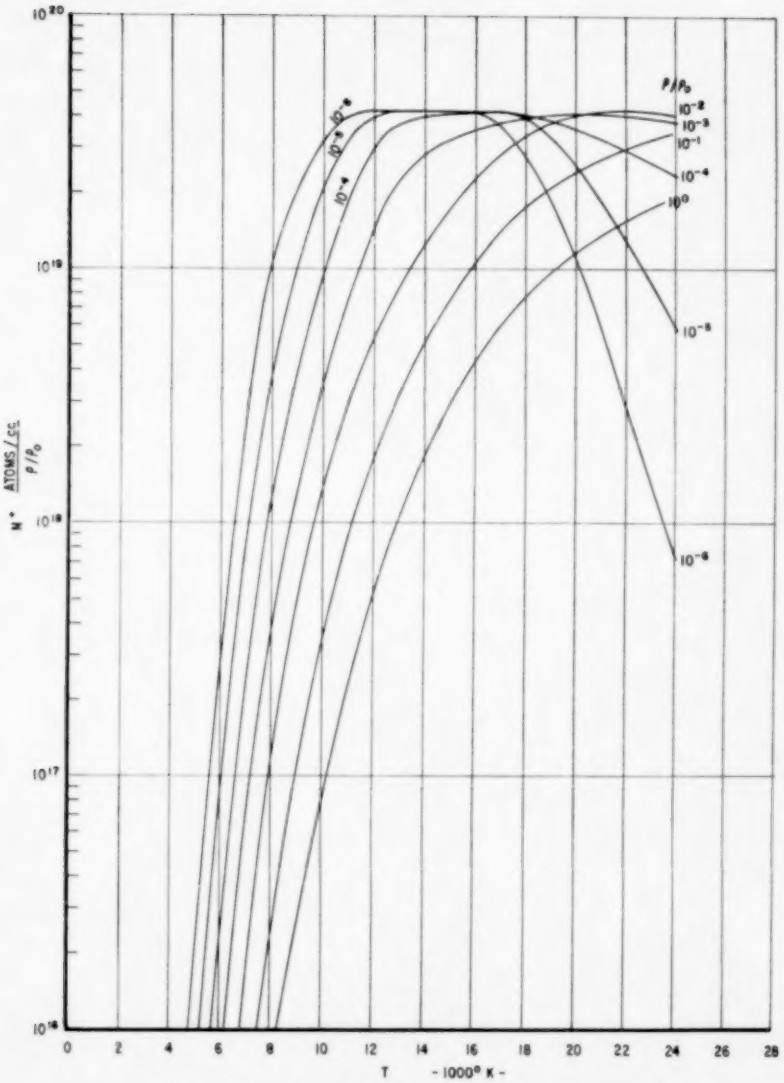

Fig. 8. Functional dependence of singly ionized nitrogen atom concentration on temperature and density ratio in air.

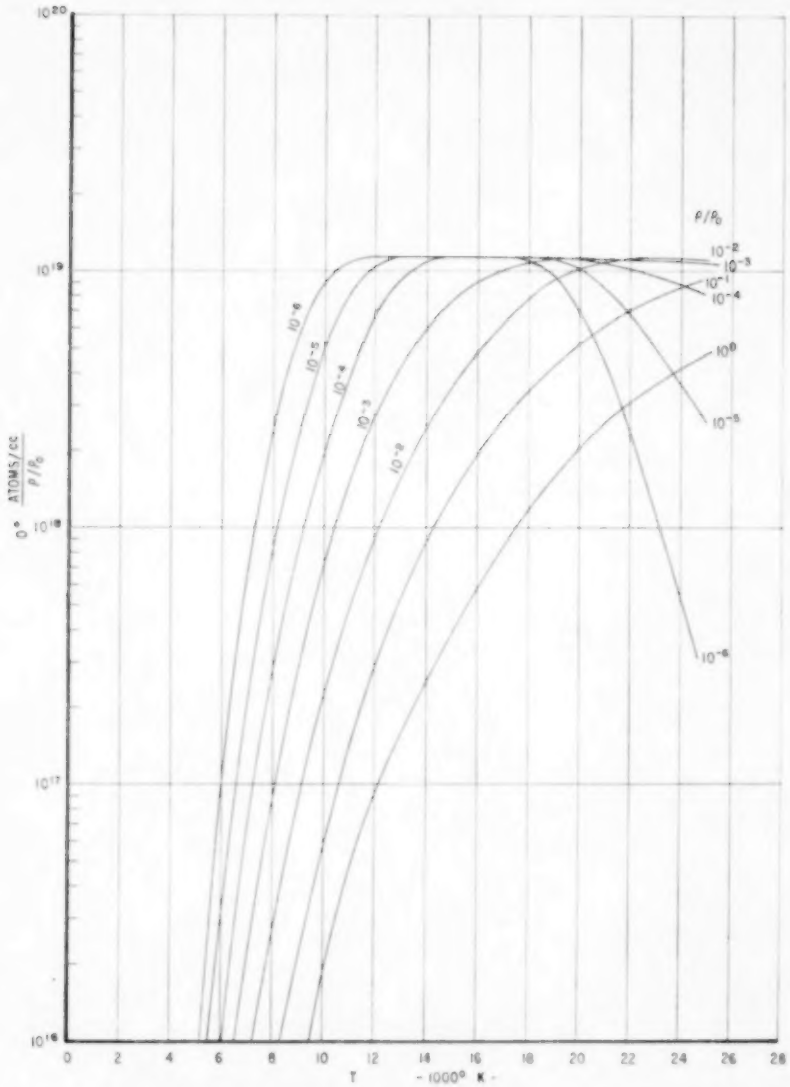

Fig. 9. Functional dependence of singly ionized oxygen atom concentration on temperature and density ratio in air.

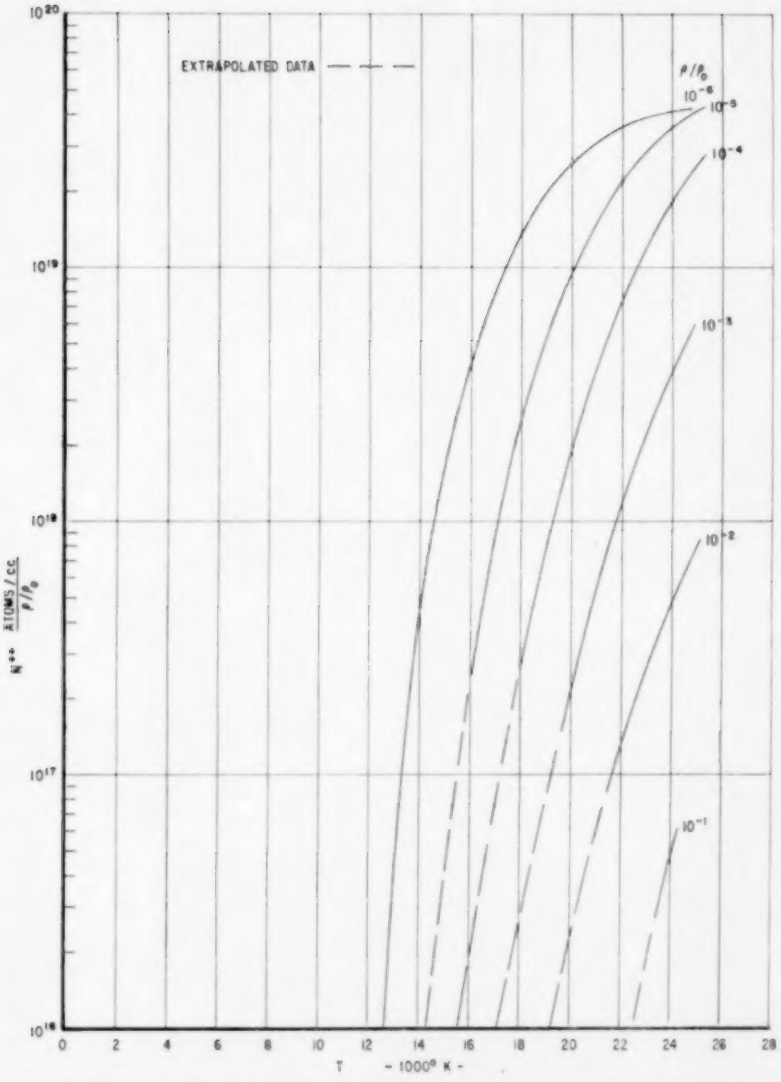

Fig. 10. Functional dependence of doubly ionized nitrogen atom concentration on temperature and density ratio in air.

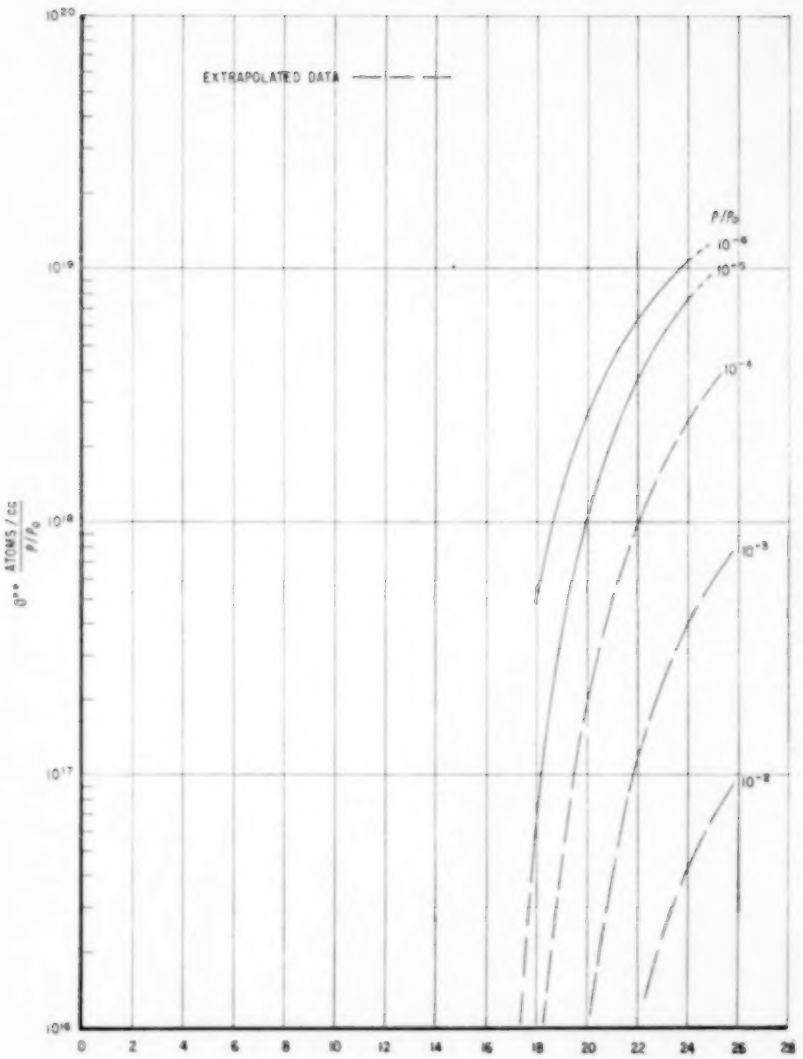

Fig. 11. Functional dependence of doubly ionized oxygen atom concentration on temperature and density ratio in air.

these curves requires that the shape of the shock around the vehicle be known.

Figs. 1–11 are valid for air in equilibrium provided the temperature and density are known and the initial (unshocked) composition has the same relative amounts of N_2, O_2, etc., at standard temperature and density. Since argon (A) and ionized nitric oxide (NO^+) have relatively small effects on the collision frequency, their composition curves have not been included.

To illustrate the use of the curves, it is assumed that the temperature and density as a function of distance from the vehicle surface at a specific altitude and velocity encountered by a typical hypersonic vehicle are known. Fig. 12 is a typical plot of such aerothermodynamic data. In order to define completely the envelope around a vehicle, the temperature–density distribution over the entire sheath must first be known. Then by employing the curves, the concentrations may be mapped for the given temperature–density distribution which also includes the boundary layer. As an example, the critical frequency determined from Figs. 1 and 12 is shown in Fig. 13.

The concentrations themselves as given are adequate for determining breakdown and radiation properties, and chemical or physical shock modification. However, for antenna impedance, propagation, scattering, and conductivity effects on power equipment, the data are more useful when converted to the dielectric constant and conductivity of the medium. These properties are readily obtainable from the concentrations

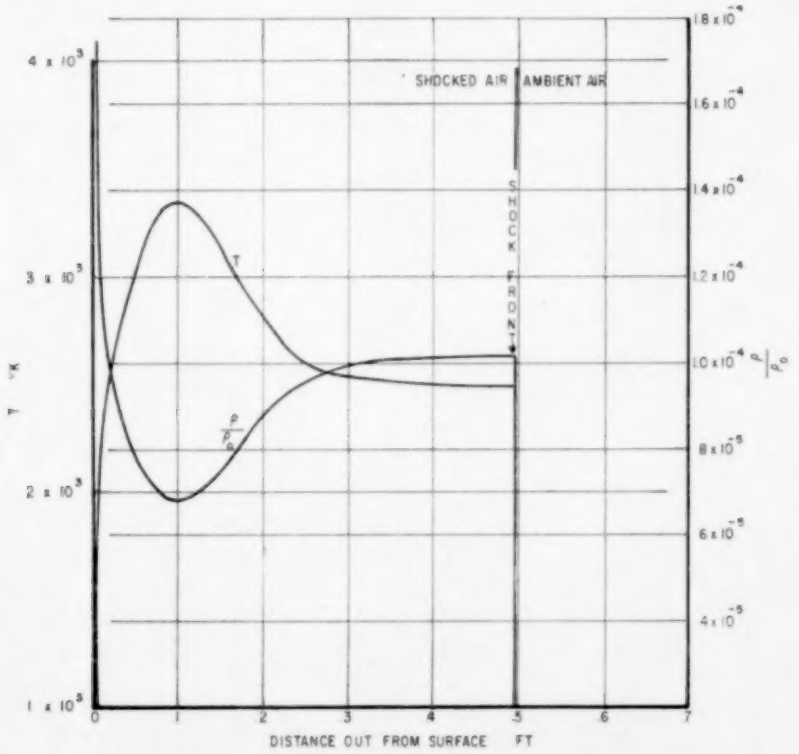

Fig. 12. A typical temperature and density ratio variation through an air plasma sheath.

and classical electromagnetic theory. Thus the conductivity (σ) and the dielectric constant (ϵ) are given by the following relations in m.k.s. units.

$$\sigma = \varepsilon_0 \frac{\omega_{cr}^2 \nu_e}{\omega^2 + \nu_e^2}$$

$$\varepsilon = \varepsilon_0 \left[1 - \frac{\omega_{cr}^2}{\omega^2 + \nu_e^2} \right]$$

where

$$\omega_{cr} = \left[\frac{N_{e^-} e^2}{\varepsilon_0 m} \right]^{\frac{1}{2}} = \text{critical frequency in radians}$$

ω = incident radiation frequency in radians
ε_0 = dielectric constant of free space
N_{e^-} = electrons/m^3
e = charge of an electron in couloumbs
m = mass of an electron in kilograms
ν_e = electron collision frequency

Taking the point 0·1 ft from the surface in Fig. 12 for example, the temperature of 3350°K and density ratio of $6{\cdot}8 \times 10^{-5}$ is obtained. The critical frequency (ω_{cr}) for this point is 600 Mc/s from Fig. 13. The collision frequency (ν_e) is given for a mixed gas by the following relation for relatively weak fields:[6]

$$\nu_e = \bar{c} \sum_{j=1}^{m} n_j Q_j$$

where

$$\bar{c} = \left(\frac{8kT}{\pi m_e} \right)^{\frac{1}{2}}$$

n_j = number of particles of component/cm^3
k = Boltzmann's constant
T = temperature in degrees Kelvin
m_e = mass of the electron in grams
Q_j = collision cross-section for the j^{th} component

Since the collision frequency (ν_e) is identical in the m.k.s. and the c.g.s. systems, c.g.s. units are used in the above expression because cross-sections are normally given in cm^2. Using the

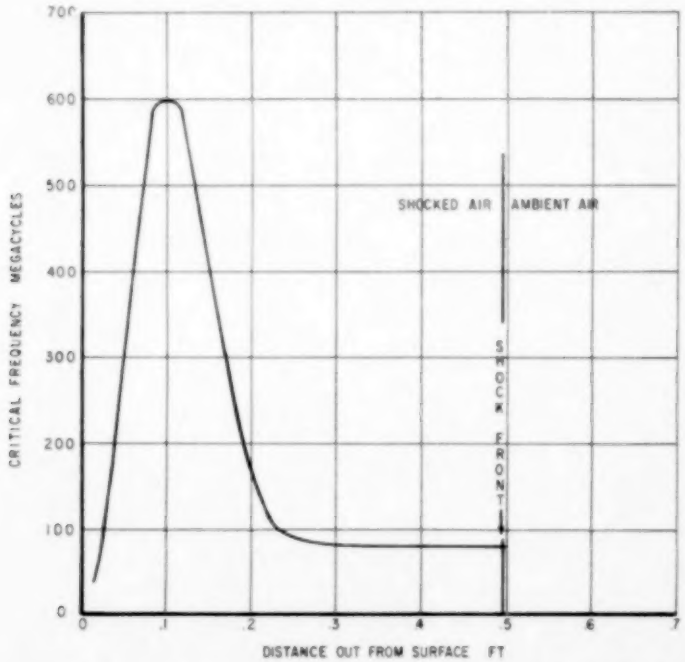

Fig. 13. Critical frequency variation through an air plasma sheath.

collision cross-sections obtainable from the literature,[7] the table below gives the information necessary to calculate the collision frequency which is $\sim 8 \times 10^7$/sec with neutral atoms.

Gaseous air components	Atoms	Collision cross-section (cm^2)
Nitrogen molecules (N_2)	$1{\cdot}4 \times 10^{15}$	$6{\cdot}8 \times 10^{-16}$
Oxygen molecules (O_2)	$2{\cdot}6 \times 10^{15}$	$3{\cdot}4 \times 10^{-16}$
Nitric oxide molecules (NO)	$1{\cdot}2 \times 10^{15}$	$7{\cdot}0 \times 10^{-16}$
Nitrogen atoms (N)	$3{\cdot}0 \times 10^{15}$	$3{\cdot}5 \times 10^{-15}$
Oxygen atoms (O)	$7{\cdot}8 \times 10^{14}$	$1{\cdot}6 \times 10^{-15}$

Data for the positive ions are not included in the table since the effect is negligible in this case. The resulting conductivity is $\sim 2{\cdot}54 \times 10^{-4}$ mhos/meter and dielectric constant is $\sim 0{\cdot}64\ \epsilon_0$ for an incident frequency of 1 kMc/s. With the conductivity and dielectric constant known, the propagation constants, attenuation (α) and phase shift β, characteristic impedance of the medium, and reflection coefficient are readily obtained from classical electromagnetic theory.

LIMITED AEROTHERMODYNAMIC DATA

Often when complete aerothermodynamic data are not available, reasonable estimates of the concentrations and corresponding electromagnetic properties can be obtained from Figs. 14–24. These curves apply to air behind a normal shock front, and were derived from the previously mentioned Refs. (1–5) and the ARDC Model Atmosphere.[8] The data were obtained by first translating the ARDC[8] and the Douglas Aircraft[2, 3] aerothermodynamic information into terms of temperature (T) and density ratio (ρ/ρ_0) as a function of altitude for various velocities. Secondly, the composition as a function of altitude for the velocities was determined, using the previously derived curves of Figs. 1–11. Figs. 14–17 represent the first translation of information and are useful in estimating the temperature and density and also temperature effects on materials. Figs. 18–24 are the composition curves.

The curves for limited aerothermodynamic data apply to air immediately after it has passed through a normal shock front. If the air is not cooled or expanded, the curves are valid up to the boundary layer. The curves may also be applied to oblique shocks[2, 3, 5] if the component of velocity normal to the shock front is used as the velocity parameter. The cross-hatched areas represent uncertainties resulting from extrapolation of the aerodynamic curves[2, 3] and the change in ambient air composition ahead of the shock front caused by the photo-dissociation of oxygen molecules at high altitudes.

To illustrate the use of Figs. 18–24, a typical trajectory of a hypersonic vehicle is plotted over Fig. 18 and presented as Fig. 25. The critical frequency is given by the right-hand scale in Fig. 18. Thus the electron concentration and the critical frequency may be directly estimated throughout the entire exit and re-entry course. The corresponding heavier particle concentrations can be estimated by the same technique, and the corresponding EM properties can be determined as a function of altitude and velocity.

ASSUMPTIONS AND LIMITATIONS

All of the curves presented apply to air in thermodynamic equilibrium. When air goes from an ambient to a shocked state, the equilibrium electron concentration often represents the true value. However, increases in the electron concentration of two or three times the equilibrium value have been observed. Critical frequencies are only slightly changed by this deviation in electron concentration because of their square root dependence on electron densities. When the shocked air is cooled by expansion, as in flow around a curved body or flow into the wake, the equilibrium electron concentrations at the temperature of the point under consideration represent minimum values. The electron densities after expansion and cooling will usually vary between the equilibrium values at the temperature

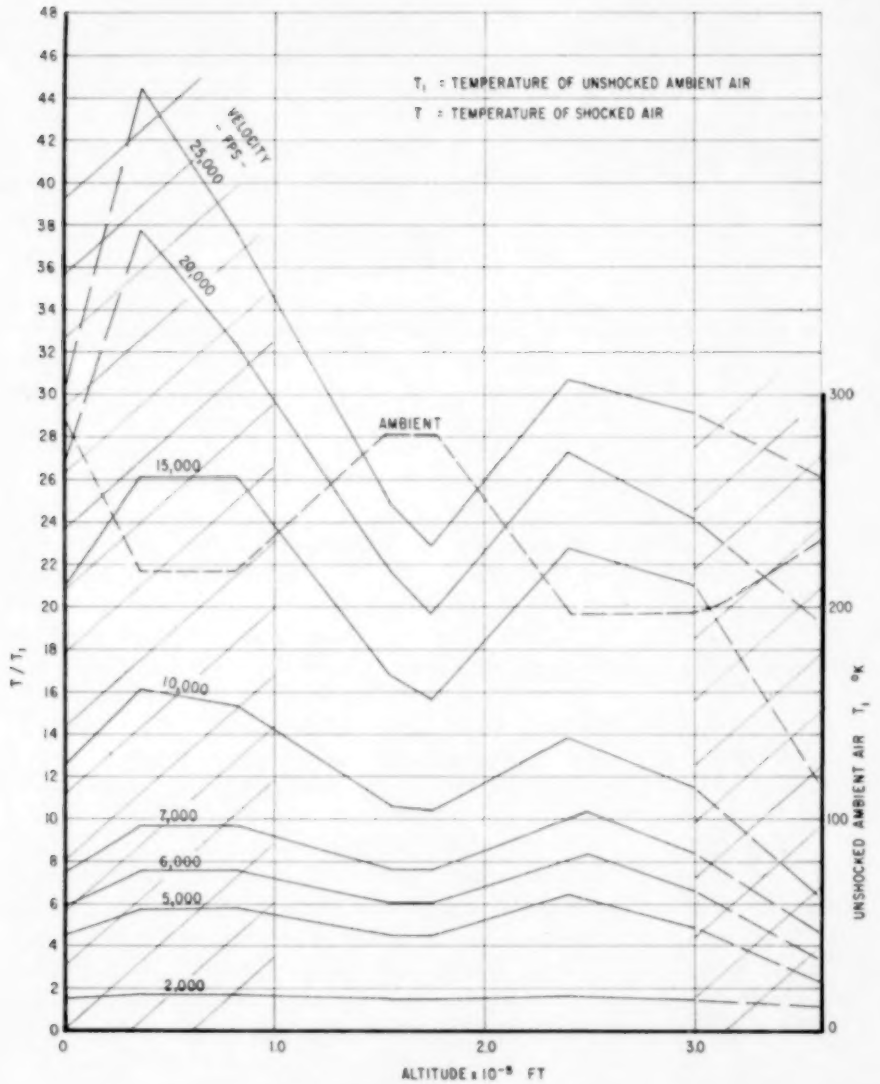

Fig. 14. Functional dependence of temperature ratio on altitude and velocity for air shocks and ambient air temperature variation with altitude.

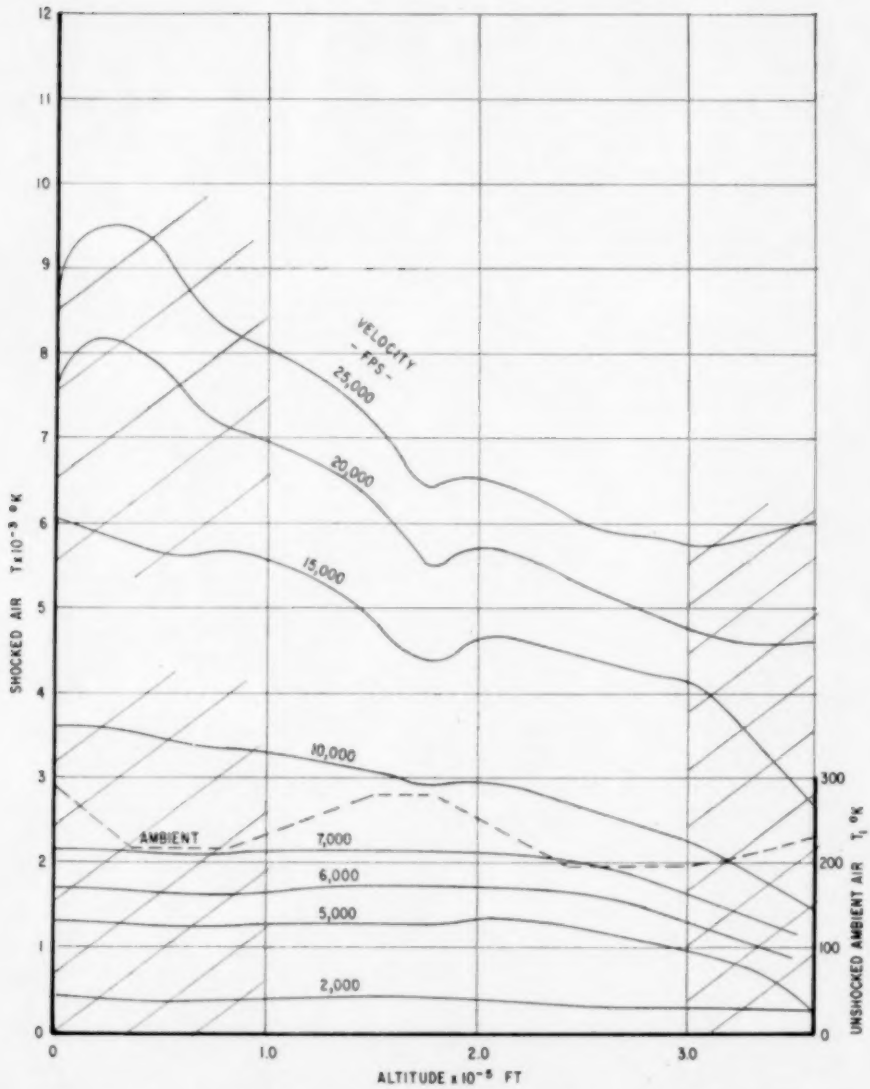

Fig. 15. Functional dependence of temperature on altitude and velocity for air shocks and ambient air temperature variation with altitude.

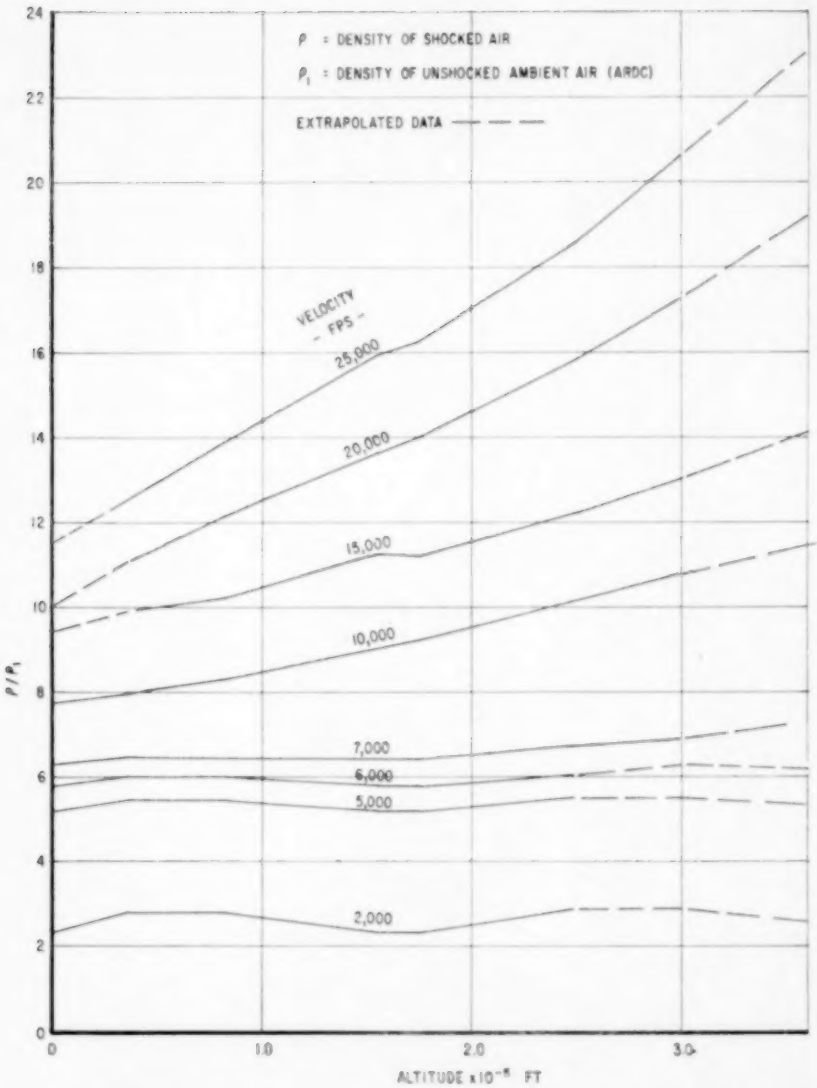

Fig. 16. Functional dependence of density ratio on altitude and velocity for air shocks.

before expansion and the equilibrium values at the temperature after expansion, depending on vehicle configuration, velocity, altitude and the electron removal rates. The temperature is defined by the translational energy content of the gas during expansion and cooling.

The curves are valid for vehicles travelling in the continuum flow regime, which is usually defined as that region where the mean free path of the gas particles is small compared to the cross-sectional area normal to the flight velocity of the vehicle. The other extreme is called free molecular flow in which the mean free path is large compared to the cross-sectional area normal to the flight velocity. The slip flow regime lies between the two extremes. The maximum and minimum electron densities are produced in the continuum flow regime and the free molecular flow regime, respectively. The mechanisms for producing ionization in free molecular flow are different

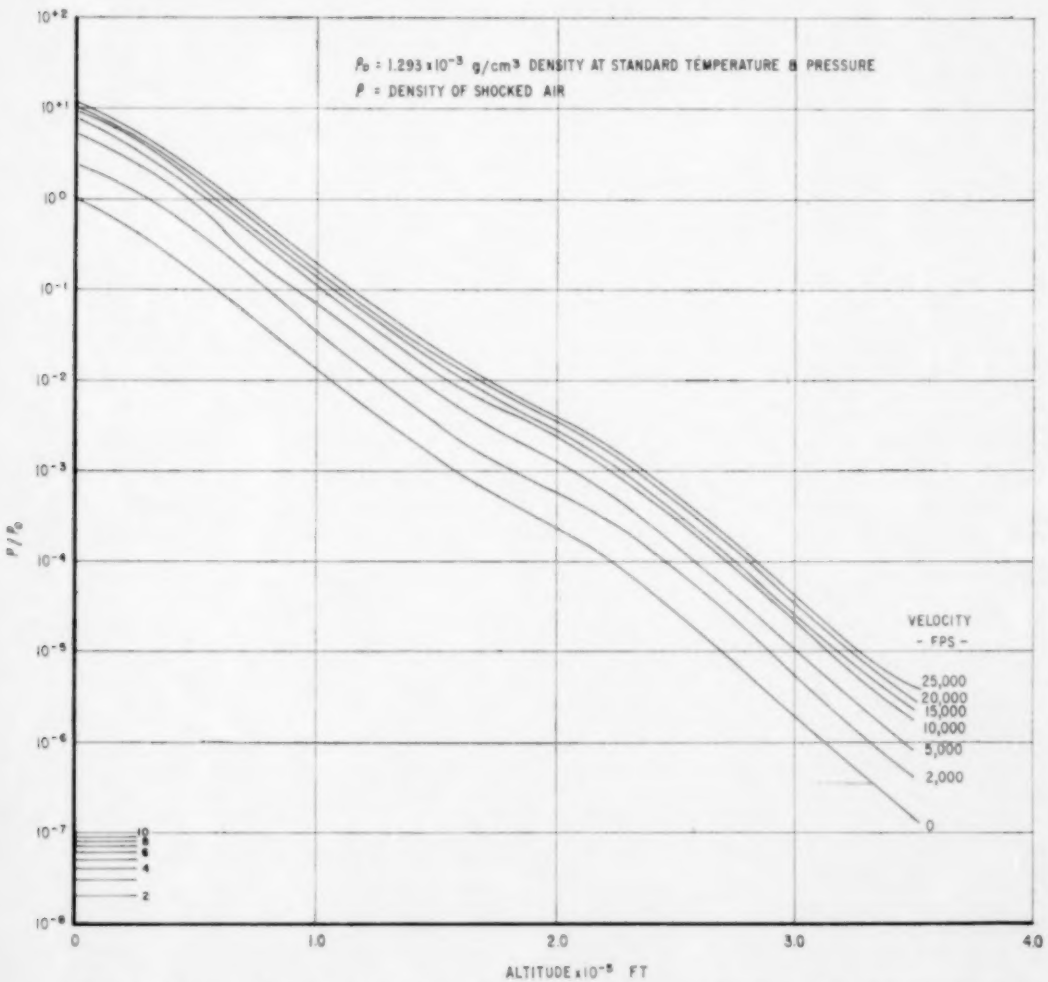

Fig. 17. Functional dependence of standard temperature and pressure density ratio on altitude and velocity for air shocks.

from those for continuum flow, and the free molecular electron density generally will be lower than in either the continuum or slip flow regimes.

CONCLUSIONS

The necessary information is presented for determining the effects of hypersonically-shocked equilibrium air on electromagnetic and other vehicle characteristics in the continuum flow regime. Further work should develop data in the non-equilibrium, slip flow, and free molecular flow regimes. For future space activities the techniques referred to may be employed to produce similar curves for other planetary atmospheres such as Mars and Venus.

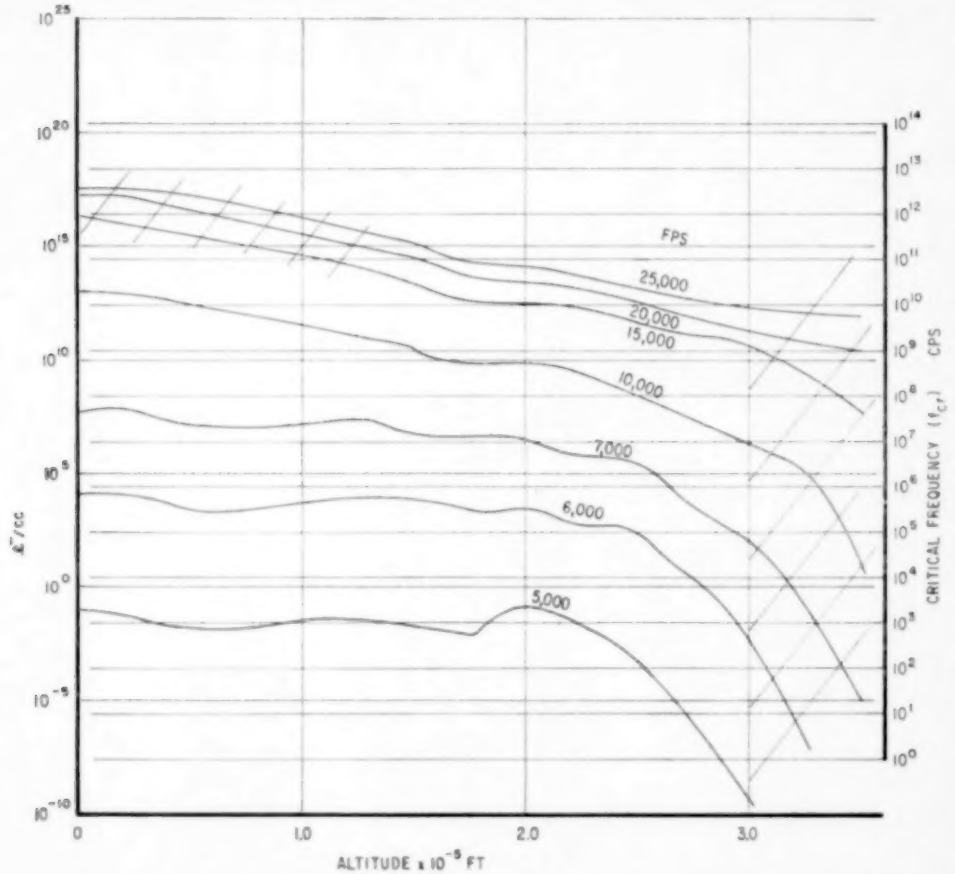

Fig. 18. Functional dependence of electron concentration and critical frequency on altitude and velocity for air shocks.

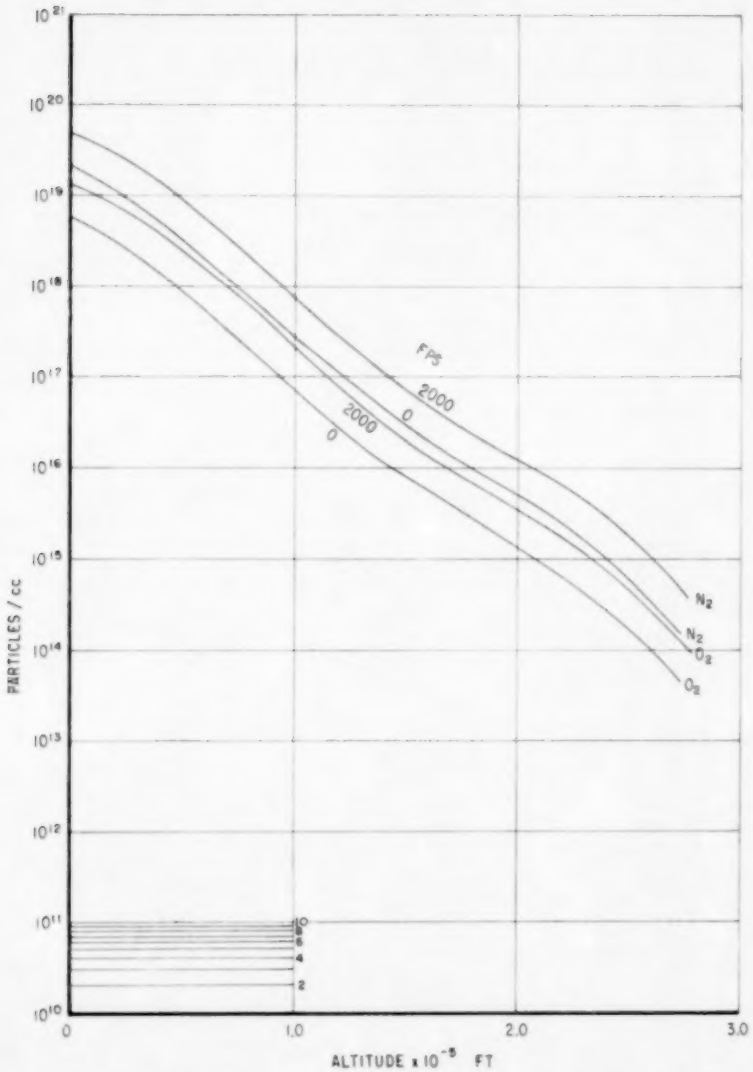

Fig. 19. Functional dependence of air composition on altitude and velocity for air shocks (0 and 2000 ft/sec).

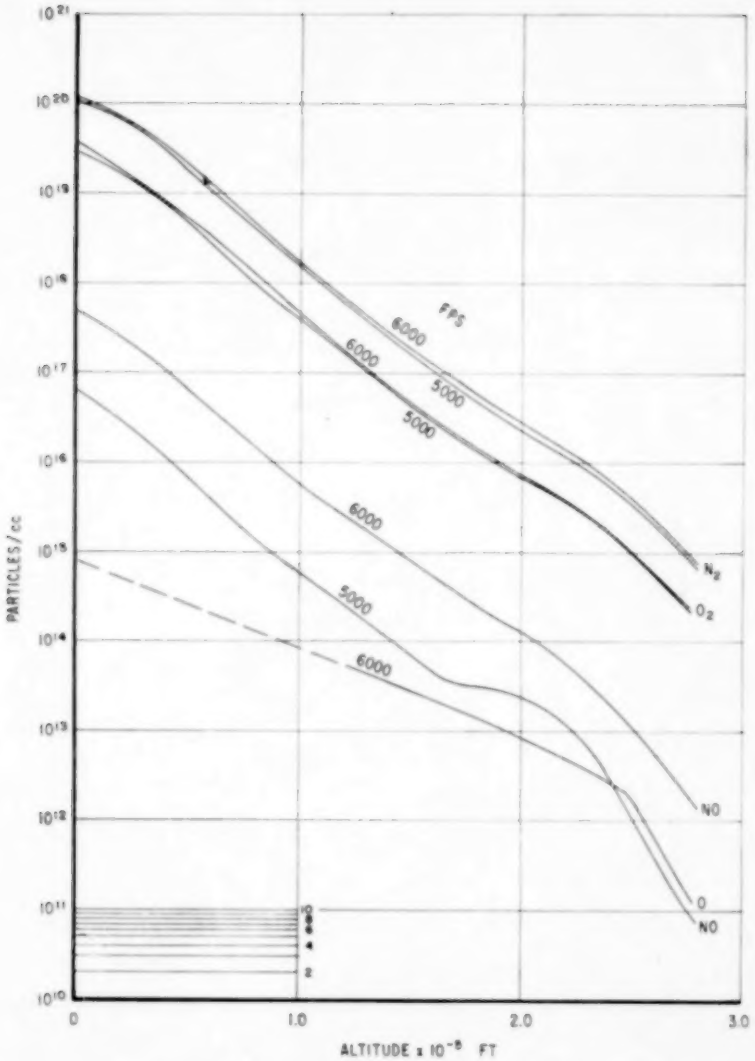

Fig. 20. Functional dependence of air composition on altitude and velocity for air shocks (5000 and 6000 ft/sec).

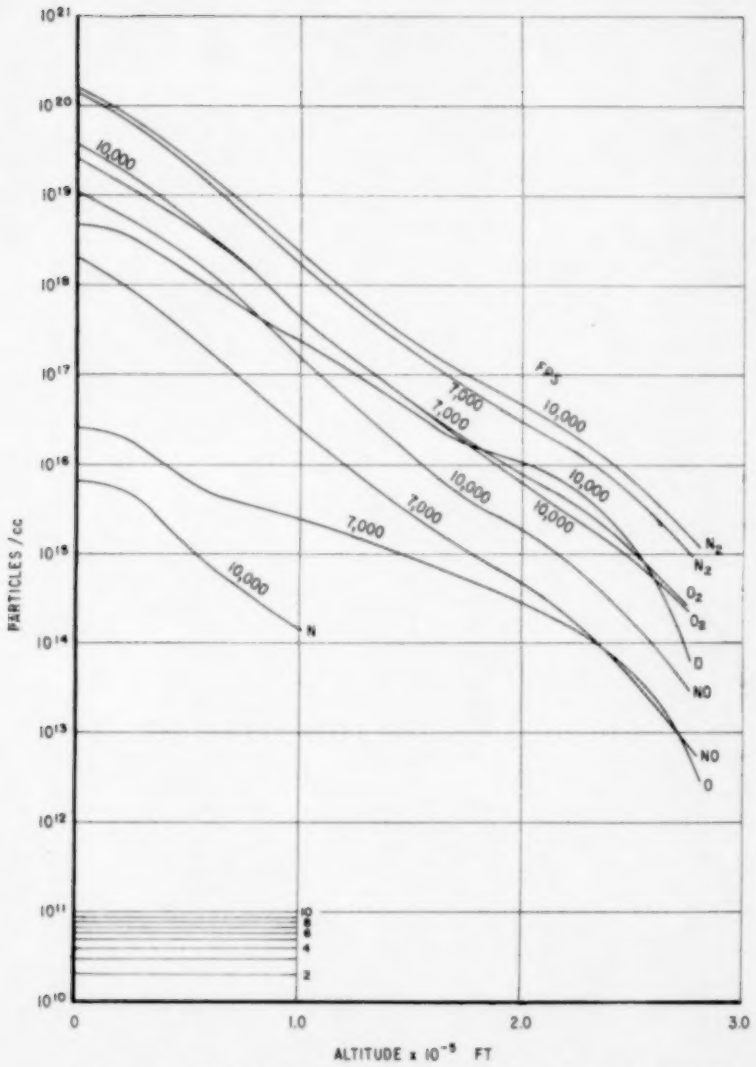

Fig. 21. Functional dependence of air composition on altitude and velocity for air shocks (7000 and 10,000 ft/sec).

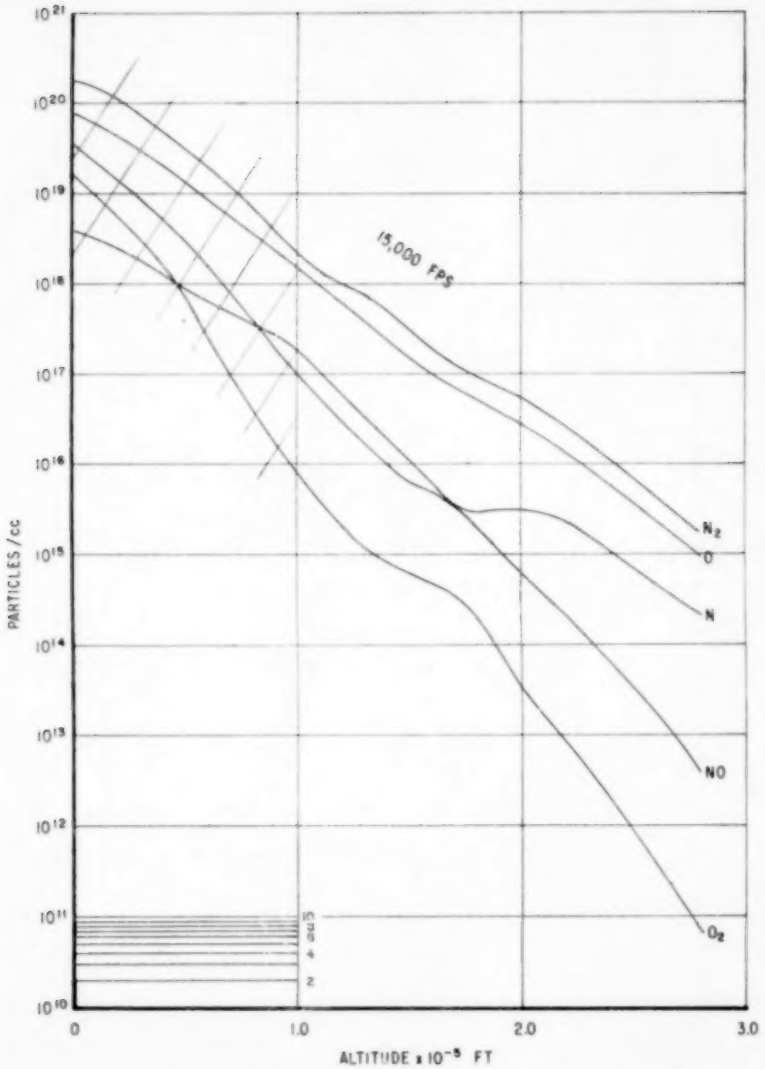

Fig. 22. Functional dependence of air composition on altitude and velocity for air shocks (15,000 ft/sec).

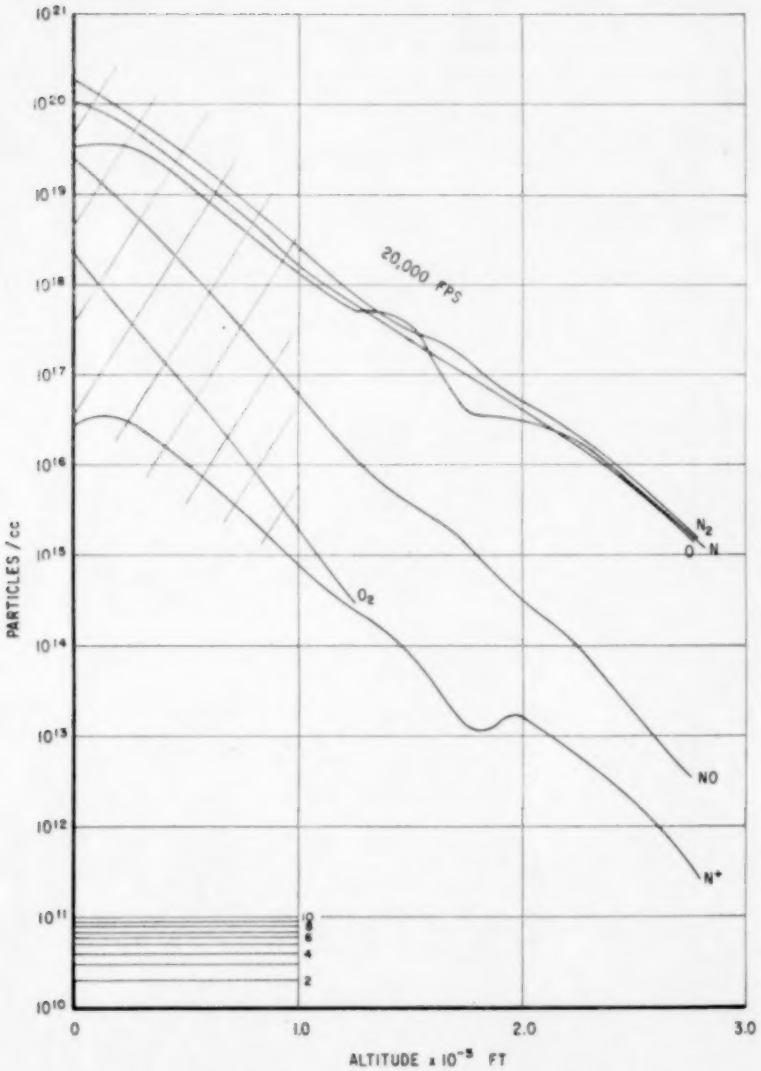

Fig. 23. Functional dependence of air composition on altitude and velocity for air shocks (20,000 ft/sec).

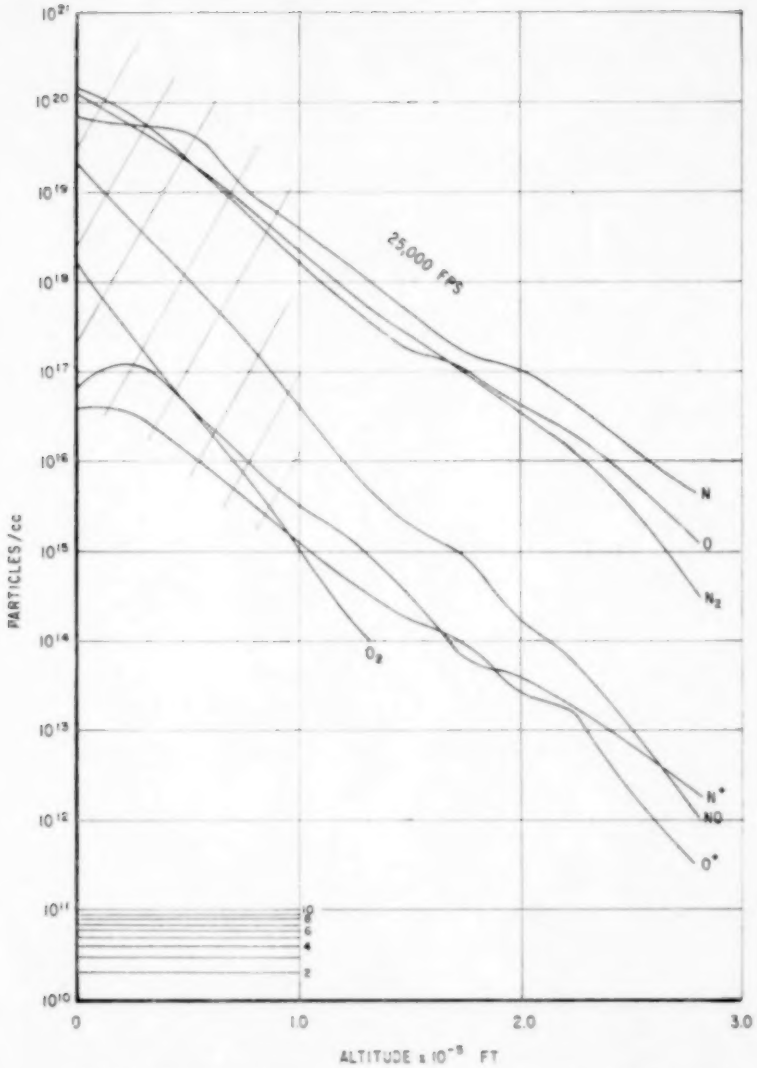

Fig. 24. Functional dependence of air composition on altitude and velocity for air shocks (25,000 ft/sec).

REFERENCES

1. C. A. Roberts, W. B. Sisco and J. M. Fiskin, *Air Composition below 3000 Degrees Kelvin* in *Research and Development Handbook, 1959–1960*, p. D–19. Space/Aeronautics, Conover-Mast Publications, New York, N.Y.
2. R. A. Batchelder *et al. Normal and Oblique Shock Characteristics at Hypersonic Speeds.* Douglas Aircraft Company, Engrg. Rep. No. LB–25599 (Dec. 1957).
3. R. A. Batchelder, *Normal and Oblique Shock Characteristics at Hypersonic Speeds, Supplement 1.* Douglas Aircraft Company, Engrg. Rep. No. LB–25599 (Feb. 1959).
4. F. R. Gilmore, *Equilibrium Composition and Thermodynamic Properties of Air to 24,000°K*, RAND Corporation, Rep. RM–1543 (Aug. 1955).
5. C. A. Roberts, W. B. Sisco and J. M. Fiskin, *Theory of Equilibrium Electron and Particle Densities behind Normal and Oblique Shock Waves in Air. Trans. Inst. Radio Engrs. on Antennas and Propagation*, AP-8, 102 (1960).
6. W. B. Sisco and J. M. Fiskin, *Effects of Relatively Strong Fields on the Propagation of EM Waves Through a Hypersonically Produced Plasma. Trans. Inst. Radio Engrs. on Antennas and Propagation*, AP-7, 240 (1959).
7. C. Brown and W. P. Allis, *Basic Data of Electrical Discharges.* MIT Res. Lab. Electr., Tech. Rep. No. 283 (June 1958).
8. *ARDC Model Atmosphere*, 1956, Geophys. Directorate, AFCRC, ARDC (Dec. 1956).

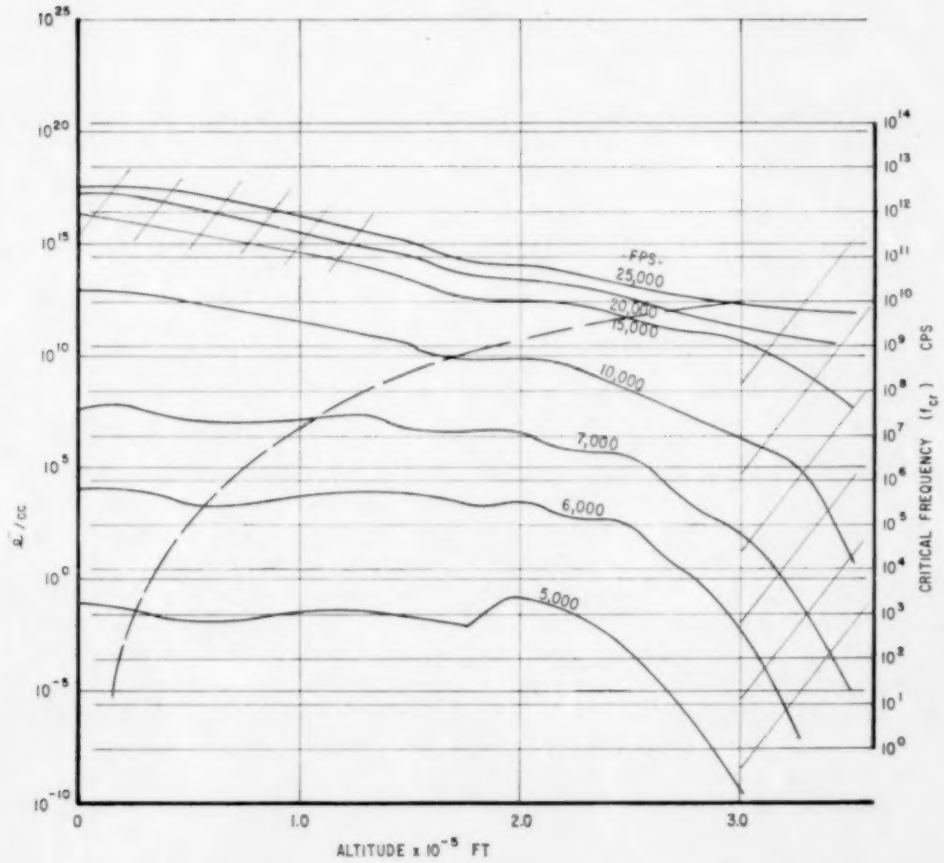

Fig. 25. A typical trajectory plotted on a concentration–altitude–velocity curve.

THE EFFECT OF ERRORS IN RATE CONSTANTS ON NON-EQUILIBRIUM SHOCK LAYER ELECTRON DENSITY CALCULATIONS*

M. H. BORTNER

Aerosciences Laboratory, Missile and Space Vehicle Department
General Electric Company, Philadelphia, Pennsylvania

Abstract—In a study of non-equilibrum ionization in shock layers, the chemical system

(1) $O_2 + X \rightleftarrows O + O + X$
(2) $O + N_2 \rightleftarrows N + NO$
(3) $O + NO \rightleftarrows N + O_2$
(4) $N + O \rightleftarrows NO^+ + e$

was adopted as the simplest system which could reasonably be used in calculation of ionization rates and times. Use of the rates of the individual reactions permitted the calculations of the electron density and other concentrations in the plasma sheath as functions of time.

Important quantities in such calculations are the reaction rate constants which, together with the concentrations, determine the actual rates. Values of these constants are greatly in doubt. A programme was set up to determine the effect of inaccuracies in these values. Each pair of rate constants was changed individually and the effect on each concentration–time curve was noted.

Large effects were found. In one typical case, a change of one order of magnitude in the rate constant of the O_2 dissociation changed the electron density after about two msec by a factor of about 200. Changes of other rate constants by an order of magnitude changed the overall rate of ionization by lesser, but still serious, factors. It is therefore concluded that non-equilibrium electron density calculations are extremely dependent on the values of the rate constants and precise values are needed.

The calculation of overall rates of ionization in the flow field of a re-entry vehicle is an extremely complicated problem. It is filled with many assumptions because of (1) the need for simplifications and (2) the lack of accurate data for some of the quantities used. It is, of course, important to know the effect of any inaccuracies or assumptions. This paper will attempt to describe the errors introduced by inaccuracies in one type of data, namely, the reaction rate constants for the chemical reactions which occur in the flow field.

It should be mentioned that this programme considers only the inviscid flow field and excludes any consideration of processes which occur in the boundary layer.

The true system of chemical reactions in the flow field would include dozens of reactions. Any reasonable and practical computer programme can only include a small fraction of these. Thus, in setting up a programme, the reactions to be included must be carefully selected so that not only are the important reactions included but also that those which are not too important are excluded. For the calculations made in this study, a set of four reversible chemical reactions was used. These are:

$$O_2 + X \underset{k_1'}{\overset{k_1}{\rightleftarrows}} O + O + X$$

* This work was performed under the auspices of the U.S. Air Force, Ballistic Missile Division, Contract No. AF 04(647)-269.

$$O + N_2 \underset{k_2'}{\overset{k_2}{\rightleftharpoons}} NO + N$$

$$O + NO \underset{k_3'}{\overset{k_3}{\rightleftharpoons}} O_2 + N$$

$$N + O \underset{k_4'}{\overset{k_4}{\rightleftharpoons}} NO^+ + e$$

Some other reactions will, of course, be of some importance under certain conditions. Among these are nitrogen dissociation, NO dissociation, attachment reactions and charge transfer reactions. The programme is also limited to a nitrogen–oxygen system. The calculations were made using as starting concentrations, the ambient densities of the individual species, N_2, O_2, NO, N, O and NO^+, each multiplied by a factor for the density ratio on the two sides of the shock front. Thus concentrations of N, O, NO and NO^+ at the start are appreciable although, in general, small.

Considering the chemical system as given by these four reversible reactions, the rate of change of the concentrations of each species can be expressed by a differential equation. Thus those equations for the important species in this system are:

$$\frac{d(N)}{dt} = k_2(N_2)(O) - k_2'(N)(NO) + k_3(NO)(O) - k_3'(N)(O_2) - k_4(N)(O) + k_4'(NO^+)(e)$$

$$\frac{d(N_2)}{dt} = -k_2(N_2)(O) + k_2'(N)(NO)$$

$$\frac{d(O)}{dt} = 2k_1(O_2)(X) - 2k_1'(O)^2(X) - k_2(O)(N_2) + k_2'(N)(NO) - k_3(NO)(O) + k_3'(N)(O_2) - k_4(N)(O) + k_4'(NO^+)(e)$$

$$\frac{d(O_2)}{dt} = -k_1(O_2)(X) + k_1'(O)^2(X) + k_3(O)(NO) - k_3'(N)(O_2)$$

$$\frac{d(X)}{dt} = k_1(O_2)(X) - k_1'(O)^2(X)$$

$$\frac{d(NO)}{dt} = k_2(N_2)(O) - k_2'(N)(NO) - k_3(O)(NO) + k_3'(N)(O_2)$$

$$\frac{d(NO^+)}{dt} = \frac{d(e)}{dt} = k_4(N)(O) - k_4'(NO^+)(e)$$

Using this set of equations, the change of the concentrations of the various species with time can be calculated. This includes the electron density. The actual calculations made in this study assumed an isothermal system although others have been made taking into account the effects of temperature and density change in the flow field. It seems reasonable that the results would be qualitatively the same for the two methods.

Calculations reported here were made for one set of conditions in the range of temperature and density of interest to the flow field problem. One computation was made using values of reaction rate constants which were designated as "standard". Then the reaction rate constants of each pair of reversible reactions were independently changed by an order of magnitude. First those of reaction 1 were changed; that is, k_1 and k_1' were increased by an order of magnitude. This is designated in the following tables as $1\uparrow$. Then k_2 and k_2' were increased by an order of magnitude, retaining the "standard" values for all the other rate constants, including k_1 and k_1'. This is designated as $2\uparrow$. Next k_3 and k_3' were decreased by one and then two orders of magnitude in runs designated as $3\downarrow$ and $3\downarrow\downarrow$. Finally, k_4 and k_4' were decreased an order of magnitude in a run designated as $4\downarrow$. In all these computations, the reaction rate constants were the same as used in the "standard" run except for the pair indicated in the designation

of that run. The rate constants for these calculations are given in Table 1.

Each of the computations was run until a time of 2 msec was reached.

The effects of these variations are seen in Tables 2 and 3 and in Figs. 1–4. Table 2 gives the calculated concentrations of N, O, NO and NO^+ or electrons in cm^{-3} after 2 msec reaction time.

Table 1. Rate Constants (cm^3 molecule^{-1} sec^{-1})

	1	2	3	4
	$O_2 + X$	$O + N_2$	$O + NO$	$N + O$
S	8.7×10^{-16}	1.8×10^{-14}	2.0×10^{-12}	1.9×10^{-14}
$O_2 + X$ $1\uparrow$	*8.7×10^{-15}*	1.8×10^{-14}	2.0×10^{-12}	1.9×10^{-14}
$O + N_2$ $2\uparrow$	8.7×10^{-16}	*1.8×10^{-13}*	2.0×10^{-12}	1.9×10^{-14}
$O + NO$ $3\downarrow$	8.7×10^{-16}	1.8×10^{-14}	*2.0×10^{-13}*	1.9×10^{-14}
$O + NO$ $3\downarrow\downarrow$	8.7×10^{-16}	1.8×10^{-14}	*2.0×10^{-14}*	1.9×10^{-14}
$N + O$ $4\downarrow$	8.7×10^{-16}	1.8×10^{-14}	2.0×10^{-12}	*1.9×10^{-13}*

This is done for each of the six runs described above. The concentrations may be compared with the equilibrium concentrations given in the last row. Table 3 gives the same concentrations (for the same runs and for equilibrium) normalized to those of the "standard" run. That is, they are given as multiples of those of the 'standard" run.

These results show some surprisingly large variations. Most dramatic are those for the NO^+ concentration, that is, the electron density. The changes of the rate constants of reactions 2, 3 and 4 each cause about an order of magnitude of change in the electron density. The change of the rate constants of reaction 1 causes a much more serious variation in the electron density, one of a factor of about 200. The concentrations of the other species for all of the runs do not seem to vary by more than an order of magnitude with the exception of the N atom concentration obtained when the rate constants of reaction 1 were changed. This is evidently caused by the production of O atoms by oxygen dissociation limiting the rate of N atom production by reaction 2.

These results are, of course, affected by the order of magnitude of the rate constants. That is, the effects caused by varying a certain rate constant from 10^{-16} to 10^{-15} might be quite different from changing it from 10^{-14} to 10^{-13}. However, the values chosen for use as "standard" and the variations from these are in the right order of magnitude to show, at least qualitatively, the effect of the variations.

Figs. 1–4 show the effects of changing rate constants on the concentrations (of NO^+, N, O, and

Table 2. Concentrations (cm^{-3}) after 2 msec

	(N)	(O)	(NO)	(NO^+)
S	1.0×10^{10}	0.76×10^{14}	0.23×10^{14}	0.91×10^{7}
$O_2 + X$ $1\uparrow$	0.32×10^{12}	0.68×10^{15}	0.20×10^{15}	0.19×10^{10}
$O + N_2$ $2\uparrow$	1.0×10^{11}	0.74×10^{14}	0.22×10^{15}	0.90×10^{8}
$O + NO$ $3\downarrow$	0.78×10^{11}	0.75×10^{14}	0.23×10^{14}	0.77×10^{8}
$O + NO$ $3\downarrow\downarrow$	0.74×10^{12}	0.77×10^{14}	0.23×10^{14}	0.76×10^{9}
$N + O$ $4\downarrow$	1.0×10^{10}	0.76×10^{14}	0.23×10^{14}	0.91×10^{6}
Equilibrium	0.23×10^{15}	0.34×10^{16}	0.38×10^{14}	0.16×10^{12}

Table 3. Concentrations after 2 msec.

	(N)	(O)	(NO)	(NO^+)
S	1	1	1	1
$O_2 + X$ 1↑	32	9·0	8·9	207
$O + N_2$ 2↑	10·0	1	9·7	9·9
$O + NO$ 3↓	7·8	1	1	8·5
$O + NO$ 3↓↓	75	1	1	83
$N + O$ 4↓	1	1	1	0·10
Equilibrium	20,000	34	2·5	5000

NO in that order) as a function of time. It can be seen, in general, that the ratios of the concentrations (the ratio of a concentration of a given species in one run to the same species in another run), is roughly about the same throughout most of the run. The ratios given in Table 3 for 2 msec are thus representative for most of the time period.

It has become obvious that accurate values of reaction constants are necessary if it is desired to make accurate calculations on the chemical system (particularly ionization) in flow fields. These data indicate that the rate constants for oxygen dissociation are the most critical. If a somewhat different choice of "standard" rate constants is used, it may be that those for another reaction would be more critical. Inclusion of other reactions might also affect the situation. However, they are all of importance and inaccuracies in the values of all of the rate constants involved should certainly be less than one order of magnitude. This applies to all temperatures. Thus the temperature dependence of the rate constants must be known. At the present time it does not seem reasonable to say that any of the rate constants is known to the desired accuracy at all temperatures of interest. Although there has been some improvement in our knowledge of these rate constants in the last few years, there is a great need for considerably more experimental work, particularly on the temperature effects.

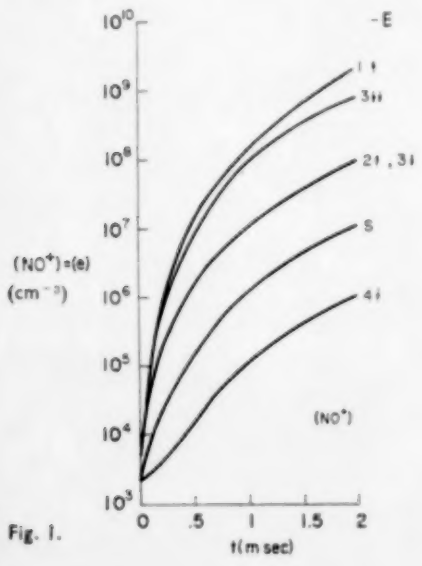

Fig. 1.

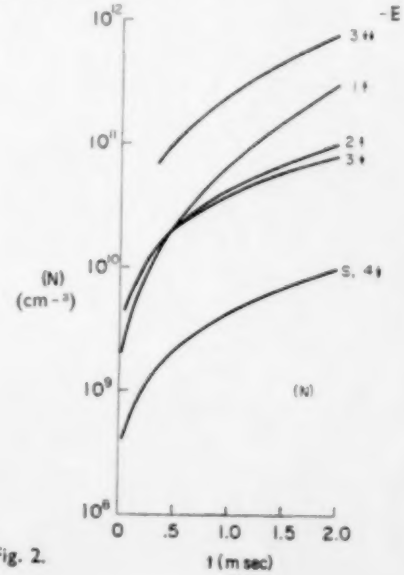

Fig. 2.

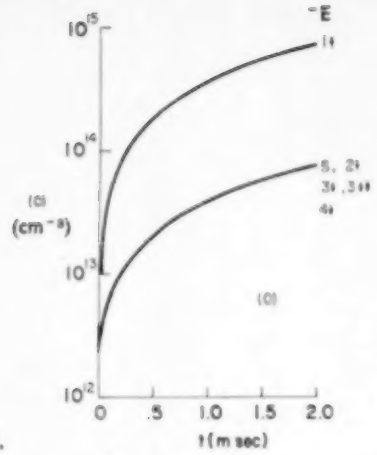
10^{15}
10^{14}
10^{13}
10^{12}
(O)
(cm^{-3})
$^{-E}$
1ϕ
5, 2ϕ
3ϕ, 3π
4ϕ
(O)
0 .5 1.0 1.5 2.0
t(m sec)

Fig. 3.

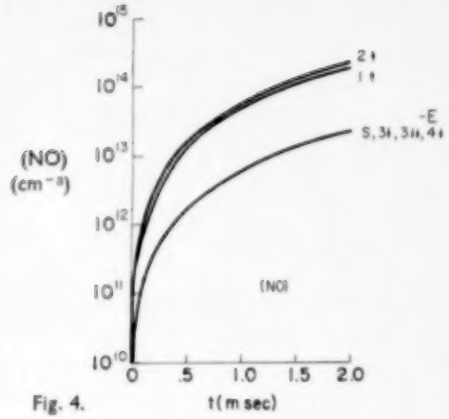
10^{15}
10^{14}
10^{13}
10^{12}
10^{11}
10^{10}
(NO)
(cm^{-3})
2ϕ
1ϕ
$^{-E}$
5, 3ϕ, 3π, 4ϕ
(NO)
0 .5 1.0 1.5 2.0
t(m sec)

Fig. 4.

ELECTRON CONCENTRATION IN CLOSED FORM FOR HIGH TEMPERATURE AIR AND AIR WITH ADDITIVES*

A. R. HOCHSTIM
Physics Section, Convair–San Diego
A Division of General Dynamics, San Diego, California

Abstract—Expression for electron concentration in closed form for high temperature oxygen–nitrogen mixtures are obtained and also for air with additives. Calculated results are well within uncertainties of more detailed treatments. Electron increasing and reducing additives in air are considered together with the effect on the electromagnetic properties of seeded air. Effect of long range Coulomb forces on total electron concentration is estimated.

TWO SIMPLE MODELS FOR OXYGEN–NITROGEN MIXTURES

The description of two thermodynamic models consisting only of O_2, O, N_2, N, and NO was reported in detail previously,[1] and are here briefly summarized. Defining the equilibrium constants (*see* Appendix)

$$K_1 = \frac{C_O^2}{C_{O_2}}; \quad K_2 = \frac{C_N^2}{C_{N_2}}; \quad K_3 = \frac{C_N C_O}{C_{NO}}, \tag{1}$$

where $C^{(i)}$ is the number of ith particles per original number of particles in the reference state we have[1] for the compressibility (no virial contributions)

$$Z = \Sigma C^{(i)}, \quad P = Z\rho RT, \quad R = R_0/M_0 \tag{2}$$

where ρ is the mass density, R_0 is the universal gas constant, M_0 the average molecular weight in an undissociated, un-ionized reference state. The molar fraction $X^{(i)}$ is connected to $C^{(i)}$ by the relation $ZX^{(i)} = C^{(i)}$. The number of particles in 1 cm^3, $N^{(i)}$, is $N^{(i)} = \left(\frac{\rho}{\rho_0}\right) L_0 C^{(i)}$, where the Loschmidt number $L_0 = 2{\cdot}6871 \times 10^{19}$. For completely dissociated air $Z = 2$.

Model I gave two quadratic uncoupled equations in C_O and C_N

$$\frac{2}{K_1}C_O^2 + C_O = 2\alpha_1; \quad \frac{2}{K_2}C_N^2 + C_N = 2\alpha_2,$$
$$C_{O_2} = \alpha_1 - \frac{1}{2}C_O \text{ and } C_{N_2} = \alpha_2 - \frac{1}{2}C_N, \tag{3}$$

where α_1 and α_2 are the original concentrations of oxygen and nitrogen in air (or in any other oxygen–nitrogen mixture) in an undissociated, un-ionized reference state. For argon-free air $\alpha_1 = 0{\cdot}21153$ and $\alpha_2 = 0{\cdot}78847$ and with argon $\alpha_1 = 0{\cdot}209795$, $\alpha_2 = 0{\cdot}780881$.

The more accurate Model II gave a fourth degree equation in C_O and C_N, or two quadratic coupled equations:

$$\frac{2}{K_1}C_O^2 + C_O + \frac{1}{K_3}C_N C_O = 2\alpha_1 \tag{4}$$

$$\frac{2}{K_2}C_N^2 + C_N + \frac{1}{K_3}C_N C_O = 2\alpha_2. \tag{5}$$

Furthermore,

$$C_{NO} = \frac{C_N C_O}{K_3}; \quad C_{O_2} = \alpha_1 - \frac{1}{2}C_O - \frac{1}{2}C_{NO};$$
$$C_{N_2} = \alpha_2 - \frac{1}{2}C_N - \frac{1}{2}C_{NO}. \tag{6}$$

These two models apply only for $Z = \Sigma C^{(i)} \leqq 2$.

* Conducted under ARPA Order No. 39-59 ARGMA Contract No. DA-04-495-ORD-1660.

The range of temperatures and densities for which these two models apply are shown in the sketch. The range is applicable for objects entering the earth's atmosphere with velocity of less than 8·8 km/sec (≈29,000 ft/sec) and for shocks travelling at sea level with velocities up to 11 km/sec. (≈36,000 ft/sec).

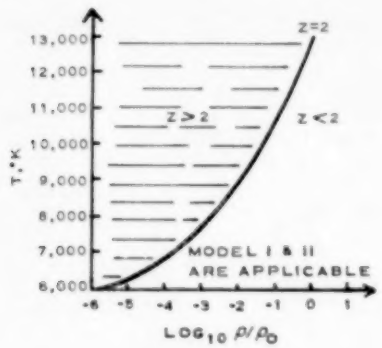

ELECTRON CONCENTRATION IN OXYGEN–NITROGEN MIXTURES

The following are the relations for the important ionization processes in oxygen–nitrogen (or oxygen–nitrogen–argon) mixtures where $Z<2$ (i.e. neglecting extremely small concentrations of N^{++}, O^{++}, etc.)

$$C_{NO}K_4=(C_{NO^+})C_{e^-};\quad C_NK_6=(C_{N^+})C_{e^-};$$
$$C_{N_2}K_8=(C_{N_2^+})C_{e^-};\quad C_OK_5=(C_{O^+})C_{e^-};$$
$$C_{O_2}K_7=(C_{O_2^+})C_{e^-};\quad K_9C_{O_2^-}=C_{O_2}C_{e^-};$$
$$K_{10}C_{O^-}=C_OC_e, \tag{7}$$

where the formulae for the equilibrium constants are listed in the Appendix.

The charge conservation equation in this case is (neglecting N^{++}, O^{++}, etc.)

$$(C_{e^-})+(C_{O^-})+(C_{O_2^-})=$$
$$=(C_{NO^+})+(C_{O^+})+(C_{N^+})+(C_{O_2^+})+C_{N_2^+} \tag{8}$$

Adding the equilibrium equations and using the charge conservation equation, we obtain,

$$C_{NO}K_4+C_OK_5+C_NK_6+C_{O_2}K_7+C_{N_2}K_8=$$
$$=[(C_{O^-})+(C_{O_2^+})+(C_{e^-})]C_{e^-}, \tag{9}$$

and

$$C_{e^-}=\left(\frac{C_{NO}K_4+C_OK_5+C_NK_6+C_{O_2}K_7+C_{N_2}K_8}{1+\dfrac{C_O}{K_{10}}+\dfrac{C_{O_2}}{K_9}}\right)^{\frac{1}{2}}. \tag{10}$$

We have calculated the term $\eta\equiv\dfrac{C_O}{K_{10}}+\dfrac{C_{O_2}}{K_9}$ from the work of Gilmore,[2] and the results are shown below:

Values of η for air

	ρ/ρ_0			
T (°K)	10	1	10^{-1}	10^{-2}
3000	5·805	0·630	0·077	0·002
6000	0·372	0·048	0·005	0·00005
12,000	0·042	0·004	0·0004	0·000003

The lower the temperature and the higher the density, the greater is the contribution from O^- and O_2^-, to the reduction of total free electron concentration (e.g., at $T=1000°K$, $\rho/\rho_0=10$, $\eta\sim10^4$).

For the case considered here equation (10) is exact if exact values of C_{NO}, C_O, C_N, C_{O_2}, and C_{N_2} are used. To a good degree of approximation, electron concentration, C_{e^-} can be obtained if approximate concentrations C_{NO}, C_O, C_N, C_{O_2} and C_{N_2} are used, as given by Model II. One can also obtain fair approximation using C_O, C_N and $C_{NO}=C_NC_O/K_3$ from Model I in equation (10).

Since O_2^+ and N_2^+ concentrations are small, we have for lower densities (neglecting O_2^- and O^-)

$$C_{e^-}=[C_{NO}K_4+C_OK_5+C_NK_6]^{\frac{1}{2}}. \tag{11}$$

Various methods of computation of partition functions for diatomic molecules[1–4] give slightly different equilibrium constants (e.g. K_3 and K_4, which yield uncertainty in C_e less than 5 per cent for $\rho/\rho_0<10$ and $T<8000°K$). Including other concentrations (NO^+, N_2O, A^+, etc.) complicates the problem and final correction to

the new C_e is still of the same order as the uncertainties in K's. The data currently available in the literature utilize the ionization energy of NO of 9·258 eV[2, 5] and 9·40 eV,[6] although the first value is probably more correct.[2, 7] The difference in electron concentration due to these values is 34 per cent at $T = 2000°K$ and diminishes at higher temperatures (Fig. 1).

ELECTRON INCREASING ADDITIVES

The addition of alkali atoms to air behind a sufficiently strong shock will result in an increase in the number of electrons due to very low ionization potential of alkali metals. The purpose of this section is to give theoretical results obtained for the increase of electron concentration in air due to seeding of air with cesium, which has the lowest known ionization potential and therefore will ionize with greater ease. The results can be applied as an upper limit of total free electron concentration in seeded air.

There are indications[8] that cesium vapour atoms at $T > 1000°K$ do not react with oxygen to form any important gaseous oxides. This being

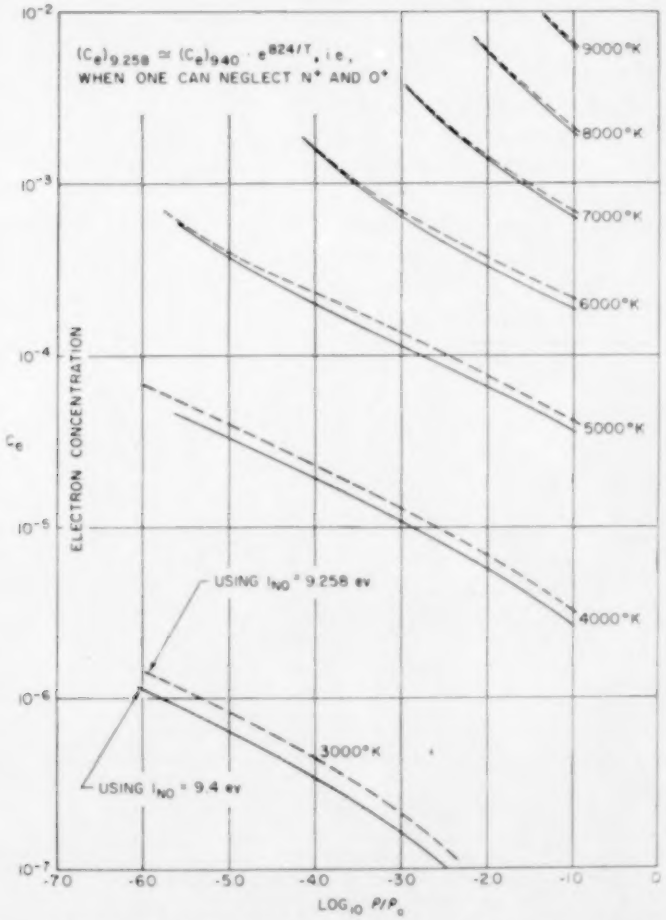

Fig. 1. Effect of two ionization energies of nitric oxide on total electron concentration of air.

true, it then may be said that the only important chemical reaction resulting from cesium seeding is that of ionization (*see* Appendix):

$$K_x = \frac{C_{(Cs+)}C_{e-}}{C_{Cs}}. \tag{12}$$

The above equilibrium equation and the conservation equation for cesium are the only additional equations to be added to the system of equations for computing the composition of air.

The partition function for Cs^+ was calculated using only the ground state ($g_0=1$) since the first excited energy level is at 154,520°K. The computation of partition function for neutral cesium is now in process including the long-range Coulomb interactions.[9] These results will given an effective partition function as a function of temperature and electron concentration.* For the preliminary calculations we have used available tables of free energies of cesium obtained through term by term summation of all available energy levels.[10] In Fig. 2 the results are compared with one using only the ground state of neutral cesium ($g_0=2$). There is no significant difference in total electron concentration of low density air (which was seeded with 10 per cent cesium) due to these two methods of computation of partition function of neutral cesium, since at low temperatures only the ground state contributes to the total sum and at high temperatures C_e are mainly from air species. At high densities the difference is increased, because of excess of electrons from Cs^+. However, the "cut-off" techniques would reduce greatly the partition function from Ref. (10), making the difference in Fig. 2 smaller (*see* Eq. 30, etc.).

If we start with 100 α_x per cent of cesium, then (neglecting N^{++}, O^{++}, N_2^+, O_2^+, O^-, O_2^-) $C_{Cs} + C_{Cs+} = \alpha_x$ and from equation (12) we obtain

$$C_{Cs} = \frac{\alpha_x C_{e-}}{C_{e-} + K_x}. \tag{13}$$

In a similar way to derivation of equations (10) and (11) we obtain

$$C_{e-}^2 = C_{NO}K_4 + C_O K_5 + C_N K_6 + \frac{\alpha_x K_x C_{e-}}{C_{e-} + K_x} \approx$$

$$\approx (C_{e-}^0)^2 + \frac{\alpha_x K_x C_{e-}}{C_{e-} + K_x}, \tag{14}$$

* See Eq. 16–37.

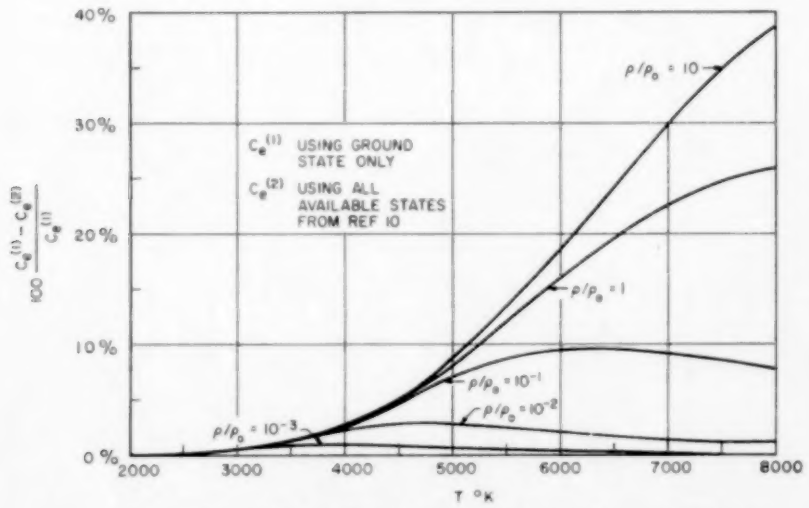

Fig. 2. Effect of two different partition functions of neutral cesium on total electron concentration in air seeded with 10 per cent Cs.

where $C_{e^-}^0$ is approximate electron concentration before seeding with small amount of cesium. This is only approximately so, because addition of cesium will change slightly the concentrations of N, O and NO. At lower temperatures, when C_e^0 is negligible, equation (14) is reduced to

$$C_{e^-}^2 + C_{e^-}K_x - \alpha_x K_x = 0, \qquad (15)$$

i.e. all electrons are from added cesium and thus given by Saha equation.

At higher temperatures C_{e^-} from air will predominate over C_{e^-} from cesium (Figs. 3–5).

We have solved the problem of addition of cesium to air utilizing numerical procedures for minimization of total Helmholtz function[11, 12] and including the following species: O, O_2, N, N_2, NO, NO^+, e^-, N^+, O^+, Cs, Cs^+, O^- and O_2^-. The effect of addition of cesium on concentration of NO^+ is shown in Fig. 6.

ELECTRON REDUCING ADDITIVE

Adding for example fluorine F_2 to high temperature air we have considered concentrations of F_2, F, F^-, F_2O (i.e., besides N, N_2, O,

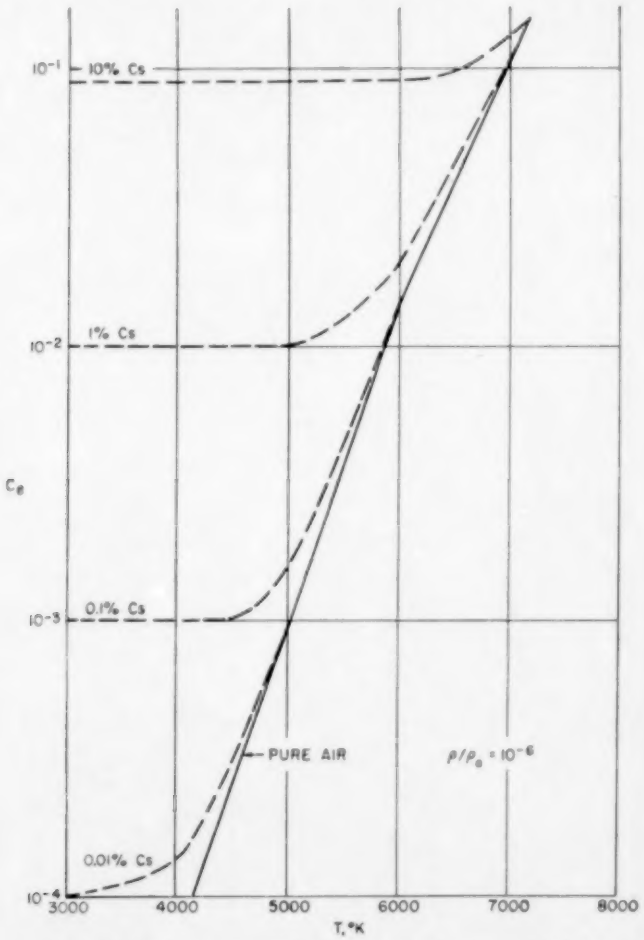

Fig. 3. Electron concentration in air and in air seeded with cesium.

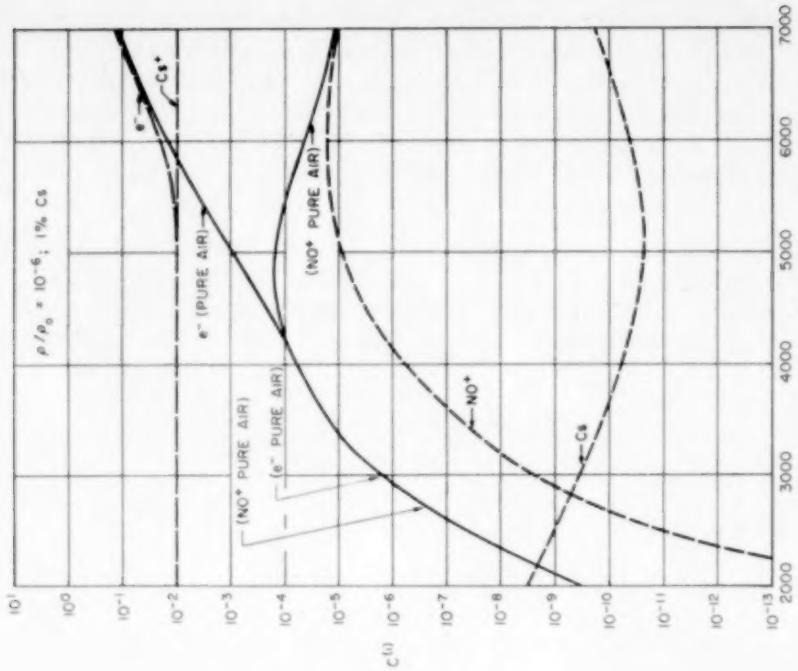

Fig. 5. Effect of addition of cesium on total concentration of electrons and on nitric oxide ions.

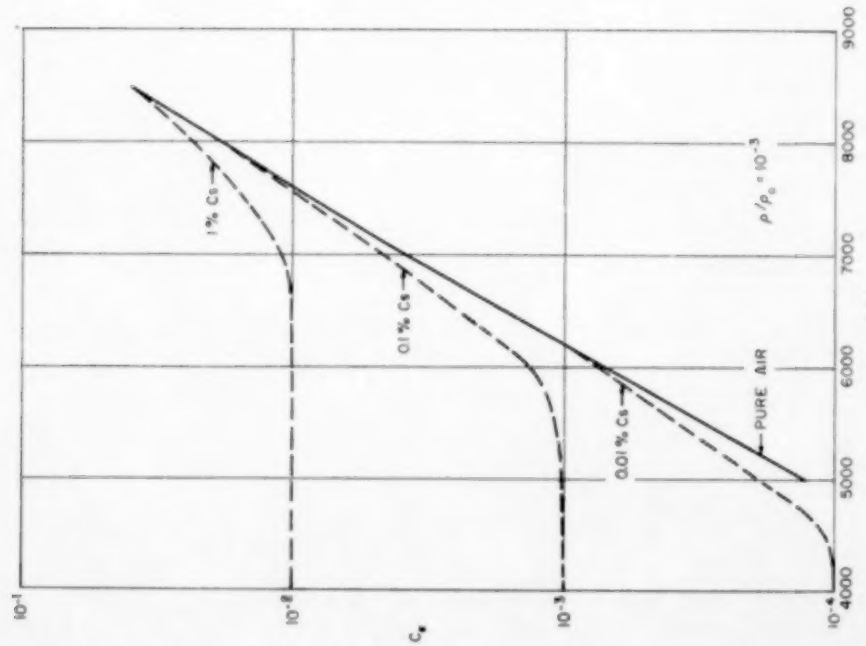

Fig. 4. Electron concentration in air and in air seeded with cesium.

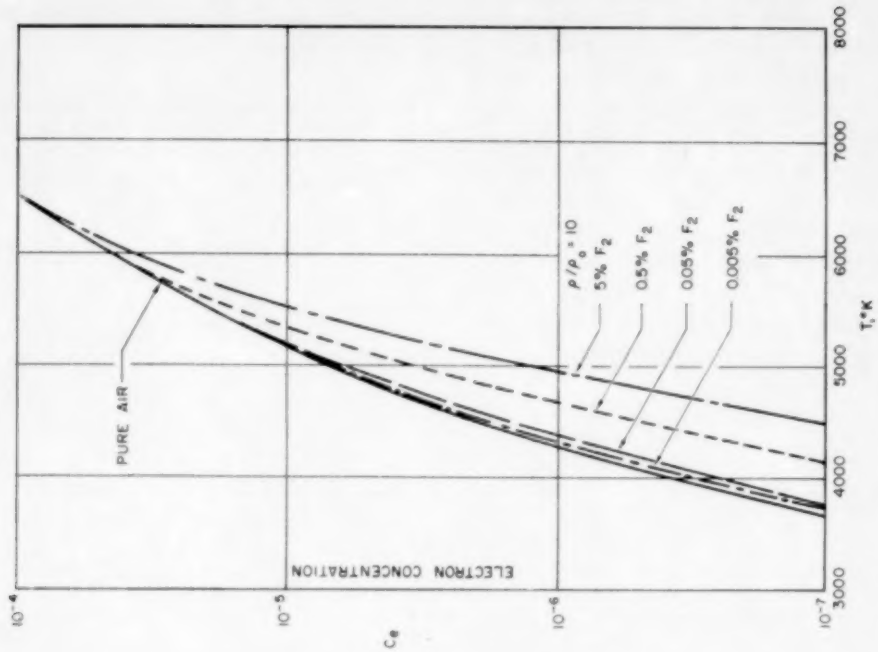

Fig. 7. Effect of addtiion of fluorine on total free electron concentration in air.

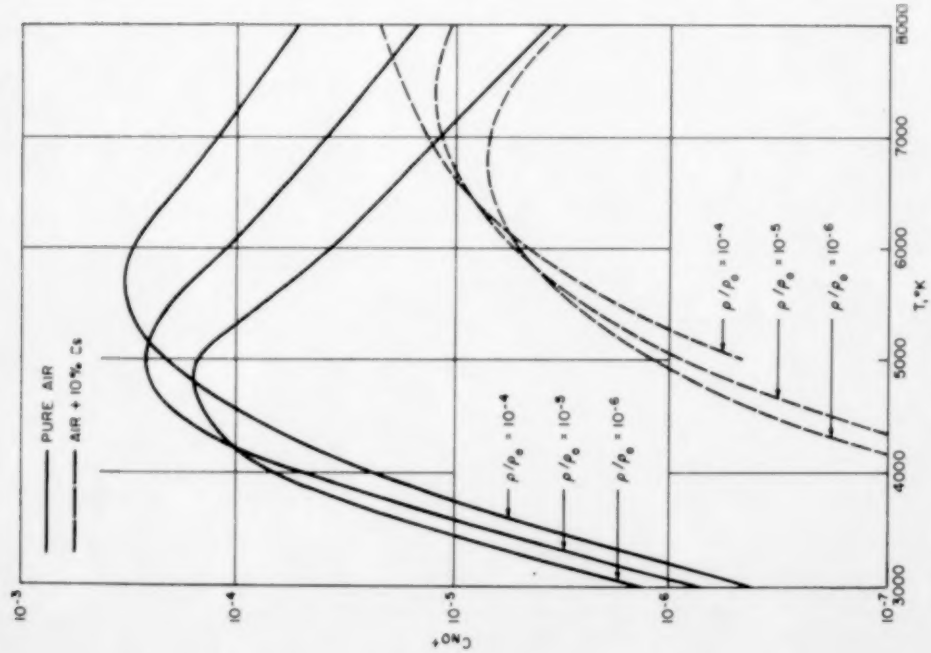

Fig. 6. Effect of addition of cesium on nitric oxide ion concentration.

O_2, O_2^-, O^-, e^-, N^+, O^+ and NO^+) and solved the problem on the IBM–704 using numerical technique for minimization of total Helmholtz function and using tabulated free energies.[10, 13] The results imply small effect of added fluorine on concentration of electrons at low densities (see Figs. 7 and 8). Also concentrations of F_2O and F_2 were found to be very small for $T <$ 1000°K. The data above 5000°K in Figs. 7 and 8 are extrapolated. Since F has very high known electron affinity, adding another element (e.g. Cl_2, Br_2, I_2) in the same amount instead of fluorine will not decrease the electron concentration any further.

EFFECT OF LONG RANGE COULOMB INTERACTIONS ON TOTAL FREE ELECTRON CONCENTRATION OF SEEDED AIR

We form the function (for air with additive)

$$\psi = \frac{A^0}{RT} - W(C_i,\rho,T) + \lambda_1\left[\frac{1}{2}\left(C_O\right) + \left(C_{O_2}\right) + \right.$$

$$\left. + \frac{1}{2}\left(C_{NO}\right) + \frac{1}{2}\left(C_{NO^+}\right) + \left(C_{O_2^+}\right) + \left(C_{NO_2}\right) + \right.$$

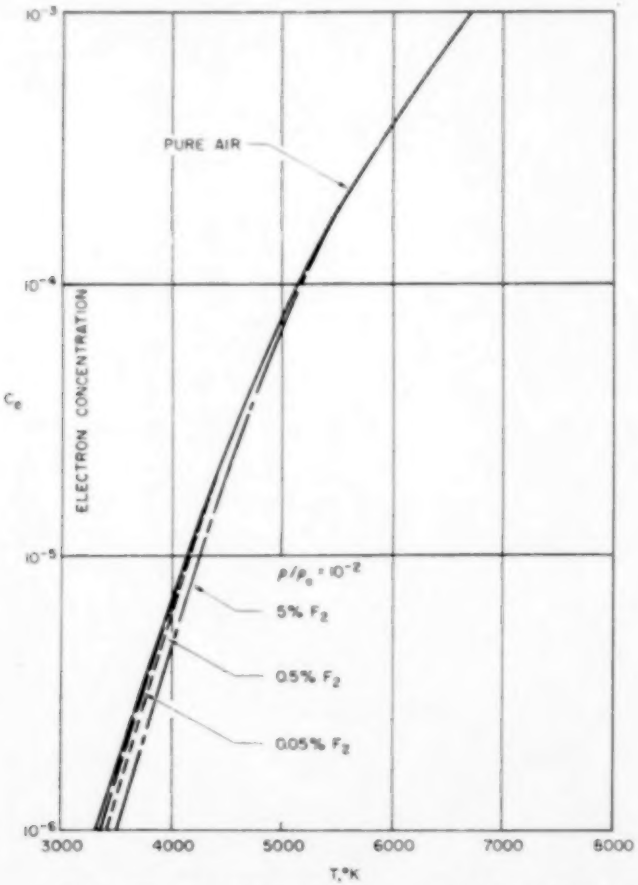

Fig. 8. Effect of addition of fluorine on total free electron concentration in air.

$$+\frac{1}{2}\left(C_{N_2O}\right)+\frac{1}{2}\left(C_{O+}\right)+\frac{1}{2}\left(C_{O-}\right)+\left(C_{O_2^-}\right)-$$
$$-\alpha_1\Big]+\lambda_2\Big[\frac{1}{2}\left(C_N\right)+\left(C_{N_2}\right)+\frac{1}{2}\left(C_{NO}\right)+$$
$$+\frac{1}{2}\left(C_{NO+}\right)+\left(C_{N_2^+}\right)+\frac{1}{2}\left(C_{NO_2}\right)+\left(C_{N_2O}\right)+$$
$$+\frac{1}{2}\left(C_{N+}\right)-\alpha_2\Big]+\lambda_3\Big[\left(C_{NO+}\right)+\left(C_{O_2^+}\right)+$$
$$+\left(C_{O+}\right)+\left(C_{N_2^+}\right)+\left(C_{N+}\right)+\left(C_{x+}\right)-$$
$$-\left(C_{e-}\right)-\left(C_{O-}\right)-\left(C_{O_2^-}\right)\Big]+\lambda_4\Big[\left(C_x\right)+$$
$$+\left(C_{x+}\right)-\alpha_3\Big], \tag{16}$$

where A^0 is the total ideal Helmholtz function $A^0 = E^0 - TS^0$, given by[1]

$$\frac{-A^0}{RT} = \Sigma C^{(i)}\Big[Y_0^{(i)} + 1 - \ln\rho/\rho_0 - \ln\frac{T}{T_0 Z_0} - \ln C^{(i)} - \frac{a^{(i)}}{T}\Big] \tag{17}$$

and where (*see* Appendix)

$$Y_0^{(i)} \equiv -\left(\frac{F^0 - E_0^0}{RT}\right)^{(i)} = -3{\cdot}66512 + \frac{3}{2}\ln M^{(i)} + \frac{5}{2}\ln T + \ln Q_{int}^{(i)}$$

is the ideal free energy function at 1 atm pressure, $a^{(i)}$ is constant added to $Y_0^{(i)}$ to account for E_0^0 (heats of formation of a given specie), $M^{(i)}$ is the molecular weight of the ith specie (chemical scale), $Q_{int}^{(i)}$ is the internal partition function, Z_0 is the compressibility of the gas in a reference state, at $T = T_0$, $\rho = \rho_0$, C_x and C_{x^+} are concentrations of the electron increasing additive X (e.g. cesium), assuming negligible concentration of species between X and oxygen and nitro en at these temperatures and densities and assuming no double ionization and no contribution from radiation, λ_1, λ_2, λ_3 and λ_4 are constant Langrange multipliers, which multiply the conservation equations of oxygen, nitrogen, charge and additive, respectively. The added function $-W(C_i,T,\rho)$ to the ideal Helmholtz function A^0/RT accounts for contribution due to long-range Coulomb interactions. W is known for small electron concentration, C_e. The equilibrium is determined so that at given temperature T and density ρ the total Helmholtz function has an absolute minimum, subject to the conservation equations, or what is the same, the function ψ should be minimized with respect to all concentrations. Therefore we form for each specie k,

$$\left(\frac{\partial\psi}{\partial C^{(k)}}\right)_{T,\rho} = 0. \tag{18}$$

These relations offer sufficient number of equations to eliminate λ's. The resulting equations give the equilibrium constants relations. (Numerical approximate techniques for such minimization procedure, now in common practice, are being used on IBM-704 in our problem.)[1, 11, 12] We obtain, for neutral species

$$-\left(\frac{\partial\psi}{\partial C_x}\right)_{T,\rho} = Y_0(\mathrm{X}) - \ln\frac{T\rho}{Z_0 T_0 \rho_0} - \ln C_x - \frac{a_x}{T} - \lambda_4 = 0, \text{ etc.} \tag{19}$$

The only terms involving W, will be

$$-\left(\frac{\partial\psi}{\partial C_e}\right)_{T,\rho} = Y_0(e^-) - \ln\frac{T\rho}{Z_0 T_0 \rho_0} - \ln C_{e-} - \lambda_3 + \left(\frac{\partial W}{C_{e-}}\right)_{T,\rho} = 0. \tag{20}$$

$$-\left(\frac{\partial\psi}{\partial C_{x+}}\right)_{T,\rho} = Y_0(X^+) - \ln\frac{T\rho}{Z_0 T_0 \rho_0} - \ln(C_{x+}) - \lambda_3 - \lambda_4 + \left(\frac{\partial W}{\partial C_{x+}}\right)_{T,\rho} = 0.$$

There are many ways of eliminating λ's, corresponding to various ways of writing equilibrium

constant, i.e. various formal ways of forming the same compound. Eliminating λ_3 and λ_4, for example, we obtain after some rearrangement,

$$\ln\frac{C_{x+}C_{e-}}{C_x} = Y_0(X^+) + Y_0(e^-) - Y_0(X) - \ln\frac{T\rho}{Z_0T_0\rho_0} + \frac{a_{x-}-a_{x+}}{T} + \Delta, \quad (21)$$

where

$$\Delta \equiv \left(\frac{\partial W}{\partial C_e}\right)_{T,\rho} + \left(\frac{\partial W}{\partial C_{x+}}\right)_{T,\rho}$$

and letting $a_x = a_e = 0$; $a_{x^+} = E_x$ where E_x is the ionization energy of X in °K and

$$\ln K_x = Y_0(x^+) + Y_0(e^-) - Y_0(x) - \ln\frac{T\rho}{Z_0T_0\rho_0} - \frac{E_x}{T}, \quad (22)$$

we obtain

$$\frac{C_{x+}C_{e-}}{C_x} = K_x e^{\Delta}. \quad (23)$$

Similarly, for any ionization reaction, if

$$\frac{\partial W}{\partial C_e} = \frac{\partial W}{\partial C_{O+}}, \quad \frac{C_{O+}C_{e-}}{C_O} = K_5 e^{\Delta}, \text{ etc.}$$

Finally, the total free electron concentration in air with electron increasing additive X is

$$\left(\text{if } \frac{\partial W}{\partial C_e} = \frac{\partial W}{\partial C_{O+}} = \frac{\partial W}{\partial C_{N+}} \ldots, \text{ etc.}\right)$$

$$C_{e-} = e^{\frac{1}{2}\Delta} \times \left(\frac{C_{NO}K_4 + C_OK_5 + C_NK_6 + C_{N_2}K_8 + C_{O_2}K_7 + C_xK_x}{1 + \frac{C_O}{K_{10}} + \frac{C_{O_2}}{K_9}}\right)^{\frac{1}{2}}$$

or for very small C_e

$$C_{e-} \simeq e^{\frac{1}{2}\Delta} \cdot \bar{C}_{e-}, \quad (25)$$

where $\bar{C}_{e-}$ is approximately the electron concentration without accounting for long range Coulomb interactions. The first term in the expression for W given by Wooley[14] is the Debye term, which in the case of single ionization is (in presence of 0^-, 0_2^- we should replace C_e by $C_e + C_{0-} + C_{0_2^-}$)

$$W_0 = \frac{4}{3}(2\pi)^{1/2}\left(\frac{e^2}{kT}\right)^{3/2}\left(\frac{P_0}{kT_0}\right)^{1/2}\left(\frac{\rho}{\rho_0}\right)^{1/2}C_e^{3/2} = \frac{B}{T\sqrt{T}}\left(\frac{\rho}{\rho_0}\right)^{1/2}C_{e^-}^{3/2}, \quad (26)$$

where $B = 1{\cdot}183 \times 10^6$. This term gives contribution to Δ

$$\Delta_0 = \frac{3}{2}\frac{B}{T\sqrt{T}}\left(\frac{\rho}{\rho_0}C_{e-}\right)^{1/2} = \frac{e^2/h}{kT} \quad (27)$$

where $h = \left(\frac{kT}{8\pi e^2 N_e}\right)^{1/2}$ is the Debye length and N_e is the number of electrons in 1 cm^3.

Because of dependence of electron concentration on temperature and density Δ_0 will be greater for higher densities and higher temperatures. For pure air at lower densities this correction is very small, e.g. at $T = 8000$°K, $\rho/\rho_0 = 10^{-6}$, $e^{\Delta_0} = 1{\cdot}002$; at $T = 3000$°K, $\rho/\rho_0 = 10^{-3}$, $e^{\Delta_0} = 1{\cdot}0001$. At higher densities Δ_0 becomes noticeable, e.g. at $T = 8000$°K, $\rho/\rho_0 = 1$, $e^{\Delta_0} \simeq 1{\cdot}08$. Similar conclusions for air were made by Hilsenrath, *et al.* at the National Bureau of Standards.[15] Stupochenko *et al.*[16] considered only the correction to the compressibility Z without modifying the equilibrium constants for the ions (*see* equation (23)) and found Debye–Hückel correction for air negligible up to pressures of 10^3 atm and $T = 14{,}000$°K (*see* equation (31)).

At low temperatures and high densities, we may neglect the electron contribution from the usual constituents of air and we obtain from equations (15) and (23) a modified Saha equation (*see* Appendix),

$$\frac{C_{e-}^2}{\alpha_x - C_{e-}} = 1{\cdot}7972 \times 10^{-4}\frac{Q(X^+)}{Q(X)}\frac{T\sqrt{T}}{\rho/\rho_0} \cdot \exp -(E_{ff}^{(1)}/T), \quad (28)$$

where $Q(X^+)$, and $Q(X)$ are the electronic partition functions for the ion and neutral atom, respectively, and where we decided to interpret $E_{ff}^{(1)}$ as the effective first ionization potential, i.e.

$$E_{ff}^{(1)} = E_0^{(1)} - T\Delta_0, \tag{29}$$

and where $E_0^{(1)}$ is the usual first ionization potential of X in °K. Thus, an increase in electron density (*see* equation (27)) decreases the effective ionization potential. For a simple self-consistent model, in accordance with this interpretation of ionization potential, we may avoid the usual divergence of partition functions at high temperatures by summing the partition function up to this effective ionization energy.

Thus,

$$Q(\mathrm{X}) = \sum_{n=0}^{k} g_n \exp -(\varepsilon_n/T), \quad \varepsilon_k = E_{ff}^{(1)}. \tag{30}$$

As can be seen from equation (27) this cut-off is equivalent to summing the series up to 0·5671 of Debye length h ($-e\mathrm{V} = \dfrac{e^2}{r}\, e^{-r/h} = kT\Delta$, $r = 0{\cdot}5671h$).

For 10 per cent cesium in an inert mixture ($\alpha_x = 0{\cdot}1$) at 7000°K and $\rho/\rho_0 = 10$, equation (29) was solved by an iteration method, using $Q(\mathrm{Cs}^+) = 1$. First we took $\Delta_0 = 0$, $Q(\mathrm{Cs}) = g_0 = 2$ and obtained $C_e = 2{\cdot}49 \times 10^{-2}$ and an effective ionization potential of 24,048 cm^{-1}. The $Q(\mathrm{Cs})$ after cutting at the 9th excited state[17] of 22,631·8 cm^{-1} gave $Q(\mathrm{Cs}) = 3{\cdot}2682$. Finally, $E_{ff}^{(1)}$ converged after fourteen iterations* to 21,247·2 cm^{-1} and C_{e-} converged to the value of $4{\cdot}750 \times 10^{-2}$, an increase of initial electron concentration of 48 per cent.

The compressibility is (*see* equations (17) and (26); $A = A^0 - RTW_0$)

$$Z = \left(\frac{\partial A/RT}{\partial \ln \rho}\right)_{T,Ci} = \Sigma C^{(i)} - \frac{1}{2}W_0 = \Sigma C^{(i)} - \frac{1}{3}C_e\Delta_0, \tag{31}$$

and in the previous example $\Delta Z/Z = \Delta P/P \simeq 1$ per cent only. For 10 per cent cesium in the air at 7000°K and $\rho/\rho_0 = 10$ with $\Delta_0 = 0$ we obtained $C_{e-} = 5{\cdot}47 \times 10^{-3}$ (a decrease over the previous case due to presence of: $C_{0^-} = 1{\cdot}07 \times 10^{-3}$, $C_{\bar{O}_2} = 6{\cdot}15 \times 10^{-5}$; $C_{\mathrm{NO}^+} = 5{\cdot}89 \times 10^{-6} > C_{\mathrm{O}^+} > C_{\mathrm{N}^+}$). In a way similar to the previous example, we adjusted the ionization potentials of N, O, NO and Cs; however, instead of using C_e in equation (27) we used $C_e + C_{\mathrm{O}^-} + C_{\mathrm{O}_2^-}$. The iterations converged (by using a numerical method of minimization of total Helmholtz free energy[11, 12] in each step) to $C_{e-} = 8{\cdot}191 + 10^{-3}$; $C_{0^-} = 1{\cdot}597 \times 10^{-3}$ and $C_{\mathrm{O}_2^-} = 9{\cdot}180 \times 10^{-5}$. Thus, for 10 per cent Cs in air, electrons, 0^-, 0_2^- and Cs^+ were increased by 33 per cent each and NO^+, N^+ and O^+ were increased by ~ 42 per cent each.

A similar procedure was used recently,[18] but the summations were cut at the value of $-eV = e^2/r = kT$, $\varepsilon_k = E_0^{(1)} - T$, which does not depend on electron concentration and may require summing beyond the Debye length (in previous example for cesium in an inert mixture this would correspond only to $r = 0{\cdot}872$ h).

If doubly or multiply ionized species are present, W_0 in equation (26) must be multiplied by[14]

$$\left(\frac{1}{2C_{e-}} \sum C_s Z_s^2\right)^{3/2} \tag{32}$$

where

$$\sum C_s Z_s^2 = C_{e-} + C_1 + 4C_2 + 9C_3 + \ldots + n^2 C_n, \tag{33}$$

and where Z_s is the charge in protonic units on s-ion, C_2 means concentration sum of all doubly ionized species, etc. By substituting the modified W_0 to equation (16) or to a similar one without air, we obtain

$$\frac{C_{\mathrm{X}^+} C_{e-}}{C_{\mathrm{X}}} = k_0 e^{\bar{\Delta}_0}; \quad \frac{C_{\mathrm{X}^{++}} C_{e-}}{C_{\mathrm{X}^+}} = k_1 e^{2\bar{\Delta}_0}; \tag{34}$$

$$\frac{C_{\mathrm{X}^{+++}} C_{e-}}{C_{\mathrm{X}^{++}}} = k_2 e^{3\bar{\Delta}_0} \ldots; \quad \frac{C_{\mathrm{X}}^{(n+1)} C_{e-}}{C_{\mathrm{X}}^{(n)}} = k_n e^{(n+1)\bar{\Delta}_0},$$

* The lengthy iteration procedure can be eliminated by specifying T and N_e and solving Eq. 28 for ρ/ρ_0. At high ρ/ρ_0 one obtains two values of N_e for the same T. However, only the solution with lower value of N_e satisfies the equilibrium condition that the Helmholtz free energy be maximum. For a singly ionizing specie in an inert mixture this condition is: $\Delta_0 < 4 + 2C_e$ (a—C_e)

where

$$\bar{\Delta}_0 = \Delta_0 \left[1 + \frac{C_2 + 3C_3 + 6C_4 + \ldots + \frac{n(n-1)}{2} C_n}{C_{e^-}} \right]^{1/2}. \tag{35}$$

The above expression was obtained by using the charge conservation equation,

$$C_{e^-} = \Sigma\, nC_n.$$

Thus, Δ_0 can be used instead of $\bar{\Delta}_0$ if concentrations of doubly or multiply ionized species are negligible. In a way similar to our previous interpretation of first effective ionization energy, we now define, first, second, etc. (reduced) effective ionization energies (in °K):

$$E_{ff}^{(1)} = E_0^{(1)} - T\bar{\Delta}_0; \quad E_{ff}^{(2)} = E_0^{(2)} - 2T\bar{\Delta}_0, \ldots$$
$$\ldots E_{ff}^{(n+1)} = E_0^{(n+1)} - (n+1)T\bar{\Delta}_0, \tag{36}$$

where $E_0^{(1)}, E_0^{(2)} \ldots$ are first, second, etc., usual ionization energies. In cutting the partition functions at those values of effective ionization energies we obtain

$$\left.\begin{aligned} Q(\mathrm{X}) &= \sum_{n=0}^{k_0} g_n e^{-\varepsilon_n/T}, \quad \varepsilon_{k_0} = E_{ff}^{(1)}; \\ Q(\mathrm{X}^+) &= \sum_{n=0}^{k_1} g_n e^{-\varepsilon_n/T}, \quad \varepsilon_{k_1} = E_{ff}^{(2)}; \\ Q(\mathrm{X}^{(s)}) &= \sum_{n=0}^{k_s} g_n e^{-\varepsilon_n/T}, \quad \varepsilon_{k_s} = E_{ff}^{(s+1)} \end{aligned}\right\} \tag{37}$$

The model for inclusion of long-range Coulomb interactions presented in this section is similar to the suggestion of Ecker and Weizel[19] in cutting the summation in the partition function before Debye radius, together with a lowering of ionization energy. These two effects can be interpreted as a consequence of an addition to the Helmholtz free energy of a function which depends on electron and ion concentration according to Debye–Hückel theory. A more rigorous theory is needed, but in view of the many uncertainties of ionization energies, original composition (e.g. of air) etc., the model described offers simple and self-consistent technique for computing long-range Coulomb effects.

ELECTROMAGNETIC PROPERTIES OF SEEDED AIR

The number of electrons in 1 cm³ is given by

$$N_{e^-} = \frac{\rho}{\rho_0} L_0 C_{e^-} \tag{38}$$

and the plasma frequency by

$$\omega_p = 2\pi f_p = \left(\frac{4\pi e^2 N_e}{m_e} \right)^{\frac{1}{2}} = 5{\cdot}641 \times 10^4 \sqrt{N_e}. \tag{39}$$

Most electromagnetic properties of a uniform plasma in equilibrium are specified if one also knows the collision frequency. The total (effective) collision frequency can be taken as

$$\nu = \nu_{e,n} + \nu_{e,i}, \tag{40}$$

where $\nu_{e,n}$ is the collision frequency of electrons with neutrals and $\nu_{e,i}$ is the collision frequency of electrons with ions. Now, $\nu_{e,n}$ is proportional to the electron–neutral cross-sections, concentration of neutral species, and velocity, i.e. independent of electron concentration. In the region of temperatures and densities, where $\nu_{e,n} \gg \nu_{e,i}$ (for air: at $\rho/\rho_0 = 10^{-6}$ for $T < 4000$°K; at $\rho/\rho_0 = 1$ for $T < 7000$° K) the increase of electron concentration due to addition of small amount of easily ionizing additive (without changing the temperature and density) will have no effect on the total ν, increasing only ω_p. For a plane electromagnetic wave incident perpendicularly on a semi-infinite, uniform plasma slab (*see* Fig. 9, suggested by L. Kraus[20]) the increase of only electron concentration, when $\nu_{e,n} \gg \nu_{e,i}$ will increase the reflectivity (e.g. $N_e' = 100\ N_e$, A → B) for a given incident frequency of microwaves. If the unionized portion of the additive X has very large electron-neutral cross-section as compared with air, so that $C_x Q_x > \Sigma C_n Q_n$, then such an additive besides increasing the total electron concentration will also increase the collision frequency. Under these conditions, as can be seen from

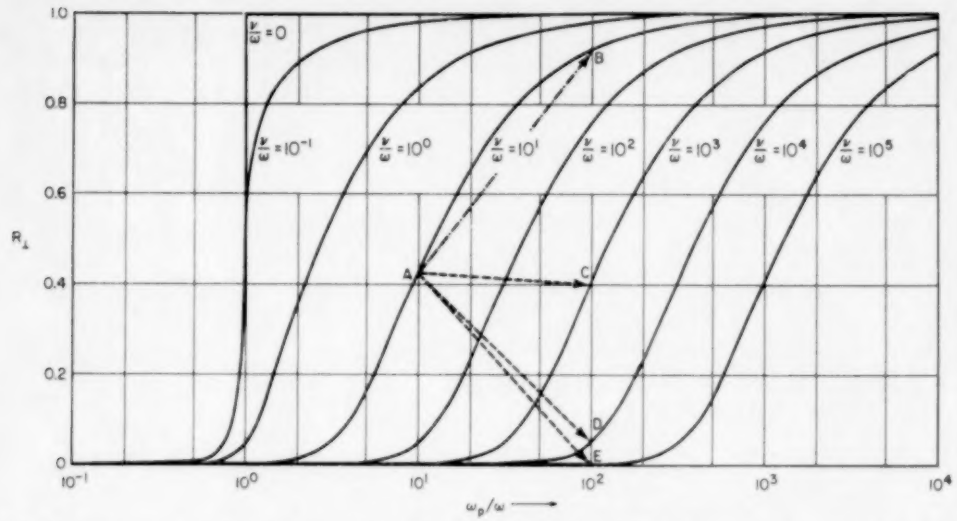

Fig. 9. Microwave reflection on perpendicular incidence from semi-infinite homogenous plasma slab.

Fig. 9, the plasma in some instances may become less reflecting (e.g. for $N'_e = 100\,N_e$, A → C, D, E).

However, when $\nu_{e,n} \ll \nu_{e,i}$, (for air: at $\rho/\rho_0 = 10^{-6}$ for $T > 5000°K$; at $\rho/\rho_0 = 1$ for $T > 9000°K$) the predominant $\nu_{e,i}$ is proportional to electron concentration and an increase in only the electron concentration will increase, besides ω_p, also the total ν. Under these conditions (at very high temperatures) the plasma in some instances may become less reflecting (*see* Fig. 9). This case, however, is hard to obtain, since a small amount of additive to the air at high temperatures will not increase appreciably the total electron concentration because the air is already highly ionized (Fig. 3).

Acknowledgements—In connection with numerical programming, computations and analysis the author wishes to acknowledge the very conscientious and active assistance of Mr. E. Solum from Convair, San Diego, Thermodynamics Group, and Mr. E. Philbin from Convair, Physics Section. The author also wishes to express his gratitude to L. Haar, Convair, Physics Section, for helpful criticism.

REFERENCES

1. A. R. Hochstim, *Approximations to High-Temperature Thermodynamics of Air in Closed Form*, presented at *Western State Section of the Combustion Institute, Los Angeles, California, November 2–5, 1959*. (Proceedings to be published by Butterworth's, London.)
2. F. R. Gilmore, *Equilibrium Composition and Thermodynamic Properties of Air to 24,000°K*, RAND Corporation, Rep. RM-1543 (Aug. 1955).
3. J. E. Mayer and M. G. Mayer, *Statistical Mechanics*. Wiley, New York (1950).
4. C. W. Beckett and L. Haar, *Thermodynamic Properties at High Temperatures*, in *Proceedings of the Joint Conference on Thermodynamic and Transport Properties of Fluids of the International Union of Pure and Applied Chemistry*. p. 27, The Institution of Mechanical Engineers, London (1958).
5. J. G. Logan and C. E. Treanor, Cornell Aeronautical Laboratory, Rep. No. BE-1007-A-3 (Jan. 1957).
6. J. Hilsenrath and C. W. Beckett, Arnold Engineering Development Centre Rep. No. TN-56-12, AD-98974, MIPR-AEDC-1, N.B.S. (1956).
7. G. G. Cloutier and H. I. Schiff, *J. Chem. Phys.* **31**, 793 (1959).
8. L. Brewer and A. W. Searey, *Ann. Rev. Phys. Chem.* **7**, 259 (1956).
9. L. Haar, *Biannual Scientific Report*, Convair, San Diego, Phys. Sect. Rep. ZPh-050 (Dec. 1959).
10. H. G. Kolsky, R. M. Gilmer and P. W. Gilles, *Thermodynamic Properties of 54 Elements Considered as Ideal Monatomic Gas*, Los Alamos Sci. Lab. Rep. U-LA-2110 (Phys.) (March 1957).
11. L. F. Feigenbutz, *Semi-Annual Progress Report*, Convair, San Diego, Phys. Sect. Rep. ZPh-030 (Apr. 1959).
12. W. B. White, S. M. Johnson and G. B. Danzig, *J. Chem. Phys.* **28**, 751 (1958).
13. L. F. Feigenbutz, G. L. Stiehl and E. L. Katz, *Combustion Charts for High Energy Fuels, I.* Convair, San Diego, Thermodyn. Group Rep. ZR-600-001 (Apr. 1958).
14. H. W. Woolley, *J. Res. Nat. Bur. Stand.* **61**, 469 (1958).

15. J. Hilsenrath, M. Green and C. W. Beckett, *Thermodynamic Properties of Highly Ionized Air*, AFSWC-TR-56-35 (ASTIA Doc. No. AD-96303) (Apr. 1957).
16. E. V. Stupochenko *et al.*, *Thermodynamic Properties of Air in the Temperature Interval from 1000 to 12,000°K and Pressure Intervals from 0·001 to 1000 atm* in *Physical Gasdynamics* p. 3, Acad. Sci. U.S.S.R. (1959). English translation in *J. Amer. Rocket Soc.* **30**, 98 (1960).
17. C. E. Moore, *Atomic Energy Levels, Nat. Bur. Stand. Circ.* No. 467 (1949).
18. H. Myers, J. H. Buss and S. W. Benson, *Thermodynamics of Ionized Gases*, paper presented to *Con. Phys. Chem. in Aerodynamics and Space Flight, September 1959*, Douglas Aircraft Company, Santa Monica, California, Paper No. 811 (1960).
19. G. Ecker and W. Weizel, *Ann. Phys., Lpz.* (6) **17**, 126 (1956).
20. L. Kraus, Unpublished work, Phys. Sect., Convair, San Diego.
21. C. E. Moore, *Atomic Energy Levels*, Nat. Bur. Stand. Circ. No. 467, **3** (1958).
22. J. Hilsenrath, M. Klein and H. W. Woolley, *Tables of Thermodynamic Properties of Air including Dissociation and Ionization from 1500 to 15,000°K*, Nat. Bur Stand., Rep. OSS-59-24, AEDC-TR-59-20, (Dec. 1959).

APPENDIX

For an equilibrium constant of the form

$$K_j = \frac{C_x C_y}{C_z} \quad (Z \rightleftarrows X + Y),$$

we have[1]

$$\ln K_j = -\left(\frac{F^0 - E_0^0}{RT}\right)^{(x)} - \left(\frac{F^0 - E_0^0}{RT}\right)^{(y)} + \left(\frac{F^0 - E_0^0}{RT}\right)^{(z)} - \frac{E_j}{T} - \ln\rho/\rho_0 - \ln T/(T_0);$$

$$-\left(\frac{F^0 - E_0^0}{RT}\right)^{(i)} = \ln Q_{\text{int}}^{(i)} + s^{(i)} + \frac{5}{2}\ln T,$$

where $s^{(i)} = -3{\cdot}66512 + \frac{3}{2}\ln M^{(i)}$ *and* $s^{(i)}$ are listed in Table I;

$$\ln Q_{\text{int}}^{(i)} = \ln \sum_{n=0} \bar{p}_n \exp - [\varepsilon_n^{(i)}/T] +$$

$$+ \delta^{(i)}\{\ln T - \lambda^{(i)} - \ln[1 - u_0^{(i)}] + \ln[1 + \gamma_0^{(i)} T]\},$$

where $\delta^{(i)} = 0$ for atoms and atomic ions, $\delta^{(i)} = 1$ for diatomic molecules and diatomic ions; $\bar{p}_n$, $\bar{\varepsilon}_n$, λ and θ_0 are listed in Table I and

$$u_0^{(i)} = \delta^{(i)} \exp - [\theta_0^{(i)}/T].$$

The above equilibrium constant is related to the equilibrium constant K_p by

$$(K_p)_j = \frac{P_x P_y}{P_z} = \frac{(C_x \rho RT)(C_y \rho RT)}{C_z \rho RT} = K_j \rho RT = K_j \frac{\rho}{\rho_0} \cdot \frac{P_0 T}{T_0}, \quad P_0 = 1 \text{ atm};$$

$$P_0 = L_0 k T_0; \quad P_0 = 1 \text{ atm} = 1{\cdot}01325 \times 10^6 \text{ dynes/cm}^2; \quad T_0 = 273{\cdot}16^\circ\text{K};$$

$$\ln\left(\frac{2\pi k}{h^2 N_A}\right)^{3/2} \frac{k}{P_0} = 3{\cdot}66512;$$

$$s^{(e)} = -3{\cdot}66512 + \frac{3}{2}\ln M_e = -14{\cdot}9273;$$

$$2\frac{(2\pi k m_e)^{3/2}}{h^3 L_0} = 1{\cdot}7972 \times 10^{-4}.$$

j	C_x	C_y	C_z	E_j, °K
1	C_O	C_O	C_{O_2}	59,369 (Refs. 2, 4)
2	C_N	C_N	C_{N_2}	113,263 (Ref. 2)
3	C_N	C_O	C_{NO}	75,507 (Ref. 2)
4	C_{NO^+}	C_{e^-}	C_{NO}	107,447 (Ref. 2)
5	C_{O^+}	C_{e^-}	C_O	158,040 (Ref. 2)
6	C_{N^+}	C_{e^-}	C_N	168,655 (Ref. 21)
7	$C_{O_2^+}$	C_{e^-}	C_{O_2}	141,797 (Ref. 2)
8	$C_{N_2^+}$	C_{e^-}	C_{N_2}	180,827 (Ref. 22)

Table 1.

	N	O	N_2	O_2	NO
$\bar{p}_0$	4	5	1	3	2
$\bar{p}_1$	10	3	6·8118	2·1276	2
$\bar{p}_2$	6	1	10·07	1·1448	1·3670
$\bar{p}_3$	0	5	0	8·2596	11·1180
$\bar{p}_4$	0	1	0	4·4494	2·773
$\bar{p}_5$	0	0	0	12·057	1·4005
ϵ_1	27665	228·1	71321	11245	173·9
$\bar{\epsilon}_2$	41497	325·9	85158	18620	64192
$\bar{\epsilon}_3$	0	22830	0	48542	64685
$\bar{\epsilon}_4$	0	48622	0	46845	75979
$\bar{\epsilon}_5$	0	0	0	68841	76824
δ	0	0	1	1	1
θ_0	0	0	3353·5	2239	2699
λ	0	0	1·7506	1·4086	0·8867
s	0·2943	0·4938	1·3340	1·5335	1·4371
$10^4\gamma_0$	0	0	0·0846	0·1497	0·1196

Table 1. Continued

	NO^+	O^+	N^+	O_2^+	N_2^+	e^-
$\bar{p}_0$	1	4	1	4	2	2
$\bar{p}_1$	0	10	3	23·253	5·2117	0
$\bar{p}_2$	0	6	5	13·340	1·6991	0
$\bar{p}_3$	0	0	5	8·260	0	0
$\bar{p}_4$	0	0	1	0	0	0
$\bar{p}_5$	0	0	5	0	0	0
ϵ_1	0	38589	70·65	45055	13022	0
$\bar{\epsilon}_2$	0	58227	188·9	52944	36671	0
$\bar{\epsilon}_3$	0	0	22037	68659	0	0
$\bar{\epsilon}_4$	0	0	47032	0	0	0
$\bar{\epsilon}_5$	0	0	67868	0	0	0
δ	1	0	0	1	1	0
θ_0	3373	0	0	2652	3129	0
λ	1·0530	0	0	1·5652	1·7107	0
s	1·4371	0·4938	0·2943	1·5335	1·3340	−14·927
$10^4\gamma_0$	0·0907	0	0	0·1380	0·1025	0

(For Argon, $g_0=1$, $h=1{\cdot}86611$ and remaining constants are zero.)

Listed are only $\epsilon_n \lesssim 60{,}000$ cm$^{-1} \simeq 86{,}000$°K. For ϵ_n not listed, we have chosen for simplicity in numerical programming $\bar{\epsilon}_n = 0$. For atoms and atomic ions $\theta_0=0$, $\lambda=0$, $\epsilon_n=\bar{\epsilon}_n$ and $\bar{p}_n=g_n$. All $\bar{\epsilon}_n$ are in °K. For diatomic molecules and diatomic ions $\bar{p}_n$'s are limiting ratios (at infinite temperature) of effective statistical weights of a given state to the ground state. For the excited states the dependence on temperature of vibration, unharmonicity and non-rigidity were incorporated as an average correction to energy levels ϵ_n for $T<12{,}000$°K. For details see Ref. (1).

RATE OF IONIZATION BEHIND SHOCK WAVES IN AIR*

S. C. LIN

Avco-Everett Research Laboratory, Everett 49, Massachusetts

Abstract—Knowledge of the ionization rate behind strong shock waves in air is essential not only for problems involving the flight of hypersonic vehicles at high altitudes, but it is also important for many interesting problems in atmospheric and geophysical research (e.g. the meteoric ionization problem). The main difficulty experienced in earlier studies[1] was the extremely fast rate observed at normal air densities, which kept the electron density profile behind strong shock waves beyond the spatial resolution of most ionization detectors that can be used for quantitative measurements.

In the present investigation, the above-mentioned difficulty has been removed through the use of a 24 in. diameter, low-density shock tube, which allows experiments to be performed at densities lower than the ordinary shock tube operating density[2] by a factor of 100. By using such a shock tube, together with a microwave reflection probe, the electron density profile behind normal shock waves in air at density corresponding to an altitude of 250,000 ft (initial shock tube pressure, $p_1 = 20\ \mu$ Hg) and in the velocity range $10{,}000 < U < 25{,}000$ ft/sec has been successfully measured. The preliminary results, which agreed grossly with a theoretical prediction by Lin and Teare,[3] indicated that at satellite velocity ($U \approx$ 25,000 ft/sec), the thermal ionization process will be completed at a distance of about 1 cm behind the shock front; while at a velocity of 15,000 ft/sec the corresponding distance will be about 10 cm. At other altitudes (up to about 300,000 ft, where atomic oxygen begins to appear in the atmosphere) the corresponding ionization distance may be scaled inversely to the atmospheric density since all the collision processes which govern the initial rise of the electron density profile are binary.

INTRODUCTION

In an earlier study of the electrical conductivity of ionized air behind plane shock waves, Lamb and Lin[1] observed that the ionization process progressed much more rapidly behind the shock front than has been expected. For example, they have found that at an initial pressure of 1 mm Hg, the ionization build-up distance even for the weakest shock wave (shock Mach number $M_s \approx 10$) appeared to be at least a factor of 10 smaller than the spatial resolution of the apparatus employed, which was about 1 in. This was several orders of magnitude faster than that observed by Petschek and Byron for shock waves in argon at corresponding shock strength,[4] even after due allowance is made for the difference in ionization potential between argon and the major chemical constituents of the shock-heated air.†

In 1958 Niblett and Blackman[5] attempted to measure the ionization relaxation time behind shock waves in air using the shock-reflection technique developed by Petschek and Byron.[4] This method was based on the assumption that the intensity of the visible light emitted by the shock-heated gas is directly related to the local electron density. While this assumption can be applied to strong shock waves in argon, where the emitted light was primarily due to the Kramer–Unsöld type radiation;[6] such a definite

* This work was supported jointly by the Air Force Ballistic Missile Division, Air Research and Development Command, United States Air Force, under contract No. AF 04(647)-278, and the Advanced Research Projects Agency under contract No. DA 19-020-ORD-4862 with the Army Rocket and Guided Missile Agency, Army Ordnance Missile Command, United States Army.

† A fair way to compare shock strength for this purpose is to scale the kinetic energy per molecule (relative to the shock front) according to the ionization potential. Thus, a Mach 10 shock wave in air ($I = 9{\cdot}25$ eV for NO; molecular wt. = 29) is comparable to a Mach 12 shock wave in argon ($I = 15{\cdot}7$ eV; molecular wt. = 40).

correlation between the light intensity and the local electron density unfortunately does not exist for shock-heated air, where the emitted light in the visible region has been found to be primarily due to molecular band systems in the range of shock strength under consideration.[7, 8]

Recently, Manheimer-Timnat and Low[9] have reported some ionization rate measurements at relatively low shock strength ($M_s = 8{\cdot}2$–$11{\cdot}4$), using the microwave attenuation technique. However, judging from the physical dimensions of the shock tube in relation to the initial pressure employed in their experiments, together with the general behaviour of shock tubes under similar operating conditions,[2] it is quite evident that the rise-time observed in their microwave attenuation signal was more related to the available testing time of their shock tube (i.e. time elapse between the arrival of the shock front and the gas interface at a fixed station) than to the ionization relaxation time.

In the course of choosing the appropriate method for probing the local electron density distribution behind shock waves in a shock tube, it may be worthwhile to compare briefly the following classes of experiment, which have been proposed or considered from time to time:

(1) Electrostatic probe as originally used by Langmuir[10] or a modification thereof.

(2) Continuum radiation as used by Petschek *et al.*[6] and by Petschek and Byron.[4]

(3) Line broadening due to Stark effect as used by Petschek *et al.*[6] and by Turner.[11]

(4) Optical interferometry as used by Alpher and White.[12]

(5) Magnetic induction method as used by Lin *et al.*[13] or a modification thereof.

(6) Microwave transmission and reflection technique as has been independently explored by Lin,[14, 15] Hayes,[16] Manheimer-Timnat and Low,[9] Schultz,[17] Jahn[18] and others.

Of these various classes of experiments, the electrostatic probe appeared to be the simplest at first sight and can in principle be made a high-spatial-resolution measurement. On the other hand, in view of the fact that the local electrostatic potential in the plasma depends on the distribution of the *net charge* instead of the actual electron or ion density (i.e. it measures, in effect, a small difference between two large quantities), a simple and unambiguous correlation between the local electron density and the observed probe potential can be made only under certain favourable conditions.[4]

The optical methods 2, 3 and 4 share the advantage of being potentially capable of high spatial resolution. However, as has already been mentioned before, the emitted light from the shock-heated air in the visible region is dominated by molecular band radiation up to the highest shock strength studied (satellite velocity) and therefore cannot be relied upon.* Even though the Kramer–Unsöld type radiation is expected to be predominant in the far infra-red region of the high temperature air spectra, the use of this spectral region for measuring the electron density profile behind strong shock waves in air will have to await the development of suitable high-speed infra-red detectors. The Stark broadening and the optical interferometry methods, while found satisfactory for the studies of strong shock waves in noble gases, unfortunately appear to work only at sufficiently high absolute electron densities. Since high electron density implies strong shock wave at high air density, which in turn leads to short ionization rise time, it remains doubtful if either of these techniques can be utilized to study the ionization history behind shock waves in air.

The last two methods, 5 and 6, while free from the drawbacks of the first four methods, unfortunately suffer one serious limitation;

* It should be mentioned that the N_2^+ first negative band system is in the visible region, but the dominant ion is expected to be NO^+, which has no strong band in the visible.

namely, poor spatial resolution. The spatial resolution of the magnetic induction method will be limited by the diameter of the sensing coil and the effective width of the magnetic field, which, in turn, is determined by the sensitivity and rise-time consideration (i.e. usable output voltage for a given electrical conductivity of the shock-heated gas). The spatial resolution of the microwave technique is simply limited by the wavelength employed.

In the section that immediately follows, we shall describe briefly the experimental technique that has been chosen to obtain the preliminary results to be reported in the present paper. It is quite apparent that this choice of technique represents more of a compromise between the relative merits of the various methods considered above, instead of a unique solution to this problem.

EXPERIMENTAL METHOD

In the present investigation, a microwave reflection probe method was used to measure the local electron density distribution behind the shock wave. As shown in Fig. 1, the microwave

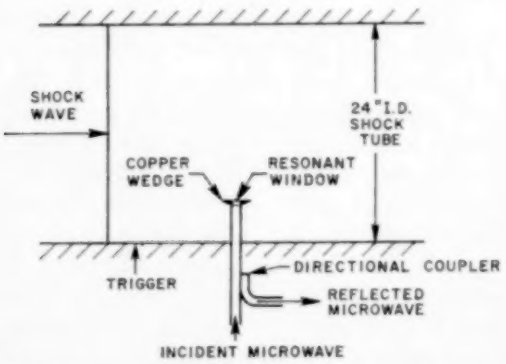

Fig. 1. Schematic diagram showing experimental arrangement for microwave probe in shock tube.

probe essentially consists of a standard rectangular wave guide terminated in a half-wave dielectric window.* The probe is inserted about 4 in. into the shock tube through the side wall and oriented normal to the shock tube axis. To minimize aerodynamic disturbance to the shock tube flow, a rectangular copper end plate (about one wavelength in width and height) was introduced at the end of the probe. The front surface of the end plate was plane and was lined up with the front surface of the dielectric window, while the back surface of the end plate was cut to form a sharp wedge along all four edges of the plate. In this manner, the shock wave and the shock-induced supersonic flow is allowed to pass over the front surface of the probe window undisturbed; while all the disturbances generated by the wave guide exposed to the supersonic stream is confined to the back side by the end plate. The main reason for the insertion of the probe several inches into the shock tube is to avoid the boundary layer generated by the side wall, which may be quite thick at large distances behind the shock. Because of the small streamwise dimension involved, the thickness of the new boundary layer generated by the front surface of the end plate and window will be small (i.e. compared with the wavelength of the microwave, even at the low operating pressure of the shock tube).

Because of the very large inside dimensions of the shock tube, the terminated wave guide can be considered as looking into free space. Even so, the electromagnetic boundary value problem for the terminated wave guide in a plasma is still quite complicated. Instead of trying to obtain analytical solutions relating the terminal impedance of the wave guide to the properties of the plasma (i.e. the shock-heated gas to which the probe is exposed during the experiment), approximate characteristics of the probe were first obtained by static calibration with artificial dielectrics. It was found that when a flat surface of a dielectric block of sufficiently large dimensions (i.e. several wavelengths) is placed against

* Both fused alumina and quartz have been used as window material. No significant difference in the resultant probe characteristics was noticed.

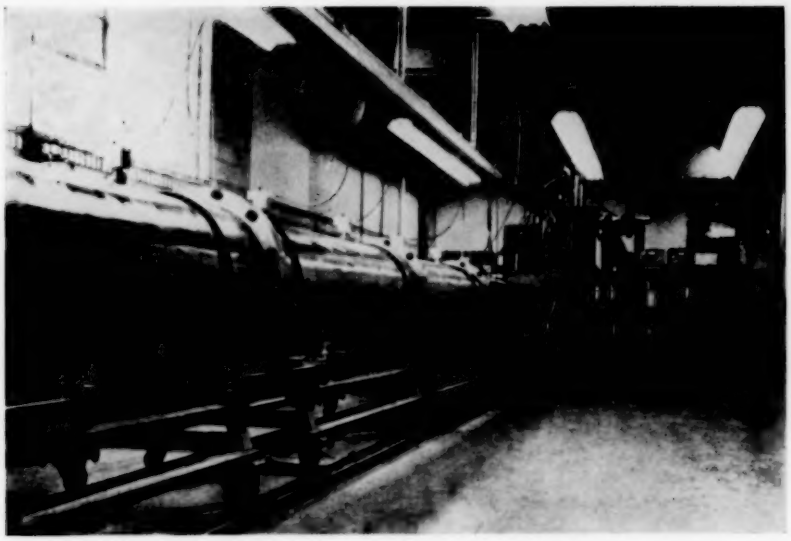

Fig. 2. The 24 in. diameter low-density shock tube.

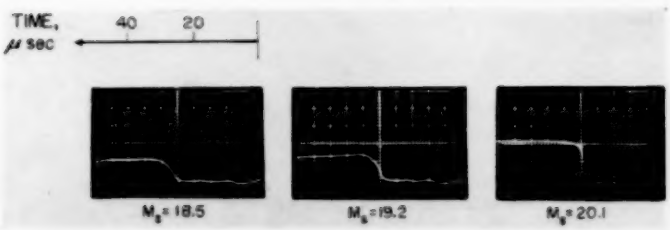

Fig. 3. Typical oscillograms from the microwave reflection detector, showing variation of the rate of rise of the reflection signal with shock Mach number M_S. $p_1 = 20\mu$ Hg AIR; $f = 33{\cdot}4$ kMc/s.

the probe window, the reflection coefficient* becomes independent of the size and geometry of the block. The value of the reflection coefficient happened to correspond quite closely to that given by plane wave reflection at normal incidence[19] from the same dielectric over a considerable range of dielectric constant. Furthermore, when the dielectric block was slid across the window, no significant change in reflectance was noticed until one edge of the block came within a fraction of a wavelength from an edge of the window, indicating that the storage field, which determines the terminal impedance of the probe in this case, was localized within a few wave guide dimensions, as expected.

As has already been mentioned, to overcome the limited spatial resolution of the probe, a large diameter shock tube operating at low density was employed in this experiment. This shock tube (Fig. 2) has an inside diameter of 24 in. and a length of about 50 ft (from the diaphragm to the measuring station).

Adequate pumping system has been provided to allow the low pressure chamber to be pumped down to about 10^{-5} mm Hg before each experiment. To provide proper purity level, the sample gas (in this case air) is continuously circulated through the shock tube at a rate at least 10^2 times the total leak rate into the tube. (When the pumping system is shut off, the rate of rise of pressure inside the tube was observed to be about 1 μ Hg/min.) The sample gas pressure was measured by two Alphatron vacuum gauges (manufactured by the National Research Corp.), one located near the diaphragm, and the other one located near the pumping station, which is located immediately downstream of the measuring station. The speed of the shock wave was measured by ionization plugs spaced 4 ft apart along the entire length of the shock tube. The averaged speed of the shock wave between each pair of ionization plugs can be measured to an accuracy of about 1/2 per cent. Even though the product of combustion of a hydrogen–oxygen–nitrogen mixture was used to drive the shock wave, the shock speed was observed to vary not more than 2 per cent in traversing the second half of the shock tube length.

Three microwave frequencies within the range $10 < f < 35$ kMc/s have been used (covered by three standard size rectangular wave guides, i.e. the *X*, *Ku* and *Ka* bands). Typical oscillograms obtained at a frequency of 33·4 kMc/s for shock waves at an initial air pressure of 20 μ Hg are shown in Fig. 3. In each case the oscilloscope was triggered by an ionization plug located about 7 in. upstream of the microwave probe, and the vertical deflection of the trace above the base line is a measure of the instantaneous reflection coefficient as seen by the probe. (The transmitted power, or total reflection power, is maintained constant, and is checked and recorded before and after each experiment. For the oscillograms shown in Fig. 3, the reflection coefficient involved was in the 10 per cent range.) It is seen that the signal generally rises at a definite rate when the shock wave arrives at the probe, reaches a steady state and then drops back to the initial zero-reflection level when the driver-gas interface arrives at the probe. (The falling part of the trace is out of sight to the left in these particular oscillograms.) The time interval between the rise and fall of the reflection signal is a measure of the length of the shock-heated gas sample (which was found to be about one foot under these conditions), while the time it takes the reflection signal to rise to the steady level can be used as a measure of the ionization rise time behind the shock front.

At the low density employed in these experiments, the collision frequency[1, 20] is smaller than the microwave angular frequency by orders of magnitude. Therefore the refractive index of the

* Defined as the ratio between the flow of cW microwave power in the backward and forward direction within the wave guide. This ratio was obtained in practice by comparing the crystal detector output at the side arm of a directional coupler connected to the probe when the dielectric block is placed against the window, and when a block of copper is placed against the window.

shock-heated gas depends only on the electron number density n_e. Thus

$$n = \sqrt{\varepsilon} = \sqrt{\left(1 - \frac{n_e}{n_e^*}\right)} \qquad (1)$$

where $n_e^* = (\pi\ m_e/e^2)f^2$ is the electron density corresponding to plasma resonance at the frequency f. If one further makes the simplifying approximation that the reflection coefficient of the probe is roughly the same as that for plane-wave reflection from the plasma at normal incidence, then the reflection signal as shown in Fig. 3 can be used to deduce the approximate electron density distribution behind the shock front in a very simple manner.

The ionization distance, which has been arbitrarily defined as the thermodynamic equilibrium electron density behind the shock divided by the maximum electron density gradient deduced from the experiments as described above, is plotted in Fig. 4 for comparison with a theoretical prediction by Lin and Teare.[3]

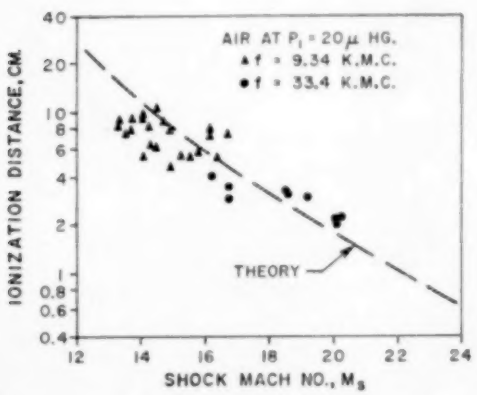

Fig. 4. Ionization distance behind shock wave in air at an initial pressure of 20 μ Hg as deduced from preliminary microwave probe measurements.

It is seen that even though the scatter of these preliminary experimental points is quite large, the magnitude of the observed ionization distance is consistent with what can be predicted from the reaction path chosen in the chemical kinetic model and the most probable values for the pertinent rate constants. It may also be mentioned that the absolute electron density deduced from the measured reflection coefficient for the steady-state region behind the shock front also agreed quite well (within a factor of about 1·5) with the theoretical prediction.†

A theoretical discussion of the shock wave ionization processes will be out of the scope of the present paper, but this will be covered by a later article.

Acknowledgement—The author wishes to acknowledge the competent assistance of Messrs. W. Fyfe and R. Neal in carrying out the experimental measurements. He also wishes to thank many of his colleagues at the Avco-Everett Research Laboratory for their advice and support in this work.

REFERENCES

1. L. Lamb and S. C. Lin, *Appl. Phys.* **28**, 754 (1957)*
2. R. E. Duff, *Phys. of Fluids* **2**, 207 (1959).
3. S. C. Lin and J. D. Teare, *Shock Wave Structure in the Hypersonic Flight Regime*, presented at A.P.S. Fluid Dynamics Divisional Meeting at San Diego, Calif., Nov. 24, 1958. *Bull. Amer. Phys. Soc.* (2) **4**, 195 (1959).
4. H. E. Petschek and S. Byron, *Ann. Phys.* **1**, 270 (1957).
5. B. Niblett and V. H. Blackman, *J. Fluid Mech.* **4**, 191 (1958).
6. H. E. Petschek, P. H. Rose, H. S. Glick, A. Kane and A. Kantrowitz, *J. Appl. Phys.* **26**, 83 (1955).
7. B. Kivel, H. Mayer and H. Bethe, *Ann. Phys.* **2**, 57 (1957).
8. J. C. Keck, J. C. Camm, B. Kivel and T. Wentink, Jr., *Ann. Phys.* **7**, 1 (1959).
9. Manheimer-Timnat and W. Low, *J. Fluid Mech.* **6**, 449 (1959).
10. I. Langmuir and H. M. Mott-Smith, *Gen. Electric Rev.* **27**, 449, 538, 762, 810 (1924).
11. E. B. Turner, Univ. of Michigan, AFOSR TB-56-150, ASTIA Document No. AD 86309 (May 1956).
12. R. A. Alpher and D. R. White, *Phys. of Fluids* **2**. 162 (1959).
13. S. C. Lin, E. L. Resler and A. R. Kantrowitz, *J. Appl. Phys.* **26**, 95 (1955).

† It should be pointed out, however, that this is not the same as the thermal equilibrium value, since the electron density behind shock front was predicted to "overshoot" the equilibrium value by a considerable factor (about 2 or 3) for a considerable length of time (several times the available test time of the shock tube) for these shock velocities and density.

14. S. C. LIN, *Ionization Phenomenon of Shock Waves in Oxygen-Nitrogen Mixtures* in *Report on 18th Annual Conference on Physical Electronics*, p. 6; Massachusetts Institute of Technology, Dept. Phys. (March 1958). Also Avco-Everett Research Laboratory Res. Rep. 33, ASTIA AD-201912 (June 1958).
15. S. C. LIN and B. KIVEL, *Phys. Rev.* **114**, 1026 (1959).
16. B. HAYES, *Determination of Some Electrical Properties of a Gas Detonation by Microwave Technique*, presented at IRE Professional Group Meeting on Microwave Theory and Techniques, Harvard Univ., Cambridge, Mass., June 1960.
17. D. L. SCHULTZ, *Microwave Studies of the Properties of Ionized Air in a Shock Tube*, presented at 4th International Conference in Ionization Phenomena in Gases, Uppsala, Sweden, August 17–21, 1959, paper IIIc, 4E.
18. R. G. JAHN, *Discussion of Some Proposed Shock Tube Experiments using the Microwave Absorption and Reflection Technique*, California Institute of Technology, private communication (Dec. 9, 1958).
19. J. A. STRATTON, *Electromagnetic Theory*, Chap. 9. McGraw-Hill, New York (1941).
20. S. C. LIN and B. KIVEL, *Phys. Rev.* **114**, 1026 (1959).

SECTION B

INTERACTION OF MICROWAVES AND IONIZED AIR

WAVES IN A PLASMA IN A MAGNETIC FIELD

R. J. PAPA and W. P. ALLIS
Massachusetts Institute of Technology

Abstract—The propagation of plane electromagnetic waves through an infinite low temperature electron plasma in the presence of a constant magnetic field is to be considered. A dispersion equation is derived by solving for a self-consistent electric field using the Boltzmann equation and Maxwell's equations. Since small deviations from the Maxwell–Boltzmann distribution are taken into account, the dispersion equation yields three double solutions for the index of refraction. In addition to the two waves whose phase velocity is of the order of light velocity, a plasma wave is present whose velocity is of the order of sound velocity. Normal wave surfaces for the three waves are plotted for various values of the parameters. The polarization of the waves is also considered.

ZERO TEMPERATURE PLASMA

In this section, the thermal motions of the electrons will be neglected, the collision frequency assumed zero, and the ions of infinite mass. The wave equation may be written:

$$\mathbf{V}\times(\mathbf{V}\times\mathbf{E})+\frac{K\cdot\mathbf{E}}{c^2}=0 \tag{1}$$

Assume $\mathbf{E}$ to be proportional to $\exp j\omega(t-\mathbf{r}\cdot\mathbf{n}/c)$, where $\mathbf{n}$ is a vector normal to the wave front. $n=|\mathbf{n}|$ is the index of refraction of the medium.

A constant magnetic field is taken along the Z-axis. The vector $\mathbf{n}$, which determines the direction of propagation, lies in the X–Z plane at an angle θ with the Z-axis.

The wave equation then becomes:

$$\mathbf{n}\times(\mathbf{n}\times\mathbf{E})+K\cdot\mathbf{E}=0 \tag{2}$$

where K, the dielectric tensor, is defined by:

$$K\equiv 1+\frac{\sigma}{j\omega\varepsilon_0} \tag{3}$$

σ, the conductivity tensor, may be derived by considering the equations of motion of an electron in the presence of a constant magnetic field under the influence of an alternating electric field.

The wave equation (2) may be written in matrix form as follows:

$$\begin{pmatrix} a_{11} & a_{12} & a_{13} \\ a_{21} & a_{22} & a_{23} \\ a_{31} & a_{32} & a_{33} \end{pmatrix}\begin{pmatrix} E_1 \\ E_2 \\ E_3 \end{pmatrix}=\begin{pmatrix} 0 \\ 0 \\ 0 \end{pmatrix} \tag{4}$$

$$\begin{aligned} a_{11}&=-n^2\zeta^2+K_{11} & a_{22}&=-n^2+K_{22} \\ a_{12}&=K_{12}=-a_{21} & a_{23}&=K_{23}=-a_{32} \\ a_{13}&=n^2\xi\zeta+K_{13}=a_{31} & a_{33}&=-n^2\xi^2+K_{33} \end{aligned} \tag{5}$$

and $\xi=\sin\theta, \zeta=\cos\theta$ are the direction cosines of $\mathbf{n}$.

The components of the dielectric tensor for a cold plasma are:

$$\begin{aligned} K_{11}&=K_{22}=1-\frac{\alpha^2}{1-\beta^2} \\ K_{33}&=1-\alpha^2 \\ K_{12}&=-K_{21}=\frac{-j\alpha^2\beta}{1-\beta^2} \\ K_{13}&=K_{31}=K_{23}=K_{32}=0 \end{aligned} \tag{6}$$

where

$$\alpha \equiv \frac{\omega_p}{\omega} = \sqrt{\left(\frac{n_0 e^2}{m\varepsilon_0}\right)} \frac{1}{\omega}$$

$$\beta \equiv \frac{\omega_b}{\omega} = \frac{eB}{m\omega} \tag{7}$$

There is no non-zero solution of equation (4) unless the determinant of the coefficient matrix is set equal to zero. Thus, the dispersion equation is obtained from $\det[a] = 0$, and may be written:

$$An^4 - Bn^2 + C = 0 \tag{8}$$

where A, B and C are functions of α, β and θ. The solutions of equation (8) may be written

$$n_{1,2} = \sqrt{[(B+D)/2A]} \tag{9}$$

where $D^2 = B^2 - 4AC$ is always positive. n is either real or purely imaginary because we have taken $T = 0$ and $\nu_e = 0$. It may be noted that n^2 changes sign only by going through zero or infinity. When $n^2 = \infty$, this is termed a resonance, when $n^2 = 0$, this is termed a cut-off. The family of solutions of equation (9) are conveniently represented on a plot of β^2 against α^2. The $\beta^2 - \alpha^2$ plane is divided up into eight regions by two resonance lines and two cut-off lines. Within each region the normal wave surfaces remain topologically the same. A normal wave surface is a polar plot of phase velocity $\mathbf{u} = c/\mathbf{n}$.

In Fig. 1, sample normal wave surfaces are drawn within each region. The radius of the dotted circle represents the velocity of light.

Equation (9) may be rewritten so that θ is expressed in terms of α, β and n:

$$\tan^2\theta = \frac{-K_p(n^2 - K_r)(n^2 - K_l)}{(n^2 - K_p)(K_T n^2 - K_r K_l)} \tag{10}$$

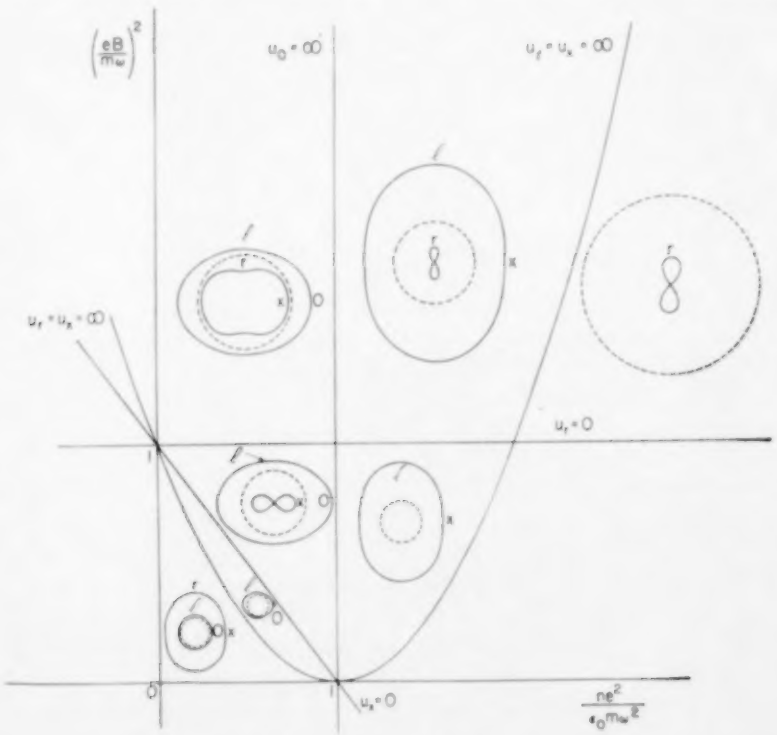

Fig. 1. Wave normal surfaces in a plasma in a magnetic field.

Where K_p, K_r and K_l are the components of the dielectric tensor in rotating co-ordinates.

$$K_T = K_{11}; \quad K_r = 1 - \frac{a^2}{1-\beta}; \quad K_l = 1 - \frac{a^2}{1+\beta};$$
$$K_p = 1 - a^2 \tag{11}$$

For propagation along magnetic field, $\theta = 0$, there are two waves

$n_r^2 = K_r$ which is right circularly polarized,

$n_l^2 = K_l$ which is left circularly polarized.

For propagation across magnetic field:

$\theta = \pi/2$ $n_0^2 = K_p$ is the ordinary wave polarized along B.

$n_x^2 = \dfrac{K_r K_l}{K}$ is the extraordinary wave polarized in the plane perpendicular to B.

LOW TEMPERATURE ELECTRON PLASMA

For a finite temperature plasma, the wave equation has the same form (2) $\mathbf{n} \times (\mathbf{n} \times \mathbf{E}) + \boldsymbol{K} \cdot \mathbf{E}/c^2 = 0$. Now, however, the dielectric tensor is different. It is derived from the conductivity tensor, $K = 1 + \dfrac{\sigma}{j\omega\varepsilon_0}$, as before, but in the calculation of σ one must take account of the finite size of the electron orbit compared to the wavelength. This has been done by Sitenko, Drummond, Bernstein, Mower* and others and their results have been used.

An example of the change in the components of K is given by the x–x component:

$$K_{11} = 1 - \frac{\alpha^2}{1-\beta^2} - \varepsilon n^2 \left[\frac{1+3\beta^2}{(1-\beta^2)^3} \zeta^2 + \right.$$
$$\left. + \frac{3\zeta^2}{(1-\beta^2)(1-4\beta^2)} \right] \tag{12}$$

where

$$\varepsilon = \frac{eT}{mc^2} \alpha^2 \tag{13}$$

The matrix form of the wave equation is still

$$\begin{pmatrix} a_{11} & a_{12} & a_{13} \\ a_{21} & a_{22} & a_{23} \\ a_{31} & a_{32} & a_{33} \end{pmatrix} \begin{pmatrix} E_1 \\ E_2 \\ E_3 \end{pmatrix} = \begin{pmatrix} 0 \\ 0 \\ 0 \end{pmatrix}$$

The dispersion relation, again obtained from $\det[a] = 0$, may be written:

$$-\epsilon a n^6 + (A + \epsilon b)\, n^4 - (B + \epsilon c)\, n^2 + C = 0 \tag{14}$$

a, b and c characterize the temperature effects and are complicated functions of α, β and θ. A, B and C are the zero-temperature coefficients of equation (9). For moderate temperatures the terms ϵb and ϵc may be neglected compared to the larger A and B, but the term in $\epsilon a n^6$ increases the order of the equation and must be kept. The dispersion equation can then be written

$$-\epsilon a n^6 + A n^4 - B n^2 + C = 0 \tag{15}$$

For indices n of order one, the solutions $n_{1,2}$ of the dispersion equation are the same as before since $\epsilon a n^6$ is much less than the other terms. These solutions may be called the fast wave solutions. There is now a third solution with large n. This solution is called a plasma wave, and denoted by n_3. Its phase velocity, $u = c/n$, is of the order of magnitude of the electron's thermal velocity. If $n_3^2 \gg n_{1,2}^2$, the constant term C may be neglected in the dispersion equation. Then,

$$n_{2,3}^2 = \frac{A \pm \sqrt{(A^2 - 4a\varepsilon B)}}{2\varepsilon a} \tag{16}$$

The first quadrant of the α^2–β^2 plane is now divided into thirteen regions, as shown in Fig. 2. There is a resonance at $\beta^2 = \frac{1}{4}$. For regions 2, 3, 6, 7 and 8 the full cubic, equation (15), was solved.

All wave surfaces were calculated with $\varepsilon = 10^{-2}$. The wave surfaces are surfaces of rotation about the Z-axis and have a plane of symmetry perpendicular to B. They are shown in Fig. 3.

*For references see L. MOWER, *Phys. Rev.* **116**, 16 (1959).

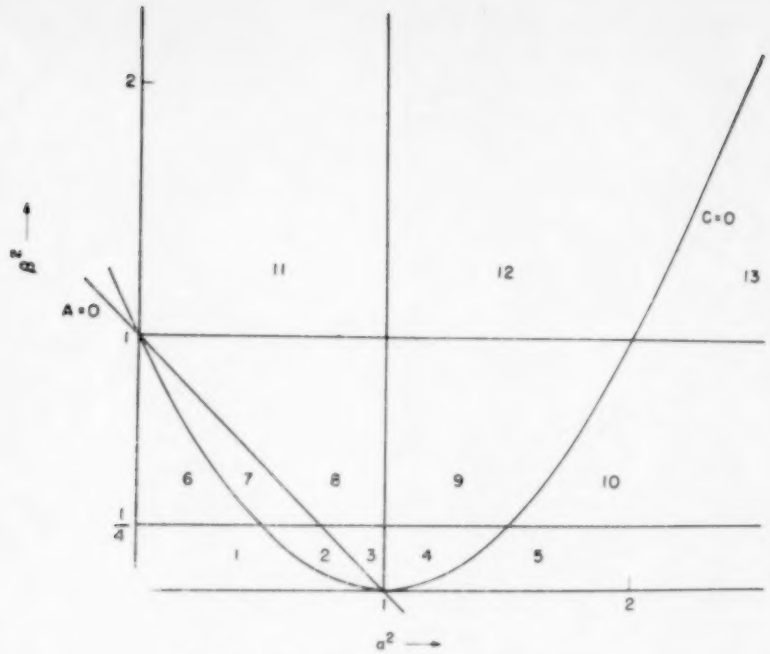

Fig. 2. Topological regions for a warm plasma.

Starting below the $\beta^2 = \frac{1}{4}$ resonance line, as α^2 increases from region 1 to 2, the normal wave surface for the plasma becomes larger, until in region 3 its phase velocity, $u = c/n$, is pretty close to the velocity of light. In regions 4 and 5 there is no plasma wave. The plasma wave surface has a butterfly shape in regions 6 and 7. In region 8, the plasma wave surface is like a lemniscate. The wave surface labelled p–x is a plasma wave near 0° and a fast wave near 180°. In regions 9 and 10 the plasma wave surface is like a lemniscate. In region 11, the plasma wave surface is a four-leaved rose, which becomes a lemniscate in regions 12 and 13. In region 11, the figure eight part of the plasma wave surface goes off to infinity as α^2 approaches 1. In regions 12 and 13, the figure eight pattern can be entirely accounted for by the fast wave solutions.

For propagation along the magnetic field, there are in general three waves.

$$n_r^2 = \frac{(1-\alpha^2)/(1-\beta)}{(1+\varepsilon)/(1-\beta)^3}$$ is right circularly polarized,

$$n_l^2 = \frac{(1-\alpha^2)/(1+\beta)}{(1+\varepsilon)/(1+\beta)^3}$$ is left circularly polarized.

The third wave for propagation along the magnetic field is the Bohm Gross plasma oscillation. This wave is a purely longitudinal wave.

$$n_p^2 = \frac{(1-\alpha^2)}{3\varepsilon}$$

For propagation across the magnetic field, there are three waves in general.

The ordinary wave is polarized with its **E** vector along the magnetic field.

$$n_0^2 = \frac{(1-\alpha^2)}{(1+\varepsilon)/(1-\beta^2)}$$

There are two extraordinary waves polarized

with their **E** vector in the plane perpendicular to the magnetic field. One extraordinary wave is a fast wave and the other is the plasma wave. Their indices of refraction are given by equation (16) where

$$\varepsilon a = \frac{3\varepsilon}{1-4\beta^2}$$

$$A = \left[(1-\beta^2-\alpha^2)+\varepsilon\left\{\frac{12\alpha^2\beta^2}{(1-\beta^2)(1-4\beta^2)} + \frac{4(1-\alpha^2-\beta^2)(1+2\beta^2)}{(1-\beta^2)^2(1-4\beta^2)^2}\right\}\right]$$

$$B = \left[(1-\alpha^2)^2-\beta^2\right]$$

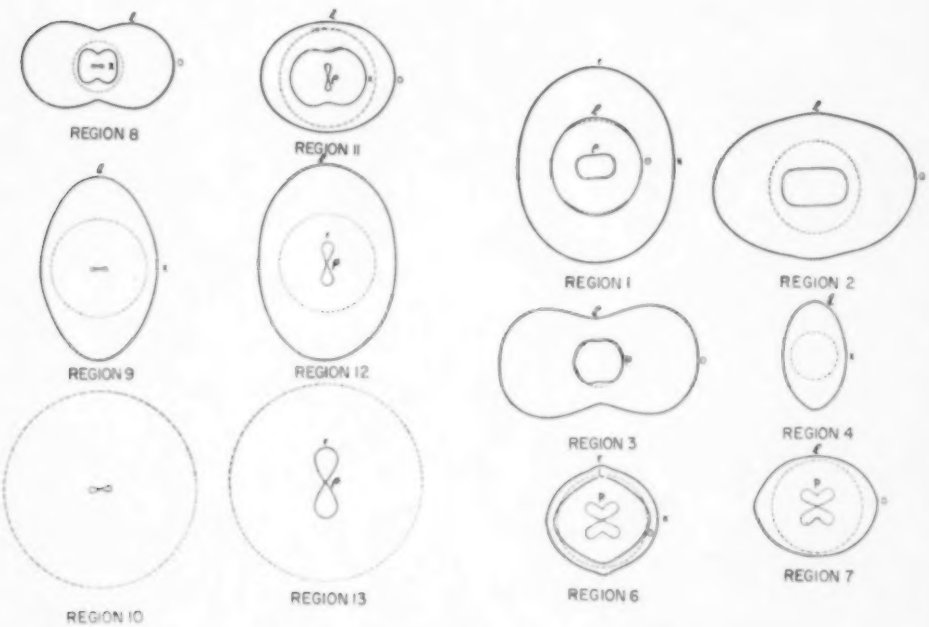

Fig. 3. Wave normal surfaces for a warm plasma.

INTERACTION OF A NON-UNIFORM PLASMA WITH MICROWAVE RADIATION*

M. M. KLEIN, H. D. GREYBER,† J. I. F. KING
Missile and Space Vehicle Department
General Electric Company, Philadelphia, Pennsylvania

and K. A. BRUECKNER‡
University of Pennsylvania, Philadelphia, Pennsylvania

Abstract—An investigation has been made of the interaction of microwave radiation with a non-uniform plasma for both normal and non-normal incidence of the radiation. For the case of normal incidence the wave equation was solved by numerical integration. The results show that, for a large range of collision frequencies, a major fraction of the incident radiation is absorbed by the plasma except for very sharp density gradients. The reflection coefficient has been obtained for a large range of the governing parameters, i.e. electron density gradient, wavelength of the incident radiation and collision frequency. For the case of non-normal incidence the radiation does not penetrate into the region of rapidly changing index of refraction so long as it is not too close to normal incidence. The ray path has therefore been calculated by geometrical optics and the absorption within the plasma has been obtained by the WKB method. Because of the greater complexity of the problem for the non-normal case, the calculations have been restricted to the short wavelength region, The results show that the absorption coefficient varies very little and remains large over a wide range of angles of incidence, but drops off rapidly beyond 45 degrees.

1. INTRODUCTION

In recent years considerable attention has been given to the problem of the interaction of electromagnetic radiation with a plasma.[1–3] In the main, these investigations have been limited to a plasma of uniform properties in which the coefficients of reflection and transmission may easily be obtained from well-known results in the theory of reflection and refraction of electromagnetic waves. In many situations of physical interest, however, the plasma properties are not uniform and the gradient of the electron density may be quite large. If the direction of the propagation constant is close to normal to the plasma surface, the plasma frequency may get quite close to the frequency of the incident radiation and large variations of the propagation constant inside the plasma will occur. It therefore becomes necessary to consider the solution of the electromagnetic wave equation for the case where the propagation constant (or index of refraction) varies rapidly in some region of the plasma. Since analytical techniques become inconvenient over the entire range of plasma frequencies, a numerical procedure has been utilized.

Because the rapid variation of the index of refraction is limited to a narrow region it is possible to utilize the WKB method,[4, 5] an approximate analytical solution valid for slowly varying wavelength, in conjunction with the numerical procedure. The region of rapid variation of index of refraction is solved by

* Based on work performed under the auspices of the U.S. Air Force, Rome Air Development Centre, Contract AF 30 (602)-1968.

† Present affiliation: Geophysics Corporation of America, Boston, Massachusetts.

‡ Consultant: General Electric Company. Present affiliation: University of California, School of Science and Engineering, La Jolla, California.

numerical integration and the remaining region may be obtained by the WKB method.

If the direction of the incident wave is not too close to normal incidence it is found that the wave does not penetrate into the region of rapidly changing index of refraction so that the WKB method approximation may be used to calculate the absorption. In addition, since the real part of the index of refraction does not vary greatly within a wavelength, simple geometrical optics may be used to compute the ray path.

In Section 2 we discuss and derive the wave equation for both normal and non-normal incldence. In Section 3 we first consider the normal case and discuss the method of solving the wave equation and calculating the reflection and absorption coefficients and the rate at which energy is deposited inside the plasma. We then take up the non-normal case, showing how to calculate the ray path by ray optics and the absorption by the WKB method. The discussion and interpretation of results are given in Section 4.

2. THEORY

We consider a semi-infinite plasma whose electron density is assumed to change only along the normal to the plasma surface which is taken as parallel to the x–z plane. An electromagnetic plane wave **E** polarized at an angle ψ to the plane of the paper (x–y plane) is incident at an angle θ to the plasma surface (Fig. 1).

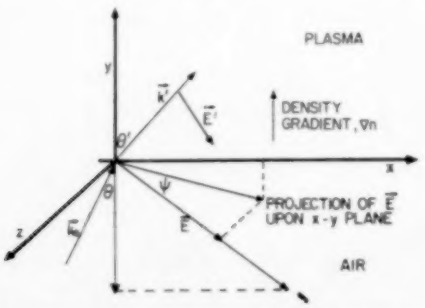

Fig. 1. Sketch of electric wave **E** polarized at angle ψ x–y plane and incident at angle θ; the plasma surface is taken parallel to x–z plane.

Because of the variation of the electron density only along the normal to the plasma surface, the analysis may be confined to the x–y plane. We wish to obtain the differential equation for the electric field **E** in terms of the electron density for arbitrary angle of incidence θ and polarization angle ψ. We first relate the field **E** to the current density **j** through the equation of motion of an electron of charge e and mass m in an electric field **E**,

$$m\ddot{\boldsymbol{\xi}} + m\nu\dot{\boldsymbol{\xi}} = e\mathbf{E} \tag{1}$$

where $\boldsymbol{\xi}$ is the displacement vector of the electron from equilibrium and ν is the frequency with which an electron collides with heavy particles. The collision frequency ν measures how rapidly energy from the field is being absorbed by the plasma. The field and displacement are assumed to vary harmonically with time, $\sim \exp(-i\omega t)$, so that the displacement $\boldsymbol{\xi}$ in equation (1) may be solved for explicitly to yield

$$\dot{\boldsymbol{\xi}} = \frac{-e\mathbf{E}/m}{\omega^2 + i\nu\omega} \tag{2}$$

where ω is the frequency of the incident radiation. The current density **j** is then given by

$$\mathbf{j} = \bar{n}e\dot{\boldsymbol{\xi}} = -i\omega\bar{n}e\boldsymbol{\xi} \tag{3}$$

where $\bar{n}$ is the average number density for electrons. Using the value of $\dot{\boldsymbol{\xi}}$ from equation (2) in equation (3) yields

$$\mathbf{j} = \frac{i\omega\bar{n}e^2}{\omega^2 + i\nu\omega}\,\frac{\mathbf{E}}{m} \tag{4}$$

We may obtain another relation between **j** and **E** by use of charge conservation and consideration of the divergence of the field. The equation of continuity and Gauss' law give (we use Guassian units in this report)

$$\operatorname{div}\mathbf{j} + \dot{n}e = 0 \tag{5}$$

$$\operatorname{div}\mathbf{E} = 4\pi e n' \tag{6}$$

where n' is the perturbed number density for electrons under the action of the electric field **E**

and is related to the instantaneous number density n by

$$n = \bar{n} + n' \tag{7}$$

Since $\dot{\bar{n}} = \dot{n}'$ and n varies harmonically with time, the perturbation density n' may be eliminated between equations (5) and (6) to yield

$$\text{div } \mathbf{E} = \frac{4\pi}{i\omega} \text{div } \boldsymbol{j} \tag{8}$$

We now use equation (4) to eliminate $\boldsymbol{j}$ in equation (8) and write

$$\text{div } \mathbf{E} = \frac{4\pi e^2/m}{\omega^2 + i\nu\omega} \text{ div } (n\mathbf{E}) \tag{9}$$

where we have dropped the bar from n. Expanding div $(n\mathbf{E})$ allows us to solve equation (9) explicitly for div E,

$$\text{div } \mathbf{E} = \frac{\omega_p^2}{\omega^2 + i\nu\omega - \omega_p^2} \frac{E.\nabla n}{n} \tag{10}$$

where ω_p is the plasma frequency given by

$$\omega_p^2 = \frac{4\pi n e^2}{m} \tag{11}$$

From Maxwell's equations

$$\left.\begin{aligned} \nabla \times \mathbf{B} &= \frac{4\pi \mathbf{j}}{c} + \frac{1}{c}\frac{\partial \mathbf{E}}{\partial t} \\ \nabla \times \mathbf{E} &= -\frac{1}{c}\frac{\partial \mathbf{B}}{\partial t} \end{aligned}\right\} \tag{12}$$

we obtain, on elimination of the magnetic field $\mathbf{B}$,

$$\nabla \times (\nabla \times \mathbf{E}) = -\left(\frac{4\pi}{c^2}\frac{\partial \mathbf{j}}{\partial t} + \frac{1}{c^2}\frac{\partial^2 E}{\partial t^2}\right) \tag{13}$$

where c = velocity of light in vacuum. We now eliminate $\mathbf{j}$ by means of equation (4), use the vector identity $\nabla \times (\nabla \times \mathbf{E}) = \nabla(\nabla.\mathbf{E}) - \nabla^2\mathbf{E}$ and equation (10) for div $\mathbf{E}$ to cast equation (13) in the form

$$\nabla^2 \mathbf{E} = -k^2 \mathbf{E} + \nabla\left(\frac{E.\nabla\omega_p^2}{\omega^2 + i\nu\omega - \omega_p^2}\right) \tag{14}$$

where $\mathbf{k}$ is the propagation constant inside the plasma when the coupling between the electric field and the density gradient is neglected, and given by

$$k^2 = \frac{\omega^2}{c^2}\left(1 - \frac{\omega_p^2}{\omega^2 + i\nu\omega}\right) \tag{15}$$

The gradient term on the right-hand side of equation (14), which gives the coupling between the electric field and the density gradient, is now regarded as a perturbation so that we may write

$$(\nabla^2 + k^2)\mathbf{E} = \nabla(\mathbf{E}_0.\mathbf{n}_1 f) = (\mathbf{E}_0.\mathbf{n}_1)\mathbf{n}_1 \frac{\partial f}{\partial y} + f\nabla(\mathbf{E}_0.\mathbf{n}_1) \tag{16}$$

where $\mathbf{n}_1$ is a unit vector along the density gradient, $\mathbf{E}_0$ is the solution obtained by neglecting the density gradient and

$$f = \frac{1}{\omega^2 + i\nu\omega - \omega_p^2} \frac{\partial \omega_p^2}{\partial y} \tag{17}$$

Since the field $\mathbf{E}_0$ is independent of the density gradient the term $\nabla(\mathbf{E}_0 \cdot \mathbf{n}_1)$ lies along the direction of propagation of $\mathbf{E}_0$ and is therefore very nearly perpendicular to $\mathbf{E}$. Any vector which is nearly perpendicular to $\mathbf{E}$ will yield a very small contribution when the scalar wave equation for E is obtained from equation (16). We may therefore, in first approximation, neglect terms in the gradient of $\mathbf{E}_0$. We now take the scalar product of equation (16) and a unit vector in the $\mathbf{E}$ direction and ignore the small difference between $\mathbf{E}$ and $\mathbf{E}_0$ on the right-hand side to obtain

$$(\nabla^2 + k^2)E = \frac{(\mathbf{n}_1.\mathbf{E}_0)^2}{E_0^2} \frac{\partial f}{\partial y} E \tag{18}$$

where $$\frac{\mathbf{n}_1.\mathbf{E}_0}{E_0} = \sin\theta \cos\psi$$

We may write equation (18) as a homogeneous wave equation,

$$(\nabla^2 + k'^2)E = 0 \tag{19}$$

where the modified propagation constant $\mathbf{k}'$ given by

$$k'^2 = k^2 - \sin^2\theta\cos^2\psi\,\frac{\partial f}{\partial y} \tag{20}$$

contains the coupling between the electric field and the density gradient. It is convenient at this point to eliminate the explicit dependence of the field upon wavelength by using the wavelength in vacuum λ_0 as the unit of length; equations (19) and (20) then take the form

$$(\nabla^2 + 4\pi^2\varepsilon'^2)E = 0 \tag{21}$$

$$\varepsilon'^2 = \frac{k'^2}{k_0^2} = \varepsilon^2 - \frac{1}{4\pi^2}\sin^2\theta\cos^2\psi\,\frac{\partial f}{\partial y} \tag{22}$$

where ε' and $\varepsilon = k/k_0$ are the indices of refraction for the non-normal and normal cases, and $\mathbf{k}_0$ is the propagation constant for free space.

3. METHOD OF CALCULATION

Normal incidence

At normal incidence the coupling term between the electric field and the density gradient in equation (21) vanishes ($\sin\theta = 0$); the index of refraction ε' reduces to ε and the problem becomes one-dimensional in y so that equation (21) takes the form

$$\frac{d^2E}{dy^2} = -4\pi^2(V + iW)E \tag{23}$$

where V and W are the real and imaginary components of ε^2. The quantities V and W are, from equation (15), calculated from

$$\left.\begin{aligned} V &= 1 - \frac{n/n_0}{1+\nu^2/\omega^2} \\ W &= \frac{\nu}{\omega}\,\frac{n/n_0}{1+\nu^2/\omega^2} \end{aligned}\right\} \tag{24}$$

where n_0 is the electron number density corresponding to the frequency of the incident wave and given by

$$\omega^2 = \frac{4\pi n_0 e^2}{m}$$

The real (phase) and imaginary (absorptive) components of the index of refraction ϵ inside the piasma are then ($\varepsilon = \varepsilon_r + i\varepsilon_i$)

$$\left.\begin{aligned} \varepsilon_r^{\,2} &= \frac{(V^2+W^2)^{\frac{1}{2}} + V}{2} \\ \varepsilon_i^{\,2} &= \frac{(V^2+W^2)^{\frac{1}{2}} - V}{2} \end{aligned}\right\} \tag{25}$$

For normal incidence the electric field penetrates into the region of high absorption where ε changes rapidly so that the WKB method may here be inaccurate. We have therefore integrated equation (21) numerically for several electron density variations and collision frequencies. In order to cover a large number of cases and still keep the numerical work to a minimum the electron density in the plasma was approximated by an exponential function

$$\frac{n}{n_0} = e^{-y/y_0} \tag{26}$$

where the parameter y_0 gives the distance (number of wavelengths) in which the electron density falls to $1/e$ of its initial value (e-folding distance) and is therefore a measure of the sharpness of the density gradient. As the wave penetrates into the plasma past the point where ω and ω_p are equal (we shall call this position the point of resonance), the absorptive component ε_i becomes large and the wave is essentially damped a short distance behind the resonance point. For purposes of starting the integration, therefore, the field could be taken as zero slightly behind the point of resonance. The integration was carried out to the point where the imaginary term W was negligibly small.

The coefficients of reflection and absorption were determined by the matching of the logarithmic derivatives of the asymptotic form of the wave and the numerical solution in the asymptotic region. The asymptotic form of the wave consists of an incident and reflected wave so that we may write

$$E = \text{const}[(\alpha + i\beta)e^{2\pi iy} + e^{-2\pi iy}] \tag{27}$$

where α and β are the components of the amplitude of the reflected wave, and the incident wave is assumed to have unit amplitude. If u and v are the components of the numerical solution we then have

$$\frac{1}{u+iv}\frac{d}{dy}(u+iv) = 2\pi i\frac{(\alpha+i\beta)e^{2\pi iy}-e^{-2\pi iy}}{(\alpha+i\beta)e^{2\pi iy}+e^{-2\pi iy}}$$

from which

$$\alpha+i\beta = \frac{1+C}{1-C}\,e^{-4\pi iy} \tag{28}$$

where

$$C = \frac{1}{2\pi i}\frac{1}{u+iv}\frac{d}{dy}(u+iv)$$

The reflection coefficient is then

$$R = \alpha^2+\beta^2 = \left|\frac{1+C}{1-C}\right|^2 \tag{29}$$

and, since we are dealing with a semi-infinite plasma where the non-reflected wave is completely absorbed, the absorption coefficient, A, is

$$A = 1-R \tag{30}$$

To determine the local details of the absorption process we need the rate of energy absorption as a function of plasma depth. When **E** and **H** are expressed in complex form the Poynting flux **F** is, aside from constants,[6]

$$\mathbf{F} = Re(\mathbf{E}^*\times\mathbf{H}) \tag{31}$$

or, using curl $\mathbf{E} = -(1/c)\dfrac{\partial\mathbf{H}}{\partial t}$,

$$F = \mathrm{Im}\left(E^*\frac{dE}{dy}\right) \tag{32}$$

where E^* is the complex conjugate of E. Writing E as $u+iv$ and taking the divergence of equation (32) we obtain

$$\mathrm{div}\ F = u\frac{d^2v}{dy^2} - v\frac{d^2y}{dy^2} \tag{33}$$

Since the functions u and v satisfy the real and imaginary parts of equation (21), we may write equation (33) in the convenient form

$$\mathrm{div}\ F = -4\pi^2|E|^2W \tag{34}$$

which gives the rate of absorption per unit depth as a function of the imaginary part of the index of refraction.

Although the WKB approximation may be inaccurate in the region of high absorption, it may be utilized in conjunction with the numerical solution by first integrating numerically a short distance past the point of resonance and then using the WKB method out to the asymptotic region. If y_n is the point at which the numerical and WKB solutions join we may write

$$E = \frac{1}{(2\pi\varepsilon)^{\frac{1}{2}}}\left[A\exp\left(2\pi i\int_{y_n}^{y}\varepsilon dy\right) + B\exp\left(-2\pi i\int_{y_n}^{y}\varepsilon dy\right)\right] \tag{35}$$

where A and B are the amplitudes of the reflected and incident waves at the point y_n. If we match logarithmic derivatives of the numerical and WKB solutions at y_n we obtain, as before,

$$\frac{A}{B} = \frac{1+C}{1-C}$$

but C is now given by

$$C = \frac{1}{2\pi i}\frac{1}{\varepsilon}\frac{1}{u+iv}\frac{d}{dy}(u+iv)$$

evaluated at y_n. To obtain the reflection coefficient, however, we need the ratio of outgoing and incoming waves in the asymptotic region. From equation (35) the asymptotic form of E is

$$E = A\exp\left(2\pi i\int_{y_n}^{\infty}\varepsilon_r dy - 2\pi\int_{y_n}^{\infty}\varepsilon_i dy\right) + B\exp\left(-2\pi i\int_{y_n}^{\infty}\varepsilon_r dy + 2\pi\int_{y_n}^{\infty}\varepsilon_i dy\right)$$

The reflection coefficient is then

$$R = \left|\frac{A}{B}\right|^2\exp\left(-8\pi\int_{y_n}^{\infty}\varepsilon_i dy\right)$$

or, in terms of C,

$$R = \left|\frac{1+C}{1-C}\right|^2\exp\left(-8\pi\int_{y_n}^{\infty}\varepsilon_i dy\right) \tag{36}$$

The form of the reflection coefficient obtained here thus differs from the previous result (equation (29)) by an exponential factor which represents the WKB solution for the attenuation of the beam from y_a to the asymptotic region. The integral occurring in equation (36) may be evaluated analytically for $\frac{\nu}{\omega} \ll 1$ (short wavelengths) or $\frac{\nu}{\omega} \gg 1$ (long wavelengths). For these cases the imaginary component W of ε^2 is small compared to the real component V (see equation (24)), and equation (25) may be approximated by

$$\left.\begin{aligned} \varepsilon_r &\cong V^{\frac{1}{2}} \\ \varepsilon_i &\cong \frac{W}{2V^{\frac{1}{2}}} \end{aligned}\right\} \tag{37}$$

For an exponential density variation (equation (26)) the value of ε_i is, from equations (24) and (37),

$$\varepsilon_i = \frac{\frac{\nu}{\omega} e^{-y/y_0}}{2\left(1+\frac{\nu^2}{\omega^2}\right)\left(1-\frac{e^{-y/y_0}}{1+\nu^2/\omega^2}\right)^{\frac{1}{2}}} \tag{38}$$

Evaluation of the ε_i integral in equation (36) then yields for the reflection coefficient

$$R = \left|\frac{1+C}{1-C}\right|^2 \exp\left\{-8\pi\frac{\nu}{\omega}y_0\left[1-\left(1-\frac{e^{-y_a/y_0}}{1+\nu^2/\omega^2}\right)^{\frac{1}{2}}\right]\right\} \tag{39}$$

For the case $\frac{\nu}{\omega} \sim 1$ (intermediate wavelengths) the ε_i integral can easily be evaluated numerically.

Non-normal incidence

As shown previously, the effect of the interaction of the density gradient and the electric field may be expressed in terms of a modified index of refraction (see equations (21) and (22)). Eikonal theory[7] tells us that, so long as the change in ε' in a unit wavelength is not large, the methods of geometrical optics may be used to obtain the ray path. Our calculations indicate that, so long as the incident ray is not too close to normal incidence, the point of maximum penetration of the plasma is not close to the region of high absorption where ε' changes rapidly, and geometrical optics is therefore valid for calculating the ray path. The change in angle $\Delta\theta$ suffered by a ray at incidence θ is going from a medium of index ε' to one of index $\varepsilon'+\Delta\varepsilon'$ is, from Snell's law, given by

$$\frac{\varepsilon'+\Delta\varepsilon'}{\varepsilon'} = \frac{\sin\theta}{\sin(\theta+\Delta\theta)} \tag{40}$$

Since we are interested in a medium with variable index of refraction we evaluate equation (40) for the case of small $\Delta\varepsilon'$ and $\Delta\theta$ to obtain

$$\frac{d\varepsilon'}{\varepsilon'} = -\cot\theta\, d\theta \tag{41}$$

Since $\cot\theta$ is the slope of the curve, y', we can replace $d\theta$ by

$$d\theta = -\frac{y''}{1+y'^2}dx$$

and therefore write equation (41) *as*

$$y'' = \frac{1}{\varepsilon'}\frac{d\varepsilon'}{dy}(1+y'^2) \tag{42}$$

For an exponential density variation the quantity ε'^2 defined by equation (22) takes the form

$$\varepsilon'^2 = 1 - \frac{n\,n_0}{1+i\nu/\omega} - a\frac{n}{n_0}\frac{(1+i\nu/\omega)}{(1-n/n_0+i\nu/\omega)} \tag{43}$$

where

$$a = \frac{\sin^2\theta\cos^2\psi}{4\pi^2 y_0^2}$$

Because of the greater complexity of the calculations required for the non-normal case than those for the normal case we restrict ourselves, at this point, to the case ν/ω small and y_0 not too small (short wavelengths). Retaining first order terms in the small quantities a and ν^2/ω^2, the real and imaginary parts of ε'^2 are given by ($\varepsilon'^2 = V' + iW'$)

$$V' = 1 - \frac{n/n_0}{1+\nu^2/\omega^2} - \frac{a\dfrac{n}{n_0}\left(1-\dfrac{n}{n_0}\right)^2}{[(1-n/n_0)^2+\nu^2/\omega^2]^2} \quad (44)$$

$$W' = \frac{\nu}{\omega}\frac{n}{n_0}\left\{\frac{1}{1+\nu^2/\omega^2} + \frac{a(1-n^2/n_0^2)}{[(1-n/n_0)^2+\nu^2/\omega^2]^2}\right\} \quad (45)$$

Making use of equations (26), (37) and (44), the appropriate value of $\dfrac{d\varepsilon'}{\varepsilon'}$ in equation (42) is,

$$\frac{d\varepsilon'}{\varepsilon'} \cong \frac{1}{2\varepsilon_r'^2}\, d(\varepsilon_r'^2)$$

$$\frac{d\varepsilon'}{\varepsilon'} = exp(-2y/y_0)\frac{\left[\dfrac{1}{1+\nu^2/\omega^2} + \dfrac{a(1+e^{-y/y_0})}{(1-e^{-y/y_0})^3}\right]}{2y_0\left[1-\dfrac{e^{-y/y_0}}{1+\nu^2/\omega^2} - \dfrac{ae^{-y/y_0}}{(1-e^{-y/y_0})^2}\right]} \quad (46)$$

The ray path was then obtained by numerical integration of equation (42), starting in the asymptotic region where ε' is nearly constant. It was found convenient to change the independent variable from x to y and write equation (42) in the form

$$x'' = -g(y)(x'+x'3) \quad (47)$$

where $g(y) = (1/\varepsilon')d\varepsilon'/dy$. The numerical integration becomes inaccurate near the point of maximum penetration (turning point) since y is practically constant here and x' becomes very large. In this region, however, $g(y)$ is essentially constant so that we may integrate equation (42) directly to obtain the parabola

$$y - y_t = g(y_t)\frac{(x-x_t)^2}{2} \quad (48)$$

where x_t, y_t are the co-ordinates of the turning point. The values of x_t and y_t were determined by fitting the parabola to the preceding values of y and y'.

Having determined the path of the ray we now determine the absorption. Since as previously indicated, the ray path does not penetrate the region of rapidly changing index of refraction we can calculate the absorption by the WKB method using the modified index of refraction in equation (20). From our previous discussion of the WKB method for the normal case we may write the solution in the form

$$E = \frac{1}{(2\pi\varepsilon')^{\frac{1}{2}}}\exp\left(2\pi i\int_0^s \varepsilon_r'^{\frac{1}{2}}ds - 2\pi\int_0^s \varepsilon_i' ds\right) \quad (49)$$

where s is arc length along the path and we have normalized E to unit incident flux outside the plasma. The rate of absorption per unit arc length s is given by the divergence of the flux which, from equation (34), is

$$\text{div } F = 4\pi\varepsilon_i'\exp\left(-4\pi\int_0^s \varepsilon_i' ds\right) \quad (50)$$

for an incident flux of unity. From equations (26), (37), (44) and (45), the appropriate value of ε_i' to first order in a and ν^2/ω^2, for use in equation (50) is,

$$\varepsilon_i' = \frac{1}{2}\frac{\nu}{\omega}\exp(-y/y_0)\frac{\left[\dfrac{1}{1+\nu^2/\omega^2} + \dfrac{a(1+e^{-y/y_0})}{(1-e^{-y/y_0})^3}\right]}{\left[1-\dfrac{e^{-y/y_0}}{1+\nu^2/\omega^2} - \dfrac{ae^{-y/y_0}}{(1-e^{-y/y_0})^2}\right]}$$

In determining the values of ε_r' and ε_i' for the ray tracing and absorption calculations it is necessary to know the values of the angles of incidence θ and of polarization ψ. The angle θ varies from the entering angle to 90° at the point of maximum penetration. Since the terms arising from the density gradient are large only very near this point it is a good approximation to replace sin θ by unity, the value at maximum penetration. The angle of polarization ψ will, in general, vary in a complicated way as the ray penetrates into the plasma because, the component of **E** normal to the x–y plane does not interact with the density gradient whereas the parallel component does. For the case $\psi = 90°$ there is no interaction with the density gradient and ψ remains constant; for the case $\psi = 0°$ the interaction is a maximum and ψ again remains constant. For the sake of simplicity in the

calculations and parallel to the approximation for θ, we have chosen for cos ψ the value unity.

4. RESULTS AND DISCUSSIONS

Normal case

The rate of absorption of flux per unit depth inside the plasma is presented as a function of plasma depth y for several collision frequencies ν/ω and e-folding distances y_0 in Fig. 2. The

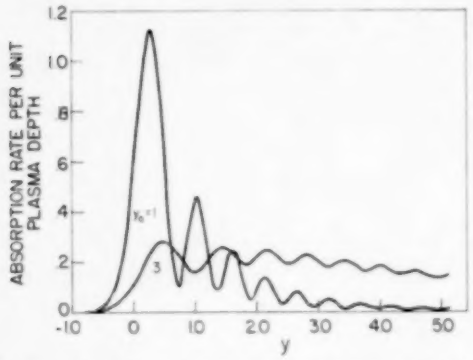

Fig. 2a. Rate of absorption per unit plasma depth as a function of position within plasma for several values of y_0; $\nu/\omega = 0{\cdot}1$. The curves are normalized to unit incident flux.

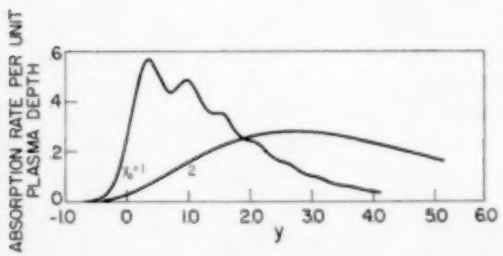

Fig. 2b. Rate of absorption per unit plasma depth as a function of position within plasma for several values of y_0; $\nu/\omega = 0{\cdot}32$. The curves are normalized to unit incident flux.

results show that, provided the electron density gradient is not too small, the absorption rate resonates strongly in the neighbourhood of $y = 0$, where the plasma and radiation frequencies are equal. As the density gradient decreases (y_0 increases), the resonant peak drops sharply so

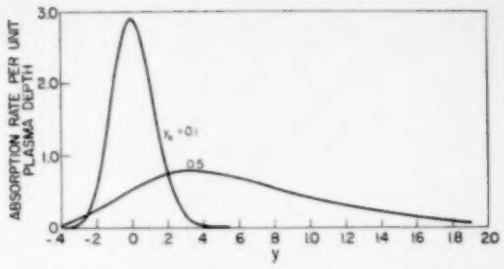

Fig. 2c. Rate of absorption per unit plasma depth as a function of position within plasma for several values of y_0; $\nu/\omega = 1{\cdot}0$. The curves are normalized to unit incident flux.

that the absorbed energy is much more evenly distributed at the larger values of y_0. The strong effect of collision frequency is also seen by comparison of Fig. 2a and b; we see that, for $\nu/\omega = 0{\cdot}1$, y_0 must increase to 3·0 before the peak is lost whereas for $\nu/\omega = 0{\cdot}32$, the peak has disappeared at $y_0 = 2{\cdot}0$. The results also show that, as expected, increasing the wavelength (higher value of ν/ω) decreases the fraction of a wavelength over which the peak occurs (compare peak in Fig. 2a with that in Fig. 2c).

The effect of collision frequency and density gradient upon the reflection coefficient R is given in Fig. 3 where we have plotted R against y_0 for a range of values of ν/ω. In order to properly cover the large range of values of y_0 a semi-log plot has been used. For small values of ν/ω (short wavelengths) the amount reflected is small until the density gradient parameter drop below $y_0 = 0{\cdot}5$. As ν/ω increases the values of y_0 which give non-negligible reflection coefficients become very small and the dependence of R

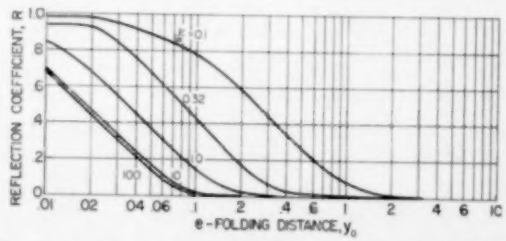

Fig. 3. Reflection coefficient R as a function of e-folding distance y_0 for a range of values of collision parameter ν/ω.

upon ν/ω decreases. For $\nu/\omega \geqq 10$, the reflection coefficient is almost independent of ν/ω. The large effect of the density gradient upon the reflection coefficient indicates strongly that large errors may be incurred by extrapolating results from a uniform plasma to one which possesses a non-negligible density gradient. The use of the WKB solution in conjunction with the numerical solution (equations 36 and 39) gave results in good agreement with those obtained by the direct numerical method, showing, as anticipated, that the WKB method is reliable so long as only regions where the index of refraction does not vary rapidly are considered.

Non-normal case

The ray paths through the plasma at $\nu/\omega = 0{\cdot}1$, for several angles of incidence, θ, and for e-folding distances y_0 of $\frac{1}{2}$ and 1, are presented in Fig. 4. The corresponding results for $\nu/\omega = 0{\cdot}32$ were, as anticipated, very close to those for $\nu/\omega = 0{\cdot}1$ and are therefore omitted. The ray paths show the typical gentle variation when first entering the plasma and the more rapid turning as the region of large index of refraction

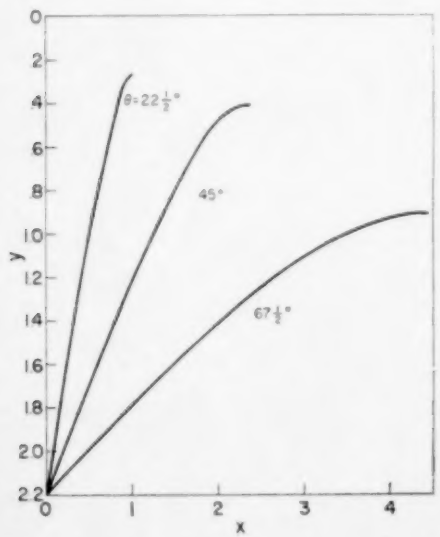

Fig 4a. Ray paths through plasma for several angles of incidence; $y_0 = 0{\cdot}5$, $\nu/\omega = 0{\cdot}1$.

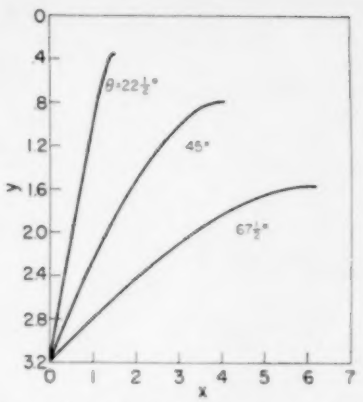

Fig 4b. Ray paths through plasma for several angles of incidence; $y_0 = 1{\cdot}0$, $\nu/\omega = 0{\cdot}1$.

is approached. As anticipated, the rays never penetrate into the region of very large variation in index of refraction, justifying the use of the WKB method in calculating the absorption.

The rate of absorption per unit y depth is

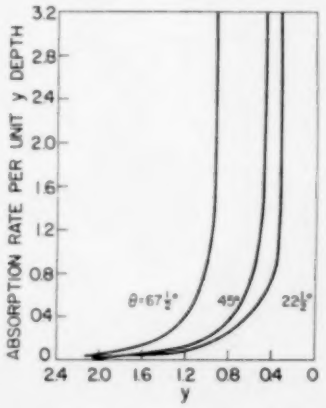

Fig. 5a. Rate of absorption per unit y depth for several angles of incidence; $y_0 = 0{\cdot}5$, $\nu/\omega = 0{\cdot}1$. The curves are normalized to unit incident flux.

presented in Fig. 5 for the several values of y_0, ν/ω and θ. The extremely rapid rise towards a vertical asymptote is, of course, due to the small changes in y as the turning point of the ray is approached. The curves in Fig. 5d ($y_0 = 1{\cdot}0$,

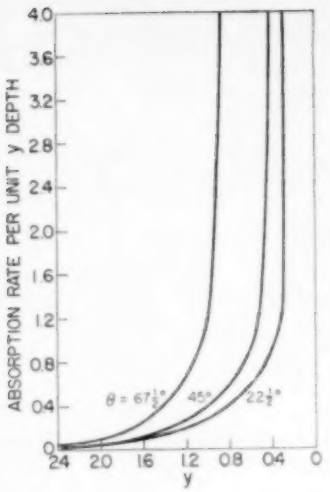

Fig. 5b. Rate of absorption per unit y depth for several angles of incidence; $y_0 = 0{\cdot}5$, $\nu/\omega = 0{\cdot}32$. The curves are normalized to unit incident flux.

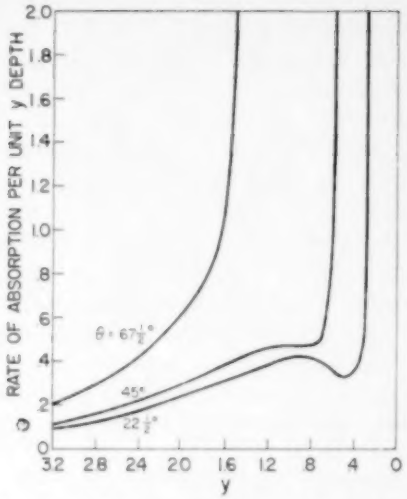

Fig. 5d. Rate of absorption per unit y depth for several angles of incidence; $y_0 = 1{\cdot}0$, ν/ω 0·32. The curves are normalized to unit incident flux.

$\nu/\omega = 0{\cdot}32$) show the development of a dip immediately before the turning point as the angle of incidence decreases. At the larger values of y_0 the absorption rate is more uniformly spread out over the plasma depth and the beam is attenuated more rapidly at the higher values of ν/ω. As the angle of incidence decreases, the beam penetrates more deeply and therefore attains a decreasing absorption rate immediately

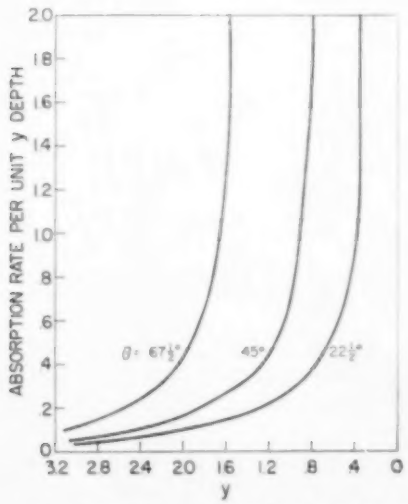

Fig. 5c. Rate of absorption per unit y depth for several angles of incidence; $y_0 = 1{\cdot}0$, $\nu/\omega = 0{\cdot}1$. The curves are normalized to unit incident flux.

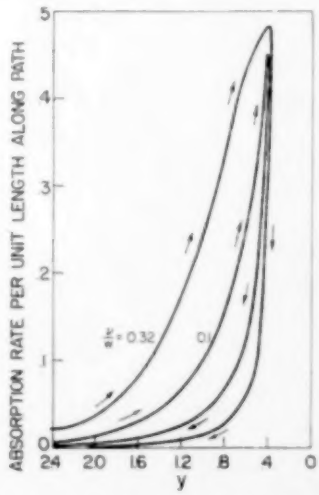

Fig. 6a. Rate of absorption per unit length along path for several values of ν/ω; $y_0 = 0{\cdot}5$, $\theta = 45°$. Ray paths are indicated by arrows. The curves are normalized to unit incident flux.

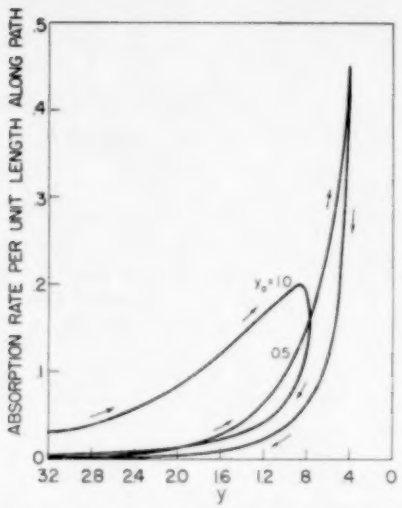

Fig. 6b. Rate of absorption per unit length along path for several values of y_0; $\nu/\omega = 0{\cdot}1$, $\theta = 45°$. Ray paths are indicated by arrows. The curves are normalized to unit incident flux.

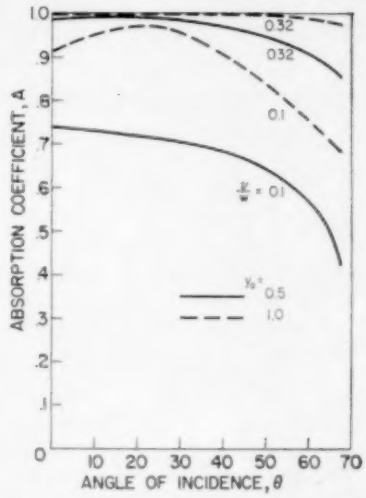

Fig. 7. Absorption coefficient A as a function of angle of incidence θ for several values of y_0 and ν/ω.

ahead of the turning point. Since, at low angles of incidence, the region of rapidly decreasing Δy is very narrow and the values of Δy have not decreased sufficiently to compensate for the decreased absorption rate, the rate of absorption per unit y depth shows a decrease just ahead of the turning point.

The rate of absorption per unit length along the path is presented in Fig. 6 for $y_0 = 0{\cdot}5, \theta = 45°$, and for the several values of ν/ω. The curves show that the point of maximum absorption along the path is not always at the point of maximum penetration, but may, for a more gentle density gradient (larger y_0) occur before the turning point (*see* Fig. 6b and Fig. 5d).

The absorption coefficient A is presented in Fig. 7 as a function of angle of incidence for the several values of y_0 and ν/ω. For the higher value of ν/ω practically all of the beam is absorbed except where the angle of incidence gets large. The curves indicate, as expected, that the higher value of ν/ω and gentler gradient gives higher absorption, and that the effect of density gradient is more marked at the lower value of ν/ω.

The curves also show that the maximum absorption coefficient need not always be at normal incidence; however, because of the gentle variation of the curves for low angles of incidence, the exact position of maximum absorption is not of great significance, and good absorption will obtain so long as the angle of incidence does not exceed 45°.

Acknowledgement—We wish to express our appreciation to Miss Janice Furey for her help in carrying out the computations.

REFERENCES

1. L. Spitzer, Jr., *Physics of Fully Ionized Gases.* Interscience publishers, New York (1956).
2. J. G. Cowling, *Magnetohydrodynamics.* Interscience Publishers, New York (1957).
3. J. H. Ratcliffe, *The Magneto-Ionic Theory and Its Applications to the Ionosphere.* Cambridge University Press (1959).
4. L. I. Schiff, *Quantum Mechanics* (2nd Ed.) Chap. 7. McGraw-Hill, New York (1955).
5. D. Bohm, *Quantum Theory*, Chap. 12. Prentice-Hall, New York (1951).
6. J. C. Slater, *Microwave Transmission* (1st Ed.) Chap. 2, Sect. II. McGraw-Hill, New York (1942).
7. L. Landau and E. Lifshitz, *The Classical Theory of Fields*, Chap. 7. Addison-Wesley, Cambridge, Mass. (1951).

RADIATION AND ADMITTANCE OF A SLOTTED-SPHERE ANTENNA SURROUNDED BY A PLASMA SHEATH*

J. W. MARINI
Electromagnetic Research Corporation, Washington, D.C.

Abstract—The radiation characteristics of an insulated slotted-sphere antenna surrounded by a uniform strongly-ionized sheath are considered. Assuming a known voltage distribution along the slot, the radiation pattern, the input admittance and the external efficiency of the antenna are determined.

The strongly ionized sheath introduces an attenuation proportional to the square-root of the frequency over a wide range of frequencies. In this range, a rather low frequency of operation is required in order to obtain an observable field through the sheath. As a result, the radiation pattern of the spherical antenna is essentially the same as that of a small loop in free space.

The input impedance depends on the geometry of the antenna and on the intrinsic impedance of the ionized sheath.

The external efficiency depends on the product of three factors representing respectively, (1) the power dissipated in the sheath by higher order modes which arise because of the geometrical configuration of the antenna but contribute little to the radiation field, (2) attenuation through the sheath of the modes which do contribute to the radiation field, and (3) reflection loss of those modes at the outer surface of the sheath.

Since the reflection loss decreases with increasing frequency while the attenuation increases, there exists an optimum frequency of operation. For the spherical model considered, this optimum frequency is one which makes the electrical thickness of the ionized sheath equal to two-and-one-half skin depths.

1. INTRODUCTION

In connection with the re-entry of a space vehicle into the earth's atmosphere, a knowledge of the characteristics of a transmitting antenna in its prevailing environment is of importance in order that the most effective design for efficient radiation may be achieved. Of particular importance is the behaviour of an antenna in a strongly ionized medium.

This paper is concerned with the radiation pattern and input admittance of a slotted sphere antenna surrounded by a strongly ionized sheath. For the sake of mathematical simplicity, the sheath will be assumed homogeneous and of uniform thickness.

A strongly ionized sheath acts like a good conductor over a wide range of frequencies,[1] and the treatment in this paper is confined to this range. In the frequency range considered, then, it is to be expected that much of the power radiated by the antenna will be lost in the conducting sheath.

In general, power is lost to the sheath through three different processes. (1) Power is delivered to the higher order modes generated. Since, as will be shown subsequently, these modes contribute little to the radiation field, this power is almost entirely dissipated in the sheath. (2) The outgoing waves that do contribute to the radiation field are severely attenuated in traversing the sheath. (3) At the outer surface of the sheath there is reflection of these waves which results in additional power being dissipated in the sheath.

* Work performed for the Missile and Ordnance Systems Department of the General Electric Co., GE PO 214-60301, under Air Force Contract AF-04-(645)-24.

The attenuation loss, being exponential, is the most significant over a wide range of frequencies. Measured in decibels, the attenuation of a wave progressing through the sheath will be directly proportional to the square root of the frequency. Consequently, lowered frequencies must be used to minimize this loss. The loss due to reflection, however, increases as the frequency is lowered, so that an optimum frequency will eventually be reached. The loss to higher order modes is not important in determining this optimum frequency, since, with a given antenna configuration, the loss to higher order modes at the lowered frequencies which must be used depends mainly on the voltage distribution on the antenna, which varies little in this range.

In all cases it is necessary that the antenna be provided with an insulating cover in the immediate vicinity of the feed in order that the assumed voltage or current distribution is realized and that conduction losses in the ionized medium may not be exorbitant.

The mathematical formulation of the problem is similar to that for a slotted sphere in free space which has been given in the literature.[2] However the radial admittances involved become much more complicated in form because of the presence of the insulating layer and the ionized sheath. The resulting formal solution to the problem is quite complicated, and to obtain usable results from it without resorting to purely numerical calculations by means of a high-speed computer, it was necessary to use the simplifying assumptions that the frequency is low and the sheath is very strongly ionized. With these assumptions, simple expressions are obtained for the input impedance of the slot, the radiation pattern and the power loss due to the ionized sheath. Also, a criterion is established for the thickness of the insulating layer in order that the conduction losses in the sheath be small.

2. FORMULATION OF THE PROBLEM

Consider a perfectly conducting sphere of radius a covered with a dielectric coating of outer radius b, which in turn is surrounded by an ionized sheath of outer radius c. On the sphere, a narrow slot of length $2l$ (measured along the surface of the sphere) and of width $2s$ is located with its centre at $\theta = \pi/2$, $\phi = 0$ and its ends at $\theta = \pi/2$, $\phi = \pm\, l/a$ (*see* Fig. 1).

The problem under consideration is to determine the (exterior) admittance of the slot (assuming that it is fed at the centre) and to obtain the radiation field. The outer medium is assumed to be free space. The electromagnetic

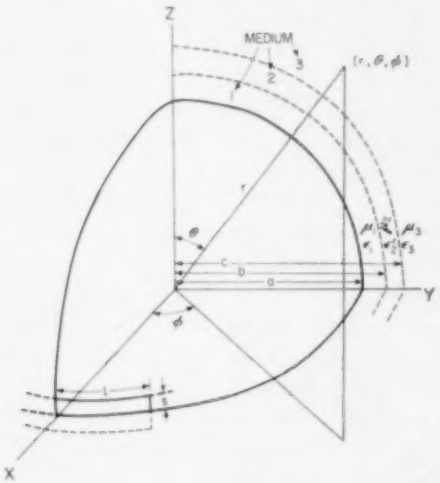

Fig. 1.

properties of the dielectric coating will be characterized by its permeability μ_1, and its complex dielectric constant ε_1'. Since the coating is assumed to have no conductivity, the complex dielectric constant is real and equal to the ordinary dielectric constant, $\varepsilon_1' = \varepsilon_1$. The properties of the ionized sheath are characterized by the constants μ_2 and ε_2'. In this case, however, the medium has finite conductivity and the complex dielectric constant ε_2' is equal $\varepsilon_2 + \dfrac{\sigma}{i\omega}$ where ε_2 is the equivalent dielectric constant and σ the equivalent conductivity of the ionized layer. The permeability, μ_2, of the ionized region is the same as that of free space, μ_0. In Ref. (1)

it was shown that the ionized sheath under the conditions considered acts like a good conductor. Thus σ is large compared to $\omega\varepsilon_2$, so that $\varepsilon_2' \approx \dfrac{\sigma}{i\omega}$. For the situations considered in this report,

$$\sigma \approx 9\pi \times 10^{-9} \frac{N_e}{\nu} \approx 9\pi \times 10^{6} \frac{N_e}{T^{\frac{1}{2}} N}$$

in which ν = collision frequency, N_e = electron density, N = particle density and T = absolute temperature.

Use will be made of the constants $k = \omega\sqrt{(\mu\epsilon')}$ and $\eta = \sqrt{(\mu/\epsilon')}$. ik is the complex propagation constant and η the complex impedance of the medium to plane waves. In mediums ① and ③ both of these constants will be real, while in the ionized sheath $k_2 \approx \sqrt{(\omega\mu_2\sigma)}\ \exp\ (-i\pi/4)$ and $\eta_2 \approx \sqrt{(\omega\mu_2/\sigma)}\ \exp\ i\pi/4)$. Rationalized m.k.s. units and a time variation $\exp\ (+i\omega t)$ are employed.

A solution to the exterior electromagnetic boundary value problem of the slotted sphere antenna of Fig. 1 in free space has been given by Mushiake and Webster.[2] Their solution for the modal admittance can be used directly to give the expression[3] below for the input admittance of the slotted sphere.

$$Y = \sum_{n=1}^{\infty} \sum_{m=0}^{n} i \frac{V_m^2}{V(0)^2} \frac{(1+\delta_{0m})\pi}{\eta_1} \left[\frac{Z_n^{H1\prime}(k_1 a)}{Z_n^{H1}(k_1 a)} \frac{m^2 \bar{P}_n^m(0)^2}{n(n+1)} - \frac{Z_n^{E1}(k_1 a)}{Z_n^{E1\prime}(k_1 a)} \frac{\bar{P}_n^{m\prime}(0)^2}{n(n+1)} \right] \tag{1}$$

Here $\delta_{0m} = 1$ if $m = 0$, $\delta_{0m} = 0$ if $m \neq 0$, the functions $\bar{P}_n^m$ (cos θ) are the normalized associated Legendre Polynomials, and V_m is the mth coefficient of the Fourier expansion of the voltage across the slot:

$$V(\phi) = \sum_{m=0}^{\infty} V_m \cos m\phi$$

$V(0)$ is the voltage across the centre of the slot, and the functions $Z_n^{E1}(k_1 r)$ and $Z_n^{H1}(k_1 r)$ are linear combinations of the functions

$$\begin{aligned} j_n(Z) &= \sqrt{(\pi Z/2)}\, J_{n+\frac{1}{2}}(Z) \\ h_n^{(1)}(Z) &= \sqrt{(\pi Z/2)}\, H_{n+\frac{1}{2}}^{(1)}(Z) \\ h_n^{(2)}(Z) &= \sqrt{(\pi Z/2)}\, H_{n+\frac{1}{2}}^{(2)}(Z) \end{aligned} \tag{2}$$

where $J_{n+\frac{1}{2}}(Z)$, $H_{n+\frac{1}{2}}^{(1)}(Z)$ and $H_{n+\frac{1}{2}}^{(2)}(Z)$ are the usual Bessel and Hankel functions of order $n + \frac{1}{2}$.

Since the voltage distribution across the slot is assumed known, the only quantities left to determine in equation (1) are the radial functions, $Z_n^{H1}(k_1 r)$ and $Z_n^{E1}(k_1 r)$. They are determined from the boundary conditions of continuity of the tangential components of the electric and magnetic intensities at the boundaries of mediums ① and ②, and ② and ③, and by the radiation condition at infinity. If the sheath is strongly ionized, it may be assumed quite safely that waves reflected from the boundary between mediums ② and ③ can be neglected at the boundary between ① and ②.

Treating the electric modes first, in medium ① let

$$Z_n^{E1}(k_1 r) = h_n^{(2)}(k_1 r) - R_n^{E1} j n(k_1 r) \tag{3}$$

which represents the superposition of outgoing and reflected waves, and in medium ② let the radial function be

$$Z_n^{E2}(k_2 r) = T_n^{E2} h_n^{(2)}(k_2 r)$$

which represents an outgoing wave only, in accordance with the assumption above that reflected waves from c may be neglected at b. R_n^{E1} and T_n^{E2}, respectively, are reflection and transmission coefficients at the boundary between the insulating layer and the ionized sheath. The boundary conditions will be met if $k_1 Z_n^{E1}(k_1 r) = k_2 Z_n^{E2}(k_2 r)$ and $\varepsilon_1 Z_n^{E1}(k_1 r) = \varepsilon_2' Z_n^{E2}(k_2 r)$ at the boundary $r = b$. Therefore we have

$$k_1 h_n^{(2)\prime}(k_1 b) - R_n^{E1} k_1 j_n(k_1 b) = T_n^{E2} k_2 h_n^{(2)\prime}(k_2 b)$$

$$\varepsilon_1 h_n^{(2)}(k_1 b) - R_n^{E1} \varepsilon_1 j_n(k_1 b) = T_n^{E2} \varepsilon_2' h_n^{(2)}(k_2 b)$$

The reflection and transmission coefficients R_n^{E1}, T_n^{E2} then are

$$R_n^{E1} = \frac{k_1\varepsilon_2' h_n^{(2)\prime}(k_1b)h_n^{(2)}(k_2b) - \dfrac{k_2\varepsilon_1 h_n^{(2)}(k_1b)h_n^{(2)\prime}(k_2b)}{k_2\varepsilon_1 j_n(k_1b)h_n^{(2)\prime}(k_2b)}}{k_1\varepsilon_2' j_n'(k_1b)h_n^{(2)}(k_2b) - \dfrac{k_2\varepsilon_1 h_n^{(2)}(k_1b)h_n^{(2)\prime}(k_2b)}{k_2\varepsilon_1 j_n(k_1b)h_n^{(2)\prime}(k_2b)}} \tag{4}$$

$$T_n^{E2} = \frac{k_1\varepsilon_1\left[j_n'(k_1b)h_n^{(2)}(k_1b) - \dfrac{j_n(k_1b)h_n^{(2)\prime}(k_1b)\right]}{k_2\varepsilon_1 j_n(k_1b)h_n^{(2)\prime}(k_2b)}}{k_1\varepsilon_2^1 j_n'(k_1b)h_n^{(2)}(k_2b) - \dfrac{j_n(k_1b)h_n^{(2)\prime}(k_1b)\right]}{k_2\varepsilon_1 j_n(k_1b)h_n^{(2)\prime}(k_2b)}}$$

With R_n^{E1} determined, $Z_n^{E1}(k_1r)$ is given through equation (3). The rest of the radial functions are obtained in a similar fashion (cf. Ref. 3). The radial functions so determined together with equation (1) make up a formal solution for the input admittance.

3. APPROXIMATE SOLUTION

The equation (1) for the input admittance can be greatly simplified if the frequency is low and the sheath is strongly ionized. Then the distance b is small compared to the wavelength in medium ① and c is small compared to the wavelength in free space, while the conductivity of medium ② is large so that b is a large number of skin depths. Then k_1a, k_1b, and k_3c are small while k_2b and k_2c are large. Functions of k_1a, k_1b and k_3c consequently can be replaced by their approximations for small arguments, while functions of k_2b and k_2c can be replaced by their asymptotic expansions for large arguments. It will be assumed that the insulating layer is thin, i.e. that

$$\frac{b-a}{a} \ll 1$$

When these approximations are made the input admittance (1) reduces to

$$Y \approx \sum_{n=1}^{\infty}\sum_{m=0}^{n}(1+\delta_{0m})\pi\left\{\frac{1}{\eta_2 + i\omega\mu_1(b-a)}\frac{m^2}{n(n+1)}\bar{P}_n^m(0)^2 + \frac{1}{\eta_2 + \dfrac{h(n+1)(b-a)}{i\omega\varepsilon_1 ab}}\frac{\bar{P}_n^{m\prime}(0)^2}{n(n+1)}\right\}\left[\frac{V_m}{V(0)}\right]^2 \tag{5}$$

In form, equation (5) represents the total admittance of two types of circuits in parallel, one circuit corresponding to each mode. The first type of circuit contains the surface impedance η_2 of the ionized sheath in series with an equivalent inductance $\mu_1(b-a)$. This circuit is associated with the currents flowing on the surface of the sphere together with those induced on the interface between the dielectric and ionized layers. The second type of circuit also contains the surface impedance η_2, this time, however, in series with an equivalent capacitance $c = \varepsilon_1 ab/n(n+1)(b-a)$ between the sphere and the interface. This circuit is associated with displacement currents flowing between the sphere and the interface.

If $b-a$ is made extremely small, the properties of the first medium disappear from equation (5), which reduces to the admittance of a sphere with no dielectric coating. The admittance would then be very large because of the low impedance η_2 of the ionized medium, so that the slot would be virtually short-circuited. This makes evident the need for an insulating covering of the sphere. We shall consider, therefore, only the case where the dielectric coating is thick enough to be completely effective in reducing the shunting effect of the ionized sheath across the slot; that is, we assume that

$$|k_2|(b-a) \gg \frac{\mu_2}{\mu_1}k_1^2 ab$$

This is equivalent to

$$|\eta_2| \ll \frac{b-a}{\omega\varepsilon_1 ab} \tag{6}$$

The requirement above, on the size of $b-a$ can be interpreted as requiring that this spacing between the plates of the equivalent capacitor be large enough so the capacitive reactance is large compared to the complex impedance of the ionized medium. In other words, we require

the spacing to be large enough to prevent the surface currents on the sphere from being short-circuited by displacement currents flowing to the ionized sheath.

Under this stipulation, which is given quantitatively by equation (6), the final expression for Y becomes

$$Y \approx \frac{1}{\eta_2 + i\omega\mu_1(b-a)} \sum_{n=1}^{\infty} \sum_{m=1}^{n} \pi \frac{m^2}{n(n+1)} \bar{P}_n^m(0)^2 \left[\frac{V_m}{V(0)}\right]^2 \qquad (7)$$

This was obtained under the assumptions that

$$k_1 b \ll 1$$

$$|k_2| b \gg 1$$

$$\frac{b-a}{\omega\varepsilon_1 ab} \gg |\eta_2|$$

$$\frac{b-a}{a} \ll 1$$

The summation in equation (7) is dependent only on the ratio l/a (through the factor $V_m^2/V_{(0)}^2$), where l is the half-length of the slot and a is the radius of the sphere. The convergence is of the order $\frac{1}{n^2}$ and $\frac{1}{m^2}$ (since $V_m^2/V_{(0)}^2$ varies as $1/m^4$ for the assumed triangular voltage distribution), so the series may be evaluated numerically without retaining very many terms. For a slot of length $l/a = \pi/2$, the results are

$$Y\big|_{l/a=\pi/2} = 0{\cdot}38 \frac{1}{\eta_2 + i\omega\mu_1(b-a)}$$

$$Z = 0{\cdot}26[\eta_2 + i\omega\mu_1(b-a)] \qquad (8)$$

$$Z = 0{\cdot}26\left\{\frac{|\eta_2|}{\sqrt{2}} + i\left[\omega\mu_1(b-a) + \frac{|\eta_2|}{\sqrt{2}}\right]\right\}$$

4. THE RADIATION FIELD

The radiation field can likewise be obtained as in Ref. (2) but with radial functions determined as indicated above. When the various approximations are used, and in particular, when it is assumed the outer radius, c, of the plasma sheath is small compared to a wavelength, the radiation field is found to be due only to the TE_{11} (H-type) mode. Other modes can be neglected because they all contain higher powers of the quantity $k_3 c$ as factors. The radiation field due to the TE_{11} mode has the form

$$\begin{cases} E_\theta^{(3)} \approx -\frac{3}{4} ik_3 c \frac{\eta_2 V_1}{\eta_2 + i\omega\mu_1(b-a)} \times e^{-ik_2(c-b)} \frac{e^{-ik_3 r}}{r} \cos\phi \\ E_\phi^{(3)} \approx \frac{3}{4} ik_3 c \frac{\eta_2 V_1}{\eta_2 + i\omega\mu_1(b-a)} \times e^{-ik_2(c-b)} \frac{e^{-ik_3 r}}{r} \cos\theta \sin\phi \end{cases} \qquad (9)$$

The electric field has components in both the θ- and ϕ-directions. These differ only in their dependence on the θ- and ϕ-co-ordinates. If a transformation is made to new co-ordinates θ', ϕ', as shown in Fig. 2, where the new polar angle θ' is measured from the y-axis, and the new

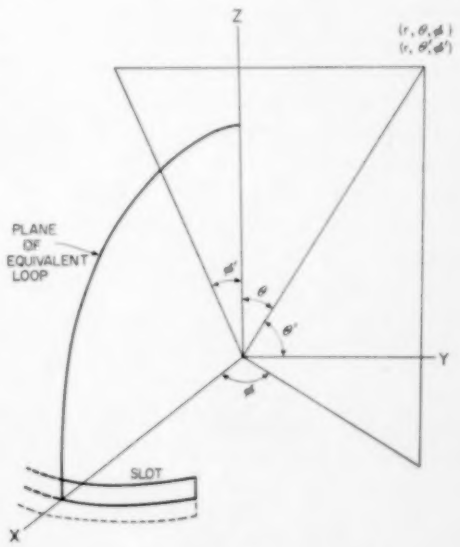

Fig. 2.

azimuth angle ϕ' is measured from the z-axis, then the electric field has only a single component, given by

$$E_{\phi'}^{(3)} = -\frac{3}{4} ik_3 c \frac{\eta_2 V_1}{\eta_2 + i\omega\mu_1(b-a)} \times e^{-ik_2(c-b)} \frac{e^{-ik_3 r}}{r} \sin\theta' \qquad (10)$$

The field pattern is now given by the factor $\sin\theta'$. This is exactly the pattern of a loop lying in the xz-plane with centre at the origin. This is the meridian plane of the currents which flow from one edge of the slot around the sphere to the opposite edge of the slot.

The factor $\exp[-ik_2(c-b)]$ in equation (10) represents the attenuation and phase shift due to the passage of the wave through the sheath, while the factor $\exp(-ik_3 r)/r$ represents a diverging spherical wave.

4.1 *Radiation intensity*

A measure of the radiation efficiency of the antenna can be obtained by dividing the radiation intensity by the input power to the slot. This ratio then can be examined for an optimum choice of the design parameters. This, however, is only a partial optimization procedure, since it does not consider all the factors which determine the overall efficiency of the antenna. In particular, it does not include the losses in the matching networks necessary to feed the slot from the source of power. These losses will depend on the Q of the matching network and the input impedance. This latter problem, however, can be evaluated since the input impedance of the slot already has been determined. The radiation intensity divided by the input power is a measure of the external efficiency of the antenna.

The radiation intensity is

$$\frac{r^2 |E_{\phi'}^{(3)}|^2}{2\eta_3} = \left(\frac{3}{4} k_3 c\right)^2 \left| \frac{\eta_2}{\eta_2 + i\omega\mu_1(b-a)} \right| \times \frac{V_1^2}{2\eta_3} e^{-\sqrt{2}\,|k_2|(c-b)} \sin^2\theta' \qquad (11)$$

The total input power, P, which includes both the power radiated and the power absorbed by the sheath, is given by the real part of $YV(0)^2/2$. From equation (7) this is found to be

$$P = \frac{1}{2\sqrt{2}} \frac{|\eta_2|}{|\eta_2 + i\omega\mu_1(b-a)|^2} \sum_{n=1}^{\infty} \sum_{m=1}^{n} \pi \frac{m^2}{n(n+1)} \bar{P}_n^m(0)^2 V_m^2 \qquad (12)$$

The ratio of the radiation intensity to the input power is

$$\frac{r^2 |E_{\phi'}^{(3)}|^2}{2\eta_3 P} = \frac{9\sqrt{2}}{16} k_3^2 c^2 \frac{|\eta_2|}{\eta_3} \frac{V_1^2}{V(0)^2} \times \frac{e^{-\sqrt{2}\,|k_2|(c-b)} \sin^2\theta'}{\sum\sum \pi \frac{m^2}{n(n+1)} [\bar{P}_n^m(0)]^2 \frac{V_m^2}{V(0)^2}} \qquad (13)$$

4.2 *External efficiency*

Equation (13) may be integrated over the surface of a unit sphere to obtain the ratio of the radiated power to input power, which is the external efficiency of the antenna. Denoting the external efficiency by ξ,

$$\zeta = \left\{ \frac{\pi \frac{m^2}{n(n+1)} [\bar{P}_n^m(0)]^2 \frac{V_m^2}{V(0)^2} \Big|_{\substack{m=1 \\ n=1}}}{\sum_{n=1}^{\infty} \sum_{m=1}^{n} \pi \frac{m^2}{n(n+1)} [\bar{P}_m^m(0)]^2 \frac{V_m^2}{V(0)^2}} \right\} \times \left\{ \left[(k_3 c)^2 \frac{4\sqrt{2}\,|\eta_2|}{\eta_3} e^{-\sqrt{2}\,|k_2|(c-b)} \right] \right\} \qquad (14)$$

Each of the brackets in equation (14) has physical significance. The first bracket is obviously the ratio of the power delivered to the magnetic type mode $n = m = 1$ (TE_{11}) (which is the only mode contributing significantly to the radiation field), to that delivered to all the modes. The second bracket is the overall power transmission coefficient for this mode (i.e. the ratio of power of this mode that is radiated to that entering the sheath). It consists of an exponential

factor representing attenuation through the sheath, and a second factor due to reflection at the outer surface of the sheath. The latter is the product of $(k_3C)^2$ and the factor $4\sqrt{2}|\eta_2|/\eta_3$ which in turn is the power reflection coefficient for a plane wave progressing across a plane surface from a medium of intrinsic impedance η_2 to one whose intrinsic impedance is η_3 (with $|\eta_2| \ll \eta_3$).

5. OPTIMIZATION PROCEDURES

The expression above is proportional to the efficiency (ratio of radiated power to total input power) of the slot antenna if it is assumed that feeding losses are not important compared to losses in the sheath. Therefore it is desirable to consider the means for maximizing the expression given in equation (14). In the first place, if the size of the vehicle is given, the quantities b and c are fairly well fixed. Since the outer medium is free space, η_3 will be equal to 377Ω. The quantity $k_3^2 \equiv \omega^2\mu_3\varepsilon_3$ varies as the square of the frequency while $|\eta_2| = \sqrt{(\omega\mu_2/\sigma)}$ and $|k_2| = \sqrt{(\omega\mu_2\sigma)}$ vary as the square-root of the frequency. Consequently ξ varies as $\omega^{5/2}\exp[-\sqrt{2\mu_2\sigma}(c-b)\omega^{1/2}]$. The latter expression is maximized by setting the exponent equal to -5:

$$\sqrt{(2\mu_2\sigma)}(c-b)\omega_{\text{opt}}^{1/2} = 5$$

The optimum frequency then is

$$f_{\text{opt}} = \frac{25}{4\pi}\,\frac{1}{\mu_2\sigma(c-b)^2}. \tag{15}$$

This is the frequency that makes the sheath thickness, $c-b$, equal to two-and-one-half skin depths in the ionized medium.

The only other quantity in equation (14) besides the frequency that can be varied to make the expression a maximum is the ratio

$$\frac{\pi\dfrac{m^2}{n(n+1)}\,\bar{P}_n^{m2}(0)\,\dfrac{V_m^2}{V(0)}\Bigg|_{\substack{m=1\\n=1}}}{\displaystyle\sum_{n=1}^{\infty}\sum_{m=1}^{n}\pi\frac{m^2}{n(n+1)}\,\bar{P}_n^{m2}(0)\,\frac{V_m^2}{V(0)^2}} \tag{16}$$

The magnitude of this can be varied by changing the length of the slot. In general, the efficiency is increased by increasing the slot length.

The thickness, $b-a$, of the dielectric layer does not appear in the expression (14) for the efficiency provided condition (6) is met. It does, however, appear in equation (8) where it is present as a term representing an additional series inductance.

REFERENCES

1. M. Katzin, *Radiation of an Electric Dipole into an Ionized Sheath*, Electromagn. Res. Corp. **Rep.** 60175-7 (Dec. 1957).
2. Y. Mushiake and R. Webster, *Trans. Inst. Radio Engrs. on Antennas*, AP **5**, 47 (1957).
3. A complete derivation is given by J. W. Marini, B.Y.-C. Koo and M. Katzin in *Radiation and Impedance of Antennas Surrounded by an Ionized Sheath*, Electromagn. Res. Corp. Rep. ERC 60301-6 (Aug. 1958).

ON THE CHANGE IN RADAR CROSS-SECTION OF A SPHERICAL SATELLITE CAUSED BY A PLASMA SHEATH

C. L. DOLPH and H. WEIL
The Radiation Laboratory of The University of Michigan, Ann Arbor, Michigan

Abstract—A uniform neutral dilute ionized gas is assumed to be perturbed by a sphere moving through it. The radar return from the disturbed region is obtained by integrating the Compton scattering from the electrons, taking phase into account, but ignoring secondary scattering and attenuation. The electron density distribution for this computation is obtained by integration of the zeroth order velocity distribution function for neutral particles obtained by Wang Chang[6] as a solution of the Boltzmann transport equation.

Numerical results are obtained for the perturbation of the electron distribution by a sphere travelling at 8 km/sec and an altitude of 500 km, and for the radar cross-section of this perturbed region when viewed broadside.*

INTRODUCTION

A sphere is assumed to move with a constant velocity, V, through a dilute, electrically neutral, ionized gas that, in its unperturbed state, is assumed to have a uniform number distribution of electrons, n. The sphere disturbs the distribution of electrons to a non-uniform one, N, with an excess ahead of the sphere and a deficiency behind it. The simplest estimate of the effect of this non-uniform, but everywhere dilute distribution on the radar return is obtained by summing the scattering by the individual electrons accelerated by the incident field. Electrons only are considered since their return is far greater than that of the much heavier positive ions or the Rayleigh scattering from non-ionized particles. The incident field on each electron is assumed to be a plane wave; this implies that secondary scattering is ignored. The approach is thus directly analogous to that used to determine the radar return from underdense meteor trails.[1]

There are three parts to the paper. The first part consists of a formulation of the expression for the back-scattered energy. This expression involves the perturbed density distribution. The condition of neutrality is used in determining this distribution since it forces the electron motion to be governed by the positive ions whose velocities and mass are similar to that of the neutral particles. This will be discussed in the second part of the paper where expressions for the distribution are found. In the third part numerical results for a specific sphere velocity and altitude are presented.

2. THE SCATTERING INTEGRAL

The radiation field of each electron yields a back-scattered power per unit solid angle per electron for unit incident power density given by

$$\sigma_e = [e^2/(4\pi\varepsilon_0 mc^2)]^2.$$

Here e is the charge on the electron, m its mass, ε_0 the permittivity of free space, c the velocity of light and m.k.s. units are to be used. The incident power is given by $PG/(4\pi r^2)$ where P is the total power emitted from the radar antenna, G the antenna gain and r the distance from antenna to electron. The effective collecting area of the antenna is $G\lambda^2/(4\pi)$ so that the

* The theoretical work and preliminary computations were supported by USAF Contract AF 30(602)-1853. The final machine computations were carried out as an unsponsored faculty research project MO2-N at the Computation Laboratory of The University of Michigan.

scattered power per electron received by the radar for large r is

$$S_e = \frac{PG^2\lambda^2\sigma_e}{16\pi^2 r^4}.$$

We now assume the radar is well out of the ionized region of interest so that r is always large. Then the net power received from this region is

$$S = \frac{\lambda^2\sigma_e P}{16\pi^2}\left|\int \frac{G}{r^2} e^{2ikr} N\,dv\right|^2,$$

where dv is a volume element. For simplicity a beam width wide enough to be essentially constant over the disturbance is assumed and the slowly varying factor r^{-2} replaced by the range R_0 to the sphere and removed from under the integral sign. Finally, N is referred to the constant n by writing $N=(N-n)+n$. The integral of n exp $(2ikr)$ vanishes except for contributions at the "edges" of the region of integration. Of course the distribution n extends beyond the beam-width of the radar and thus we know these "edges" are not physically significant. They may be neglected with the result that the desired quantity, the net power received due to the disturbance of the density distribution is given by

$$S_D \sim \frac{\lambda^2\sigma_e PG^2}{16\pi^2 R_0^4}\left|\int e^{2ikr}(N-n)\,dv\right|^2.$$

The integration is to be extended over the region of interest. In general this will include the entire region over which $N-n$ differs appreciably from zero. However, one might also be interested in considering separately the effects of the region ahead of the sphere and the region behind it. If these were to act as independent scatterers the average returned power (averaged over all relative phases) would be the sum of two expressions S_{D_1} and S_{D_2} corresponding to S_D with the integration in S_{D_1} over the region ahead of the sphere and the region in S_{D_2} over the region behind the sphere.

To put the integral in S in a form suitable for computation it is convenient to refer to Fig. 1.

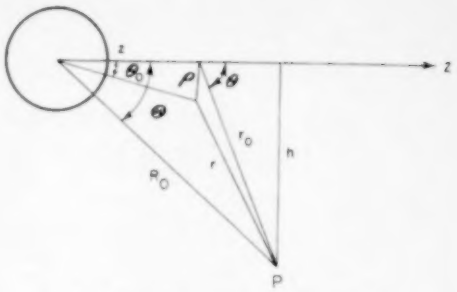

Fig. 1. Satellite-receiver geometry.

The density N must be symmetric about z so that it is convenient to use cylindrical coordinates ρ, ψ, z in the integration. Furthermore, one can simplify the integral by using in the expression for $\mathbf{r}(\boldsymbol{\rho})$

$$(\mathbf{r}\boldsymbol{\rho}) = \mathbf{r}_0 - \boldsymbol{\rho}; \quad r^2 = r_0^2 + \rho^2 - 2\mathbf{r}\cdot\boldsymbol{\rho}$$

the fact that $\dfrac{\rho}{r_0} \ll 1$, so that

$$r = r_0\left[1 + \frac{\rho^2}{r_0^2} - \frac{2\rho}{r_0}\sin\theta\cos(\phi-\psi)\right]^{1/2}$$

$$\sim r_0 - \rho\sin\theta\cos(\phi-\psi) + \frac{1}{2}\frac{\rho^2}{r_0} - \frac{1}{8}\frac{\rho^2}{r_0}\sin^2\theta\cos^2(\phi-\psi) + \ldots$$

In turn r_0 is approximated by

$$r_0 \simeq R_0 + \frac{z^2}{2R_0} - 2z\cos\Theta - \frac{1}{8}\frac{z^2}{R_0}\cos^2\Theta + \ldots$$

We shall be interested in $60^\circ < \Theta < 120^\circ$ and hence will neglect the last term as well as those of higher order in z/R_0. Then

$$S = \frac{\lambda^2\sigma_e PG^2}{16\pi^2 R_0^4}\left|\int_0^{2\pi} d\psi \int_{-\infty}^{\infty} dz \int_0^{\infty} \rho\,d\rho[N(\rho,z)-n]\,e^{2ikr(\rho,\psi,z)}\right|^2$$

$$\simeq \frac{\lambda^2\sigma_e PG^2}{4R_0^4}\left|\int_{-\infty}^{\infty} dz.\ \exp\left[2ik\left(\frac{z^2}{2R_0} - z\cos\theta\right)\right]\right.$$

$$\left\{\int_0^\infty \rho\, d\rho[N(\rho,z)-n]J_0[2k\rho \sin\theta(z)]\right\}\Bigg|^2$$

The term $\frac{1}{2}\rho^2/r_0$ is neglected in the phase since it will appreciably affect the phase only if $\Theta=90°$ and then only where ρ exceeds $\sim 0.1\sqrt{R_0}$. For such large ρ's the amplitude $N-n$ is negligible. This is not quite true for corresponding values of z. In this consideration we have assumed $k < \sim 20\, m^{-1}$. Note that in this integral $\sin\theta(z)=R_0 \sin\Theta/r_0(z)$.

2. COMPUTATION OF THE ELECTRON DISTRIBUTION

The steady-state problem of a point charge moving through a fully ionized medium of sufficiently low density has been treated by Kraus and Watson.[2] Their work was extended to the case where a constant magnetic field is present by Greifinger.[3] A good deal of insight into the physical meaning of the above theories which started from the linearized Landau–Vaslov equation was provided by the report of Pappert.[4] In this report Pappert deduced the results of Kraus and Watson from the random phase approximation of Bohm and Pines[5] and also demonstrated the equivalence of these methods to the linearization of the equations of motion and continuity for the ions and electrons under the assumption that an isothermal state exists.

The problem of an object of finite size has been approached by using the expression obtained in 1950 by Wang Chang.[6] She obtained the zeroth order velocity distribution function for a sphere of radius R at rest in a neutral gas with a streaming velocity V under the assumption that the sphere was sufficiently small and the gas sufficiently dilute that the collisions between the main stream particles and those reflected from the sphere could be neglected. The distribution function so determined satisfies:

(a) The collision-free Boltzmann transport equation in the absence of external forces;

(b) A boundary condition on the surface of the sphere that implies that the sphere neither absorbs nor emits gas particles by itself so that all particles that hit the sphere are re-emitted;

(c) The property that it reduces to the Maxwell–Boltzmann distribution around the steaming velocity at infinity independent of angle.

In addition, this distribution allows for arbitrary amounts of diffuse or specular reflection at the spherical surface. Since the region of interest here involves velocities of the sphere much greater than that of the ions and at the same time much smaller than that of the electrons and altitudes where the mean free paths are large compared to the expected dimensions of the disturbed area, Chang's distribution may be used to provide an order of magnitude estimate of the electron distribution around the sphere when it is assumed that the charge on the sphere is so small that it can be ignored so that the ions will (to all intents and purposes) behave as neutral particles as far as their interaction with the sphere is concerned. The strong Coulomb forces should provide electrical neutrality which will then force the electrons to assume a distribution identical in form to Chang's in which only the mass and velocity parameters can be different.

This use of electrical neutrality, while appropriate in ionospheric physics, is less exact than the assumptions usually used in physics of confined plasmas where[7] it is more customary

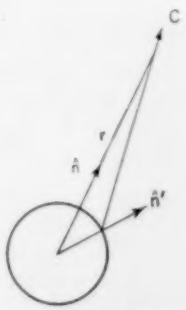

Fig. 2. Relation between **C** and $\hat{n}$.

to assume electrical neutrality except for consideration of Poisson's equation while here we ignore any deviations from neutrality in this equation as well. While it would be more exact to assume the Chang distribution as the first term in a perturbation procedure for the Landau–Vlasov equations, it is unlikely that such a refined analysis would affect the radar cross-section results.* Other approaches such as that used by Bernstein and Rabinowitz[9] in their discussion of spherical probes would seem to encounter even more intractable analytical difficulties were the Chang distribution to be used in place of the mono-energetic one used by them.

The zeroth order velocity distribution obtained by Chang is expressed in terms of the following variables.

$\mathbf{V}'$ = the velocity of the main stream

R = the radius of the sphere

$\mathbf{r}$ = the point under consideration, or the point at which the velocity is being calculated

$\hat{n}$ = the outward normal to the sphere which passes through the point; $\mathbf{r}=r\hat{\mathbf{n}}$ if the centre of the sphere is taken as the origin of the co-ordinate system

$\mathbf{C}'$ = the velocity vector of gas particles

α = the fraction of molecules that is diffusely reflected from the sphere

$1-\alpha$ = the fraction of molecules that is specularly reflected from the sphere

$\mathbf{V}$ = $\mathbf{V}'/\sqrt{2kt/m}$, non-dimensional streaming velocity

$\mathbf{C}$ = $\mathbf{C}'/\sqrt{2kt/m}$, non-dimensional velocity vector

$\hat{n}'$ = the normal to the sphere at the point from which the molecules arriving at $\mathbf{r}$ with velocity $\mathbf{C}$ originated. From Fig. 2 it is found that

$$\hat{n}' = \frac{\mathbf{r}}{R} - \frac{\mathbf{r}\cdot\mathbf{C}}{RC^2}\mathbf{C} + r\sqrt{\frac{(\mathbf{r}\cdot\mathbf{C})^2}{r^2C^2} - \left(1-\frac{R^2}{r^2}\right)}\,\frac{\mathbf{C}}{RC}$$

$\hat{n}_C$ = unit vector in the direction of $\mathbf{C}$

n = the number of particles present in the unperturbed state

$$\operatorname{erfc}(x) = \frac{2}{\sqrt{\pi}}\int_x^\infty \exp(-t^2)\,dt = 1-\operatorname{erf}(x)$$

S = $S(x, y, z, \hat{n}_C)$, a discontinuous function which is zero if the particles of velocity $\mathbf{C}$ at point $\mathbf{r}(y, x, z)$ come from the sphere and which is one otherwise. That is, $S=0$ if $\hat{n}_C$ points away from the sphere and lies in the solid angle subtended by the sphere at the point under consideration.

The distribution can be written as

$$f(\alpha) = \frac{n}{\pi^{3/2}}\{S\exp -(\mathbf{C}-\mathbf{V})^2 + \alpha[\exp-(\mathbf{V}\cdot\hat{n}')^2 - \\ -\sqrt{\pi}(\mathbf{V}\cdot\hat{n}')\operatorname{erfc}(\mathbf{V}\cdot\hat{n}')](1-S)\exp -C^2 + \\ +(1-\alpha)(1-S)\exp -[\mathbf{C}-\mathbf{V}-2\hat{n}'(\hat{n}'\cdot C)]^2\}$$

The function S which is described above can be represented analytically as

$$S = \tfrac{1}{2}(1-\operatorname{sign}(\hat{n}\cdot\mathbf{C}) + [\tfrac{1}{2}(1+\operatorname{sign}(\hat{n}\cdot\mathbf{C})] \\ \left[1+\operatorname{sign}\left\{\left(1-\frac{R^2}{r^2}\right)^{1/2} - \frac{\hat{n}\cdot\mathbf{C}}{C}\right\}\right]$$

and it has the properties that for r approaching infinity, S approaches 1, while for r approaching the sphere R,

$$S = \tfrac{1}{2}(1-\operatorname{sign}\hat{n}\cdot\mathbf{C}).$$

Furthermore, if θ is the angle between $\mathbf{r}$ and $\mathbf{C}$ then, as can be seen from Fig. 3,

$$S = 0 \text{ if } 1 \geqslant \cos\theta \geqslant \left(1-\frac{R^2}{r^2}\right)^{1/2} = \cos\theta_1$$

$$S = 1 \text{ if } \cos\theta < \cos\theta_1.$$

* Actually the indicated procedure for the second approximation is presently under investigation under another contract for a different purpose. Preliminary analysis seems to indicate the existence of oscillatory solutions for the electron density with frequencies of the order of those characteristic for plasmas modified by an increment dependent upon electron temperature and form factors appropriate to the geometry. See Ref. (8).

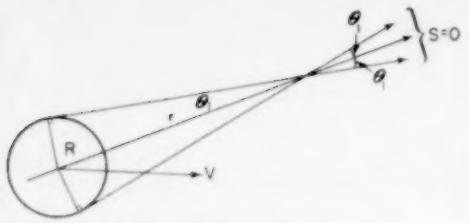

Fig. 3. Region where S = 0.

The Density Distribution for Ions and Electrons in the Neighbourhood of the Sphere for the Case of Diffuse Reflection

The necessary calculations are considerably simplified if it is assumed that only diffuse reflection occurs so that α may be set equal to unity. Fortunately this appears to be a good approximation to the physical situation.[6, 10, 11]

We shall therefore calculate

$$\int f(1)\, d^3\mathbf{C}$$

and take up the two terms separately, treating first the contribution

$$I_1 = \frac{n}{\pi^{3/2}} \int S \exp -(\mathbf{C}-\mathbf{V})^2\, dV$$

from the main stream. To evaluate I_1 we determine S in rectangular C space C_x, C_y, C_z. For convenience set n in the direction of C_z. If

$$\left(1-\frac{R^2}{r^2}\right)^{1/2} - \frac{C_z}{(C_x^2+C_y^2+C_z^2)^{1/2}} < 0$$

then $C_z > 0$ and

$$S = \tfrac{1}{2}[1-\text{sign } C_z] = 0,\ C_z > 0.$$

Also, for all $\mathbf{C}$ for which

$$\left(1-\frac{R^2}{r^2}\right)^{1/2} - \frac{C_z}{(C_x^2+C_y^2+C_z^2)^{1/2}} > 0,$$

$S=1$. Since both sides of the first inequality are positive it may be squared and solved for C_z. The result is

$$C_z > \left(\frac{r^2}{R^2}-1\right)^{1/2} (C_x^2+C_y^2)^{1/2} \equiv C_{z_0},$$

so that if $C_z \geqslant C_{z_0}$, $S=0$. Similarly if $C_z < C_{z_0}$, $S=1$.

Thus we must evaluate

$$\mathrm{I}_1 = \frac{n}{\pi^{3/2}} \int_{-\infty}^{\infty} dC_x \int_{-\infty}^{\infty} dC_y \int_{-\infty}^{C_{z_0}} dC_z \exp - \\ - [(C_x-V_x)^2 + (C_y-V_y)^2 + (C_z-V_z)^2].$$

The C_z integral is

$$\int_{-\infty}^{C_{z_0}} \exp -(C_z-V_z)^2\, dC_z = \int_{-\infty}^{C_{z_0}-V_z} \exp\,(-t^2)\, dt = \frac{\sqrt{\pi}}{2}\left[\text{erf}\,(C_{z_0}-V_z)+1\right].$$

Hence

$$I_1 = \frac{n}{2} + \frac{n}{2\pi} \int_{-\infty}^{\infty} \int_{-\infty}^{\infty} \exp -[(C_x-V_x)^2 + (C_y-V_y)^2] \\ \text{erf}\,(C_{z_0}-V)\, dC_x dC_y.$$

Introduce polar co-ordinates as follows:

$$C_x = \rho\cos\phi \qquad V_x = \sqrt{(V^2-V_z^2)}\cos\psi$$
$$C_y = \rho\sin\phi \qquad V_y = \sqrt{(V^2-V_z^2)}\sin\psi.$$

Then

$$I_1 = \frac{n}{2}\left\{1 + \frac{1}{\pi}\exp -(V^2-V_z^2) \int_0^{\infty} d\rho\,\rho \right. \\ \exp(-\rho^2)\,\text{erf}\left[\rho\sqrt{\left(\frac{r^2}{R^2}-1\right)}-V_z\right] \times \\ \left. \times \int_0^{2\pi} \exp\,[2\rho\sqrt{(V^2-V_z^2)}\cos(\phi-\psi)]d\phi\right\}$$
$$= \frac{n}{2}\left\{1+2\exp -(V^2-V_z^2) \int_0^{\infty} d\rho\,\rho\exp(-\rho^2) \right. \\ \left. \text{erf}\left[\rho\sqrt{\left(\frac{r^2}{R^2}-1\right)}-V_z\right] I_0\left[2\rho\sqrt{(V^2-V_z^2)}\right]\right\}$$

where $I_0[\ ]$ is the Bessel function of imaginary argument and zero order and

$$V_z = \mathbf{V}\cdot n = V\cos\theta_0$$
$$V^2-V_z^2 = V^2\sin^2\theta_0.$$

Hence

$$I_1 = \frac{n}{2}\left\{1+2\exp(-V^2\sin^2\theta_0)\int_0^\infty d\rho\,\rho\exp(-\rho^2)\right.$$
$$\left.\operatorname{erf}\left[\rho\sqrt{\left(\frac{r^2}{R^2}-1\right)}-V\cos\theta_0\right]I_0(2\rho V\sin\theta_0)\right\}$$

In the limiting case, $r=R$,

$$I_1 = \frac{n}{2}\left\{1+2\exp(-V^2\sin^2\theta_0)\operatorname{erf}(-V\cos\theta_0)\right.$$
$$\left.\int_0^\infty d\rho\,\rho\,\exp(-\rho^2)I_0(2\rho V\sin\theta_0)\right\}.$$

To carry out the integration, integrate once by parts to obtain

$$1 = \int_0^\infty \exp(-\rho^2)\rho I_0(2u\rho) = -\tfrac{1}{2}\exp(-\rho^2)\Big|_0^\infty$$
$$+ u\int_0^\infty \exp(-\rho^2)I_1(2u\rho)\,d\rho,$$

with $u=V\sin\theta_0$. The integral on the right is given in the Bateman Manuscript Project series[12] leading to the result

$$I = \frac{1}{2}+\frac{\sqrt{\pi}}{2}u\exp\left(\frac{u^2}{2}\right)I_{1/2}\left(\frac{u^2}{2}\right).$$

Since

$$I_{1/2}(z) = \sqrt{\left(\frac{2}{\pi z}\right)}\sinh z$$

one gets

$$I = \tfrac{1}{2}\exp(u^2),$$

and hence for $r=R$,

$$I_1 = \frac{n}{2}\left\{1+\operatorname{erf}(-V\cos\theta_0)\right\} = \frac{n}{2}\operatorname{erfc}(V\cos\theta_0).$$

This checks the direct integration of I_1 for r set equal to R in advance, since in this case $S=1$ only if $C_x\leqslant 0$.

When $r\to\infty$,

$$\operatorname{erf}\left(\rho\sqrt{\frac{r^2}{R^2}-1}-V_z\right)\to\operatorname{erf}(\infty)=1$$

and one obtains

$$I_1\to\frac{n}{2}\left\{1+1\right\}=n$$

as one should.

For the two cases of $\theta_0=0$ and $\theta_0=\pi$ the quantity I_1 can be evaluated exactly if spherical co-ordinates are used. If one uses r as axis

$$\mathbf{r}=r\,(0,\,0,\,1)$$

$$\mathbf{V}=V\,(\sin\theta_0\cos\phi_0,\,\sin\theta_0\sin\phi_0,\,\cos\theta_0)$$

$$\mathbf{C}=C\,(\sin\theta\cos\phi,\,\sin\theta\sin\phi,\,\cos\theta)$$

and

$$I_1 = \frac{n}{\pi^{3/2}}\int_0^\infty C^2dc\int_0^{2\pi}d\phi\int_0^{\theta_1}\sin\theta$$
$$\exp\{-(C^2+V^2)+2CV[\cos\theta\cos\theta_0+$$
$$+\sin\theta\sin\theta_0(\cos\phi-{}_0]\}\,d\theta.$$

By straightforward integration of this form of I_1 when $\theta_0=0$ one finds

$$I_1(0) = \frac{n}{2}\left\{\operatorname{erfc}V+\exp(-V^2\sin^2\theta_1)\right.$$
$$\left.\cos\theta_1\operatorname{erfc}[-V\cos\theta_1]\right\}$$
$$= \frac{n}{2}\left\{\operatorname{erfc}V+\sqrt{\left(1-\frac{R^2}{r^2}\right)}\right.$$
$$\left.\exp\left(-V^2\frac{R^2}{r^2}\right)\operatorname{erfc}\left[-V\sqrt{\left(1-\frac{R^2}{r^2}\right)}\right]\right\}.$$

A similar discussion for $\theta_0=\pi$ leads to the value

$$I_1(\pi) = \frac{n}{2}\left\{\operatorname{erfc}(-V)+\sqrt{\left(1-\frac{R^2}{r^2}\right)}\right.$$
$$\left.\exp\left(-V^2\frac{R^2}{r^2}\right)\operatorname{erfc}\left[V\sqrt{\left(1-\frac{R^2}{r^2}\right)}\right]\right\}.$$

For $r=R$ both of these reduce to our previously obtained approximation since the additional term is zero there. Likewise in the limit as $r\to\infty$ we obtain the free stream density as we should.

For either $\theta = 0$ or $\theta = \pi$ the above reduces to

$$\lim_{r\to\infty} I_1 = \frac{n}{2}\left[\operatorname{erfc}(V) + \operatorname{erfc}(-V)\right] = n$$

which is correct.

To evaluate the term containing the effect of the diffusely reflected particles, it is necessary to consider the integral

$$I_2 = \frac{n}{\pi^{3/2}} \int d^3C[\exp -(\mathbf{V}\cdot\hat{n}')^2 - \sqrt{\pi}(\mathbf{V}\cdot\hat{n}')\operatorname{erfc}(\mathbf{V}\cdot\hat{n}')](1-S)\exp(-C^2).$$

Introducing r as the polar axis again so that

$$\hat{n}' = \{(-\cos\theta)\, r/R + r/R \sqrt{[\cos^2\theta - (1-R^2/r^2)]}\}\sin\theta\cos\phi,$$

$$\{(-\cos\theta)\, r/R + r/R \sqrt{[\cos^2\theta - (1-R^2/r^2)]}\}\sin\theta\sin\phi,$$

$$(r/R)\{(-r\cos\theta)/R + r/R \sqrt{[\cos^2\theta - (1-R^2/r^2)]}\}\cos\theta$$

leads to

$$V\cdot\hat{n}' = \frac{Vr}{R}\{\cos\theta_0 - [\cos\theta - \sqrt{\cos^2\theta - (1-R^2/r^2)}]\,[\cos\theta\cos\theta_0 + \sin\theta\sin\theta_0\cos(\phi-\phi_0)]\}$$

so that I_2 is quite intractable without approximation. However, as mentioned earlier $(1-S)=1$ if and only if

$$0 \leqslant \theta \leqslant \theta_1 = \arccos\left(1-\frac{R^2}{r^2}\right)^{1/2}$$

and in this range

$$\cos\theta - \sqrt{\left[\cos^2\theta - \left(1-\frac{R^2}{r^2}\right)\right]}$$

is a very slowly varying function which has extremes at $\theta = 0$ and $\theta = \theta_1$, with values $(1-R/r)$ and $\sqrt{(1-R^2/r^2)}$, respectively. We will therefore replace the complicated expression for $(\mathbf{V}.\hat{n}')$ in $\exp -(\mathbf{V}.\hat{n}')$ and $\operatorname{erfc}(\mathbf{V}.\hat{n}')$ by its first term

$$V\cdot\hat{n}' \cong Vr\,\frac{\cos\theta_0}{R}.$$

The integral I_2 is therefore evaluated as

$$I_2 \cong I_2^A = \frac{n}{\pi^{3/2}}\int_0^\infty \exp(-C^2)C^2 dC \int_0^{2\pi} d\phi \int_{\theta=0}^{\theta_1} \sin\theta\, d\theta \left[\exp\left(-\frac{V^2r^2}{R^2}\cos^2\theta_0 - \sqrt{\pi}(\mathbf{V}\cdot\hat{n}')\operatorname{erfc}\left(\frac{Vr\cos\theta_0}{R}\right)\right)\right]$$

where the full expression for $(\mathbf{V}\cdot\hat{n}')$ is used where it appears explicitly. Straightforward integration then yields the following expression for I_2^A

$$I_2^A = \frac{n}{2}[-\cos\theta]_0^{\theta_1}\exp\left(-\frac{V^2r^2}{R^2}\cos^2\theta_0\right) - \frac{n}{4\pi}\int_0^{2\pi}\sqrt{\pi}\operatorname{erfc}\left(\frac{Vr}{R}\cos\theta_0\right)\int_0^{\theta_1}(\mathbf{V}\cdot\hat{n}')\sin\theta\, d\theta\, d\phi$$

$$= \frac{n}{2}\left[1-\sqrt{\left(1-\frac{R^2}{r^2}\right)}\right]\exp\left(-\frac{V^2r^2}{R^2}\cos^2\theta_0\right) - \frac{n}{2}\sqrt{\pi}\operatorname{erfc}\left(\frac{Vr}{R}\cos\theta_0\right)I_3$$

where

$$I_3 = \int_0^{2\pi}\int_0^{\theta_1}(\mathbf{V}\cdot\hat{n}')\sin\theta\, d\theta\, d\phi$$

$$= 2\pi\int_0^{\theta_1}\frac{Vr}{R}\left\{\cos\theta_0 - \left[\cos\theta - \sqrt{\cos^2\theta - \left(1-\frac{R^2}{r^2}\right)}\right]\cos\theta\cos\theta_0\right\}\sin\theta\, d\theta$$

$$= 2\pi\frac{Vr}{R}\cos\theta_0\left\{1 - \sqrt{\left(1-\frac{R^2}{r^2}\right)} + \frac{1}{3}\frac{R^3}{r^3} - \frac{1}{3}\left[1-\left(1-\frac{R^2}{r^2}\right)^{3/2}\right]\right\}.$$

The approximation of I_2 by I_2^A is poorest in intermediate ranges of r and hence it is of interest to have an upper bound in this region. The difference between I_2^A and I_2 is bounded above by

$$\left\{\exp\left[-\left(\frac{Vr}{R}\right)^2\left(\cos\theta_0 + \sqrt{1-\frac{R^2}{r^2}}\right)^2\right]\right.$$

$$-\exp\left[-\left(\frac{Vr}{R}\right)^2 \cos^2\theta_0\right]\Bigg\}\cdot\left(1-\sqrt{1-\frac{R^2}{r^2}}\right)+$$

$$+\sqrt{\pi}\left(\frac{Vr}{R}\right)^2\sqrt{1-\frac{R^2}{r^2}}\cos\theta_0$$

$$\exp\left[-\left(\frac{Vr}{R}\right)^2\left(\cos\theta_0+\sqrt{1-\frac{R^2}{r^2}}\right)^2\right]\times$$

$$\times\left\{1-\sqrt{1-\frac{R^2}{r^2}}+\frac{1}{3}\frac{R^3}{r^3}-\right.$$

$$\left.-\frac{1}{3}\left[1-\left(1-\frac{R^2}{r^2}\right)^{3/2}\right]\right\},$$

for all r and θ_0 such that $\sqrt{[1-(R^2/r^2)]} < 2|\cos\theta_0|$. The plus sign is to be used for $\cos\theta_0 < 0$ and the minus sign for $\cos\theta_0 > 0$.

3. NUMERICAL RESULTS FOR ELECTRON DENSITY DISTRIBUTION AND RADAR CROSS-SECTIONS

The formulas of Part 2 were applied to a typical[7] case of interest for which V = 5. This corresponds, for example, to a satellite altitude of 500 km and speed $V' = 8$ km/sec. Curves of constant relative density N/n are presented in Figs. 4 and 5. They clearly show the build-up of density ahead of the sphere and the "hole" developed in the rear. The ion deficiency in the rear extends to about 50 sphere radii.

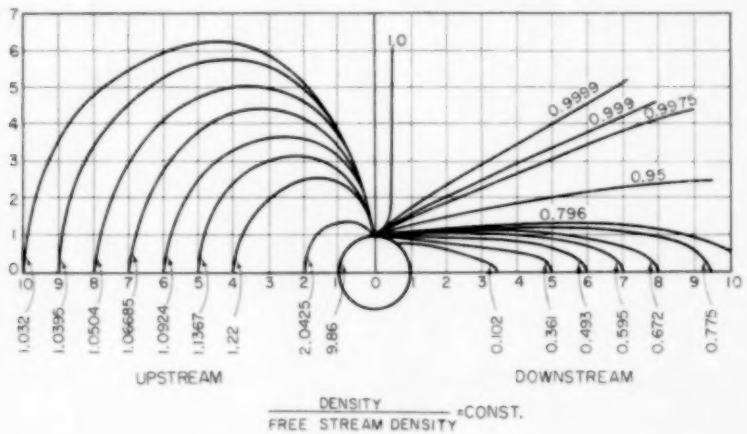

Fig. 4. Equi-density contours.

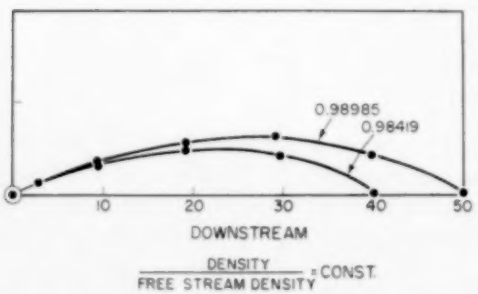

Fig. 5. Downstream equi-density contours.

More detailed data for N on the sphere and along the positive z axis (behind the sphere) is given in Table 1.

Radar cross-sections (4π times differential cross-sections) were computed from the formula

$$\sigma = 4\pi\sigma_e n^2\left|\int_V\left(\frac{N}{n}-1\right)e^{2ikr}dv\right|^2$$

according to the development in Part 1. For electrons $4\pi\sigma_e \sim 10^{-28}\ m^2$. A value of $n = 10^{12}$ electrons/m^3 is used for the electron density at

500 km altitude and the resulting values of σ as well as

$$\int \left(\frac{N}{n} - 1\right) e^{2ikr} dv$$

are given in Table 2 for various regions V. It was assumed that $k = (2\pi/\lambda) = 1\ \mathrm{m}^{-1}$, that the sphere radius is 1 m, and that the sphere was viewed broadside, i.e. $\Theta = 90°$.

Table 1. Density ratio = Density/Free Stream Density $= \frac{N}{n}$

On sphere ($r = R$)		Behind sphere (at 0°)	
θ	N/n	z	N/n
0°	$9{\cdot}0 \times 10^{-13}$	1	$9{\cdot}0 \times 10^{-13}$
5°	$1{\cdot}0923 \times 10^{-12}$	2	$1{\cdot}6718 \times 10^{-3}$
10°	$1{\cdot}9443 \times 10^{-12}$	3	$5{\cdot}8621 \times 10^{-2}$
15°	$4{\cdot}9876 \times 10^{-12}$	4	$2{\cdot}0296 \times 10^{-1}$
20°	$1{\cdot}7947 \times 10^{-11}$	5	$3{\cdot}6045 \times 10^{-1}$
25°	$8{\cdot}7137 \times 10^{-11}$	6	$4{\cdot}9237 \times 10^{-1}$
30°	$5{\cdot}4587 \times 10^{-10}$	7	$5{\cdot}9422 \times 10^{-1}$
35°	$4{\cdot}1834 \times 10^{-9}$	8	$6{\cdot}7133 \times 10^{-1}$
40°	$3{\cdot}6932 \times 10^{-8}$	8·5	$7{\cdot}0258 \times 10^{-1}$
45°	$3{\cdot}5343 \times 10^{-7}$	9	$7{\cdot}2990 \times 10^{-1}$
50°	$3{\cdot}4398 \times 10^{-6}$	9·5	$7{\cdot}5384 \times 10^{-1}$
55°	$3{\cdot}1943 \times 10^{-5}$	10	$7{\cdot}7490 \times 10^{-1}$
60°	$2{\cdot}6707 \times 10^{-4}$	20	$9{\cdot}3824 \times 10^{-1}$
65°	$1{\cdot}9583 \times 10^{-3}$	30	$9{\cdot}7206 \times 10^{-1}$
70°	$1{\cdot}1018 \times 10^{-2}$	40	$9{\cdot}8419 \times 10^{-1}$
75°	$5{\cdot}0194 \times 10^{-2}$	50	$9{\cdot}8985 \times 10^{-1}$
80°	$1{\cdot}7613 \times 10^{-1}$		
85°	$4{\cdot}7471 \times 10^{-1}$		
86°	$5{\cdot}6145 \times 10^{-1}$		
87°	$6{\cdot}5761 \times 10^{-1}$		
88°	$7{\cdot}6306 \times 10^{-1}$		
89°	$8{\cdot}7739 \times 10^{-1}$		
90°	1·0		

Table 2

Region (V)	$\frac{1}{R^3}\int_V (\frac{N}{n} - 1)e^{2ikr} dv$	$\sigma(\mathrm{cm}^2)$
$z > 0$ (behind)	−1·1	1·3
$z < 0$ (ahead)	0·64	0·41
$-\infty < z < \infty$ entire cloud	−·48	0·23
$-\infty < z < \infty$ entire cloud, with power contribution from $z < 0$ and $z < 0$ added (i.e. the average result for random relative phase)	—	1·7

The first two σ values above are of interest if the radar beam is respectively lagging or leading the satellite while the 1·7 cm² result would be most appropriate, for example, if many radar pulses are being received and added with a radar which is tracking inaccurately, "hunting" around the target.

It is of interest to compare these results with a comparable cross-section estimate obtained by Davis[13] in a much cruder but far simpler fashion. Davis neglected the density build-up ahead of the sphere and assumed the electrons were completely swept out of a cylindrical column one sphere diameter wide. On this assumption his computations led to a length estimate of 10 sphere diameters behind the sphere. The radar return from such a cavity is that of a column of electrons embedded in a vacuum and of electron number density given by the unperturbed number density. This number of electrons per unit volume was then referred to an equivalent line density and the problem replaced by that of coherent scattering by a line source for which the cross-section is proportional to line density times λ^4. To scale Davis's numerical result of $\sigma = 0{\cdot}1$ cm² for a 0·25 m radius sphere in a medium of $n = 10^{12}/\mathrm{m}^2$ to the present 1 m radius sphere problem his equivalent line density (2×10^9/cm) is scaled by $(100/25)^2 = 16$ and the fact that σ is proportional to line density squared leads to a scale factor of 256. On the other hand the present computations were made for $\lambda = 2\pi$ m while Davis apparently used 15 m. Hence an additional wavelength scaling factor of $(2\pi/15)^4$ is needed or a net scale factor of ~ 8. The cross-section value to compare with ours is thus

$$\sigma_D \sim 0{\cdot}8\ \mathrm{cm}^2.$$

An instructive insight into the behaviour of the perturbation at various distances ahead or behind the sphere is furnished by a plot of the contribution to the volume integral of the various axial stations; i.e. a plot of

$$S(z) = \int_0^\infty \rho\, d\rho \left(\frac{N}{n} - 1\right) J_0[2k\rho \sin\theta]$$

vs. z. This is furnished in Fig. 6. The somewhat odd transition in $S(z)$ as z crosses the origin reflects the fact that N within the sphere is zero. To complete the volume integration this function is to be multiplied by $\exp\left[2ik\left(\frac{z^2}{2R} - z\cos\theta\right)\right]$ and integrated. It is clear that as Θ and hence θ deviate from 90° or as k increases the rate of oscillation of the exponential will increase and the net contributions from both regions $z > 0$ and $z < 0$, will rapidly decrease

Acknowledgements—The authors would like to thank Professor K. M. Siegel for suggesting the physical bases which enabled the use of the postulate of a neutral gas to be used for determining the ion and electron distributions. The authors would also like to acknowledge helpful discussions with Professor G. E. Uhlenbeck and Professor P. C. Clemmow. Finally, the authors wish to acknowledge the help of Larry B. Evans in coding the formulas for computation and to express their appreciation to The University of Michigan Computing Centre, directed by Professor R. C. F. Bartels, for the computing time necessary to complete this work.

REFERENCES

1. H. Brysk, *J. Geophys. Res.* **63,** 693 (1958).
2. L. Kraus and K. M. Watson, *Phys. of Fluids* **1,** 40 (1958).
3. P. Greifinger, *RAND Rep.* R339 No. 19 (June 1959).
4. R. Pappert, *Convair Rep.* ZPH-026 (Dec. 1958).
5. D. Pines and R. Bohm, *Phys. Rev.* **85,** 338 (1952).
6. C. S. Wang Chang, *Univ. Michigan Eng. Res. Inst. Rep.* CM-654 (Dec. 1950).
7. L. Spitzer, Jr., *Physics of Fully Ionized Gases.* Interscience, New York (1956).
8. C. L. Dolph and R. K. Osborn, *Univ. Michigan Radiation Lab. Memo* No. 2764-547-M (1959).
9. I. B. Bernstein and I. N. Rabinowitz, *Physics of Fluids* **2,** 112 (1959).
10. U. R. Stalder and V. J. Zurick, NACA TN 2423 (July 1951).
11. F. C. Hurlbut, *RAND Rep.* R339 No. 21 (June 1959).
12. A. Erdelyi editor, *Higher Transcendental Functions,* Vol. 2, Eq. 27, p. 92. McGraw-Hill, New York (1953).
13. A. Davis, *Proceedings of the Conference on Interaction of Satellites with the Ionosphere,* pp. 33.34, U.S. Naval Research Lab., Washington, D.C. (March 1958).

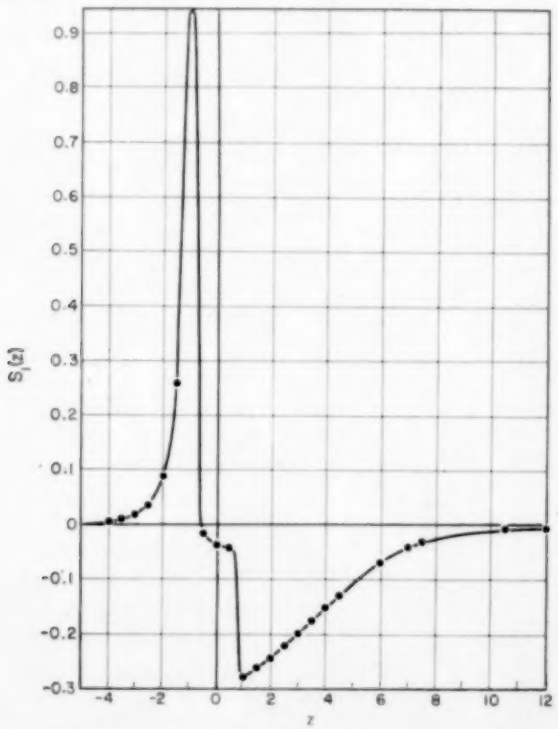

Fig. 6. Contribution to cross-section of the axial locations.

ECHO AREA OF A PLASMA-COATED SPHERE

L. PETERS, Jr. and R. B. GREEN
Antenna Laboratory, Department of Electrical Engineering
The Ohio State University, Columbus, Ohio

Abstract—The general problem of scattering characteristics of configurations involving plasmas is considered. Effects of transmission, reflection and focusing are considered. Means of modelling plasma sheaths which are valid for both echo area and transmission characteristics are also presented. Some problems with relatively simple geometry are considered in greater detail. These include the plasma sphere, metallic sphere coated with a plasma, and other simple shapes.

The plasma-coated metallic sphere is considered in greatest detail. Besides the exact solutions for echo area of this configuration, approximate expressions are also given along with numerical data and curves obtained from these approximate solutions. Means of extending these results to missile shapes other than the sphere and to more general ion distributions is indicated.

INTRODUCTION

In this paper, several approximate methods for determining the echo area of various bodies immersed in plasma are considered. These approximate methods are based on simple physical concepts. The first of these concepts is the focusing (or defocusing) of energy on the body as caused by the plasma. The second of these concepts consists of considering the scattering that occurs at the air-plasma interface. The third concept involves the effect of plasma on the echo area of long thin bodies.

Mie, in 1908, presented a method for obtaining an exact solution for the electromagnetic scattering of bodies of spherical shape.[1, 2] This problem has been applied by Aden and Kerker[3] to the problem of the back scattering (or echo area) from concentric spheres. Scharfman[4] has made use of these methods to obtain the echo area of dielectric coated spheres. Scharfman interpreted his results by representing the coated sphere as an end-loaded dipole. Such an interpretation would fail to explain the decrease in echo area that is obtained in certain cases for a relative dielectric constant less than unity.

Since the echo area of spherical shapes is in general amenable to an exact solution, the first two concepts may be demonstrated by considering a perfectly conducting sphere encased in an isotropic, homogeneous, lossless spherical shell. Calculated results obtained from the exact theory of Aden and Kerker are to be compared with approximate results to verify the validity of the first two concepts. These approximations as verified by the spherical shapes should be readily applicable to arbitrary objects.

The solutions of echo area problems using the third concept for the case of long thin bodies are in general based on approximate techniques.[5] For the cases that have been considered previously, the validity of these approximate techniques have been demonstrated by means of experiment. The conclusions drawn by considering these bodies immersed in a plasma shell have also been demonstrated by means of experiment. However, for practical reasons the plasma shell has been constructed of a material whose relative dielectric constant is greater than one. The experimental echo area of such a target is in good agreement with the theoretical echo area, thus indicating the validity of the theory.

MODEL OF PLASMA-COATED SPHERE

The general problem is that of the back

scattering or echo area of radar targets when they are influenced by a plasma sheath. The particular problem that has been considered in some detail is the effect of a lossless spherical dielectric sheath relative (dielectric constant $\varepsilon_r < 1$) on the echo area of the sphere. This model is shown in Fig. 1. This problem is

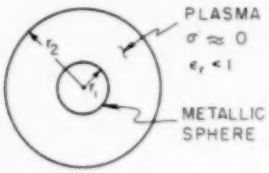

Fig. 1. Model of plasma-coated sphere.

chosen for study because the exact solution has been obtained by Aden and Kerker and it was hoped that by studying the results of this case, approximate techniques could be evolved that would apply to the case of the arbitrary radar target. Comparison of the results obtained using the approximate techniques could then be compared to the results obtained from the exact theory to check the accuracy of the approximations. The lossless dielectric medium is chosen because it avoids the necessity of considering spherical functions of complex arguments. Modern computor techniques should make a solution possible in such cases but this would introduce unnecessary expense and complication. Results given in this paper are all obtained using a desk calculator. Furthermore, the ionic medium is adequately represented by a lossless dielectric medium for certain frequency ranges and ion densities.[6] Most of the exact echo areas of this configuration are restricted to the region of Rayleigh scattering and in the vicinity of the first resonant peak. This restriction is imposed first to keep computations as simple as possible and second because poorest agreement with optical methods should be expected in this region.

APPROXIMATE METHODS

Approximate methods for obtaining the echo area of the dielectric coated sphere make use of the following concepts:

(a) direct reflections from the air-dielectric interface,

(b) defocusing.

The echo area due to direct reflections from the interface for the case of the sphere may of course be calculated exactly but this would mean that a new and rather cumbersome calculation would be needed if any parameter is changed. An approximate solution that is simple to apply consists of multiplying the echo area of a metallic body of the same shape and size by the square of the Fresnel reflection coefficient. In this case normal incidence is assumed. The echo area for the dielectric sphere has the form

$$\sigma = \sigma_m \left[\frac{1-\sqrt{\varepsilon_r}}{1+\sqrt{\varepsilon_r}}\right]^2 = K\sigma_m \qquad (1)$$

where ε_r is the relative dielectric constant of the sphere and σ_m is the echo of a metal sphere of the same radius.

This approximation is compared to the exact solution of the echo area of a dielectric sphere in Fig. 2 for $\varepsilon_r = 0{\cdot}75$. Note that poor agreement is

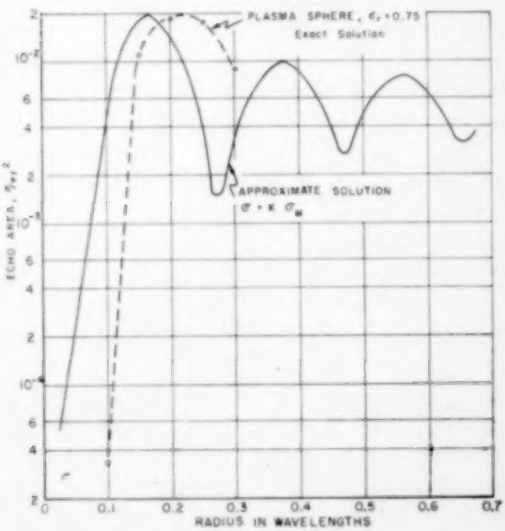

Fig. 2. Echo area of homogeneous dielectric sphere $\epsilon_r = 0{\cdot}75$.

obtained in the region of Rayleigh scattering but the approximation becomes reasonable in the vicinity of the first resonant peak. Periodicity is in error but certainly order of magnitude results are obtained.

Use of this approximation is indicated by considering a metallic sphere of radius r_1 equal to $0{\cdot}05\lambda$ in a dielectric sheath with a radius r_2. The solid curve of Fig. 3 is obtained by applying

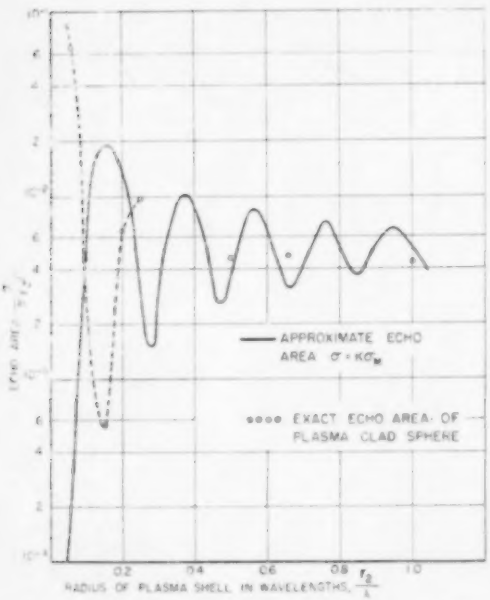

Fig. 3. Echo area of metallic sphere of radius $0{\cdot}05\lambda$ in dielectric shell $\epsilon_r = 0{\cdot}75$.

the approximation of equation (1) and the exact points are obtained from the theory of Aden and Kerker. Poor agreement exists between the exact theory and the approximation when the body is small in terms of wavelength where reflections from the metallic sphere must also be considered. However, the agreement is surprisingly good as the radius of the dielectric sphere becomes greater than $0{\cdot}45\lambda$ and the reflections from the air-dielectric interface are now dominant.

The approximation should also be valid for the general case of the convex surface whose radii of curvature are sufficiently large.

Defocusing occurs for the case of the spherical shell when the relative dielectric constant is less than unity. This concept may be readily demonstrated by use of optics when the dielectric constant is greater than one. In this case focusing occurs. Fig. 4 is a photograph of two $\frac{1}{8}$ in. diameter rods one of which is contained in a polystyrene sheath. The focusing action causes a magnification of the rod.

The concept as applied to the spherical shell is illustrated by Fig. 5. The rays shown are those

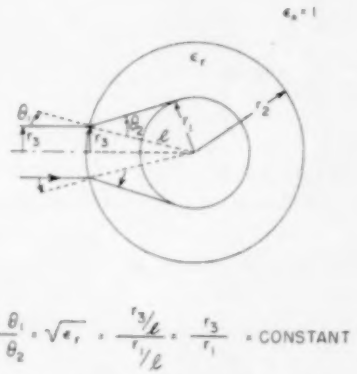

Fig. 5. Derivation of apparent radius.

that would be tangent to the metallic sphere as predicted by Snell's law, i.e.

$$\frac{\sin\theta_1}{\sin\theta_2} = \sqrt{(\varepsilon_r)}.$$

Furthermore the apparent radius of the sphere (r_3) is independent of the radius of the plasma as may be shown by applying Snell's law as follows

$$\frac{\sin\theta_1}{\sin\theta_2} = \frac{r_3/l}{r_1/l} = \frac{r_3}{r_1} = \sqrt{\varepsilon_r)} = \text{constant}.$$

The approximation therefore consists of taking the echo area of this configuration as the echo area of a metallic sphere of radius r_3, the

apparent radius of the sphere in free space. This approximate solution is compared in Fig. 6 with the exact solution as a function of r_2, the radius of the plasma shell when the metallic sphere has a radius of 0·15λ. Note that the exact solution

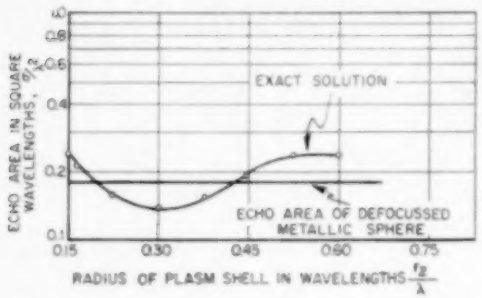
EXACT SOLUTION
ECHO AREA OF DEFOCUSSED METALLIC SPHERE
ECHO AREA IN SQUARE WAVELENGTHS, $\frac{\sigma}{\pi r_2^2}$
RADIUS OF PLASM SHELL IN WAVELENGTHS $\frac{r_2}{\lambda}$

Fig. 6. Echo area of metallic sphere of radius 0·15λ in dielectric shell $\epsilon_r = 0{\cdot}75$ vs. shell radius r_2.

tends to oscillate about the approximate solution when the radius of the plasma shell is varied. Similar results obtained for the case when the metallic sphere has a radius of 0·05λ are given in Fig. 7. The results of a combined approximation obtained by adding corresponding Mie coefficients

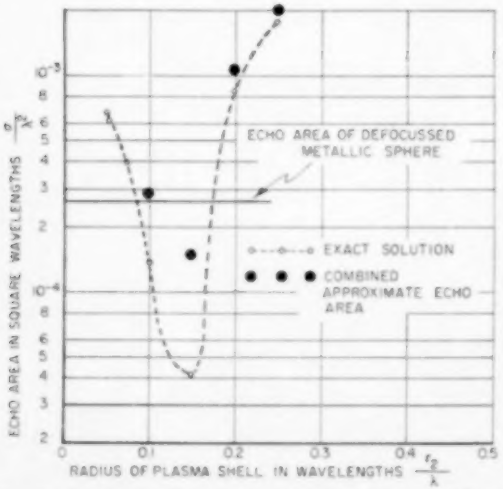
ECHO AREA OF DEFOCUSSED METALLIC SPHERE
EXACT SOLUTION
COMBINED APPROXIMATE ECHO AREA
ECHO AREA IN SQUARE WAVELENGTHS $\frac{\sigma}{\pi r_2^2}$
RADIUS OF PLASMA SHELL IN WAVELENGTHS $\frac{r_2}{\lambda}$

Fig. 7. Echo area of metallic sphere of radius 0·05λ in dielectric shell $\epsilon_r = 0{\cdot}75$ vs. shell radius r_2.

of a plasma sphere of radius r_2 to those of a metal sphere of radius r_1 are also shown.

To further demonstrate the validity of the defocusing concept the exact echo area of the metallic sphere in a plasma medium with $\varepsilon_r = 0{\cdot}75$ and the ratio (plasma sphere radius)/(metallic sphere radius) equal to two is compared in Fig. 8 to the echo area of the apparent metallic

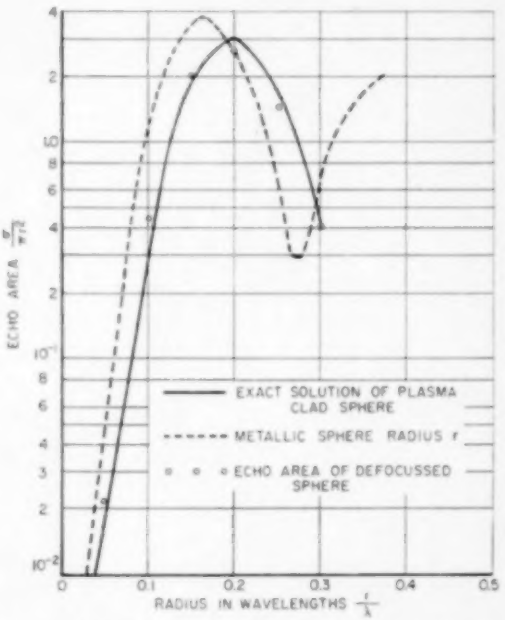
EXACT SOLUTION OF PLASMA CLAD SPHERE
METALLIC SPHERE RADIUS r
ECHO AREA OF DEFOCUSSED SPHERE
ECHO AREA $\frac{\sigma}{\pi r^2}$
RADIUS IN WAVELENGTHS $\frac{r}{\lambda}$

Fig. 8. Echo area of metallic sphere of radius r enclosed in dielectric shell ($\epsilon_r = 0{\cdot}75$) of radius $2r$.

sphere obtained using the defocusing concept. The echo area of the metallic sphere in free space is also shown. The approximate result (obtained from defocusing) again gives good agreement with the exact result. It is certainly a better approximation than would be the echo area of the metallic sphere in free space.

EXTENSION OF APPROXIMATE METHODS

There is, of course, nothing about the sphere of supreme interest to those interested in radar echo area of targets except that an exact solution

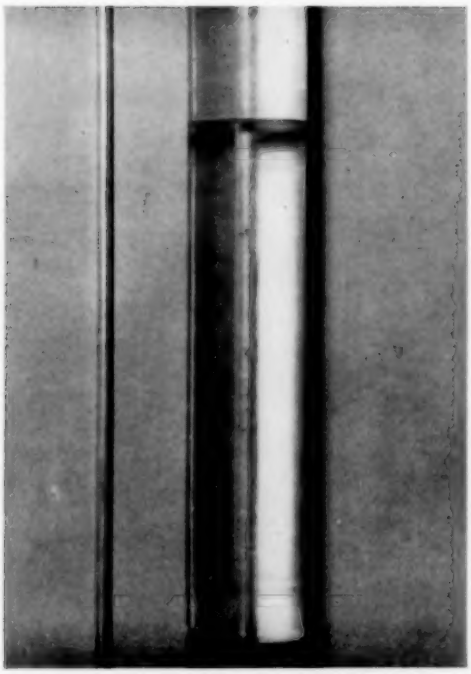

Fig. 4. Illustration of focusing concept.

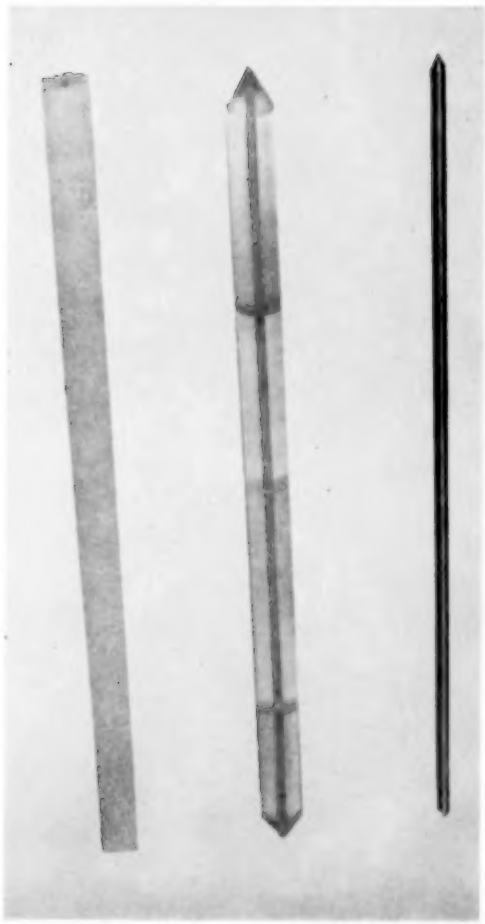

Fig. 13. Long thin bodies for which $p < 1$.

can be obtained. The shape of the plasma, the body of interest, and indeed the characteristics of the ionic plasma will in general be different from those considered in this paper. No exact solution will exist for the echo area of these bodies.

However the approximate methods suggested should be readily adapted to other configurations. The effect of the plasma shape can be readily determined using optical methods. Indeed optical methods can be applied to the plasma diffraction when its dielectric properties vary with distance from the target. The Luneberg lens is an example that is treated in this manner.

Targets other than the sphere could be treated in much the same manner as above. The echo area of the target plasma could be estimated by considering the defocusing effect or the effect of the air plasma interface depending upon which is dominant or by combining the two approximations.

Also other problems such as the lossy plasma could be treated by using the attenuation factor for the medium and estimating the path length in that medium to obtain an estimate of the power lost in the medium.

EFFECT OF PLASMA ON THE ECHO AREA OF LONG THIN BODIES

The echo area of a class of targets for which the dominant mode is a travelling wave along the surface of the target has been calculated[5] by assuming the target to be a thin linear travelling wave antenna. In this section, the effect of a plasma sheath will be estimated by assuming that the major physical effect of this sheath is to alter the relative phase velocity of a wave travelling along the surface of the target.

In order to calculate the echo area of such a body, it is first assumed to be a receiving antenna which couples energy from the field to a fictitious antenna terminal pair as shown in Fig. 9. A portion of this energy is then reflected by any mismatch existing at the terminals and this

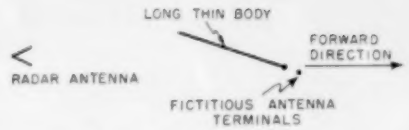

Fig. 9. Position of antenna terminals on long thin body.

reflected energy is then re-radiated by the body now acting as a transmitting antenna. The echo area of such a body has been shown to be

$$\sigma = \gamma^2 \frac{G^2(\theta, \phi)}{4\pi} \lambda^2 \tag{2}$$

where γ is the voltage reflection coefficient at the terminals; $G(\theta, \phi)$ is the gain of the antenna; λ is the wavelength; and θ, ϕ are the usual polar co-ordinates. It has been assumed that the equivalent antenna is lossless and hence the gain is equal to the directivity. The directivity of such an antenna has been computed using the well-known equation for its magnetic field

$$H\phi = K \frac{\sin \theta}{1 - p \cos \theta} \sin \frac{\beta L}{2} (1 - p \cos \theta) \tag{3}$$

where $p = v/c$ is the relative phase velocity along the surface of the antenna; $\beta = 2\pi/\lambda$ is the propagation factor; L is the length of the antenna, and θ is the polar angle.

The reflection coefficient γ is determined experimentally by comparing the measured echo area with shorted terminals to the echo area of the target with the short removed.

The echo area of a rod 39λ long for which $p = 1$ has been measured and compared[5] with theory. Good agreement exists. Also an ogive has been treated by considering the relative phase velocity to be the average value of the phase velocity in the direction of the axis when a wave is travelling along the surface with a relative phase velocity of unity. Again good agreement with the theory has been obtained.

Now let us consider the model shown in Fig. 10 of such a target surrounded by a plasma sheath. It is to be assumed that the only effect

Fig. 10. Metallic rod in dielectric shell.

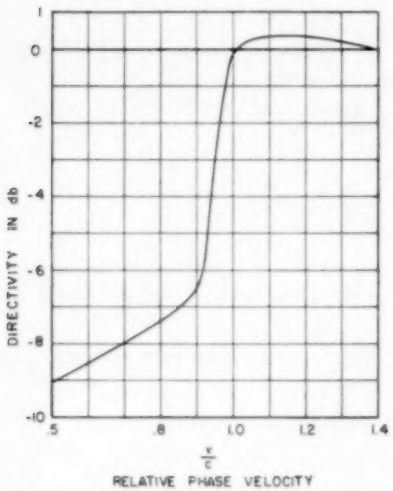

Fig. 11. Directivity of long wire antenna; L(free space) = $13{\cdot}3\lambda$.

of the plasma sheath is to alter the value of the relative phase velocity $p=v/c$. In this case p becomes greater than one as the dielectric constant in the ionized medium becomes less than unity. The effect of altering p is shown in Fig. 11 where the directivity of a long thin antenna $13{\cdot}3\lambda$ long has been plotted as a function of p. Again if the body is assumed to be lossless its echo area may be obtained from this curve as described above.

Next the echo area of a body with a free space length of 39λ is compared in Fig. 12 for values of $p=1{\cdot}0$ and $1{\cdot}5$. This corresponds to a lossless sheath with a relative dielectric constant equal to $1{\cdot}0$ and $0{\cdot}445$, respectively, the latter case being the ionized sheath. Note that while the magnitude of the echo area is altered only slightly by the ionized sheath, the angle at which the maximum occurs has shifted from 8° to 48°. If this long thin body represented a missile approaching a target, the likelihood of radar detection at the target site would be greatly reduced. The position of the echo area maximum is readily obtained by obtaining the limit of

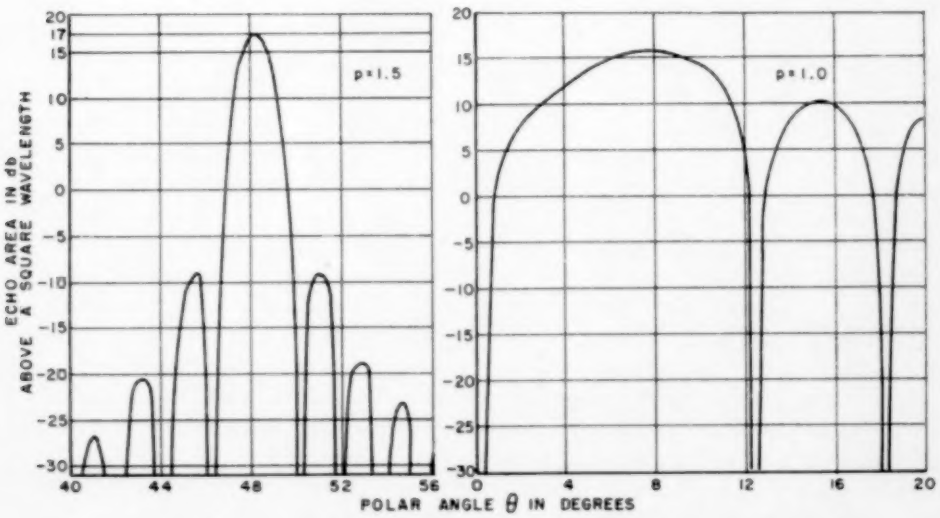

Fig. 12. Echo area of rod in dielectric shell.

equation (2) as the denominator approaches zero. This limit occurs for

$$\theta_M = \cos^{-1}\frac{1}{p} = \cos^{-1}\frac{c}{v},$$

an equation which is well known in the theory of travelling wave slot antennas,[7] which show that θ_M is dependent only on the properties of the plasma.

Many difficulties would be encountered if one were to attempt experimentally to verify the preceding results for $p > 1$. However, the effect of changing p may be verified readily for $p < 1$. One such case has already been mentioned, i.e. the ogive for which the relative phase velocity has been taken as the average of the relative phase velocity in the direction of the axis when a wave is travelling along the surface with a phase velocity of unity. As has been indicated, good agreement between theory and experiment exist in this case.

A second possibility is that of encasing the rod in a dielectric sheath. Fig. 13 shows a rod encased in a styrofoam and polystyrene sheath. The endfire echo area of these devices was measured using the K band pulse radar facility at Ohio State University. The echo area for the rod in the styrofoam sheath is shown in Fig. 14.

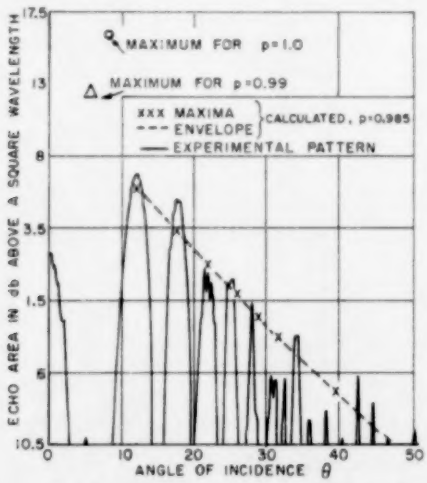

Fig. 14. Echo area of styrofoam clad rod.

The calculated maxima are obtained by assuming γ to be unchanged and that the relative phase velocity p corresponds to that of a wave travelling in styrofoam or

$$p = \frac{v}{c} = \frac{1}{\sqrt{(\varepsilon_r)}} = 0{\cdot}985$$

where ε_r is the relative dielectric constant.

Again good agreement with the theory is noted. The maximum echo areas obtained for $p = 1{\cdot}0$ and $0{\cdot}99$ are also shown. The changes in these maxima demonstrate the sensitivity of the echo area with respect to the relative phase velocity which is being changed only by a small amount.

Note that the experimental echo area corresponding to $p = 0{\cdot}985$ has a significant lobe at $\theta = 0$ where none has existed before. This is due to higher order modes being set up in the dielectric media. These modes correspond to those that exist in dielectric antennas. Their effect is much more pronounced in the case of the rod encased in the polystyrene sheath. In this case there is no conclusive evidence of the principal wave mode as the echo area due to this mode is only 10·5 dB less than a square wavelength (assuming the reflection coefficient to be unchanged) and is no longer a dominant mode.

A third possible way of altering the phase velocity of the wave is to "corrugate" the surface of the rod. Querido[8] has shown that for the case of a post structure over a ground plane that a relative phase velocity of about 0·9 could be obtained by using a post height of $0{\cdot}11\lambda$. An attempt to approximate this case at K_a-band was made by using a section of commercially available threaded stock ($\frac{3}{8}$–16). This threaded rod is shown in Fig. 13 where the ends have been tapered to avoid specular reflections from the end. The echo area of this device obtained using the K_a-band pulsed radar system is shown in Fig. 15. The calculated results are obtained by setting the reflection coefficient $\gamma = 0{\cdot}56$ which is chosen to give best agreement with the measured

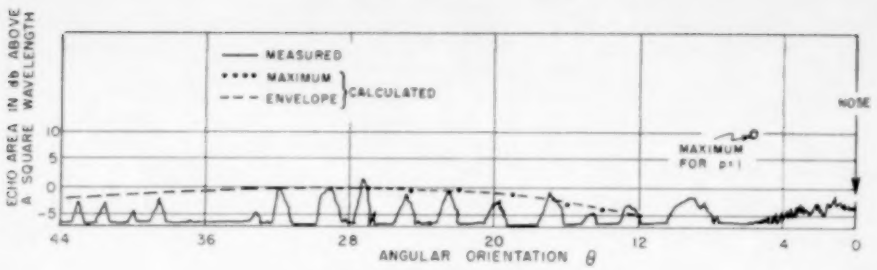

Fig. 15. Echo area of threaded rod.

curve. In spite of this apparently good agreement, these results must be viewed with suspicion, however, because first they represent an extremely small echo area to be measured on this particular system and second because of the gross approximations made in the theory. However, the measured maximum echo area of a $\frac{1}{8}$ in. diameter rod of the same length is shown and there is certainly no evidence of this mode in the present results. It is therefore concluded that the phase velocity has been altered significantly and that this can be considered to be a model of a long thin body with a relative phase velocity less than unity.

The agreement between theory and experiment demonstrates the validity of the method suggested for relative phase velocity less than unity.

Travelling wave slot antennas[9] which have a TE_{01} mode have been constructed for values of $p > 1$ and have similar properties to those discussed for the rod with $p > 1$. In so far as both these slot antennas and the plasma coated rod may both be represented approximately by a line source, Babinet's principle may be applied to show that these two cases should give approximately the same result with E- and H-fields everywhere exchanged. Thus the theory should also predict accurately the behaviour of plasma-coated structures when the relative phase velocity is greater than unity.

CONCLUSIONS

Some approximate methods of calculating the echo area of the plasma-clad sphere have been suggested. The validity of these methods has been demonstrated in the region of Rayleigh scattering and the first resonant peak for one particular plasma. Additional calculations should be made to determine any effects introduced by changing either the plasma or the size of the bodies.

The greatest value of the approximate methods suggested is that they can be applied to shapes other than the sphere. These methods offer promise of a practical technique of determining the echo area of the arbitrary body when immersed in any type of plasma. Additional research to determine the usefulness of such applications is needed.

The effect of plasma on the echo area of long thin bodies has been estimated and verified by experiment. The most significant change in this case is that the aspect θ_M at which the maximum echo area appears is determined solely by the properties of the plasma, i.e.

$$\theta_M = \cos^{-1}\frac{c}{v}$$

In general it appears that this angle is increased significantly by the presence of plasma.

Acknowledgements—Acknowledgement is due to Professor T. E. Tice and Mr. R. K. Long who first called the authors' attention to this problem. Their continued interest and many suggestions have offered great stimulation. The authors also wish to acknowledge the continued interest and suggestions of Professors T. G. Hame, C. H. Walter, J. H. Richmond and Mr. E. K. Damon. Measurements were made by Mr. J. R. Gillard.

The work described in this paper was sponsored in part by Air Research and Development Command, Wright Air Development Centre, Wright-Patterson Air Force Base, Ohio, under Contract AF 33(616)-5341.

REFERENCES

1. G. Mie, *Ann. Phys., Lpz.* **25,** 377, 1908.
2. J. Stratton, *Electromagnetic Theory*, pp. 563–573. McGraw-Hill, New York (1941).
3. A. L. Aden and M. Kerker, *J. Appl. Phys.* **22,** 1242 (1951).
4. H. Scharfman, *J. Appl. Phys.* **23,** 1352 (1954).
5. L. Peters, Jr., *Trans. Inst. Radio Engrs. on Antennas* **6,** 133 (1958).
6. E. C. Jordan, *Electromagnetic Waves and Radiating Systems*, pp. 659–673. Prentice Hall, New York (1950).
7. B. T. Stephenson and C. H. Walter, *Approximate Pattern Synthesis for Continuous Line Sources*, Rep. Antenna Lab. Ohio State Univ. Res. Fdn. No. 486-41 (June 1955); prepared under Contract AF 18(600)-85, Wright Air Development Centre, Wright-Patterson Air Force Base, Ohio.
8. H. B. Querido, *Surface Wave Fields and Phase Velocity Variations of Grounded Dielectric Sheets and of Periodic Structure of Metal Posts on a Ground Plane*, Rep. Antenna Lab. Ohio State Univ. Res. Fdn. No. 667-46 (Nov. 1958); prepared under Contract AF 33(616)-3353, Wright Air Development Centre, Wright-Patterson Air Force Base, Ohio.
9. J. N. Hines, V. H. Rumsey and C. H. Walter, *Proc. Inst. Radio Engrs.* **41,** 1624 (1953).

SECTION C

VOLTAGE BREAKDOWN OF ANTENNAS

POWER-HANDLING CAPABILITY OF ANTENNAS AT HIGH ALTITUDE*

W. E. SCHARFMAN and T. MORITA
Stanford Research Institute, Menlo Park, California

Abstract—The factors influencing the power-handling capability of antennas at high altitude are considered in this paper. The physical mechanism involved, including the roles of attachment, free diffusion, ambipolar diffusion, and non-uniform field distribution in the breakdown process, is qualitatively described. These factors are illustrated by breakdown curves for various antenna configurations under both CW and pulse conditions. Normalized data, which are useful for estimating breakdown fields when the conditions for scaling are fulfilled, are presented.

The effect of missile environment on breakdown characteristics is discussed, and an experiment that involves artificially introducing ionization near the surface of the antenna is described.

Methods are then considered for increasing the power-handling capability, and typical results are given showing the increase in power that can be achieved.

1. INTRODUCTION

Examination of the received signal from electronic systems on various missiles has indicated the presence of antenna voltage breakdown in the altitude range of 50,000–300,000 ft at VHF, UHF and microwave frequencies. The presence of antenna voltage breakdown is manifested by a decrease in transmitted signal intensity, change in the input impedance and radiation pattern of the missile antenna, modification of the pulse shape and noise modulation on the signal.[1] Since it is important in many cases to obtain continuous telemetry and tracking information to determine impact position and system performance data, an experimental investigation has been carried out to study the power-handling capabilities of antennas at high altitude. The principal aims of this study are (1) to determine the physical mechanism involved, (2) to measure and tabulate experimental data on breakdown field for various types of antennas and (3) to study methods for improving the power-handling capability of antennas.

2. BREAKDOWN MECHANISM

The high frequency breakdown mechanism has been thoroughly investigated in the past for circuit elements such as transmission lines and cavities.[2, 3] The source of primary ionization is due to electron motion, and breakdown occurs when the gain in electron density becomes equal to the loss of electrons by diffusion and attachment. This relationship is expressed as:

$$\frac{\partial n}{\partial t} = (\nu_i - \nu_a)n + S + \nabla^2(Dn) \qquad (1)$$

where

n is the electron density,

ν_i is the ionization rate,

ν_a is the attachment rate,

S is the ionization produced by an external source,

D is the diffusion coefficient for electrons.

The measurements reported here confirm that

* The work reported in this paper was supported by the Air Force Cambridge Research Centre under AF Contract AF 19(604)-3458.

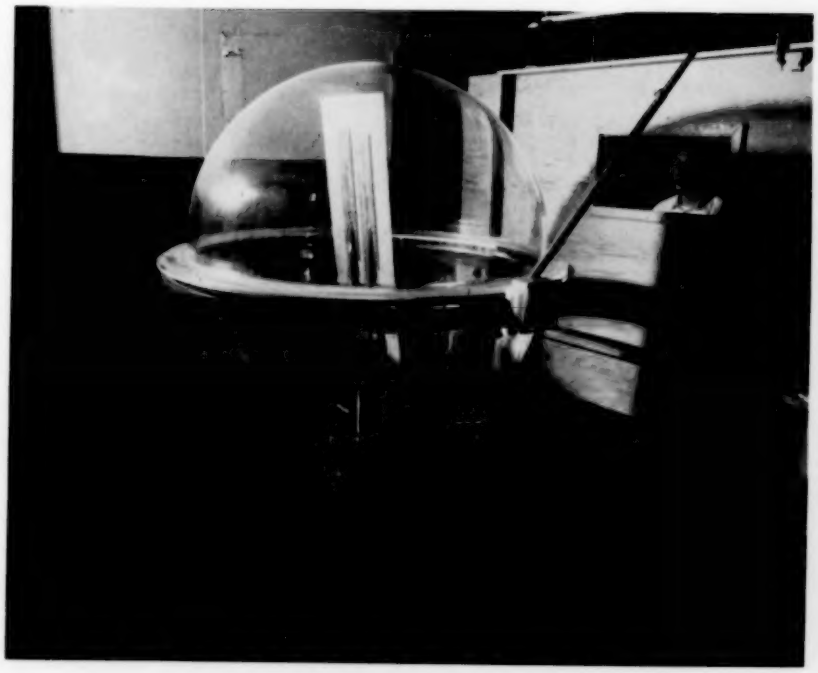

Fig. 1. Photograph of altitude chamber.

the processes that are important for microwave circuit elements also determine the minimum power-handling capability of antennas in air at low pressure.

For a parallel plate configuration, the solution of the electron continuity equation (1) gives for the breakdown condition:

$$\frac{\nu_i - \nu_a}{D} = \Lambda^2 \tag{2}$$

where Λ is the characteristic diffusion length. For spacing L between parallel plates

$$\Lambda = \frac{L}{\pi} \tag{3}$$

The complex antenna geometry and field configuration do not in general permit the use of a diffusion length, and only antennas with similar geometry and field can be compared.

For breakdown in air the diffusion coefficient D_F is due to diffusion of free electrons and is given by

$$D_F = \mu_e \frac{kT_e}{e} \tag{4}$$

where μ_e = electron mobility $= \dfrac{e}{m(j\omega + \nu)}$

k = Boltzmann's constant

T_e = electronic temperature.

The free diffusion condition exists at low pressure (high altitude) and can be simulated in a vacuum chamber.

A phenomenon which is unique to high altitude missile operation is the transmission of signal through the ionized envelope created when the missile re-enters the earth's atmosphere. The presence of the ionized gas changes the electron loss mechanism from free diffusion to ambipolar diffusion.[4] The diffusion of electrons from a neutral plasma brings about the increased mobility of the heavy positive ions since the plasma tends to charge neutrality. A positive space charge is developed as a sheath around the antenna which retards the high velocity electrons and accelerates the positive ions. In the plasma to be considered in this paper, the electron temperature is large compared to the positive ion temperature, and the ambipolar diffusion coefficient is then given by:

$$D_A \approx \mu_+ \frac{kT_e}{e} \tag{5}$$

with μ_+ = positive ion mobility.

Thus, $\dfrac{D_A}{D_F} \approx \dfrac{\mu_+}{\mu_e}$, and since $\mu_e \gg \mu_+$, the net result is to decrease the diffusion rate of electrons, thus decreasing the power handling capability.

3. EXPERIMENTAL RESULTS

Fig. 1 is a photograph of a 4-ft diameter plexiglass sphere used for the experiments. This chamber can be evacuated to 4 micron pressure which corresponds to an altitude of about 300,000 ft. The incident, reflected and transmitted power are monitored as well as the pulse shape, frequency spectrum and radiation pattern.[1]

(a) *Monopole antenna*

The effect of antenna height and diameter on breakdown power of a monopole over a conducting ground plane has been investigated with CW power at 240 and 400 Mc/s and with pulse power at 9400 Mc/s. These results, as well as results from other measurements, show that for geometrically similar antennas, frequency scaling is applicable.[5] Also, if the form of the near-zone field remains the same with some varying dimension (as with parallel-plate transmission line with varying spacing, narrow slot-antennas with varying width and monopoles with varying diameter), the value of the ratio of effective electric field E_e to pressure required for breakdown is a function of pressure times the characteristic dimension. The effective electric field is defined to produce the same energy transfer as a d.c. field and is given by

$$E_e = \frac{E\nu_c}{\sqrt{(\nu_c^2 + \omega^2)}} \tag{6}$$

These results for monopoles are shown in Fig. 2. For purposes of breakdown calculation, the concept of a monopole as a coaxial line with large ratio of outer to inner conductor radius was applied to obtain an approximate solution for the electron continuity equation(1).[6]

Fig. 3 is the plot of the power required to initiate and maintain breakdown on a $\lambda/4$ monopole. For CW measurement the power required to initiate breakdown is about 6 to 9 dB higher than the power required to maintain breakdown. For initiation of breakdown, free diffusion is the dominant loss mechanism, while for maintaining breakdown, ambipolar diffusion and attachment is the dominant loss mechanism.

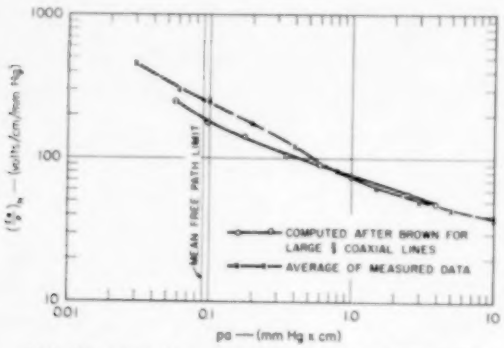

Fig. 2. Coaxial line and monopole breakdown data.

(b) *Aperture antennas*

Measurements made on slot antennas with a dielectric cover show that the electric fields required to initiate breakdown are considerably higher than for a rectangular waveguide of the same cross-section. This is shown in Fig. 4. The loss of electrons to the dielectric cover is much greater than the loss to the walls in the waveguide case. Furthermore, the fast fall-off of the near-zone field measured normal to the aperture also increases the diffusion loss. Also shown is the field strength required to maintain breakdown, computed on the basis that field distribution has not changed after breakdown.

(c) *Pulsed breakdown*

For pulse repetition rates of interest in radar

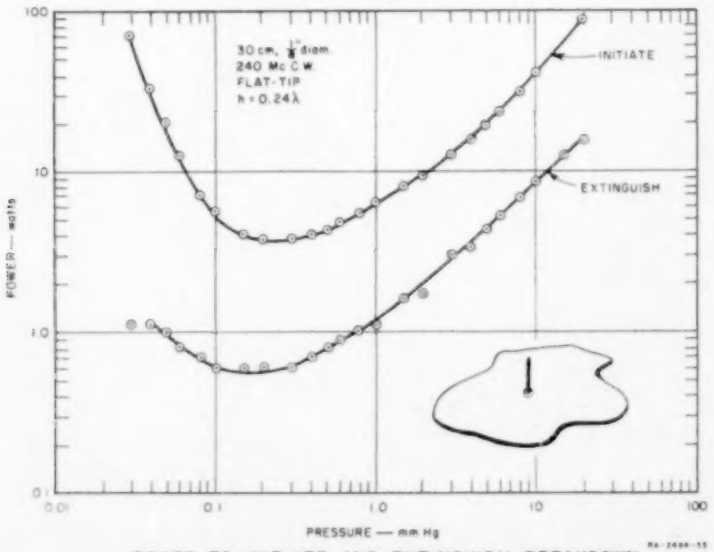

Fig. 3. Power to initiate and maintain breakdown for 0·24λ monopole.

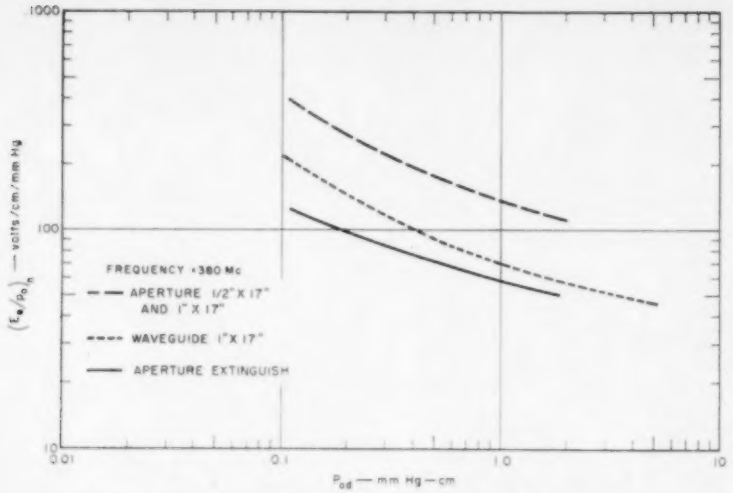

CW APERTURE AND WAVEGUIDE BREAKDOWN

Fig. 4. CW aperture and waveguide breakdown.

systems, breakdown is a single pulse phenomenon with breakdown extinguishing at the end of each pulse. Fig. 5 is a plot of $\frac{E_e}{P_0}$ plotted vs. $p_0\tau$, where τ is the pulse width, for an X-band waveguide radiator with dielectric cover and for an X-band waveguide. Here the parameter, p_0b, is the pressure times the guide height. For large $p_0\tau$, the two curves converge since attachment is the principal loss-mechanism. Furthermore, they converge towards the CW value which is shown on right.[2, 3, 7] For small p_0b, the diffusion to the cover greatly increases the breakdown field for the slot radiator with the dielectric cover.

(d) *Antenna operation in a weakly ionized medium*

The effect on the breakdown power of an antenna when its environment includes a plasma has been investigated. A d.c. glow discharge was formed with the negative glow area of the discharge located over the aperture of a slot antenna radiating at 373 Mc/s. While the density of electrons in this plasma is of the same order of magnitude as for a re-entry body, the gas temperature itself is very low. In the negative glow area, the plasma is essentially neutral with a maximum electron density of 10^{11} electrons/

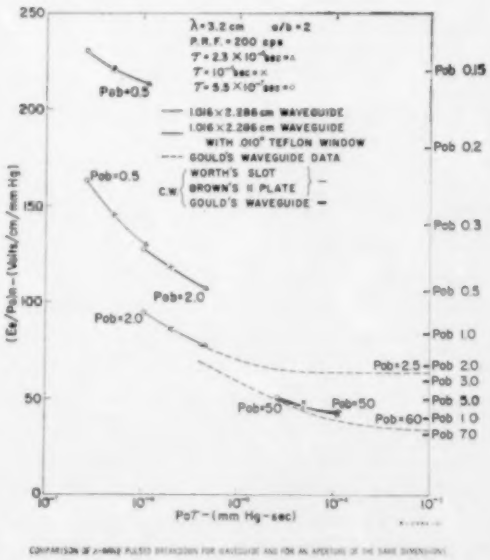

Fig. 5. Comparison of X-band pulsed breakdown for waveguide and for an aperture of the same dimensions.

cm^3 [8] decreasing to zero over the antenna aperture. Figs. 6 and 7 show the results obtained when the effective plasma frequency ($f_p = 8900\sqrt{N}$) is approximately one-half and twice the r.f. frequency. The plasma frequency was obtained from the transmission and reflection measurement prior to r.f. breakdown, with the collison frequency assumed equal to the r.f. frequency.

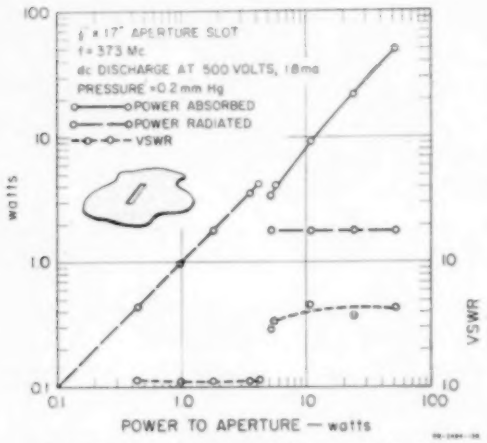

POWER HANDLING CHARACTERISTICS OF SLOT ANTENNA IN THE PRESENCE OF A 500 VOLT dc DISCHARGE

Fig. 6. Power-handling characteristics of slot antenna in the presence of a 500V d.c. discharge.

For Fig. 6, where the plasma frequency is approximately one-half the r.f. frequency, the attenuation is negligible and the transmitted and reflected power increase directly with the incident power. After the occurrence of voltage breakdown at 4·5W the transmitted power remains almost constant while the absorbed power increases directly with the incident power. The transition to r.f. breakdown is shown to be double-valued, since the conditions abruptly change at breakdown. For Fig. 7, where the plasma frequency is approximately twice the r.f. frequency, the characteristic after r.f. breakdown is almost identical to the Fig. 6.

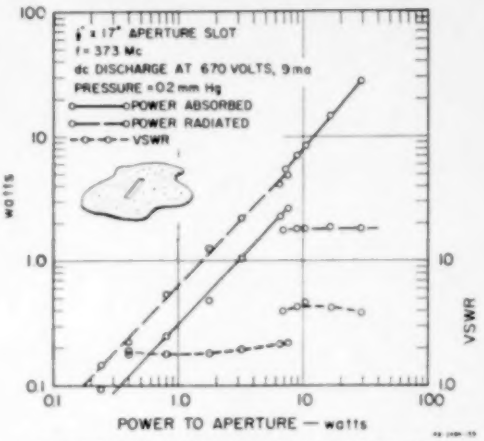

POWER HANDLING CHARACTERISTICS OF SLOT ANTENNA IN THE PRESENCE OF A 670 VOLT dc DISCHARGE

Fig. 7. Power-handling characteristics of slot antenna in the presence of a 670V d.c. discharge.

However, before r.f. breakdown occurs, there is r.f. attenuation and the VSWR is higher than for Fig. 6. Before r.f. breakdown the r.f. conductivity appears to be constant, independent of the applied field. In the absence of a plasma, this antenna required about 41W for breakdown as compared to 7·5W with a plasma. The maintaining power without a d.c. plasma was 7W.

One interesting result of this study is that the power-handling capability of the slot in the presence of an ionized medium appears to be about the same as the power required to maintain the breakdown. Since ambipolar diffusion is the main loss mechanism for both cases, this would be true if the r.f. field distribution were approximately the same.

(e) *Methods for increasing the power-handling capability of antennas*

There are several methods to increase the power-handling capability of an antenna. One method is to increase the electron-loss mechanism. This may be accomplished by the use of a d.c. bias, either negative or positive, to capture

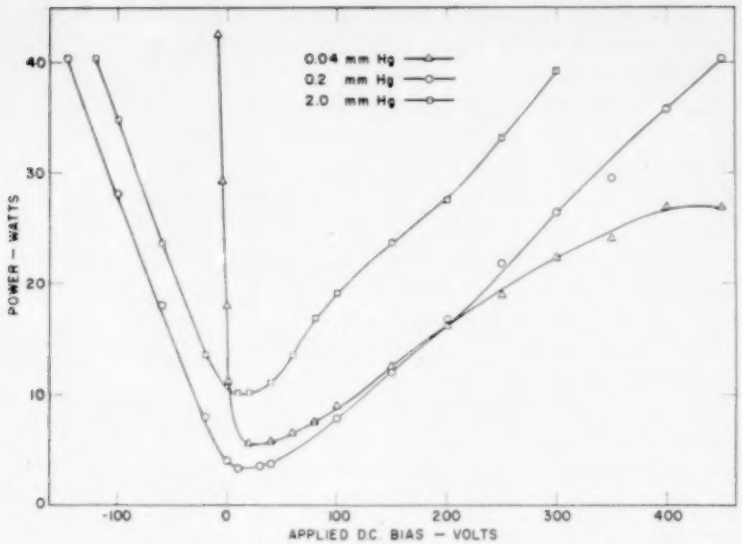

Fig. 8. Effect of d.c. bias on power-handling capability of 0·24λ monopole.

the electrons to the antenna or repel the electrons from its vicinity. Fig. 8 shows the large increase in power-handling capability obtained for a λ/4 monopole with a d.c. bias. Similar results are obtained for a narrow-slot radiator. However, as the slot width is increased, the near-zone field drop-off decreases considerably and the d.c. field is less effective. For example, for an X-band waveguide aperture with a dielectric cover, only 3-dB increase in power-handling capability could be obtained with various biasing arrangements. It should be pointed out that d.c. bias will not be effective with an antenna imbedded in a dielectric, since the d.c. voltage will appear across the dielectric, rather than in the region where electrons are being formed.

Another method for increasing the power-handling capability is to decrease the electric field strength in the region of low gas density. The use of a pressurized radome over the antenna structure to enclose the high field regions near the antenna accomplishes this. Another possibility is top loading as illustrated in Fig. 9. This top-loaded monopole is only 0·10λ in height, but handles 25W as compared to 0·20W for a $\frac{1}{8}$ in. diameter monopole of the same height.

Increasing the *field strength* required for breakdown may not always be desirable, since

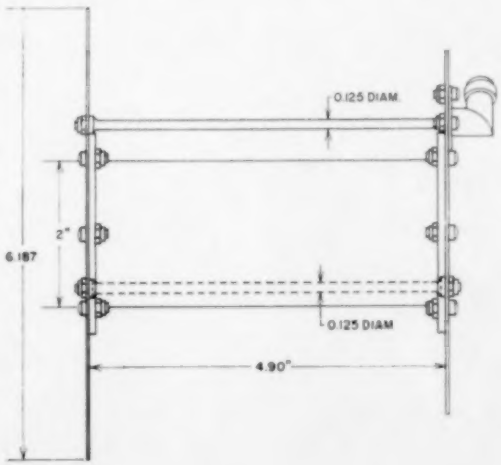

TOP-LOADED FOLDED MONOPOLE

Fig. 9. Top-loaded folded monopole.

it is the maximum *radiated* power which is desired and not maximum near-zone field strength. As an illustration, consider the case of an open waveguide slot with no dielectric cover. The field strength for breakdown can be increased by decreasing the slot width since the loss of electrons to the wall is increased as the walls are brought closer together. However, the increase in field strength per watt as the slot width is decreased is faster than the increase in breakdown field strength, so that the power-handling capability decreases even though the field strength for breakdown is increased.

In general it has been found that antennas with higher power-handling capability under free diffusion condition will also have higher power required to maintain breakdown. Further work is required to see whether this is also true for antennas operating in an ionized medium.

Acknowledgement—The authors acknowledge the assistance of Mr. Willard Wadsworth in the performance of the experimental work.

REFERENCES

1. J. Chown, W. Scharfman and T. Morita, *Proc. Inst. Radio Engrs.* **47,** 1331, 1337 (1959).
2. S. C. Brown, *Proc. Inst. Radio Engrs.* **39,** 1493 (1951).
3. L. Gould and L. W. Roberts, *Appl. Phys.* **27,** 1162 (1956).
4. W. P. Allis and D. J. Rose, *Phys. Rev.* **93,** 84 (1954).
5. A. D. MacDonald, *Proc. Inst. Radio Engrs.* **43,** 436 (1959).
6. M A. Herlin and S. C. Brown, *Phys. Rev.* **74,** 910 (1948).
7. F. Worth, *A Study of Voltage Breakdown in the Cavity Fed Slot Antenna*, Lockheed Aircraft Corp., Missile Syst. Div. Rep. MSD 2030 (Jan. 1957).
8. J. D. Cobine, *Gaseous Conductors, Theory and Engineering Applications*, pp. 212–226, Dover Publications, NY (1958).

R. F. ANTENNA BREAKDOWN CONDITIONS IN THE PRESENCE OF THE PLASMA SHEATH*

R. F. WHITMER and A. D. MACDONALD†
Microwave Physics Laboratory, Sylvania Electric Products, Mountain View, California

Abstract—Antennas on nose cones and re-entry vehicles are known to be susceptible to voltage breakdown at relatively modest microwave field strengths. The voltage required to produce breakdown has been calculated, as a function of altitude, for typical nose cones re-entering the atmosphere. The effects of the ionized sheath have been included and it is shown that the sheath can greatly modify the usual breakdown conditions. The effects of ambipolar diffusion within the sheath are of major importance and can modify the breakdown voltage by as much as 50 per cent. This correction is discussed in detail. When the electron density within the sheath approaches the density needed to cut off the microwave signal, a further correction to the breakdown voltage is required. Breakdown conditions, for CW and pulsed operation, will be discussed as a function of Mach number, nose cone angle, frequency and pulse width.

A brief discussion will be given of the limitations of the present theory. The theory is greatly limited by the lack of knowledge of certain basic plasma parameters. Methods for obtaining these parameters on in-flight tests will be discussed.

The purpose of this paper is to discuss the modifications which must be made to the usual r.f. breakdown theories in order to account for the effects, on the r.f. breakdown conditions, of the plasma sheath about a hypersonic re-entry vehicle. The typical theories for r.f. breakdown in the atmosphere account for the gas density variation in the atmosphere as a function of altitude. However, in the case of a re-entry vehicle a plasma sheath, in which the gas density and the ambient electron density may be considerably different from the normal atmospheric conditions, may be formed about the vehicle. Consequently, the r.f. breakdown conditions may be modified appreciably by the presence of the plasma sheath.

The ARDC (1957) model[1] of the atmosphere has been used to obtain the ambient atmospheric conditions at the respective altitudes. The term "pressure" is used in this paper to conform with the terminology in the gas discharge literature. However, the parameter of prime importance is the gas density, which is determined by both pressure and temperature. The pressures used in this paper have been adjusted to include the temperature variations so that pressure is proportional to gas density (1 mm. of Hg is equivalent to $3{\cdot}5\times10^{16}$ particles/cm^3). The distinction between gas density and pressure in their relation to breakdown phenomena becomes very important when considering hypersonic missiles. The ratio of the pressure within the shock to that in the undisturbed space is, in general, quite different from the ratio of the densities.

1. CW BREAKDOWN

(a) *Low ambient electron density*

The analysis in this section follows closely that in Refs. (2) and (3). Therefore, only an outline of the analysis will be given.

The equation which describes breakdown[4] is

$$\nu_i - \nu_a = D/\Lambda^2 \qquad (1)$$

* This study was supported by the Boeing Airplane Company.

† Dalhousie University, Halifax, Nova Scotia.

where ν_i is the ionization rate, ν_a is the attachment rate, and D is the diffusion coefficient. Recombination has been neglected as an electron loss mechanism. This is a valid approximation except in the case of an extremely highly ionized sheath (electron densities greater than $10^{15}/cm^3$). In the absence of diffusion loss, i.e. very large Λ, breakdown is determined by attachment. In order to simplify the analysis we shall express attachment loss in terms of an attachment length, Λ_a, so that $\nu_a = D/\Lambda_a^2$. The frequency of attachment, ν_a, is approximately equal to $4 \times 10^{-6}\,\nu_c$, where ν_c is the collision frequency.[5] The diffusion coefficient is the average value of $l^2\nu_c/3$, where l is the electron mean free path. The mean free path for electrons in air is not independent of energy, but it may be approximated by setting $l = 1/35\,p$, where p is the pressure in mm of Hg and l is in cm. Combining these we have $\Lambda_a = 12/p$. One can then find the CW breakdown fields by using the appropriate diffusion length, Λ, of equation (1) with the data of Gould and Roberts.[6] (It is assumed that $\Lambda = \lambda/2$.)

Figs. 1 and 2 are illustrations of the graphs of breakdown fields as a function of altitude. The breakdown field for a 12° nose cone moving with a velocity of Mach 6 is plotted in Fig. 1 for a transmitter frequency of 3 kMc/s. The field required to produce breakdown under Mach 0 conditions, i.e. atmospheric breakdown conditions which exist in the absence of the nose cone, is plotted with dashes and the breakdown field for Mach 6 conditions is plotted with dash-dots. It can be seen that the pressure increase due to the build-up of a shock wave about the vehicle in effect shifts the breakdown conditions to higher altitudes. The actual field required to produce breakdown for the Mach 6 conditions is then given by the lowest values of the combination of these two curves. This assumes that if breakdown does not occur within the plasma sheath itself on the low altitude side of the minimum, then breakdown will occur in the atmosphere immediately outside the ionized plasma layer. This is shown as the upper solid line. Fig. 2 shows a similar plot for a 6° nose cone, Mach 36, and frequency 100 Mc/s.

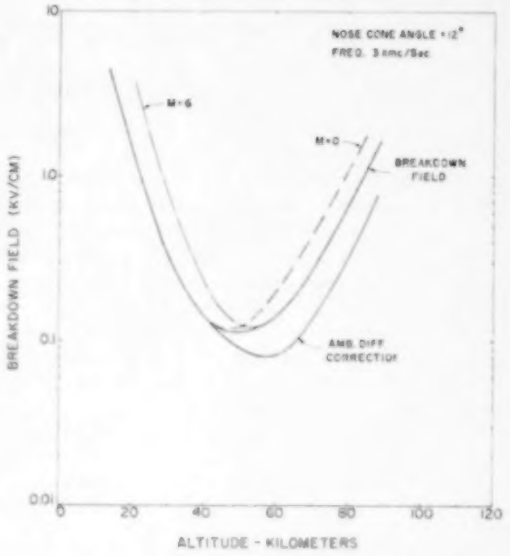

Fig. 1. Breakdown field versus altitude.

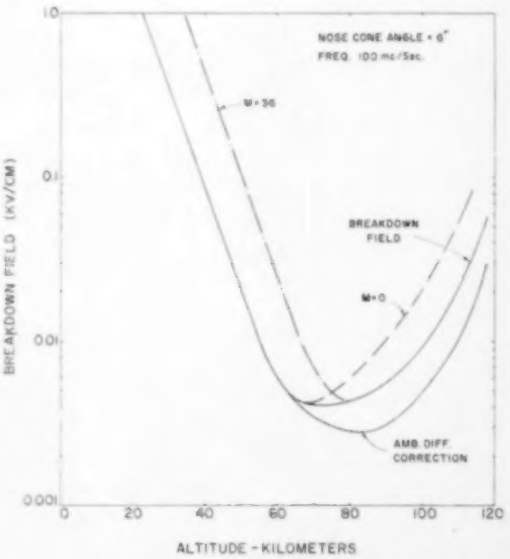

Fig. 2. Breakdown field versus altitude.

(b) *Additional effects of shock wave ionization*

The preceding considerations assume that the ionization in the region near the antenna is well below the plasma resonant density. When the initial electron density in the shock wave is close to the plasma density ($\omega \approx \omega_p$ where $\omega_p^2 = ne^2/m\varepsilon_0$), two effects must be considered. First, the electrons are produced by thermal ionization and we have, in effect, an additional ionization rate which must be added to the field ionization rate. Secondly, the diffusion changes from free particle diffusion to ambipolar diffusion, which lowers the required breakdown field.

1. *Ambipolar diffusion.* When electron concentrations are low, electrons diffuse freely in the usual manner. However, when the electron and ion concentrations become large, the attraction between the ions and electrons is large and the electron diffusion is slowed down to a rate between that of the ions and the electrons by themselves, because the ions must then diffuse along with the electrons. This is called ambipolar diffusion and, because it results in a lower loss rate, it leads to lower breakdown fields. The transition from free to ambipolar diffusion has been studied in detail by Allis and Rose.[7] They have shown that the transition from free to ambipolar diffusion takes place over several orders of magnitude in electron concentration. The study of Allis and Rose indicates that when the initial concentration, n_0, is equal to or greater than $10^{-4}\, n_p$, a correction must be made for ambipolar diffusion (n_p is the electron density such that $\omega = \omega_p$).

The ratio between the free diffusion coefficient and the ambipolar diffusion coefficient is different for each gas; therefore, we cannot use the Allis–Rose calculations for hydrogen. There are two ways of calculating the required ratio. First, we may state that

$$D_a = 2D_- \frac{\mu_+}{\mu_-} \tag{2}$$

where μ_+ and μ_- are the mobilities of the ion and electron, respectively. (This case is called the isothermal case by Allis and Rose, and it is appropriate to the case where the walls are far removed from the discharge; i.e. there is no sheath.) We now need the mobilities of the positive ions of nitrogen and oxygen and of electrons in air. These can be found from the data on drift velocities quoted by Brown and Allis.[8] In the present case, we are actually interested in the ions N^+ and O^+ and not the molecular ions, because the gas in the shock wave is completely dissociated at temperatures well below those required for appreciable thermal ionization.[9] However, ionic mobilities are inversely proportional to the masses and the mobility of N^+ is just twice that of N_2^+. Varney's data quoted on p. 125 of Ref. (8) gives μ for N_2^+ at an E/p of 20 as $0{\cdot}22/p$ m.k.s, units and a similar value for oxygen. The mobility of electrons in air at the same value of E/p is $40/p$ m.k.s. units. The ratio is then 180 for N_2^+ and 90 for N^+. This gives a value of the ambipolar diffusion coefficient as $D_a = D_-/45$. Another method of getting the ratio, which is perhaps better, makes use of the value of D_a for O^+ measured by Schultz–DuBois and is quoted on p. 131 of Ref. (8). This value is given by $D_a p = 225$ (cm²/sec) for ions with energy corresponding to 300°K. This yields $D_a p = 9000\ \bar{u}$ (cm²/sec) for an average energy $\bar{u}$ (in volts). The value we have used for electron diffusion is $Dp = 3{\cdot}2 \times 10^5\ \bar{u}$. Combining these results we get a ratio of free to ambipolar diffusion coefficients of 35. Both methods used involve some extrapolation beyond measured values; therefore, we choose the average of the two results, giving $D_-/D_a = 40$.

The breakdown condition for the CW case involves setting $\nu = D/\Lambda^2$. When the diffusion rate is reduced by the ambipolar effect, the required ionization rate to produce breakdown is similarly altered. This means that the ionization rate required is reduced by a factor of 40. It is required to know ν as a function of pressure, electric field and wavelength in order to find this correction. ν has been measured by Herlin and

Brown[10] who have presented their results in terms of the high frequency ionization coefficient, ξ (equal to ν/DE^2), as a function of $p\lambda$ and E/p. In order that we may extract from their work values of ν, we must compute the diffusion coefficient, D. Details of this calculation have been given in Ref. (2), where it was shown that

$$Dp = 3{\cdot}2 \times 10^5 \bar{u} \tag{3}$$

where $\bar{u}$ is the average electron energy. From the data of Healey and Reed[11] we find that $\bar{u}$ is approximately equal to 0·036 E_e/p, where E_e, the effective electric field, is defined by the relation

$$E_e^2 = E^2(1+\omega^2/\nu_c^2) \tag{4}$$

and E is the r.m.s. value of the electric field. The collision frequency for electrons in air, ν_c, is not independent of energy, but a good approximation is made by setting it equal to $5{\cdot}3 \times 10^9 p$. The expression for the effective electric field becomes

$$E_e = E/[1(+36/p\lambda)^2]^{.1/2} \tag{5}$$

A useful form in which to express ν is to find $\nu\lambda$ by multiplying the measured values of ν/DE^2 by $(E/p)^2 p\lambda Dp$. This method of using the data of Herlin and Brown was first used by Rose[12] and enables one to simplify the calculation of maximum fields. A graph of $\nu\lambda$ as a function of $p\lambda$ for various values of $E\lambda$ is shown in Fig. 3. This figure shows that the field for breakdown must be reduced by multiplying by 0·45, for the case $D_-/D_a = 40$. This correction is to be applied only when the ambient electron density is greater than $10^{-4} n_p$, and then only on the high altitude side of the minimum of the breakdown curves. At altitudes below this minimum the breakdown is controlled by attachment, which is not significantly affected by the high ambient electron density. At the minimum of the curves plotted without the ambipolar diffusion correction, both processes enter the determination of breakdown fields; and we must effect a smooth transition between the two. This is done by lowering the minimum by about 20 per cent and applying

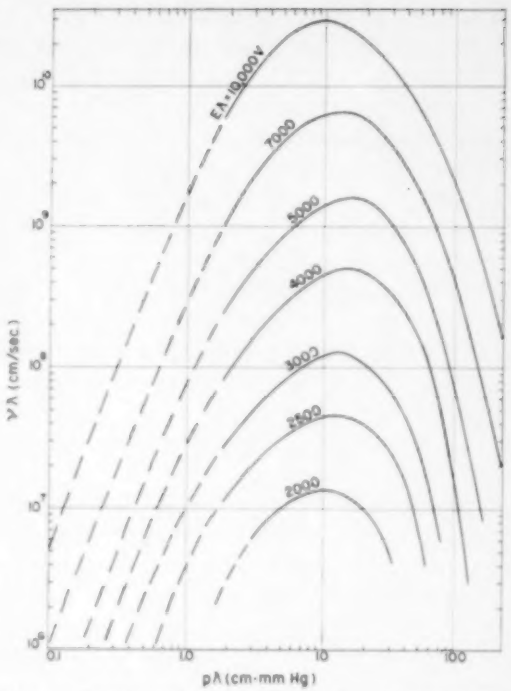

Fig. 3. Effective ionization rate as a function of $p\lambda$ for various $E\lambda$.

the full correction factor of 0·45 at about 10–15 km above the minimum. This effect is shown in Figs. 1 and 2.

2. *Thermal ionization.* Thermal ionization is generally calculated using Saha's equation, which was derived for equilibrium conditions and probably is not very accurate for the case at hand. It will therefore be sufficiently accurate to assume that if the electron concentration produced in a shock is a given fraction of the plasma or breakdown density, the thermal ionization rate is the same fraction of the total ionization rate required for breakdown. This means that the ionization rate normally required to produce breakdown, by the electric field, at low initial ionization is accordingly reduced. We can then use Fig. 3 to find the reduction in field necessary to reduce the ionization rate to the required value. Fig. 4 presents the reduction

factor for CW breakdown fields. On the ordinate is shown the ratio of the breakdown field required when the initial concentration is appreciable to that required when the initial concentration is low. The abscissa is the ratio of the initial density, n_0, to the plasma resonant density, n_p. When the initial density is equal to or less than one-tenth of n_p, the effect is negligible; and, of course, when the initial density is n_p, breakdown has already taken place.

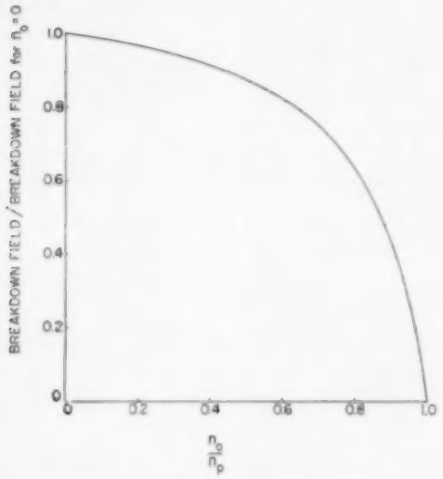

Fig. 4. Breakdown field correction versus ambient electron density.

If both ambipolar diffusion and the change in ν_i are important, the breakdown field can be found by first obtaining the field from the lower solid curve and then multiplying that by the appropriate fraction obtained from Fig. 4 to obtain correction for the ambient electron density, n_0.

2. PULSED BREAKDOWN

The breakdown analysis follows closely that found and described previously.[3] Pulses during which there is an increase of electron concentration are considered.

There may be appreciable signal transmitted through some concentrations of electrons; therefore, breakdown may be tolerated, provided the electron density produced in front of the antenna is not too great. The electron concentration above which there is practically no transmission is the "plasma resonant density", n_p, which is equal to $10^{13}/\lambda^2$ electrons per cm^3 if λ is in cm. When the concentration is $n_p/2$, signal absorption and reflection are negligible; and when the concentration is $2n_p$, no signal gets through; therefore, n_p may be considered a sharp upper limit for transmission.

Consider now a pulse in which the electric field is larger than that required for breakdown. The electron concentration will start to increase at the rate $e^{\nu t}$, where $\nu = \nu_i - \nu_a$, and will continue to increase until the pulse is turned off. If the concentration at the end of the pulse just reaches n_p, practically the entire pulse will be transmitted. In order to find the electric field for which this will happen, we set $n_p = n_o e^{\nu\tau}$, where n_0 is the initial electron concentration and τ is the pulse length. We shall assume that vehicle speeds are greater than 1000 ft/sec and that the interval between pulses is at least 1 msec. This will mean that successive pulses are separated in space by at least one foot; therefore, we shall not need to consider any electrons left over from a previous pulse. If speeds were so slow or repetition rates so fast that discharges were not separated in space, the electron concentration left over from one pulse would provide the initial concentration for the next. However, we consider only those cases where the initial concentration is that existing in space or is the ionization produced by the shock wave. If there are no electrons existing in the space occupied by the electric field, there can be no breakdown.

Figs. 5 and 6 illustrate typical results for a 12° nose cone for a frequency of 10 kMc/s with an initial density of 10^6 electrons/cm^3. Pulse widths of 0·05 μ sec and 1 μ sec are shown. The power levels at the minima have been computed on the basis of linear arrays.[3]

It can be shown that the free diffusion of electrons modifies the breakdown field by less

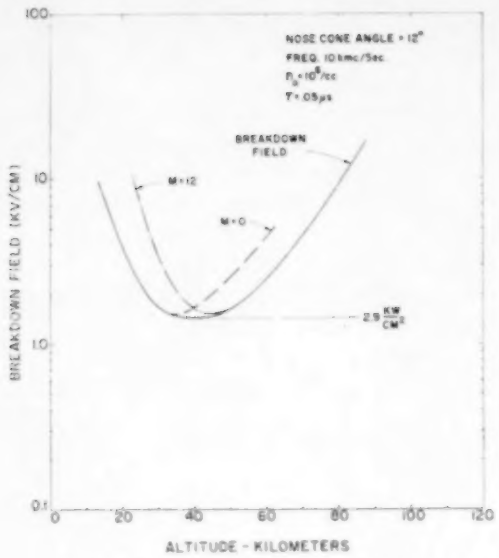

Fig. 5. Breakdown field versus altitude.

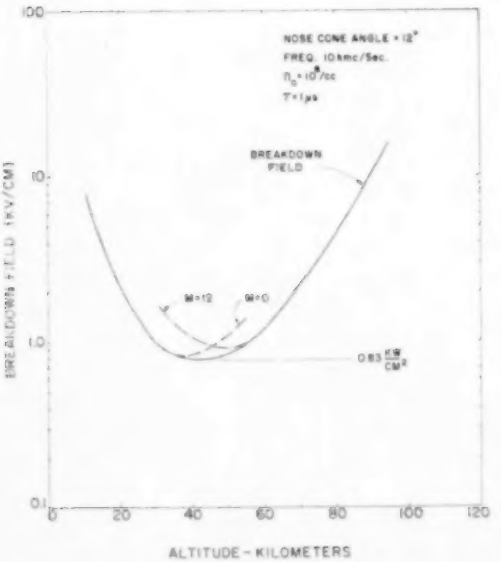

Fig. 6. Breakdown field versus altitude.

than 5 per cent in the pulse case and, therefore, it was neglected. Since the effect of ambipolar diffusion is to lower the free diffusion rate, ambipolar diffusion can be neglected in the pulse case.

3. CONCLUSIONS

It has been shown that the normal breakdown conditions in the atmosphere can be considerably modified by the presence of a plasma sheath about a re-entry vehicle. Two additional effects must be considered when making the breakdown calculations. These are the effects of ambipolar diffusion in the highly ionized sheath and the effects of a high initial electron density in the sheath. Typical results have been given, including these effects, for representative nose cones.

The results are limited because of the accuracy with which the attachment and diffusion coefficients are known for the atmosphere. These parameters have been estimated on the basis of present date; however, these estimates are probably not accurate to within 20 per cent.

REFERENCES

1. *ARDC Model of the Atmosphere* (1957).
2. A. D. MacDonald, *RF Breakdown in Air as a Function of Altitude*. Sylvania Tech. Rep. No. MPL-2 (Oct. 1956).
3. A. D. MacDonald, *Proc. Inst. Radio Engrs.* **47**, 456 (1959).
4. S. C. Brown, *High Frequency Gas Discharge Breakdown*, Massachusetts Inst. Technol. RLE Rep. No. 301 (July 1955).
5. L. B. Loeb, *Basic Processes of Gaseous Electronics* p. 430. University of California Press, Los Angeles (1955).
6. L. Gould and L. W. Roberts, *J. Appl. Phys.* **27**, 1162 (1956).
7. W. P. Allis and D. J. Rose, *Phys. Rev.* **93**, 84 (1954).
8. S. C. Brown and W. P. Allis, Massachusetts Inst. Technol. RLE Tech. Rep. No. 283 (1958).
9. H. W. Liepman and A. Roshko, *Elements of Gas Dynamics*, NACA Tech. Note 3270 (1957).
10. M. A. Herlin and S. C. Brown, *Phys. Rev.* **74**, 291 (1948).
11. R. H. Healy and J. W. Reed, *The Behaviour of Slow Electrons in Gases*. Amalgamated Wireless, Ltd., Sydney (1941).
12. D. J. Rose, private communication.

MICROWAVE BREAKDOWN OF ANTENNA RADOMES AT HIGH ALTITUDES

P. P. KEENAN
General Engineering Laboratory, General Electric Company, Schenectady, New York

Abstract—This paper presents data obtained from experimental measurements of antenna–radome breakdown using pulsed power at X-band frequencies and compares the results with those predicted by analysis. Parameters that were investigated experimentally are: antenna dimensions, radome depth, radome material, pulse width, pulse repetition frequency and pressure.

The equivalent diffusion lengths calculated from the measured breakdown data depend on these parameters in a manner which has been incorporated into the theoretical analysis. Furthermore, it has been observed that the antenna breakdown power drops off sharply above a certain critical pulse repetition frequency. This behaviour is attributed to an increasing radome surface charge which is also taken into account in the analysis.

The breakdown data have been reduced to generalized radome breakdown curves which permit the breakdown conditions to be determined for a wide range of parameters. The effects of a plasma sheath surrounding the antenna radome are briefly discussed, and scaling laws appropriate to antenna-radome breakdown are outlined.

1. INTRODUCTION

The antenna breakdown power limits the power handling capacity of microwave transmitting systems at high altitudes. In general, waveguide breakdown can be prevented by adequate pressurization. To prevent breakdown of the antenna, however, it is necessary to cap the antenna with a radome of sufficient depth to reduce the field at the outside surface of the radome to a value that will permit transmission without breakdown. It is usually desirable to minimize radome depth for good aerodynamic characteristics, and the problem generally of interest is to determine the minimum radome depth for the given operating conditions.

Selection of the optimum radome depth is not a simple matter, since the breakdown of air at the surface of a radome is a complex phenomena which depends on the environment surrounding the antenna as well as the radome depth, radome material, radiated antenna pattern and micro-wave frequency. In addition, if the antenna radiation consists of short pulses of r.f. energy, the antenna breakdown will depend on the pulse width and pulse repetition frequency.

This paper presents data obtained from experimental measurements of antenna–radome breakdown using pulsed power at X-band frequencies and compares the results with those predicted by analysis. In general, the results indicate that increasing the radome depth, antenna beam width or pulse repetition frequency decreases the breakdown field. It was also determined that the equivalent diffusion length for antenna–radome breakdown is not solely a function of geometry but also varies with the applied field intensity and pressure. The effects of ionized media surrounding the antenna radome are briefly discussed.

The method employed in the analysis of antenna–radome breakdown, where essentially an unbounded medium exists above the radome surface, should also be applicable to other breakdown problems where there are no sharply defined diffusion boundaries.

2. DESCRIPTION OF EQUIPMENT

Fig. 1 shows a block diagram of the breakdown measuring equipment and Fig. 2 gives a photograph of the equipment with the antenna and radome in place underneath the 30 in. diameter × 46 in. high bell jar and with the radiation shields placed alongside the jar. The viewing window grid in the radiation shield through which the antenna–radome breakdown is observed is evident in Fig. 2 as are the microwave circuitry, the liquid nitrogen traps and the low pressure pump in the background. The condition of breakdown is indicated by a bluish glow that can be seen at the top of the radome by looking through the viewing shield. A cobalt (Co^{60}) ion source is placed near the radome to ensure that breakdown will occur consistently at the minimum power level. Power is supplied from a high power X-band magnetron driven by a modulator whose pulse repetition frequency can be adjusted from 0 to 6000 pulses/sec. Pulse widths of 0·37, 1·0 and 2·1 μsec were used in the experiments. A power divider is used to adjust the input power in order to ensure a constant pulse shape.

The ratio of electric field to pressure constants determined from the high pressure antenna–radome breakdown data simulating continuous wave breakdown were compared to the continuous wave breakdown data given by Rose and Brown.[15] The comparison indicated that the radome breakdown fields were the order of 7 per cent lower than those given by Rose and Brown for air that has previously been broken down which constitutes reasonable agreement.

Radomes located at the aperture and in the near and far fields of the antennas were investigated. In the near and far field, hemispherical radomes of varying radii were attached to the ground plane of the horn antennas. Flat plate radomes were used for measuring the breakdown power in the aperture field of the antennas. The antennas consisted of pyramidal X-band waveguide horns whose half power beam widths varied from approximately 30° to 60° with antenna gains ranging from 12 dB to 15 dB. The mouths of the horns lay in conducting planes to which the radomes could be fastened. The antenna with the radome was placed inside the 30 in. diameter bell jar to provide the low

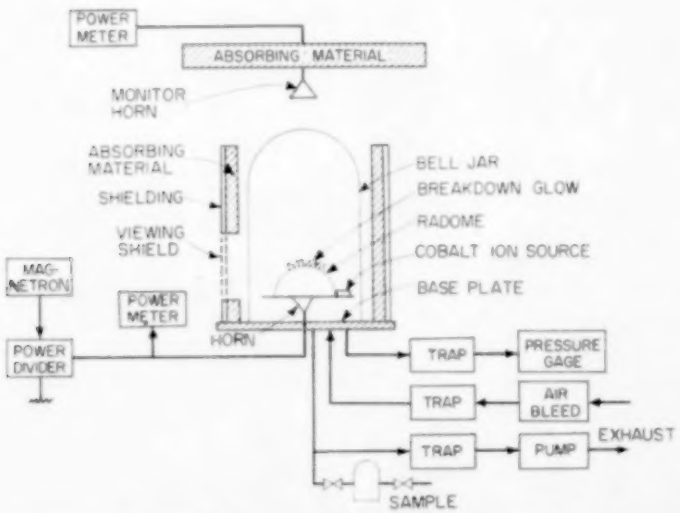

Fig. 1. Block microwave breakdown system.

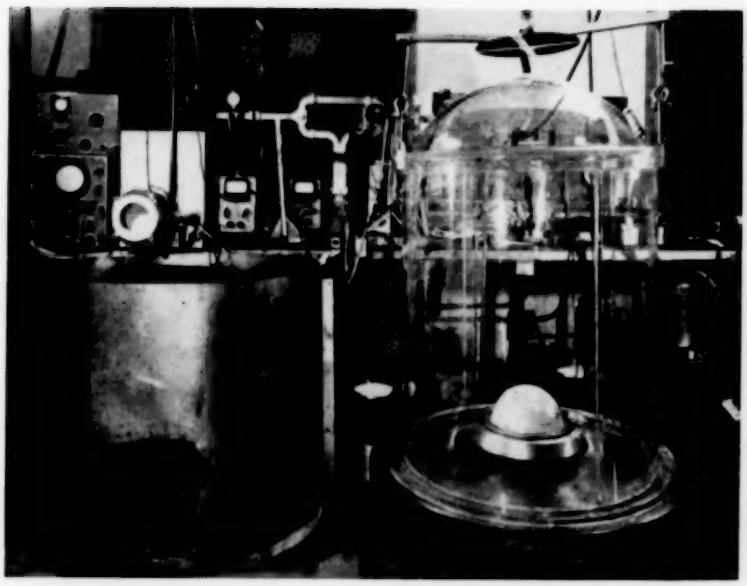

Fig. 2. Microwave breakdown equipment, shields removed.

pressure region. The peak pulse power for breakdown was measured at several pressures to determine the minimum breakdown power for a given radome radius. At low pulse repetition frequency essentially single pulse breakdown was achieved. At the higher pulse repetition frequencies essentially continuous wave breakdown was achieved.

The breakdown fields corresponding to the measured antenna–radome breakdown powers for radomes in the near field of the pattern were calculated using the near field gain correction curves derived from the data of Braun[9] and Lechtreck.[5] As a check, the far field gain of one of the horns were experimentally measured and was found to be in good agreement with the relation given by Silver.[11] The standard relation between electric field and waveguide power, equation (2), was used to calculate the electric fields for radomes located at the aperture. It was found that the narrow pulse breakdown fields at low pulse repetition frequencies were relatively independent of radome depth and antenna dimensions. Using these data, it was possible to determine experimentally the ratio of the breakdown power corresponding to a given radome depth to that corresponding to a radome located at the antenna aperture. These experimentally determined ratios were found to be in good agreement with those ratios calculated from electromagnetic relations, thus verifying the electric field calculations.

3. EXPERIMENTAL MEASUREMENTS

The antenna–radome breakdown power was measured as a function of pressure, pulse repetition frequency, radome depth, pulse width and antenna geometry. The experimental testing was done at a fixed X-band frequency (9170 Mc/s); however, as will be indicated later, it is possible to approximately scale these data at X-band to other frequencies. Also investigated were the effect of the radome material on antenna–radome breakdown and the effect of plasma on pulsed transmission where the plasma was created by breakdown of the radome.

(a) *Breakdown power versus pressure and pulse repetition frequency*

In Fig. 3a and 3b are given typical curves of antenna–radome breakdown power as a function of pressure for various pulse repetition frequencies. The minimum X-band breakdown

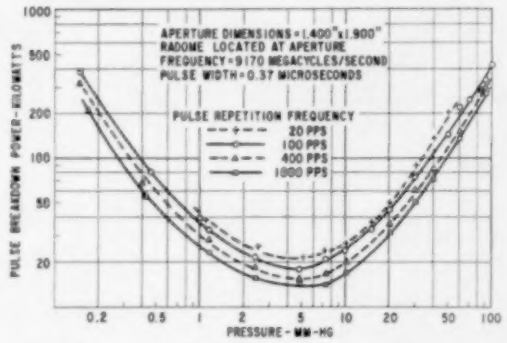

Fig. 3a. Pulse breakdown power vs. pressure.

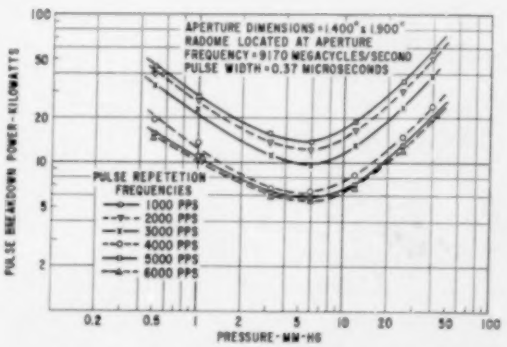

Fig. 3b. Pulse breakdown power vs. pressure.

power occurs at a pressure of approximately 5 mmHg which corresponds to an altitude of approximately 22 miles. These data correspond to a radome located at the aperture of the antenna. Single-pulse breakdown conditions were observed below approximately 20 pulses/sec while continuous wave breakdown conditions were obtained above approximately 5000 pulses/

sec. These limits are more clearly indicated in Fig. 4 which gives the breakdown power as a function of pulse repetition frequency for several pressures.

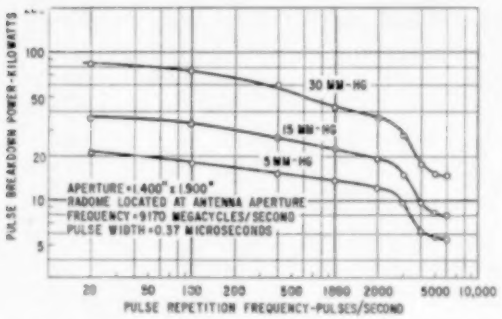

Fig. 4. Pulse breakdown power vs. pulse repetition frequency.

(b) *Phenomenon of critical pulse repetition frequency*

It may be observed that above approximately 2500 pulses/sec that the breakdown power abruptly drops to the ultimate continuous wave breakdown level. This abrupt drop in breakdown power above a critical pulse repetition frequency is not observed in cavity or waveguide breakdown. Initially, pulse deterioration was suspected; however, a check indicated that the pulse shape was stable. The phenomenon, therefore, appears to be a characteristic of antenna–radome breakdown. The analysis has shown that antenna–radome breakdown is characterized by a diffusion length which increases with radome surface charge and which also increases as the ratio of field strength to pressure decreases. This variable diffusion length, which is not encountered in cavity breakdown, affords a logical explanation of the rapid drop in breakdown power above a critical pulse repetition frequency. That is, as the pulse repetition frequency is increased, the surface charge on the radome builds up which results in an increased diffusion length. This increased diffusion length lowers the breakdown field which, in turn, further increases the diffusion length since the diffusion length is a function of field intensity. The effect is, therefore, cumulative and would appear to account for the sudden drop in breakdown power above a critical pulse repetition frequency. This explanation is also in agreement with the diffusion lengths calculated from the experimental measurements since it was observed that the diffusion lengths rapidly increased above the critical pulse repetition frequency.

This phenomenon appears to be associated with the approach to continuous wave antenna–radome breakdown and an analysis has been made which indicates that the critical pulse repetition frequency should be approximately inversely proportional to the pulse width. This relation is approximately indicated in Fig. 5, in that the frequencies, above which the pulse

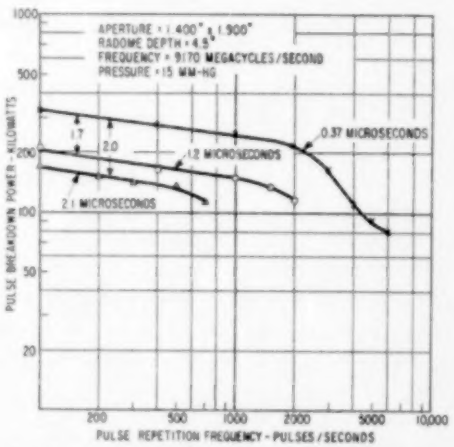

Fig. 5. Comparison of radome breakdown powers for various pulses.

breakdown power begins rapidly to decrease, are approximately inversely proportional to pulse width. Equipment limitations prevented extending the wider pulse width curve to higher pulse repetition frequencies and, thus, the curves in Fig. 5 require additional data at higher pulse repetition frequencies before the dependence of the critical pulse repetition frequency on pulse width can be completely resolved.

(c) *Effects of Plasma signal transmission*

Measurements of pulsed signal transmission through the breakdown glow at the radome surface have been made and are presented in Fig. 6 for conditions of low pressure breakdown. It may be noted that the leading edge of the pulse is relatively unaffected by the ionization while the trailing edge is attenuated. This is a general characteristic of pulsed transmission through self excited breakdown. If the ionization were independent of the field intensity, the entire pulse would be attenuated. As is well known, the plasma has a relatively small effect on signal transmission when the applied r.f. frequency is greater than the plasma resonant frequency. These results suggest that maximum signal transmission would be obtained with narrow pulses and r.f. frequencies somewhat greater than the plasma resonant frequency.

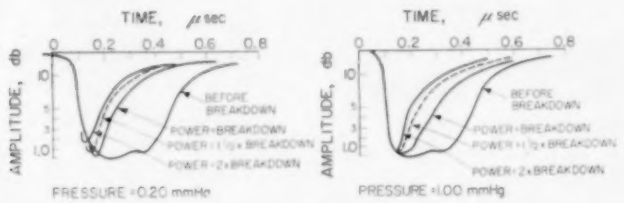

Fig. 6. Effect of breakdown glow on transmitted pulse.

Calculations of the effects of a uniform density plasma sheath on plane wave transmission and breakdown have been given by Whitmer.[14] These calculations indicate that ambipolar diffusion due to increased electron density considerably lowers the breakdown fields. Based on the analysis of antenna–radome breakdown, it would appear that ambipolar diffusion must also be considered in determining the effective diffusion lengths, and that the effective diffusion lengths will be a function of the spatial distribution of field intensities. It would appear that this problem could be solved in a manner similar to that which is employed in the analysis of antenna–radome breakdown.

4. NORMALIZED ANTENNA–RADOME BREAKDOWN CURVE FOR SELECTION OF MINIMUM RADOME DEPTH

In many instances the antenna–radome breakdown field is relatively independent of antenna dimensions or radome depth. For example, at high pressures the breakdown field is not controlled by diffusion and, hence, is independent of antenna–radome geometry. Similarly, for pulsed breakdown at low pulse repetition frequencies with narrow pulses, the breakdown field is controlled by the pulse width and is also independent of antenna–radome geometry. In such cases it is possible to determine a unique curve of normalized antenna–radome breakdown power versus normalized radome depth which can be used for a range of antenna sizes for selection of the minimum radome depth consistent with a given power requirement.

Experimental breakdown measurements indicate that far field breakdown conditions, where the breakdown power is proportional to the square of the radome depth, are achieved when the normalized radome depth is greater than unity. The normalized radome depth is defined by the usual criterion for far field radiation, as follows:

$$\text{Normalized radome depth} = R/(2d^2/\lambda) \quad (1)$$

where R = radome depth

d = geometrical average of the aperture dimensions $= (a\,b)^{\frac{1}{2}}$

λ = wavelength

a = aperture H-plane dimension

b = aperture E-plane dimension.

If the effects of higher order modes at the aperture of the horn are assumed to be negligible and it is assumed that the aperture is illuminated with a TE_{10} rectangular mode, the aperture breakdown power is given by[10]

$$P_{apt} = 1{\cdot}33 \times 10^{-3}(ab)(\lambda/\lambda_g)E_{apt}^2 \quad (2)$$

where P_{apt} = aperture breakdown power (W)
a = aperture H-plane dimension (cm)
b = aperture E-plane dimension (cm)
(λ/λ_g) = ratio of free space to guide wavelength in the aperture
$(\lambda/\lambda_g) = [1-(\lambda/2a)^2]^{\frac{1}{2}}$
E_{apt} = electric breakdown field for radomes located at the aperture of the horn ($V_{r.m.s.}$/cm)

The breakdown power for radomes located in the far field of the antenna is given by

$$P_{far} = 4\pi R^2(E_{far}^2/120\pi)/G \quad (3)$$

where P_{far} = far field radome breakdown power (W)
R = radome radius (cm)
E_{far} = electric breakdown field for radomes located in the far field of the horn ($V_{r.m.s.}$/cm)
G = antenna gain (per unit)

For large rectangular apertures illuminated by the TE_{10} mode, the antenna gain is given by Silver[11] as

$$G = 10{\cdot}2\frac{(\text{area of aperture})}{\lambda^2} = 10{\cdot}2(ab)/\lambda^2 \quad (4)$$

Assuming that the breakdown field is independent of radome depth and antenna dimensions, it is found that the ratio of far field to aperture breakdown power for a normalized radome depth equal to unity is approximately equal to a constant which is independent of aperture dimensions, i.e.

$$[P_{far}/P_{apt}] = 9{\cdot}8\ (\lambda_g/\lambda) = 9{\cdot}8 \text{ approximately} \quad (5)$$

In general, the (λ_g/λ) factor is approximately unity for most apertures. This result indicates that it should be possible to construct a normalized radome breakdown power curve as a function of normalized radome depth that is relatively independent of aperture dimensions. Under the restrictions that the breakdown fields at the aperture and in the far field should be approximately equal, the normalized graph should also be relatively independent of: (1) microwave frequency, (2) pressure, (3) pulse width and (4) pulse repetition frequency.

With the exception of the dependence upon microwave frequency, which has not been investigated, the experimental results indicate that the proposed characteristics are in agreement with experiment, even for non-symmetrical antennas and for pulse repetition frequencies approaching continuous wave breakdown. For example, in Table 1 the normalized radome breakdown powers are given as a function of pressure and pulse repetition frequency for a 1·400 in. × 1·900 in. antenna aperture with a 4·5 in. radome depth which corresponds to a normalized radome depth of unity.

Table 1. Normalized Radome Breakdown Power as a Function of Pressure and Pulse Repetition Frequency

Pressure (mm Hg)	100 p.p.s	400 p.p.s.	1000 p.p.s.	2000 p.p.s.	3000 p.p.s.	4000 p.p.s.	5000 p.p.s.	6000 p.p.s.
1	10·3	10·8	10·0	10·0	9·30	9·70	9·35	9·20
5	11·2	11·3	11·2	11·9	11·3	11·2	10·1	9·50
15	9·85	10·4	11·3	11·1	11·0	11·4	10·5	9·90

1·400 in. × 1·900 in. antenna, 4½ in. radome depth, 0·37 μ sec. pulse, critical p.r.f. = 2000 pulses/sec, 9170 Mc/s.

Since the variation of the normalized radome breakdown power is only of the order of ± 10 per cent for a pressure ratio of 15–1, these data appear to confirm that the normalized radome breakdown curve is approximately independent of pressure, as predicted. The data also indicate that the normalized radome breakdown power is relatively insensitive to pulse repetition frequency.

In Fig. 7, normalized breakdown curves derived from experimental measurements are

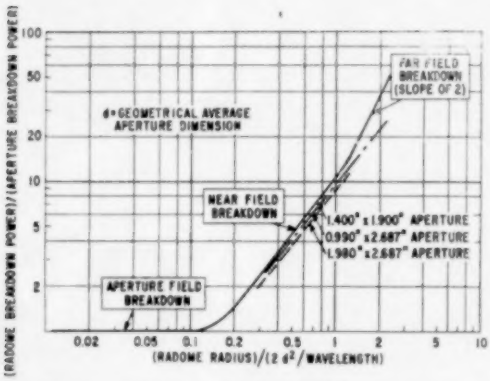

Fig. 7. Normalized radome breakdown power vs. normalized radome depth.

given for various antennas. These curves are in general agreement with the proposed theory in that the normalized powers range between 9–11 for a normalized radome depth of unity. Since the date of the 0·990 in. $\times$ 2·687 in. antenna aperture are in good agreement with the data of other, more symmetrical antennas, it appears that the normalized curve is relatively independent of antenna dimensions. Such a curve, therefore, appears to be useful for selection of minimum radome depth for a given antenna power requirement.

Data taken with the 2·1 μsec pulse were also found to be in good agreement with that taken with the 0·37 μsec pulse which also indicates that the normalized curve is relatively independent of pulse width.

To aid in the calculation of radome breakdown power for X-band frequencies, in Fig. 8 are given the experimentally determined breakdown fields for a radome located at the aperture of an antenna. For the antennas tested it was found that the aperture breakdown fields were relatively independent of antenna dimensions.

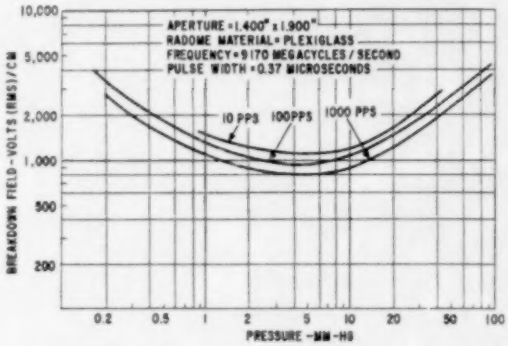

Fig. 8. Antenna aperture breakdown fields.

5. ANALYSIS OF ANTENNA–RADOME BREAKDOWN

The analysis of antenna–radome breakdown is more complex than the more familiar waveguide or cavity breakdown since the antenna breakdown geometry has no enclosing metal boundaries at which the electron density becomes zero. The distribution of electrons above the radome is not fixed by the configuration of the antenna and radome alone, therefore, but will vary with pressure, pulse width and pulse repetition frequency. Previous analyses of antenna breakdown by others have assumed that the diffusion length for antenna breakdown is a constant. In general, the latter model does not agree with the experimental results. This paper presents a more complete analysis of antenna breakdown which takes into account the variable character of the electron distribution above the radome surface. The detailed analysis is given in the appendix. The following will describe qualitatively the steps in the analysis and the results obtained.

(a) *Continuous wave antenna–radome breakdown*

The method of analysis is similar, in principle, to the analysis of cylindrical cavity breakdown by Herlin and Brown.[2] That is, starting from the condition defining CW breakdown

$$\nabla^2(Dn) + \frac{v}{D}(Dn) = 0 \tag{6}$$

where D = diffusion coefficient
n = electron density
v = net ionization frequency.

The ratio of the ionization frequency divided by the diffusion coefficient is expressed in terms of the electric field existing at the top of the radome and the resulting differential equations are solved in accordance with the boundary conditions applicable to antenna–radome breakdown. Inspection of the solutions of the differential equations indicates that the effective diffusion length for antenna–radome breakdown is given by

$$\Lambda_{CW} = \left[\frac{R_0^2}{p^2 u}\right]^{\frac{1}{2}} \left[\frac{k_r^2}{1+4_s{}^2 k_r^2}\right]^{\frac{1}{2}} \left[\frac{8D_0 p}{(v_0/p)\beta}\right]^{\frac{1}{2}} \tag{7}$$

where R_o = radome depth
p = pressure
u = antenna beam width parameter
k_r = proportionality constant for diffusion tangential to the radome surface
s = radome surface charge parameter
D_o = diffusion coefficient corresponding to the maximum field intensity at the top of the radome
v_o = net ionization frequency corresponding to the maximum field intensity at the top of the radome
β = ionization exponent

The surface charge parameter, s, ranges between zero and unity, depending on the degree of ionization adjacent to the radome surface and the dielectric constant of the radome material. For large surface charge, $s = 0$, while for no surface charge, $s = 1$. Experimental comparisons indicate that this parameter is approximately zero for continuous wave antenna–radome breakdown.

The analysis indicates that the proportionality constant for diffusion tangential to the radome surface should be approximately, $k_r = 1/\pi$. This value is also in agreement with experimental comparisons. The effective parallel plate spacing, d, is related to the diffusion length by $d = \pi\Lambda$;[13] therefore, selecting $s = 0$ and $k_r = 1/\pi$, the effective parallel plate spacing for CW antenna–radome breakdown is given by

$$d_{CW} = \left[\frac{R_0^2}{p^2 u}\right]^{\frac{1}{2}} \left[\frac{8D_0 p}{(v_0/p)\beta}\right]^{\frac{1}{2}} \tag{8}$$

The second bracketed quantity is a function of the effective field divided by the pressure and is given in Fig. 9.

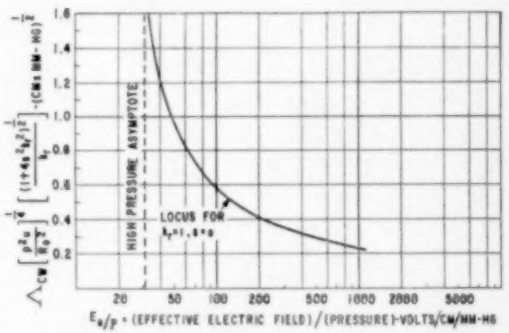

Fig. 9. Diffusion length for CW antenna–radome breakdown.

$$\Lambda_{CW} = \left[\frac{R_0{}^2}{p^2 u}\right]^{\frac{1}{2}} \left[\frac{k_r{}^2}{1 + 4s^2 k_r{}^2}\right]^{\frac{1}{2}} \left[\frac{8D_0 p}{(v_0/p)\beta}\right]^{\frac{1}{2}}$$

The general definition of the effective field is given by Margenau.[3] Gould and Roberts[4] indicate that the effective field for air is given approximately by

$$\frac{E}{E_e} = \left[1 + \left(\frac{36}{p\lambda}\right)^2\right]^{\frac{1}{2}} \tag{9}$$

where p = pressure at 20°C (mmHg)
λ = wavelength (cm).

It may be noted in Fig. 9 that as the ratio of the

effective field divided by the pressure approaches 30 V/cm/mmHg, the diffusion length for antenna–radome breakdown increases very rapidly. This asymptote corresponds to breakdown at high pressures. This graph is applicable to any antenna or radome geometry, providing an equivalent beam width and radome depth can be defined. The data of Lechtreck,[5] or of Barrar and Wilcox[6] could be used to define an equivalent beam width in the near field of an antenna.

Significantly, the diffusion length for continuous wave antenna–radome breakdown is not independent of pressure or field intensity and is not a linear function of radome depth. This is in contrast to cavity or waveguide breakdown where the diffusion length is a constant which depends only on geometry and is a linear function of the cavity dimensions. This means that the usual scaling laws for microwave breakdown (where the diffusion length is proportional to the wavelength) must be re-examined for application to antenna–radome breakdown.

Given experimental measurements of breakdown field as a function of pressure, it is possible to determine the experimental diffusion lengths corresponding to these data from data available in the literature for the breakdown of cavities.[2, 4] Such experimentally determined diffusion lengths are given in Figs. 10 and 11 as functions of pressure for various radomes and antennas. In the low pressure region it may be noted that the diffusion lengths are approximately inversely proportional to the square root of the pressure, which agrees with the suggested theoretical behaviour since the experimental breakdown fields indicate that the quantity $[(8D_a p)/(v_a/p)\beta]^{\frac{1}{2}}$ is relatively independent of pressure for low pressure antenna–radome breakdown (in general, less than 10 mmHg at X-band frequencies). In addition, it may be noted that the diffusion lengths increase as radome depth or antenna beam width are increased. The relative increases in diffusion length with increased radome depth or antenna

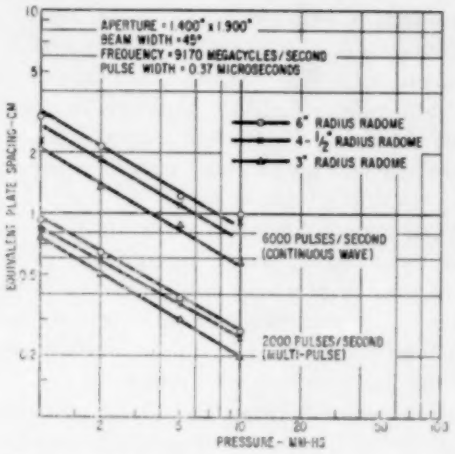
APERTURE = 1.400" x 1.900"
BEAM WIDTH = 45°
FREQUENCY = 9170 MEGACYCLES/SECOND
PULSE WIDTH = 0.37 MICROSECONDS
6" RADIUS RADOME
4 - 1/2" RADIUS RADOME
3" RADIUS RADOME
6000 PULSES/SECOND (CONTINUOUS WAVE)
2000 PULSES/SECOND (MULTI-PULSE)
EQUIVALENT PLATE SPACING - CM
PRESSURE - MM-HG

Fig. 10. Diffusion lengths for various radomes.

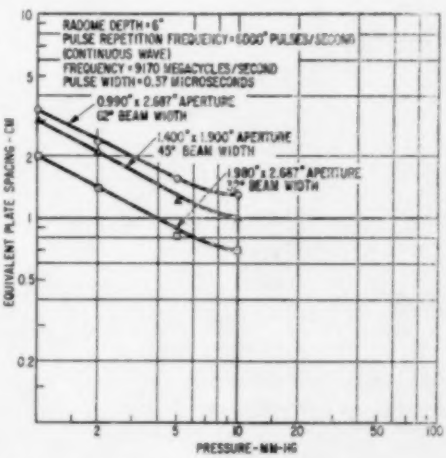
RADOME DEPTH = 6"
PULSE REPETITION FREQUENCY = 6000 PULSES/SECOND (CONTINUOUS WAVE)
FREQUENCY = 9170 MEGACYCLES/SECOND
PULSE WIDTH = 0.37 MICROSECONDS
0.990" x 2.687" APERTURE 62° BEAM WIDTH
1.400" x 1.900" APERTURE 45° BEAM WIDTH
1.980" x 2.687" APERTURE 32° BEAM WIDTH
EQUIVALENT PLATE SPACING - CM
PRESSURE - MM-HG

Fig. 11. Diffusion lengths for various antennas.

beam width are approximately equal to that predicted by theory. The experimental diffusion lengths also indicate that the diffusion length is less sensitive to variations in radome depth and antenna beam width at lower pulse repetition frequencies. This is seen in Fig. 10, for example, where the spacing between the diffusion length curves is smaller for 2000 pulses/sec than for the corresponding curves at 6000 pulses/sec which approximate continuous wave breakdown. These

data clearly indicate the variable nature of antenna–radome diffusion both as a function of geometry as well as pressure and field intensity and also pulse repetition frequency. In general, such a variable diffusion length would be encountered in any unbounded media where non-uniform field intensities exist.

Further analysis has been made which indicates that the diffusion length for antenna–radome breakdown is relatively independent of radome material. Experimental data with glass (dielectric constant = 5·7) and Teflon (dielectric constant = 2·0) are in agreement with that analysis.

The experimental antenna–radome breakdown fields calculated from the measured breakdown powers are compared in Figs. 12 and 13 with the CW breakdown fields calculated by using the theoretical diffusion length obtained from equation (7) together with the breakdown data available in the literature for parallel plate and cavity breakdown.[2, 4, 15] As discussed above, the quantities k_r and s in equation (7) were set equal to $1/\pi$ and 0, respectively. Also included in Figs. 12 and 13 are the CW breakdown fields calculated by assuming the diffusion length is a constant equal to $\lambda/2$. The experimental data correspond to a radome depth of 3 in. and antenna beam widths of 32° and 45°. The measured data were taken with pulsed X-band power; however, for the pulse repetition frequency (6000 pulses/sec) and pulse width (0·37 μ/sec) used in the tests, it was observed that continuous wave breakdown conditions were approximately achieved.

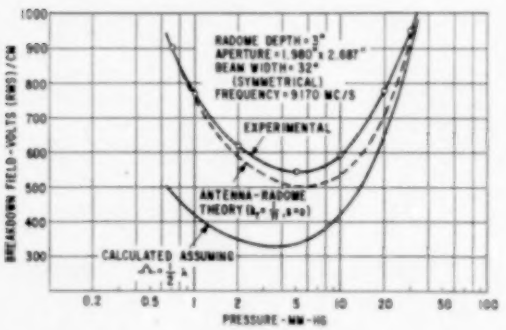

Fig. 12. Comparison of experimental and theoretical antenna–radome CW breakdown fields.

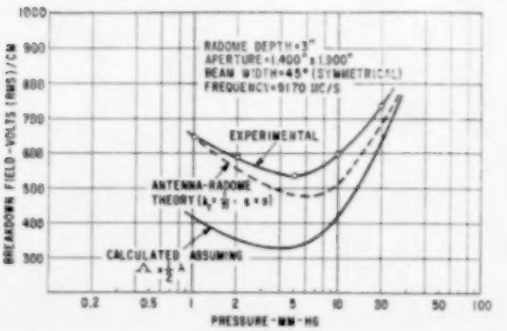

Fig. 13. Comparison of experimental and theoretical antenna–radome CW breakdown fields.

As is indicated in Figs. 12 and 13, the agreement between experimental and theoretical breakdown fields is good over the range of pressures tested. The slight difference at higher pressures is due in part to using breakdown data for pure air to compute the diffusion lengths which resulted in a diffusion length that was slightly larger than that corresponding to breakdown data for impure air. The breakdown data of Rose and Brown[15] for impure air were used in computing the breakdown fields from the theoretical diffusion lengths and pressure since this corresponded to the experimental breakdown conditions. The comparison indicates that the assumption sometimes made that the diffusion length equals $\lambda/2$ may be seriously in error in some instances.

(b) *Single pulse antenna–radome breakdown*

The problem of single pulse breakdown in cavities is relatively straightforward since the diffusion length for single pulse breakdown is essentially identical to the diffusion length for continuous wave breakdown. In general, this is not the case for unbounded media such as is encountered above the surface of the radome. For such unbounded media, the transient motion of electrons during the time the r.f.

pulse is applied must be considered. If it is assumed that the ionization is initiated at the radome surface, and the root-mean-square distance the glow diffuses is L_g, during the pulse duration, t for one dimensional diffusion is given by[8]

$$L_g = \text{glow diffusion distance} = (2Dpt/p)^{\frac{1}{2}} \quad (10)$$

It would appear that this glow diffusion distance would constitute an effective diffusion length for short pulses since it defines the outer bound of electron density. Assuming this to be the case, it would be expected that

$$\Lambda_p = L_g \quad \text{when} \quad Lg \ll \Lambda_{CW}$$
$$\Lambda_p = \Lambda_{CW} \quad \text{when} \quad \Lambda_{CW} \ll L_g$$

where Λ_p = diffusion length for single pulse breakdown

Λ_{CW} = diffusion length for CW breakdown

A function which satisfies these conditions is the exponential function

$$\Lambda p/\Lambda_{CW} = 1 - \exp(-L_g/\Lambda_{CW})$$

Further analysis of pulsed antenna–radome breakdown indicates that a correction factor (Λ_0), is required which includes the effect of the extent of ionization above the radome surface due to the finite pulse duration. Including this factor, the diffusion length for single pulse antenna–radome breakdown is approximated by

$$\Lambda_p/\Lambda_{CW} = (1+\Lambda_0/L_g)[1-\exp(-L_g/\Lambda_{CW})] \quad (11)$$

where $\Lambda_0 = R_0/(v_0 t\beta)$

In Fig. 14 the experimental diffusion lengths calculated from the antenna–radome pulsed breakdown data are compared to the glow diffusion distance. The agreement between the curve corresponding to single pulse breakdown and the glow diffusion distance is good for pressures less than 10 mmHg. The divergence at higher pressures is attributed to the Λ_0 correction factor, since calculations using the experimental breakdown fields indicate that this correction predominates above approximately 10 mmHg. The experimental diffusion lengths corresponding to the single pulse breakdown data were calculated using single pulse breakdown curves similar to that given by Lathrop and Brown,[7] or Gould and Roberts.[4] The experimental diffusion lengths corresponding to multi-pulse breakdown data were also calculated from the single pulse breakdown curves by using a modified pulse width which incorporates the effect of the pulse repetition frequency.

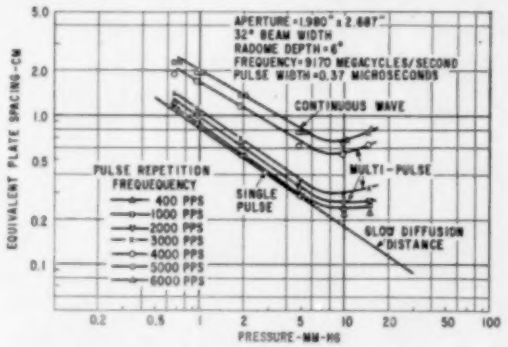

Fig. 14. Diffusion length vs. pressure.

A comparison is made in Table 2 between the experimental diffusion lengths calculated from measured antenna–radome breakdown powers for pulse widths of 0·37 μsec and 2·1 μsec. As seen in this table, the diffusion lengths are approximately proportional to the square root of the pulse widths as predicted.

Table 2. Single Pulse Diffusion Lengths for Pulse Widths of 0·37 and 2·1 μsec

pulse width (μsec)	diffusion length (cm)	experimental ratio	theoretical ratio	difference (%)
2·1	0·75	2·14	2·4	10
0·37	0·35			

aperture = 1·400 in. × 1·900 in., pressure = 5 mmHg, frequency = 9170 Mc/s, radome located at antenna aperture.

(c) *Multipulse antenna–radome breakdown*

It is possible to analyse the case of multipulse breakdown using single pulse breakdown curves by defining an effective pulse width which incorporates the effect of pulse repetition frequency. Such an effective pulse width is defined by

$$t_{\text{eff}}/t = (1/pT)\left[\frac{\ln(n_b/n_0)}{v_a/p + D_a p/(p\Lambda_a)^2}\right] \qquad (12)$$

where t = pulse duration
T = pulse off time = (pulse repetition frequency)$^{-1}$
n_b = electron density at breakdown
n_0 = ambient electron density
v_a = attachment frequency in the afterglow between pulses
D_a = diffusion coefficient in the afterglow between pulses
Λ_a = diffusion length in the afterglow

Single pulse breakdown is defined by $t_{\text{eff}}/t = 1$.

Low pressure pulsed breakdown occurs when the electron density becomes so large that ambipolar diffusion sets in. The pulse repetition frequency for which single pulse antenna–radome breakdown conditions were achieved experimentally was compared with the pulse repetition frequency predicted by assuming that ambipolar diffusion losses were predominant during the afterglow between pulses. The close agreement indicated that ambipolar diffusion was the principal loss mechanism; consequently, that assumption was used in computing the effective pulse widths for multipulse antenna–radome breakdown. The experimental diffusion lengths were calculated using this definition of effective pulse width together with single pulse breakdown data similar to that given by Gould and Roberts.[4] In Fig. 14 are given the experimental diffusion lengths calculated from the measured multipulse breakdown powers. It may be noted that the calculated diffusion lengths are approximately inversely proportional to the square root of the pressure.

6. SCALING LAWS FOR ANTENNA–RADOME BREAKDOWN

As has been previously indicated, the diffusion length for continuous wave antenna–radome breakdown is proportional to the square root of the radome depth; therefore, it is not obvious that normal scaling laws (where the diffusion length is proportional to the wavelength) will necessarily apply to antenna–radome breakdown. Wavelength, pressure, and pulse width scaling laws will be discussed in the following, starting from fundamental relationships of microwave breakdown theory.

(a) *High pressure antenna–radome breakdown*

At high pressures diffusion has a negligible effect on breakdown. Under these conditions the breakdown field at the radome surface is independent of radome depth and antenna dimensions, and is proportional to pressure. Therefore, if the pressures are selected to be inversely proportional to wavelength, the ratio of the breakdown fields is

$$E_1/E_2 = p_1/p_2 = \lambda_2/\lambda_1 \qquad (13)$$

Considering two geometrically similar, scaled antenna–radomes, the breakdown power ratio is

$$P_1/P_2 = (R_1/R_2)^2(E_1/E_2)^2 = \\ = (\lambda_1/\lambda_2)^2(\lambda_2/\lambda_1)^2 = 1. \qquad (14)$$

For these high pressures, therefore, normal wavelength scaling holds and the breakdown power ratio equals unity when pressures are selected inversely proportional to wavelength.

The same holds true for pulsed breakdown at lower pressures if the pulse width is narrow enough and the pulse repetition frequency is low enough so that breakdown is controlled by the pulse width and is independent of diffusion. In this case the single pulse breakdown fields are functions of pressure times pulse width.[4] The effects of pulse width on antenna–radome breakdown can be readily determined from a plot of the high pressure single pulse breakdown fields as a function of pressure and pulse width such as are given by Gould and Roberts.[4] For

example, in Table 3 the measured power ratios taken from Fig. 5 and those predicted from the single pulse breakdown graph for several pulse widths are compared.

Table 3. Comparison of Radome Breakdown Powers

t (μsec)	$p\,t$ (mmHg, sec)	Theory E_e/p (V/cm/mm)	PWR ratio (theory)	PWR ratio (experiment)
0·37	$0{\cdot}56 \times 10^{-5}$	67	1·0	1·0
1·2	$1{\cdot}80 \times 10^{-5}$	52	1·7	1·7
2·1	$3{\cdot}15 \times 10^{-5}$	47	2·0	2·0

Aperture dimensions = 1·400 in × 1·900 in., radome depth = 4·5 in., frequency = 9170 Mc/s, pressure = 15 mmHg.

(b) *Low pressure antenna–radome breakdown*

As has been previously indicated, the diffusion length for antenna–radome breakdown is of the form

$$\Lambda_{CW} = \left[\frac{R_0^2}{p^2 u}\right]^{\frac{1}{4}}\left[\frac{k_r^2}{1+4s^2k_r^2}\right]^{\frac{1}{4}} \quad [\text{function of } E_e/p)]$$

If conditions near the minimum of the breakdown field versus pressure curve are considered, it is a reasonably good approximation to assume that E_e/p is relatively constant and independent of wavelength. This is indicated, for example, in the calculations given by MacDonald.[12] The theory of microwave breakdown indicates that the ratio of pressures for minimum breakdown for two different wavelengths and diffusion geometries is given by[13]

$$(p_1/p_2)_{\min} = [(\Lambda_2\lambda_2)/(\Lambda_1\lambda_1)]^{\frac{1}{2}} \qquad (15)$$

Considering, therefore, conditions near the minimum of the breakdown curve, the ratio of diffusion lengths for two scaled antenna–radomes is given approximately by

$$(\Lambda_1/\Lambda_2)_{\min} \doteq \lambda_1/\lambda_2 \qquad (16)$$

That is, normal scaling laws hold approximately for antenna–radome breakdown near minimum breakdown which is, of course, the condition of most interest in practical applications.

Substituting this result, it is found that the pressures for minimum breakdown are also inversely proportional to wavelength. Furthermore, the theory of microwave breakdown indicates that minimum breakdown occurs when the collision frequency is approximately equal to the applied r.f. frequency. This being true, along with the assumption that E_e/p is relatively constant, it is found that the minimum antenna–radome breakdown fields are also inversely proportional to the wavelength.

An analysis of very low pressure antenna–radome breakdown indicates that a similar scaling law should also apply approximately if the pressures are selected inversely proportional to the wavelength. For example, the theory of microwave breakdown indicates that at very low pressures the effective breakdown voltage, defined as the product of the effective field times the diffusion length, is approximately constant.[13] Also, for low pressure breakdown, the r.m.s. breakdown field is approximately proportional to the effective breakdown field divided by the product of pressure times wavelength. Substituting these relations and selecting the pressures inversely proportional to the wavelengths, it is found that a scaling law similar to equation (13) approximately holds since, for low pressure breakdown (high values of E_e/p), the antenna–radome diffusion length becomes an insensitive function of E_e/p, as is indicated in Fig. 9.

The above discussion indicates that, to a first approximation, normal scaling laws should hold for antenna–radome breakdown for low pressure as well as high pressure breakdown. It should be appreciated, however, that these scaling laws appear to apply only approximately to antenna–radome breakdown in contrast to their exact application to cavity breakdown. Further measurements of antenna–radome breakdown at S-band frequencies are planned to test the applicability of these scaling laws by comparison with present X-band data.

7. BREAKDOWN IN UNBOUNDED MEDIA

As has been discussed in the preceding sections, the diffusion length for continuous wave breakdown in media where there are no sharply defined diffusion boundaries will, in general, be functions of the pressure as well as the magnitude and spacial distribution of the field intensity. In addition, if pulsed r.f. is employed, the equivalent diffusion lengths will also be functions of the pulse width and the pulse repetition frequency. The exact solution for the complex situation encountered in the re-entry of a missile, for example, would be extremely difficult; however, it appears that techniques similar to those used in the analysis of antenna–radome breakdown should be applicable.

In considering pulsed breakdown in an unbounded media, it has been found that the equivalent diffusion length is approximately of the form

diffusion length for pulsed breakdown
= (pulse width/pressure)$^{\frac{1}{2}}$ (function of geometry)
= (pulse width/pressure)$^{\frac{1}{2}}$ d_0

Using this definition of diffusion length, it is possible to determine the relation between the single pulse breakdown fields, the pressure and pulse width from single pulse breakdown data already available in the literature.[4] This is indicated in Fig. 15 which gives the single pulse breakdown fields as functions of pulse width, pressure, and the geometrical diffusion length factor (d_0). These curves should be useful for estimating the pulsed breakdown fields in unbounded media. It should be noted, however, that these curves are based on an assumed ratio of breakdown electron density to ambient electron density of 10^8 which corresponds to an ambient electron density of the order of 10 electrons/cm^3. A correction would have to be included for other ambient ionizations.

8. CONCLUSIONS

It has been found that the equivalent diffusion lengths calculated from the measured breakdown data exhibit a dependence on radome depth, radome material, pressure, pulse repetition frequency, pulse width, and antenna beam width. These relationships have been incorporated into the analysis. Furthermore, it has been observed experimentally that the antenna breakdown power drops off sharply above a certain critical pulse repetition frequency and appears rapidly to approach the ultimate continuous wave breakdown level. The latter behaviour is attributed to an increasing radome surface charge and can be determined from the analysis.

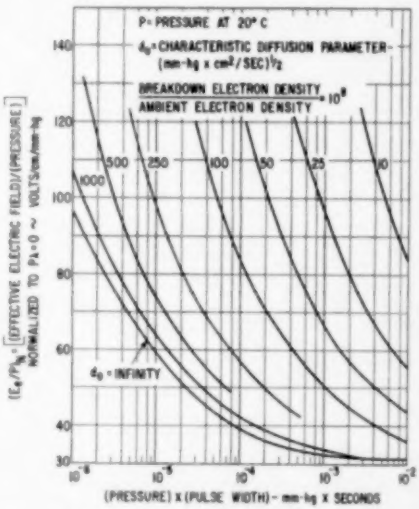

Fig. 15. Single pulse breakdown fields for unbounded media.

In general, the results indicate that increasing the radome depth, antenna beam width or pulse repetition frequency decreases the breakdown field; however, for a limited range of conditions, it was found that the breakdown field was relatively independent of the radome depth or antenna beam width. Under these conditions the investigation has shown that it is possible to construct graphs of normalized radome breakdown power as a function of normalized radome

depth. With a knowledge of the breakdown field for a radome located at the antenna aperture, the radome breakdown power for a range of radome and antenna sizes can be readily determined from a single graph.

Analysis of the measured breakdown data has also shown that outward diffusion of electrons occurs in radome breakdown, and that the effective diffusion length is proportional to the distance which the electrons travel in a time, t, equal to the pulse width. According to diffusion theory, this distance in an unbounded medium is proportional to $(t/p)^{\frac{1}{2}}$ where p is the pressure. From these results, a graph of the single-pulse breakdown field has been constructed as a function of pressure, pulse width, and a diffusion length which is proportional to $(t/p)^{\frac{1}{2}}$. Such a graph appears to be generally applicable to pulsed breakdown conditions where electron diffusion throughout an unbounded medium must be considered.

It appears that techniques similar to those used in the analysis of antenna–radome breakdown are applicable to the problem of breakdown in the region of the plasma sheath; however, additional basic data on the characteristics of ionized gases under conditions similar to those encountered in re-entry appear to be required before an accurate analysis can be made.

Acknowledgements—The author wishes to express his appreciation to Mr. B. W. Rechnitzer and to Mr. C. C. Allen of the General Engineering Laboratory of the General Electric Company and to Mr. E. B. Mullen of the Defence Systems Department of the General Electric Company. Mr. Rechnitzer conducted much of the testing, and the correlation between theory and experiment that was observed is due to his care in making the measurements. Mr. Allen and Mr. Mullen contributed much appreciated guidance, discussion and encouragement.

APPENDIX

Analysis of continuous wave antenna–radome breakdown

The antenna–radome geometry being considered is indicated in Fig. 16 which shows a horn antenna capped with a hemispherical radome of radius "R_0". For simplicity it will

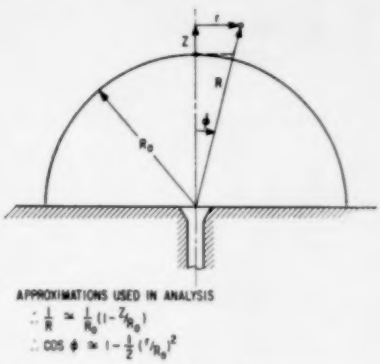

Fig. 16. Radome geometry.

be assumed that the antenna radiation pattern is circularly symmetric. The radiation pattern of horn antennas down to the 1/2 power level can be adequately represented by

$$E/E_0 = \left(\frac{R_0}{R}\right)\cos^u\phi \qquad \text{(A1)}$$

where E/E_0 = relative electric field intensity with respect to intensity at the top of the radome
ϕ = angle measured from the centre of the beam
u = exponent that is a function of the beam width at the $\frac{1}{2}$ power level
R = radius vector from the horn to point in space
R_0 = radome radius

Because the ionization frequency is a sensitive function of the field intensity, it is necessary to consider only a small region near the top of the radome. Considering r and z to be small compared to the radome radius, the field intensity near the top of the radome is given by

$$(E/E_0) = [1-z/R_0][1-\tfrac{1}{2}u(r(R_0)^2] \qquad \text{(A2)}$$

As is indicated by Herlin and Brown,[1] the condition for CW breakdown is given by

$$\nabla^2(Dn) + \frac{V}{D}(Dn) = 0 \qquad \text{(A3)}$$

where D = diffusion coefficient
n = electron density
v = net ionization frequency which takes account of attachment.

Following the lead of Herlin and Brown,[2] the ratio of the ionization frequency divided by the diffusion coefficient is related to the electric field by

$$(v/D)/(v_0/D_0) = \gamma_0 E_0^2 (E/E_0)^\beta \qquad \text{(A4)}$$

where $\gamma_0 = v_0/D_0E_0^2$ = high frequency ionization coefficient given by Herlin and Brown (V^{-2})
E_0 = maximum field intensity (V/cm)
β = ionization exponent

γ_0 and E_0 refer to the ionization coefficient and electric field at the point of maximum field while E refers to the electric field at another point in space. Both the ionization coefficient, γ_0, and the ionization exponent, β, are known functions of E/p.[1]

Substituting the expression for the electric field near the top of the radome (equation 2) into the above relation and neglecting second order quantities, the condition for antenna–radome breakdown is expressed by

$$\nabla^2\psi + \tfrac{1}{2}\gamma_0 E_0^2 \psi[1 - 2\beta z/R_0 + 1 - \beta u(r/R_0)^2] = 0 \qquad \text{(A5)}$$

where $\psi = (Dn)$

Assuming a product solution, $(Dn) = R(r)Z(z)$, we have

$$\nabla_r^2 R + \tfrac{1}{2}\gamma_0 E_0^2[1 - \beta u(r/R_0)^2]R + k_1^2 R = 0 \qquad \text{(A6)}$$

$$\nabla_z^2 Z + \tfrac{1}{2}\gamma_0 E_0^2[1 - 2\beta z/R_0]Z + k_1^2 Z = 0 \qquad \text{(A7)}$$

where k_1^2 is the separation constant.

Since it is physically impossible for the ionization frequency to be negative, the solutions to the above equations must be restricted to regions where the quantities in brackets are greater than or equal to zero. The physics of the problem also indicate that $R(r)$ must be an even function of r and must decrease with increasing r. Since the surface charge conditions at the radome surface are not known, one can not say that $Z(z)$ will necessarily be a decreasing function of z near to the radome surface. In fact, one might expect the solution close to the radome surface to be similar to the charge distribution for parallel plate breakdown when the plates have a surface charge; that is,

$$Z(z) = Z_0 \cos \pi s(z - L/2)/L \qquad \text{(A8)}$$

where L = plate spacing
s = surface charge parameter
Z_0 = maximum charge density at mid-point between plates.

Although the above approximations to the ionization frequency are only of first order, the approximations are good in regions of maximum field intensity and are inaccurate only in regions of low ionization which have little effect on breakdown.

Solutions for the electron density in regions far removed from the radome surface could be approximately obtained by setting the ionization frequency equal to zero; however, these solutions would not be of interest in this analysis since the diffusion lengths encountered in antenna–radome breakdown are relatively small.

It is found that the solutions for $R(r)$ and $Z(z)$ near to the radome surface are

$$R(r) = \exp\left[-(r/r_0)^2\right] \qquad \text{(A9)}$$

where $r_0 = [8R_0^2/(\gamma_0 E_0^2 \beta u)]^{\frac{1}{4}}$ (A10)

and $k_1^2 = -\tfrac{1}{2}\gamma_0 E_0^2 + 4/r_0^2$ (A11)

$$Z(z) = \exp\left[a_0 z + (1/3)a_2 z^3 + (1/4)a_3 z^4 + \ldots\right] \qquad \text{(A12)}$$

where $a_0 = \pm j2/r_0$
$a_2 = \tfrac{1}{2}\gamma_0 E_0^2 \beta/R_0$
$a_3 = \pm j(1/3)(2/r_0)\gamma_0 E_0^2 \beta/R_0$, etc.

Analysis of the measured radome breakdown data indicates that for the E/p ratios encountered in radome breakdown, the higher order terms in $Z(z)$ are negligible for $z \leq r_0$; therefore, to a good

approximation near the radome surface, $Z(z)$ is of the form

$Z(z)$=sinusoidal function with the kernel $(2z/r_0)$.

Since approximately uniform field conditions apply close to the radome surface, $Z(z)$ will have a form similar to that for parallel plate breakdown where the plates have a surface charge; that is,

$$Z(z) = \cos \pi s(z - L/2)/L \qquad \text{(A13)}$$

where $L = \frac{1}{2}r_0\pi$

s=surface charge parameter.

For no surface charge on the radome, $s = 1$, while for very large surface charge on the radome, $s = 0$. The surface charge parameter (s) also includes the effect of the image charges in the dielectric material of the radome surface. Low ionization of the air adjacent to the radome and a very high dielectric constant are equivalent to zero surface charge, or $s = 1$. Experimental comparisons indicate that for continuous wave breakdown the surface charge parameter is approximately zero, $s = 0$.

The effective diffusion length for diffusion in both the radial and normal directions is then

$$1/\Lambda_e^2 = 1/\Lambda_r^2 + 1/\Lambda_z^2 \qquad \text{(A14)}$$

where $$\Lambda_r = k_r r_0 \qquad \text{(A15)}$$

and $$\Lambda_z = \tfrac{1}{2}r_0/s \qquad \text{(A16)}$$

The diffusion length for continuous wave antenna–radome breakdown, therefore, is

$$\Lambda_{CW} = k_r r_0/(1 + 4s^2 k_r^2)^{\frac{1}{2}}$$

The parameter (k_r) is a proportionality constant. Experimental comparisons indicate that this constant approximately equals $(1/\pi)$. This value appears reasonable in that, if the diffusion were only in one dimension the constant (k_r) would approximately equal two since the electron distribution in the radial direction would approximate that for parallel plate breakdown. Since radial diffusion occurs over an angle of (2π) radians, however, the equivalent radial diffusion length is given approximately by

$$\Lambda_r = k_r r_0 \doteq (2/2\pi)r_0 = (1/\pi)r_0.$$

It can be shown that the quantity

$$[(\gamma_0/p^2)E_0^2\beta] = [(v_0/p)\beta/(D_0 p)]$$

which is a function of the effective field divided by the pressure. The diffusion length is, therefore, given by

$$\Lambda_{CW} = \left[\frac{R_0^2}{p^2 u}\right]^{\frac{1}{4}}\left[\frac{k_r^2}{1+4s^2k_r^2}\right]^{\frac{1}{4}}\left[\frac{8D_0 p}{(v_0/p)\beta}\right]^{\frac{1}{4}} \qquad \text{(A17)}$$

where the final quantity in brackets is a function of E_e/p and $k_r \doteq 1/\pi$ and $s \doteq 0$.

REFERENCES

1. M. A. Herlin and S. C. Brown, *Breakdown of a Gas at Microwave Frequencies*, Massachusetts Inst. Technol. RLE Tech. Rep. No. 60 (May 1948).
2. M. A. Herlin and S. C. Brown, *Microwave Breakdown of a Gas in a Cylindrical Cavity of Arbitrary Length*, Massachusetts Inst. Technol. RLE Tech. Rep. No. 77 (July 1948).
3. H. Margenau, *Phys. Rev.* **60**, 508 (1946).
4. L. Gould and L. W. Roberts, *J. Appl. Phys.* **27**, 1162 (1956).
5. L. W. Lechtreck, *Trans. Inst. Radio Engrs. on Antennas* **3**, 138 (1955).
6. R. B. Barrar and C. H. Wilcox, Trans. *Inst. Radio Engrs. on Antennas* **6**, 43 (1958).
7. J. W. Lathrop and S. C. Brown, *The Relationship of Pulsed to C-W Breakdown of a Gas at Microwave Frequencies*, Massachusetts Inst. Technol. RLE Tech. Rep. No. 146 (Dec. 1949).
8. L. B. Loeb, *Fundamental Processes of Electrical Discharges in Gases* p. 175. Wiley, New York (1939).
9. E. H. Braun, *Proc. Inst. Radio Engrs.* **41**, 109 (1953).
10. L. Gould, *Microwave High Power Breakdown Study in Handbook on Breakdown of Air in Waveguide Systems.* Navy Department, Bureau of Ships, Electronics Division, Contract Nobsr 53295, Index No. NE-111616 (April 1956).
11. S. Silver, *Microwave Antenna Theory and Design* p. 347. McGraw-Hill, New York (1949).
12. A. D. MacDonald, *Proc. Inst. Radio Engrs.* **47**, 436 (1959).
13. S. C. Brown, *Proc. Inst. Radio Engrs.* **39**, 1439 (1951).
14. R. F. Whitmer, *Electromagnetic Effects Associated with Hypersonic Re-entry Vehicles*, paper presented at *Wescon Conference, August 1959.*
15. D. J. Rose and S. C. Brown, *J. Appl. Phys.* **28**, 561 (1957).

SECTION D

EXPERIMENTAL TECHNIQUES FOR EXPLORING THE INTERACTION OF MICROWAVE ENERGY WITH IONIZED FLOWFIELDS

EXPERIMENTS WITH PLASMAS PRODUCED BY ALKALI-METAL-SEEDED CYANOGEN–OXYGEN FLAMES FOR STUDY OF ELECTROMAGNETIC WAVE PROPAGATION AT THE LANGLEY RESEARCH CENTER

P. W. HUBER
National Aeronautics and Space Administration, Washington, D.C.

Abstract—Development of a facility capable of producing a plasma stream of known constituency with an electron concentration to 10^{15} electrons/cm^3 is described. The technique discussed involves seeding of the combustion products of a cyanogen–oxygen flame with vaporized potassium, and computations of the plasma temperature and electron concentration are outlined. Experimental diagnosis of the plasma stream using microwave beams of 1½ and 3 cm is described, with plasma temperatures of over 4400°K determined. This equipment is shown to be directly applicable to the measurement of electromagnetic wave propagation through plasma layers in the range of electron concentrations from 10^{12} to 10^{15} electrons/cm^3 and election collision frequencies also in the range of that for flight of a hypersonic vehicle. Preliminary propagation and attenuation measurements of telemeter (219·5 Mc/s) signals from models and antennas immersed in the ionized stream are presented and future test plans outlined.

It will certainly not be necessary at this point to review the radio-blackout problem or to discuss the importance of research concerned with transmission through plasma layers. My discussion will be about the methods which we are using at the Langley Research Center of the National Aeronautics and Space Administration to study this problem both theoretically and experimentally. This work represents the combined efforts of several groups at the Center—in particular, the plasmadynamics group and the Instrument Research Group. Our approach is from a very basic point of view—and that is to attempt to understand the mechanism which takes place in the simplest laboratory interaction of an electromagnetic wave and plasma layer. It is the belief that knowledge gained from such basic studies can be applied to a wide variety of problems, providing the pertinent qualifications and limitations in each case are recognized. I would like to begin by describing our method of plasma creation.

It is well known in the case of air that the large degrees of ionization found about hypersonic bodies are due mainly to the very high temperatures involved, say up to 9000°K. There is a way, however, to simulate these very hot plasmas by adding easily ionized alkali metals to

plasmas of much lower temperature. One such scheme was proposed at this laboratory about 2 years ago by Hess and Patterson, who also made preliminary computations of the ionization levels to be expected. Detailed computations have been recently made by Hess and Sabol. The scheme involves the combustion of a cyanogen–oxygen mixture and the seeding of the products of this reaction with vaporized potassium. Cesium is also used for such purposes in some smaller apparatus. This cyanogen–oxygen combustion produces a flame with a temperature of 4850°K at atmospheric pressure and the reaction is shown in Fig. 1. Here we see that the products of this reaction are 2 moles of CO and one mole N_2 with a liberation of 125·4 kcal/mole. The

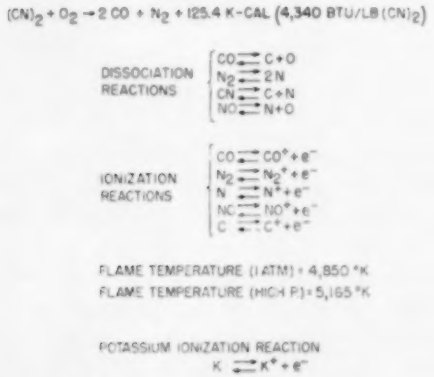
(CN)2 + O2 → 2 CO + N2 + 125.4 K-CAL (4,340 BTU/LB (CN)2)
DISSOCIATION REACTIONS
CO ⇌ C+O
N2 ⇌ 2N
CN ⇌ C+N
NO ⇌ N+O
IONIZATION REACTIONS
CO ⇌ CO+ + e−
N2 ⇌ N2+ + e−
N ⇌ N+ + e−
NO ⇌ NO+ + e−
C ⇌ C+ + e−
FLAME TEMPERATURE (1 ATM) = 4,850 °K
FLAME TEMPERATURE (HIGH P) = 5,165 °K
POTASSIUM IONIZATION REACTION
K ⇌ K+ + e−

Fig. 1. Cyanogen–oxygen reaction.

temperature of 4850°K, which is one of the highest flame temperatures known, is largely due to the high stability of the products, not particularly due to the exothermicity. These are the two most stable molecules and only a slight quantity of these secondary reactions is present. At high pressure, say about 50 atm, the subdual of these reactions would increase the temperature to 5165°K. Combustion of other carbon–nitrogen molecules (i.e. C_2N_4) with oxygen or ozone will produce somewhat higher temperatures. This type combustion has been studied in detail at Temple University.[1] Fig. 2 shows the theoretical electron concentration and flame temperature as a function of the seeding factor, R, which is the ratio of moles of K–vapour to moles of $(CN)_2$, and is shown over a range from

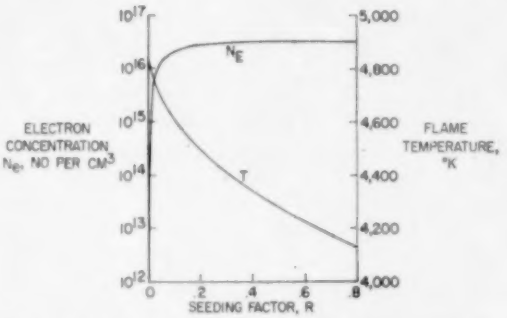

Fig. 2. Plasma characteristics of seeded cyanogen flame

0 (unseeded) to the higher values. It is seen here that the electron concentration rises very rapidly with small addition of potassium while the temperature drops slightly. At some larger value of R there is an optimum point where the product of mole-fraction ionized and amount of potassium injected is a maximum. At higher R's the cooling due to large additions of potassium becomes predominant and the concentration is reduced although a broad range of R is covered before appreciable reduction occurs. The important thing to notice here is that the value of N_e is about 3×10^{16} e^-/cm^3 at a temperature of about 4400°K. In Fig. 3 we see how these numbers compare with those values expected in flight. Here is plotted the electron concentration behind a normal shock in air as a function of velocity. Altitude and temperature are also cross-plotted. The curves were computed using the normal shock relations, the ARDC standard atmosphere, and electron mole-fraction values from Logan and Treanor (Refs. 2 and 3). It is seen that for glider-type flights, values of N_e of about 10^{12} e^-/cm^3 may be encountered behind the shock and for ballistic flights may be of the order of 10^{16} e^-/cm^3. Stagnation point values

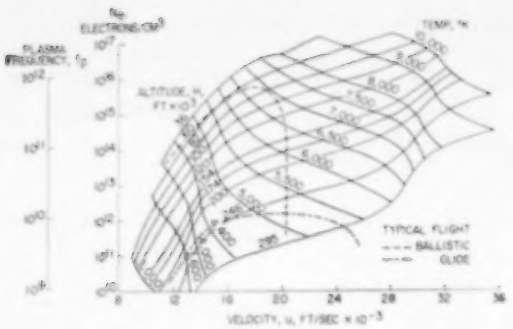

Fig. 3. Equilibrium electron concentration behind a normal shock in air.

would be only a few per cent higher than these, and on the after-portions of the vehicles the values will be, of course, lower. The important thing to be seen is that the electron concentrations for the more extreme flight plasma conditions are of the same order as those obtainable using the seeded-flame technique. Also shown here are the values of plasma frequency corresponding to these electron concentrations. More will be said about this later.

For the simplest attenuation model—that is, plane-wave propagation through a homogeneous plasma of uniform thickness—it is well known that three parameters essentially describe the problem. These are the plasma frequency, the electron–particle collision frequency and the signal frequency. The electron collision frequency for our seeded flame varies from $1/2 \times 10^{11}$ to 6×10^{11} rad/sec and this is in the range found in flight at the lower altitudes. It is therefore shown that such an experimental scheme as is here proposed should provide a means to study the attenuation of signals through plasma sheaths under plasma conditions similar to those of flight.

Before proceeding to the results of our investigation, I would like briefly to describe the apparatus which is used and to point out some of the more major considerations involved in the design. I should say first that considerable literature searching was required and some extrapolation of data on physical properties was involved for design of the cyanogen, cyanogen–oxygen, and potassium systems. Also, some preliminary work was done in an autoclave to check chemical stabilities and real-gas properties, as well as some flame stability tests in a small burner. The schematic arrangement of the systems as used here to produce the plasma is shown in Fig. 4.

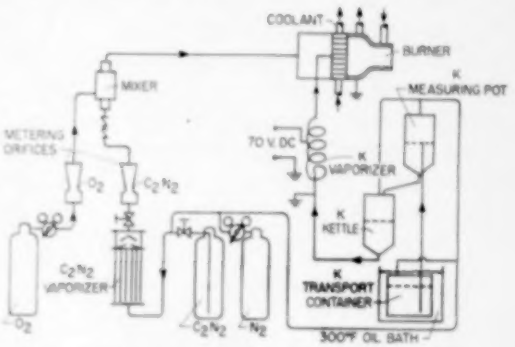

Fig. 4. Schematic diagram of C_2N_2–O_2–K systems.

Liquid cyanogen is forced from the storage container by its saturated-vapour pressure into a boiler. From the boiler the vapour flows through a control valve and metering orifice to a mixer. Oxygen flows from the storage container and regulator through a metering orifice and into this same mixer. The mixed gases then flow into a settling chamber at the burner. The scheme requires that potassium be injected in vapour form so as not to require vaporization by the flame, and hence seriously lower the temperature. The potassium system operates as follows: The solid is melted in the storage container by hot oil around the vessel. The liquid is forced by N_2 pressure into the potassium pot where a small quantity, sufficient for 1 run, is isolated. This quantity is drained into the potassium kettle and pre-heated to the boiling point (1400°F) by electric heaters. At the time of a test, N_2 is valved over the liquid in the kettle and it then flows through a vaporizer to the burner. The vaporizer is a long coil of inconel tube, joule-heated with a welding generator to about 1800°F,

through which the potassium flows. This tubing is maintained hot all the way to the burner to prevent condensation of the potassium. The flow rate is only known approximately from the quantity used and the length of the run. However, as we saw earlier, electron concentration was relatively constant and close to maximum for a broad range of potassium flow, so this is not at all serious. The vapour enters the burner at the centre of the combustion chamber and mixes with the products of combustion as shown in Fig. 5. Premixed, gaseous combustion was

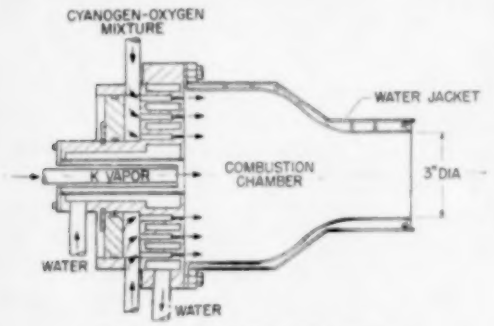

Fig. 5. Cross-section of burner.

selected because of its inherent smoothness and flame speed relative to other means. Also, a smaller combustion chamber could be used and hence less heat loss to the cooled walls. Water-cooling was required because of the high temperature and luminosity associated with the flame. The gas mixture is injected into the combustion chamber at high velocity through a large number of small orifices. This is done to provide both a uniform distribution in the combustion chamber and to prevent flashback of the flame, particularly during the starting operation where transient pressure increase occurs at ignition. The combustion products then flow through a nozzle to increase the velocity to a high enough value to reduce the effects of windage of the free jet. The velocity is about 500 ft/sec. A hypersonic stream would be nice, but the complications in the systems and the cost, not to mention development time, would be very great.

The complete system is mounted on a large trailer bed and tests are conducted in a field to reduce the reflections from ground objects. The burner is mounted about 15 ft. in the air for the same reason.

Signal attenuation measurements were made using this apparatus for the case of telemetered models immersed in the plasma stream and for microwave beams sent transversely through the flame. The tests were made at two plasma conditions. The first condition was the unseeded stoichiometric flame, with an electron concentration of 4×10^{11} e^-/cm^3 and the other was a seeded condition corresponding to a theoretical concentration of 1×10^{16} e^-/cm^3. The models used had self-contained telemetry transmitters and the signal was monitored at five remote receiving antenna locations with the signal-strength recorded prior to, during, and following each test. Fig. 6 shows the general

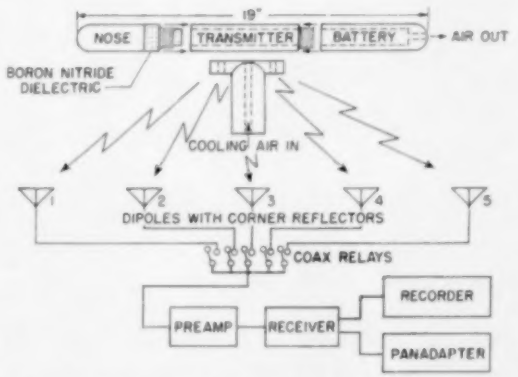

Fig. 6. Schematic of telemeter system (219·5 Mcs).

scheme for the tests using telemetered models. The remote receiving antennas consist of 5 dipole antennas arranged about the model in a semi-circle of 75-ft radius. The pattern and pattern-shift are determined from these signals during rotation of the burner and model combination through a 45° arc in the plane of the antennas.

Fig. 7 shows a typical telemeter record. This

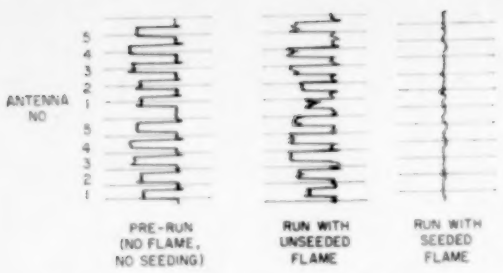

Fig. 7. Typical telemeter records (219·5 Mcs).

gives the attenuation of the received signal. No pattern shift was detected.

Tests were also made using x- and K-band microwave beams sent transversely through the plasma stream. This scheme is illustrated in Fig. 8. For simplicity, we show here only the main components. The horns were about 11 cm.

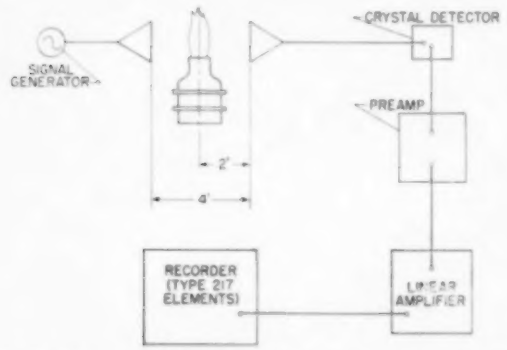

Fig. 8. Schematic of MW generator and recording system.

in height and 20 cm. wide, and were fairly well focused. The horns are mounted rigidly to a kind of optical bench. By moving the burner laterally a survey of the plasma stream may be made. An example of such a survey is shown in Fig. 9 where the change of signal with flame position is seen. Fig. 10 shows an attenuation record with the burner at a fixed centre position, and where the fuel ratio was varied. It is seen that a point of maximum attenuation occurs at stoichiometric ratio. Also evidence of chemi-ionization is given by the large peak observed during the starting phase.

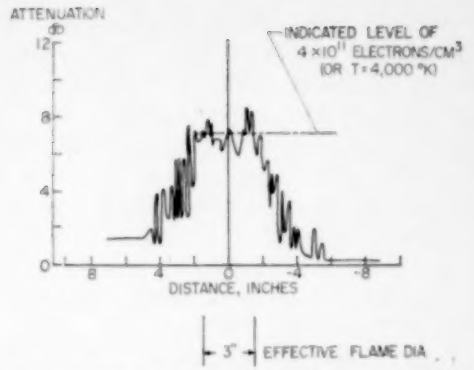

Fig. 9. Transverse survey of unseeded flame (1·5 cms waves.)

The total attenuations which were observed in these tests for both the telemetering and microwave frequencies have been reduced to attenuation in dB/cm by estimating the plasma thickness pertinent to each test. Unfortunately, this thickness is not easily determined because of the mixing of the plasma with the atmosphere, and also some reaction with the atmosphere. One would expect a mixing zone which would begin at the nozzle exit on the periphery of the stream and spread laterally in both radial directions with downstream position. This would leave an inner unmixed plasma core of conical shape, surrounded by this mixing zone. These thicknesses have been estimated and the attenuations are plotted in Fig. 11 for comparison with the simple theoretical model. For the unseeded

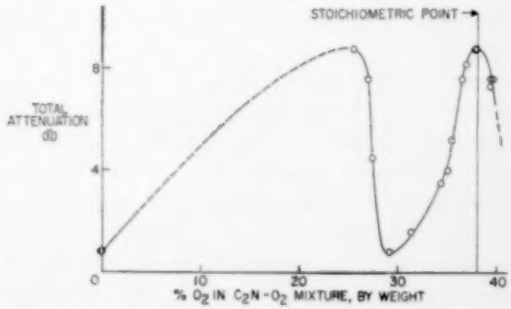

Fig. 10. Variation of total attenuation with fuel mixture (wavelength: 3·75 cm, flame thickness: 8 cm).

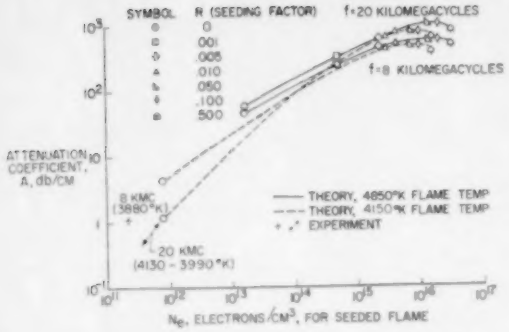

Fig. 11a. Attenuation in cyanogen flame (flame pressure: 1 atm).

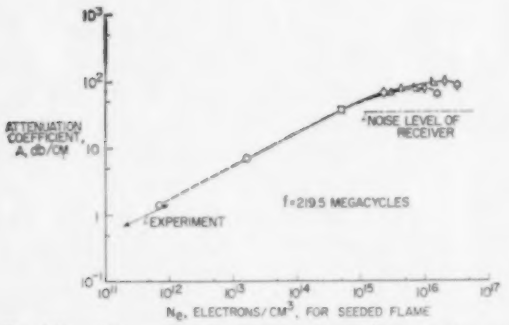

Fig. 11b. Attenuation in cyanogen flame (flame pressure: 1 atm).

flame, the three frequencies used show less than expected attenuation. The arrows indicate the uncertainty in reading the signal records and estimating the plasma thickness. The seeded results are difficult to show here, since the received signal was in all cases lost in the noise level of the equipment. We give a dashed line for the telemetering test to indicate that the attentuation per cm was this much, or higher. Unfortunately, we were limited by our equipment to about this one seeded condition, and we are since changing the system to permit seeding with intermediate amounts of potassium so that measurable attenuations can be obtained. Our microwave results have indicated that the unseeded flame temperature of our combustion products is approximately 4000°K, and this temperature defect from the theoretical value of 4850°K is found to be due to cooling in the combustion chamber and nozzle. Using this temperature, a theoretical equilibrium electron concentration for the unseeded flame can be calculated using the chemical equilibrium relations listed (see Fig. 1). The experimental points are plotted at values on the abscissa corresponding to these calculated inner plasma core electron concentrations. The dashed curves are the theoretical attenuations based on the unseeded flame temperature of 4150°K and are intended to show the effect of temperature loss. For the seeded case, there is very little effect of temperature seen but for the lower electron concentrations, a much stronger effect is seen, that is, cooling due to mixing, radiation, etc., may noticeably lower the attenuation.

Next, it should prove interesting to apply simple theoretical concepts to some flight signal attenuation problems. To do this let us first recall that we showed earlier a plot of electron concentration behind a normal shock as a function of velocity with altitude and temperature lines drawn in. Now I would like to show this a little differently. In Fig. 12 on an altitude–velocity

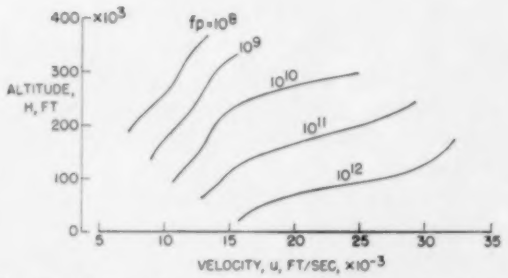

Fig. 12. Estimated minimum signal frequency based on stagnation point condition.

plot, lines of constant plasma frequency are plotted for the normal shock case, which is very near the stagnation point case. On this plot could be present an overlay of a hypersonic missile altitude–velocity history, and hence the point of signal loss would be noted when the value of plasma frequency equalled the signal

frequency. This concept is justified, because sudden and large attenuation is known to occur at plasma frequencies equal to the signal frequency. This can best be seen in Fig. 13 where

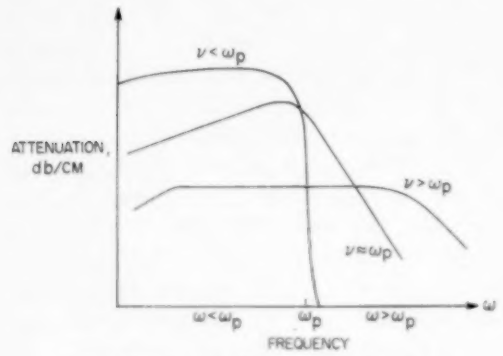

Fig. 13. Criteria for blackout concept.

the qualitative effect on attenuation versus frequency of the relationship of ν to ω_p is seen. For $\nu < \omega_p$ the signal is highly attenuated for values of $\omega < \omega_p$, so that in re-entering the atmosphere, as the plasma frequency increases, cut off will occur when this equals the signal frequency. For $\nu \approx \omega_p$, the cut off is not so sharp but rises to a broad peak at the point where $\omega = \omega_p$. In the region where $\nu > \omega_p$ the attenuation begins to drop where $\omega = \nu$ but the absolute value of attenuation is not nearly so high, so that more involved computations of attenuation for a particular case would be required. Before we return to the altitude–velocity plot, let us consider one further point. It is very doubtful that the plasma at the nose of the vehicle is really the one to be considered generally. Actually, the plasma on the aft portions of a body will be at a much lower electron density because of the lower pressure and temperature here. While this flow is exceedingly difficult to compute accurately, some estimates may be made. Fig. 14 shows such an aft estimate superimposed on the preceding stagnation plot. Here, the aft plasma frequency was based on flat plate flow behind a blunt nose, and a gross value assigned which is

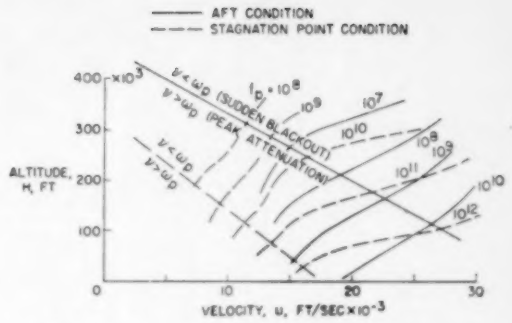

Fig. 14. Estimated minimum signal frequency.

to be merely representative of the flow between the body and shock at this aft location. It is seen that the blackout criteria here is much less serious than for the curves based on nose plasma, but is none the less a problem. The slanting lines are meant to divide the region in which the sharp cut-off criteria may be assumed.

We will now look at some flight blackout data plotted in this manner (Fig. 15). Here, the point

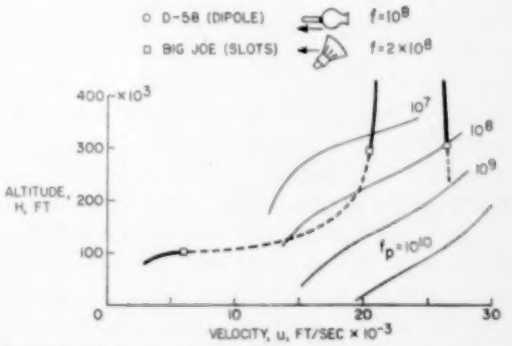

Fig. 15. Comparison of flight blackout data with estimated aft plasma frequency.

of signal loss for two flights made by the NASA is compared with the plasma frequency estimated for the aft conditions. In the case of the D–58 flight, the signal was lost at a point almost exactly described on the basis of this aft plasma computation. For the case of the Big-Joe (or Mercury) vehicle, the signal loss occurred earlier than

would be indicated by the flat-plate computation. It may be of significance, however, to note that—since the vehicle was flying in the direction indicated by the arrow—the plasma conditions may well be stronger than the generalized flat-plate case. It is certainly interesting to note in any case that the plasma conditions for the aft flow are much more pertinent to the problem than the much more serious nose conditions. This is not an unexpected result, of course. The point of signal recovery is not in the region where this cut-off concept is applicable as based on plasma frequency. This was shown on the earlier Fig. 13 as the case of $\nu > \omega_p$. In this region the attenuation should decrease when $\omega \approx \nu$, and the point is seen to be in this direction. Because of security classification, other flight blackout data which are available cannot be shown here.

This then is the status of our work to date on the problem of radio transmission through plasma layers. We believe that the use of cyanogen–oxygen flame seeded with an alkali-metal represents a controllable, specifiable method of plasma generation. These plasmas can be used to simulate the ionization levels existing on hypersonic bodies in flight under the most extreme flight conditions. Comparison of the measured attenuations for three signal frequencies and two plasma concentrations with a simplified theoretical concept of the problem shows a reasonable agreement. It appears that the application of these simple concepts to flight signal attenuation problems may result in the approximate prediction of signal-loss conditions, or alternately, aid in selection of signal-transmitting specifications such as to minimize this problem. However, a real solution to the blackout problem probably will be the result of basic researches in magnetoplasmadynamics. Out of these may come entirely new means for the generation of high power r.f. radiation and new methods for radiating from hypersonic vehicles, possibly using the plasma for this purpose. Because of the utility of this method for production of a large range of plasma conditions, the seeded flame would appear to be a very helpful tool for a wide variety of magnetoplasmadynamic studies.

Acknowledgements—I would like to acknowledge the close co-operation in this programme of Mr. Gooderum, who carried out the cyanogen-seeded plasma tests, Mr. Sims and Mr. McIver of the Instrument Research Division who handled the telemetering part of the programme, and Mr. Burlock and Mr. Grantham, of the Instrument Research Division, who did the microwave phase of the programme. As mentioned at the beginning, Hess, Patterson, and Sabol made the theoretical construction of the plasma model.

REFERENCES

1. J. B. Conway and A. V. Grosse, *J. Amer. Chem. Soc.* **80**, 2972 (1958).
2. P. W. Huber, *Tables and Graphs of Normal-Shock Parameters at Hypersonic Mach Numbers and Selected Altitudes*, NACA TN 4352 (Sept. 1958).
3. J. G. Logan, Jr., and C. E. Treanor, *Tables of Thermodynamic Properties of Air from 3,000°K to 10,000°K at intervals of 100°K*, Rep. No. BE-1007-A-3. Cornell Aero. Lab. (Jan. 1957).

EXPERIMENTAL INVESTIGATION OF ELECTROMAGNETIC PROPAGATION THROUGH THE PLASMA SHEATH IN A HYPERSONIC LOW DENSITY WIND TUNNEL*

R. L. CHUAN
Engineering Centre, University of Southern California, Los Angeles, California

Abstract—A hypersonic free jet flowing at hypersonic speed past an aerodynamic model in a very large test chamber provides proper conditions for the study of signal attenuation through an ion sheath. The test chamber surrounding the free jet is large enough to house all the necessary radar gear, so that all the electronics (both transmitting and receiving) is housed inside the wind tunnel. The pressure in the interior of the wind tunnel can be maintained continuously at those corresponding to altitudes of from 130,000 to 400,000 ft by use of cryopumping. Flows at Mach numbers up to 15 and stagnation temperatures near 5,000 K will be produced by the combination of cryopumping and r.f. heating of the gas. Electron densities of the order of 10^{12} are expected. The wind tunnel facility, the instrumentation and the testing programme will be described.

1. INTRODUCTION

In treating any complex physical phenomenon one must necessarily make a number of simplifying assumptions, the validity of which one hopes to establish with experimental measurements. As far as the interaction between an e.m. radiation and a uniform plasma or a one-dimensional plasma field is concerned, one may consider the problem to be adequately treated theoretically by such works as of Margenau[1] and Cahn,[2] and well summarized in the light of contemporary engineering problems by such workers as Whitmer[3] and Sisco.[4] As rockets began to attain hypersonic speeds, with attendant thermal ionization of constituents of the atmosphere in the vicinity of the rockets, telemetry fade-outs were noted. Now, as missile technology becomes more sophisticated, and communication and detection problems compound, the study of plasma–electromagnetic radiation interaction has come of age. A number of now well-known papers have dealt with the attenuation of radio signals in traversing through the partially ionized atmosphere surrounding a hypersonic vehicle. In combining the e.m.–plasma interaction problem with the problem of hypersonic flow fields, one must recognize the many limitations of our present state of knowledge of the latter. Presumably the electronic theorist can, upon being given a set of conditions regarding the electromagnetic properties of a gaseous medium, predict the influence these will have on an e.m. signal traversing the medium, provided the medium is homogeneous or possesses certain simple spatial qualities (such as one-dimensional variation of properties). These properties must be the result of the aerodynamic treatment of the flow field, which, unfortunately, is far from being very complete or realistic. This paper will attempt to point out the inadequacies of aerodynamic theories in relation to the e.m. interaction problem; to discuss ways in which some further understanding can be achieved by experimental investigation; to suggest similarity considerations; and, finally, to describe some specific experiments to be conducted at the USCEC.

2. HYPERSONIC FLOW FIELDS

In discussing flow fields about hypersonic

* Work performed under Contract AF 19(604)-5722.

vehicles a number of steps of increasing sophistication may be considered. To begin with, the simplest picture is that of a thermodynamically perfect gas (by which is meant a gas obeying the simple equation of state and with constant specific heats) with no transport mechanisms, flowing through a mathematical discontinuity (the shock wave), and around an obstacle. Such a picture obviously has no relevance with respect to the present problem, since no ionized particles would be present. The next step is to consider a real gas which is capable of having internal energy states excited, including ionization; and the energy partition is taken to be that appropriate to thermodynamic equilibrium at the local state of the gas, but still treating the flow field between the shock wave and the body as a non-viscous one with no transport. There may now be the presence of ionized particles if the temperature of the gas is sufficiently high. But the resulting situation still may not be very realistic. At this juncture one or both of two steps may be taken to render the situation realistic. One is to allow transport mechanisms, which then bring forth the existence of a viscous flow field bounded on one side by the body. The other is to permit local thermodynamic non-equilibrium in energy partition, or relaxation effects. These two departures bring on enormous analytical difficulties, compounded by lack of understanding of the basic physics of the problem relating to transport and relaxation mechanisms.

Depending on the relative significance of the non-viscous to viscous effects (characterized by the Reynolds number) the flow field, starting at the shock front and ending at the body surface, may or may not be divided into convenient and distinct regions to make each amenable to separate analysis. Fig. 1 shows, in a highly idealized manner, the qualitative appearance of the flow field in various regimes of flight conditions. Fig. 1(a) represents the idealized non-viscous flow field with a shock wave of zero thickness ahead of the body. Fig. 1(b) shows a viscous layer which is thin compared to the

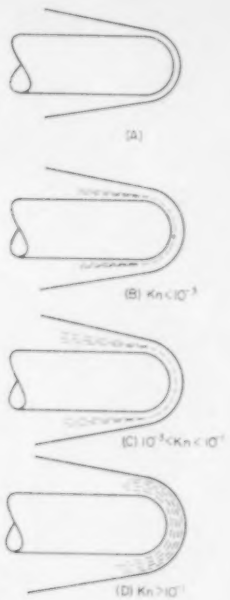

Fig. 1. Hypersonic flow fields.

extent of the flow field between the shock and the body. Here the main field may still be analysed using non-viscous theory, and the presence of the viscous layer near the body surface may be considered a small perturbation on the main flow. An examination of the properties of the viscous layer will show, however, that its presence may not be a mere perturbation with respect to electromagnetic considerations. Fig. 2 shows typical temperature profiles for three locations along the body, for non-viscous flow and for flow with a viscous layer (dotted profiles). It is clear that where non-viscous theory would predict negligible free electron density because of low stream temperature, the actual free electron density may be quite appreciable because of high temperature in the boundary layer caused by the retardation of the flow by the solid boundary, with consequent non-negligible influence on e.m. propagation.

Fig. 1(c) shows a much extended viscous region and a shock front which has a definite thickness. This is a difficult situation in which

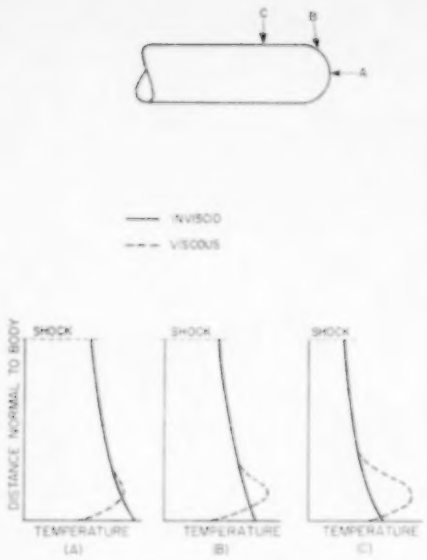

Fig. 2. Temperature profiles.

both the flow field and the propagation field are profoundly affected by the presence of the viscous region; the problem, while formally definable, is not amenable to ready solution. As the Reynolds number continues to decrease, not only is the distinction between a definable viscous region and a definable non-viscous region lost, but the shock structure, too, is merged into the viscous flow field; so that a single description (of the merged regions) must be made of the entire flow field adjacent to the body. This is a problem which is not even adequately formulated.

In flows where viscous effects predominate, a more meaningful characterization, instead of the Reynolds number, is the Knudsen number, defined as the ratio of the molecular mean free path to the characteristic dimension of the problem. In the cases cited in Fig. 1, if the characteristic dimension is taken as the nose radius of the vehicle and combined with the mean free path in the undisturbed gas ahead of the body to define the Knudsen number, its orders of magnitude are as indicated in the figure. Most problems of engineering interest, as far as e.m. propagation is concerned, occur in the regime described by Fig. 1(c) and at flight speeds of 5×10^5 cm/sec and higher.

If a characteristic length of 1 m is chosen, a Knudsen number ranging from 10^{-3} to 10^{-1} would place the vehicle in an altitude range of approximately 80–120 km (or about 250,000–350,000 ft) flying at a Mach number of about 18. At altitudes much above 120 km, the atmospheric density is so low (with consequent low plasma frequency) as to cause no difficulty as far as propagation is concerned. Much below an altitude of 80 km, flight speeds are generally too low (except for missile re-entry) to cause the formation of a plasma sheath.

The flow field under the conditions in question is rather poorly described analytically. Qualitatively it may be said that an extended viscous region (in which there is considerable transport of momentum, energy and gas species) separates the body from the shock front and the predominantly non-viscous flow behind it. At the present time little can be said of the detailed structure of the flow field either by equilibrium or non-equilibrium theory.

It thus appears that, short of an adequate theoretical account of the flow field structure around a hypersonic vehicle, the best that can be achieved in the way of a phenomenological understanding of the propagation problem is to conduct experiments under known and controlled laboratory flow conditions.

3. EXPERIMENTAL INVESTIGATION AND SCALING CONSIDERATIONS

It would be ideal to perform full scale experiments in the laboratory to study propagation through a plasma sheath. While it is possible to use full scale equipment as far as the electronic aspects are concerned, it is, however, not possible within the limitations of our present technology to provide full-scale aerodynamic simulation. This being so, model test at reduced scale must be resorted to, which brings forth the question of scaling. To yield meaningful results,

it is required that the model test and full-scale situation be geometrically, aerodynamically and electromagnetically similar. For the present problem it is possible to point out some simplifying conditions which render complete similarity unnecessary.

It is taken for granted that the energy density of the electromagnetic radiation incident upon the plasma sheath is small compared to the energy density of the latter, so that the flow field is not affected by the radiation. It is further understood that the degree of ionization in the sheath flow is small (of the order of 1 per cent) so that magnetohydrodynamic effects need not be considered; and the flow is treated within the framework of gasdynamics with considerations of transport and relaxation. As far as the equilibrium flow is concerned, then, it will only be necessary to maintain the same Mach number and Reynolds number (or Knudsen number) for the model case as for the full-scale case.

Since real gas effects are not susceptible to explicit analytical description relating energy partition to such parameters as temperature, density and pressure, true similarity cannot in general be achieved. If temperature can be simulated to an extent not too far from the flight situation, there will however be sufficient ionization present in the flow to make its electromagnetic properties realistic. The effect of relaxation on flow field similarity must next be considered. Similarity can be achieved in the presence of relaxation only if relaxation distances are made geometrically similar between model and full-scale configurations. Suppose

$$\frac{R_m}{R} = \frac{\text{Model nose radius}}{\text{Full scale nose radius}} = \eta \tag{1}$$

Then similarity with respect to relaxation requires that

$$\frac{(d_\tau)_m}{d_\tau} = \eta \tag{2}$$

where

d_τ = full scale relaxation distance

$(d_\tau)_m$ = model relaxation distance

If

$$\frac{T_m}{T} = 1 \tag{3}$$

Then

$$\frac{U_m}{U} = 1 \tag{4}$$

$$\frac{\tau_m}{\tau} = \eta \tag{5}$$

Since the relaxation time is approximately inversely proportional to gas density (if temperature is constant), this leads to

$$\frac{\rho_m}{\rho} = \frac{1}{\eta} \tag{6}$$

and, again for $\frac{T_m}{T} = 1$ and neglecting the dependence of degree of ionization on gas density (which is permissible if densities do not differ by more than an order of magnitude),

$$\frac{(n_e)_m}{n_e} = \frac{1}{\eta} \tag{7}$$

The corresponding plasma frequencies for the model and full-scale configurations are then in the ratio

$$\frac{\omega_m}{\omega} = \frac{1}{\sqrt{\eta}} \tag{8}$$

The ratio of the wavelengths of the propagation signals is then

$$\frac{\lambda_m}{\lambda} = \sqrt{\eta} \tag{9}$$

The compatibility of the above conditions (3, 6 and 9) to other similarity requirements and to laboratory practicability may now be examined.

The requirement

$$\frac{M_m}{M} = 1 \tag{10}$$

can be met, or very nearly met. The requirement

$$\frac{\mathrm{Re}_m}{\mathrm{Re}} = \frac{\rho_m u_m R_m \mu}{\rho u R \mu_m} = 1 \tag{11}$$

becomes, when (3) and (10) are included (and assuming μ to be dependent only on T),

$$\frac{\rho_m}{\rho} = \frac{R}{R_m} = \frac{1}{\eta}$$

which agrees with condition (6).

Since η is less than unity, $\frac{\rho_m}{\rho}$ is greater than unity, which, from the laboratory standpoint, is a desirable condition, since the maintenance of very low gas density high speed flow is a very difficult task. Table 1 shows the full-scale and model Knudsen numbers at various altitudes for $R = 1$ m and $\eta = \frac{1}{10}$. It is seen that laboratory similation (at least as far as Knudsen number is concerned) of full-scale conditions at 300,000–350,000 ft altitude can be accomplished at simulated altitudes of 250,000–300,000 ft which is well within the realm of present wind tunnel capability.

Table 1. Knudsen Number vs. Altitude

Altitude (k ft)	Knudsen Number	
100	10^{-6}	10^{-5}
150	10^{-5}	10^{-4}
200	10^{-4}	10^{-3}
250	10^{-3}	10^{-2}
300	10^{-2}	10^{-1}
350	10^{-1}	1

$R = 1$ m

The condition $\frac{\lambda_m}{\lambda} = \sqrt{\eta}$ is not difficult to meet. It should be noted here, however, that the usual assumption of the propagation of a plane wave is, in general, not valid; and the assumption becomes especially poor when the properties of the transmission medium vary appreciably in the direction normal to the direction of propagation. In this case it becomes desirable to maintain similarity in beam widths, which then directly affect antenna sizes. In this sense it would be better to have $\frac{\lambda_m}{\lambda} = \eta$. However, the fact that $\frac{\lambda_m}{\lambda} = \sqrt{\eta}$ is not critical, particularly for a case in which $\eta = \frac{1}{10}$.

4. HYPERSONIC WIND TUNNEL EXPERIMENTS

The basic requirements for propagation studies in a wind tunnel are the following:

1. Proper Mach number, temperature and Reynolds number simulation.
2. Reasonable size of model (η not too much less than $\frac{1}{10}$).
3. Minimum interference with the radio signal outside the plasma sheath.

These requirements can be met by the use of a low density, hypersonic free jet flowing in a large chamber wherein all the necessary electronic gear may be housed. In this manner the transmission and reception of signals can be accomplished without having to go through solid walls surrounding the flow and through the boundary layers adjacent to these walls.

The low density hypersonic wind tunnel at the USCEC can maintain the following conditions:

1. Altitude simulation from 200,000 to 500,000 ft.
2. Hypersonic Mach number from 8 up.
3. Stagnation temperature of 3,000°K and higher.
4. Flow duration up to 10 hr.

A free jet of up to 40 in. in diameter can be maintained in a test chamber measuring 9 ft by 10 ft by 15 ft, so that there is adequate space for internal housing of all instrumentation where necessary. The high speed low density flow is produced by cryopumping, in which a helium refrigerated condenser at 20°K maintains the necessary vacuum at high volume flow. (*See* Refs. 5 and 6, and Figs. 3–5 for further descrip-

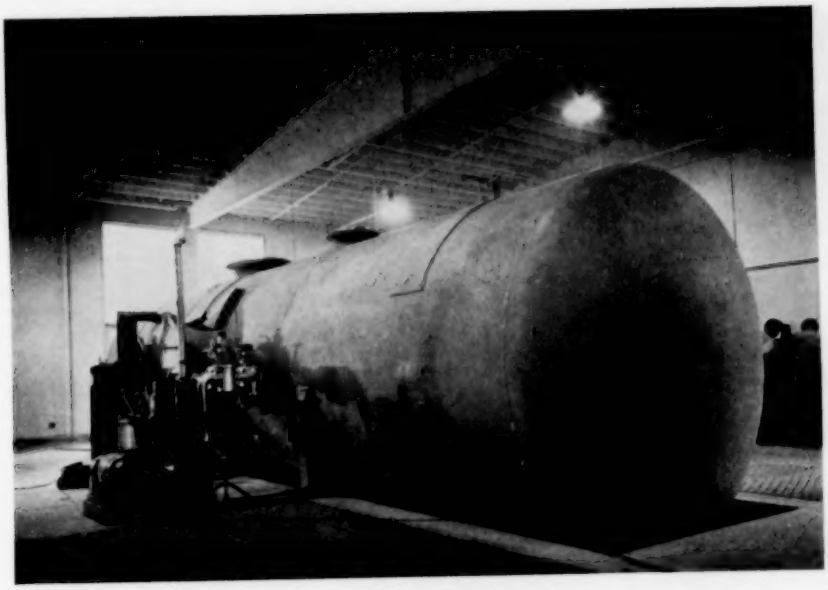

Fig. 3. External view of tunnel.

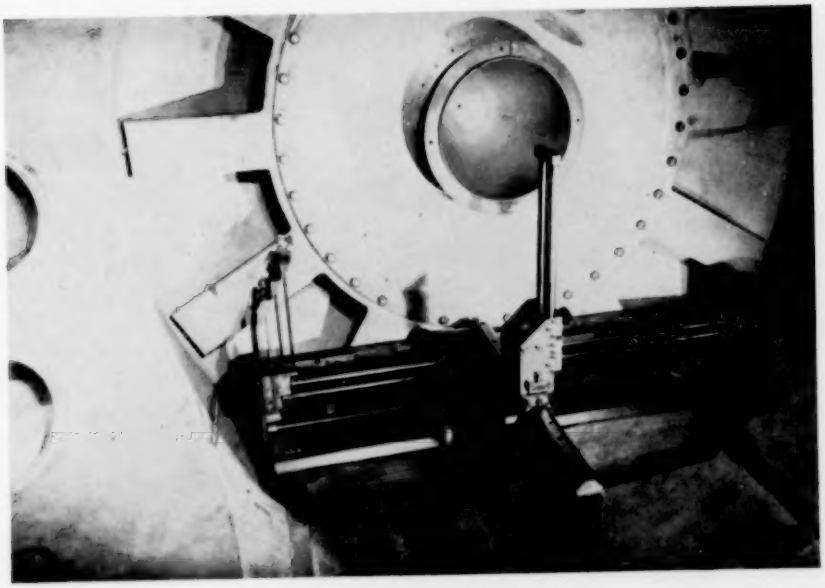

Fig. 4. Test section view.

Fig. 5. Condenser.

tion of the facility.) The high stagnation temperature is produced by the decay of a radio-frequency, discharge-produced air plasma. The discharge is effected in supersonic flow without the gas coming in contact with the electrodes. Details of this technique may be found in Refs. 7–10.

The conditions under which the early propagation measurements are to be made are:

$$M = 14$$
$$U_\infty = 4{\cdot}5 \times 10^5 \text{ cm/sec}$$
$$T_\infty = 290^0\text{K}$$
$$T_s = 4{,}000^0\text{K}$$
$$P_\infty = 10^{-3} \text{ mm Hg.}$$

With these conditions in the free stream the particle density in the neighbourhood of the stagnation point behind the shock wave will be of the order of 10^{14} l/cm^3 and the electron density of the order of 10^{12} l/cm^3. Downstream of the stagnation region this value may be expected to decrease because of lower temperatures and densities, but may not decrease as fast as we may expect from equilibrium theory because of diffusion from regions of higher electron density, and of relaxation in electron–ion recombination.

Microwave antennas will be placed inside a hemisphere–cylinder model of about 8 in. diameter (*see* Fig. 6). Propagation characteristics will be measured at several locations on the model, from the stagnation region to points sufficiently downstream where attenuation is negligible.

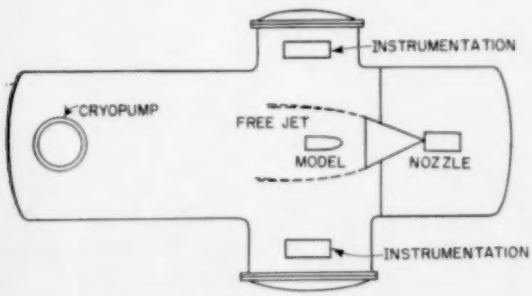

Fig. 6. Schematic of test section.

A full assessment of the validity of both the theory and the experiment is only possible when it is possible to measure the local electron density in regions behind the shock front by independent means (other than microwave techniques). To this end considerable efforts remain to be expended by workers in the area of plasma diagnostics. The classical Langmuir probe will not yield meaningful results when placed in a high velocity stream. Microwave probe, even if based on reliable theory, cannot be made to determine local properties, especially in a complex flow field like that behind a hypersonic shock front.

Until such sophisticated diagnostic techniques are developed, one can only be content with a less detailed phenomenological description of the problem. To this extent, it is expected that the present series of experiments will yield useful results in the very near future.

REFERENCES

1. H. Margenau, *Phys. Rev.* **69**, 508 (1946).
2. J. H. Cahn, *Phys. Rev.* **73**, 309 (1948).
3. R. F. Whitmer, *Microwave J.* **2**, 17; **3**, 47 (1959).
4. W. B. Sisco and J. M. Fiskin, *Shock Wave Ionization and Its Effect in Space Communication*, Paper No. 656, Douglas Aircraft Co., Long Beach (June, 1958).
5. R. L. Chuan and K. Krishnamurty, *Principle and Application of the Two Phase Wind Tunnel System*, USCEC Interim Rep. 42–201 (June 1956).
6. R. L. Chuan and B. M. Bailey, *Cryopumping for High Vacuum with Low Power*, presented at *Fifth National Vacuum Symposium, October 22–24, 1958, San Francisco, California.*
7. R. L. Chuan, *Plasma Heating of Hypersonic Gas Flow*, USCEC Rep. 56–203; AFOSR TN 58–650 (July 1958).
8. J. C. Williams, III; P. C. Wilber and R. L. Chuan, *Analytical Study of the Heating of Hypersonic Air Flow by Electrode-Less High-Frequency Discharge*, USCEC Rep. 68–101; AEDC TR 59–23 (July 1959).
9. R. L. Chuan, *A Note on the Addition of Heat to a Gas Through Electrical Discharge*, USCEC Rep. 68–201; AFOSR TN 59–50 (Jan. 1959).
10. F. O. Smetana, *Some Further Results on Heating a Supersonic Gas Stream with a Radio Frequency Discharge*, USCEC Rep. 56–207; AFOSR TN 59–1127 (Nov. 1959).

MICROWAVE TECHNIQUES FOR HYPERSONIC BALLISTIC RANGES

R. I. PRIMICH
Defence Telecommunications Establishment
Shirley Bay, Ottawa, Ontario, Canada

Abstract—DRTE and CARDE are carrying out a programme of microwave measurements on hypersonic ballistic ranges, located at CARDE for the purpose of studying the ionized field in the vicinity of a high velocity projectile.

Two simple types of measurement are being carried out. In one a simple CW Doppler radar observes the projectile at a nose-on aspect for most of its flight. In the other a beam, at right angles to the projectile, is used to obtain resolution along the flight path. Present equipment will be described and some results will be given.

1. INTRODUCTION

The usefulness of a hypersonic ballistic range in the study of re-entry phenomena, needs little discussion, especially in a conference of this nature. The Defence Research Telecommunications Establishment (DRTE) at Ottawa and the Canadian Armament Research and Development Establishment (CARDE) at Quebec City, both of the Defence Research Board (DRB) of Canada, are engaged in a joint programme in which microwave techniques are being employed to study the plasma generated by a high-speed projectile. CARDE develop and operate various ballistic ranges, together with various types of instrumentation. DRTE is developing and installing microwave equipment on some of these ranges, with the intention of determining the role of real gas effects on the radar echoing area of high speed missiles. These real gas effects have been considered in detail elsewhere.[1-4]

Two basic techniques which are under development and partially in use, will be described in detail. Methods by which the properties of the ionized field may be determined with the aid of these techniques will be briefly outlined. Emphasis will be placed on the techniques rather than on specific results.

2. THE HYPERSONIC BALLISTIC RANGE

In the hypersonic ballistics range, a projectile ranging in size from a half-inch diameter (or smaller) object to one several inches in diameter, is projected at velocities up to 16,000 ft/sec into an evacuated tunnel.

Two ranges will be considered here. The first has a tunnel 3 ft in diameter and 25 ft long (useful part of the range). The second range has a tunnel 6 ft in diameter and 80 ft long. Further details will be given elsewhere.[5]

3. MICROWAVE TECHNIQUES

In the experimental determination of the effect of ionization on echoing area, two approaches are possible, i.e.

(a) direct measurement of echoing area in flight;

(b) probing of the ionized field in the vicinity of the missile.

Both approaches have been adopted since each has its respective merits. The first yields the integrated effect of the plasma, whereas the second yields the distribution of ionization and consequently sheds some light on the physical process taking place.

A CW Doppler radar with the beam located

along the flight direction provides a convenient means of measuring the nose-on echoing area of a projectile in flight.

Some form of microwave beam normal to the flight path is the most obvious way of attempting to study the plasma distribution in the vicinity of the projectile.

These form the two basic techniques and it will be shown that all the usual plasma properties can be determined from them individually or together.

In Fig. 1 a typical experimental arrangement is shown.

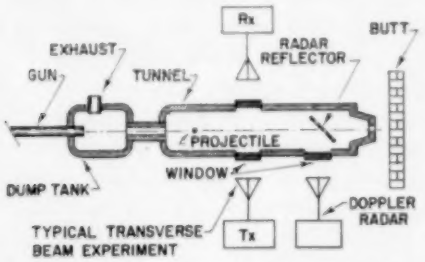

Fig. 1. Hypersonic ballistics range with microwave instrumentation.

4. THE CW DOPPLER RADAR

In the direct measurement of echoing area, advantage has been taken of the discreet Doppler shift produced by a moving projectile in a CW radar. This shift provides a convenient method of isolating the desired signal from the clutter arising out of a stationary background.

The design of such a radar requires that the following unusual factors be taken into account:

(a) The antenna system has to operate in a confined space.

(b) Suitable wavelengths, available power and small target echoing areas may require the best possible noise figures.

(c) The dynamic range of the amplitude of the received signal is at least 40 dB.

(d) The available data rate is very high and only in a few exceptional cases can this be matched in a recorder.

Each of these factors will be considered in turn.

4.1. *The antenna system*

The beamwidth of the antenna should be narrow enough to prevent reflections off the walls of the tunnel from causing unwanted interference effects. The gain should be sufficiently high so that an adequate signal-to-noise ratio for small targets can be obtained. However, it should not be so high that the near-zone region of the antenna would form a significant fraction of the useful operating range. The selection of beamwidth has been made on the arbitrary assumption that incident power at the walls of the tube at maximum range is 3 dB down on that at the centre of the beam. For a cosine-squared aperture field distribution the power at the walls at half range is then approximately 10 dB down. This particular value of range is significant in that maximum interference occurs due to specular reflection off the walls at this point. At lesser ranges the specular reflection occurs at larger angles and will be further attenuated by the beam shape. This is illustrated in Fig. 2.

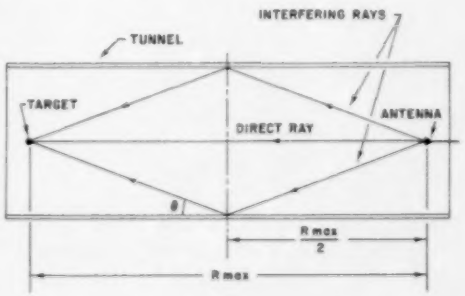

Fig. 2. Sidewall interference.

The 3 dB beamwidth is given by:

$$\text{BW} = 1{\cdot}45\,\frac{\lambda}{a} = \frac{d}{R}$$

d = dia. of tunnel

a = size of antenna aperture

λ = wavelength
R = maximum range

Then $$R = \frac{d}{1{\cdot}45}\frac{a}{\lambda}$$

For a given d, R as a function of a/λ has been plotted in Fig. 3.

It is apparent that a large antenna will provide an extended range. However, as the antenna size is increased the near field, which is characterized by loss of gain and a complex field structure, extends farther from the antenna and the useful operating range is reduced. The usual criterion for maximum operating range (beyond which a reasonable approximation to a far field exists) is taken to be $R=2a^2/\lambda$. It has been shown experimentally that negligible error is introduced by operating at ranges of a quarter of this value, i.e. $R=a^2/2\lambda$. This relation is plotted in Fig. 3.

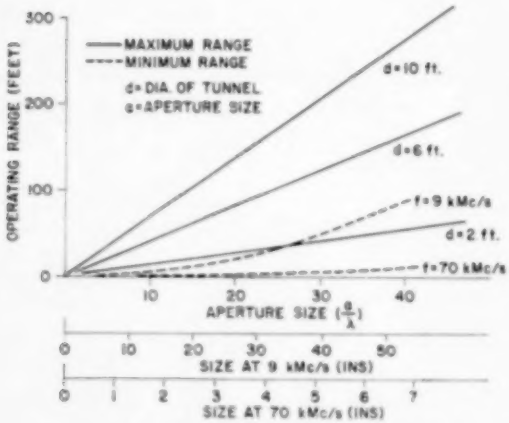

Fig. 3. Operating range of CW Doppler radar.

The length of ordinate between the maximum and minimum range curves for a given aperture size (in wavelengths), defines the useful operating range.

The choice of operating range in a given tunnel virtually determines the antenna aperture dimensions and the wavelength. The antenna gain is then determined and if, for available powers, the signal-to-noise ratio is inadequate, a reduction in operating range has to be accepted. It is apparent that in the present application, wavelengths closer to 4 mm than 3 cm are to be preferred, because of the greater operating ranges and smaller antenna sizes which are obtained. Although available transmitter power falls off with wavelength, this power, in our applications, has proved to be sufficient for adequate signal-to-noise ratios.

4.2. *Sensitivity and noise factor*

In current microwave superheterodyne receiver practice the IF is usually tens of megacycles. Then noise contributions from the mixer crystals that fall in the IF passband are small. If the IF were allowed to approach zero this noise would become excessive. The use of a balanced mixer normally provides adequate suppression of the noise contributions that arise as a result of beats between the LO and its own noise sidebands.

The design, construction and operation of a CW Doppler radar receiver is simplified if a portion of the transmitter power can be used for LO purposes. Then the IF is identical to the Doppler frequency. The use of LO circuitry is avoided and transmitter frequency variations are of secondary importance. However, if the Doppler frequency shift is low, then these advantages may be offset by the high noise factor.

When the noise factor is prohibitively large it is necessary to use a separate LO which should track the transmitter accurately at the chosen IF. Care has to be taken in beating the IF down to the Doppler frequency, otherwise the resulting Doppler shift is inaccurate. These requirements usually lead to the use of some form of phase-locking technique, which operates quite satisfactorily but is fairly complicated. The Doppler frequency shift as a function of missile velocity, for various carrier frequencies, is plotted in Fig. 4. It can be seen that at the lower carrier frequencies (10 kMc/s) the use of a separate LO is indicated, whilst at the higher frequencies

(35 and 70 kMc/s) the use of auto-mixing (i.e. the use of a portion of the transmitter power for LO purposes) looks promising.

4.3. *Recording the Doppler waveform*

A major problem in the use of a CW radar in a hypersonic range, occurs in the recording of the received Doppler waveform. The duration of a typical flight is from 1 to 10 m/sec. At the same time the Doppler shift may be as high as 3 Mc/s.

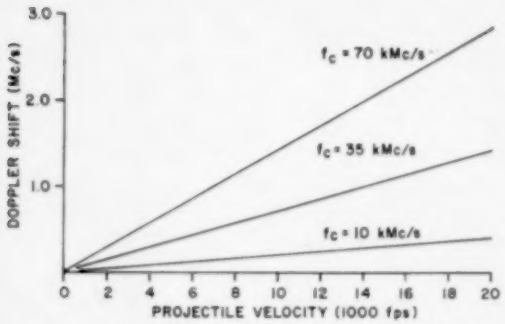

Fig. 4. Doppler frequency shift on a CW carrier.

Without discussing the details here, it can be shown that magnetic tape recording offers the most flexible approach. This method has the following advantages:

(a) Large recording capacity;
(b) high frequency response (in principle);
(c) the record is permanent; data reduction offers many possibilities for automatic analysis of waveform, etc.
(d) large dynamic range.

Recorders are now available which can record up to 4 Mc/s per channel, with 7-channel capacity. However, the cost is prohibitive in this application and an upper limit of 100 kc/s has had to be accepted. This has dictated the use of special mixing circuits which convert the Doppler frequency to any one of a number of channels with a maximum response of 100 kc/s.

4.3.1. *Data rate.* At a velocity of 10,000 ft/sec, the Doppler shift can range from 200 kc/s to 1·5 Mc/s. In the worst case a useful piece of information can be obtained every $10^6/2 \times 10^5 = 5\mu$ sec, which corresponds to 0·05 ft of flight. However, the conversion of these frequencies to values below 100 kc/s could allow the recorded frequencies to approach zero unless means are taken to prevent this. The lower frequency limit has been chosen arbitrarily to be 50 kc/s which results in a minimum data rate of one piece of information in 20μ sec or in 0·2 ft of flight. This is still quite adequate.

4.3.2. *Dynamic range.* As the range to the target varies from about 100 ft to a few feet, the receiver power, which varies inversely as the fourth power of this distance, increases by at least 40 dB. Dynamic ranges of this order pose some special problems. Two alternative approaches have been adopted. In the first of these, a compression amplifier reduces the variation to less than 10 dB. In the second approach an attempt is made to use the full dynamic range of the tape recorder. The first approach is much more convenient in practice but presents a formidable design problem.

4.3.3. *Mixer circuits.* The conversion of the Doppler frequencies to lower recordable values is carried out using the superheterodyne principle. The exact manner in which this is done is more conveniently discussed in conjunction with a specific radar design.

5. SOME SPECIFIC RADAR DESIGNS

5.1. *A 35 kMc/s radar*

35 kMc/s radars have been designed for both ranges. They are similar except that appropriate antenna systems have been used in each range.

The complete system diagram is shown in Fig. 5. The beam is deflected along the flight path by a thin expendable reflecting sheet. It enters the range through a thick sheet of polystyrene (Polypenco *Q*200·5) which has simulated quarter-wavelength surface layers for minimum reflection. The absorbing tunnel is instrumental in reducing antenna side-lobes and in preventing

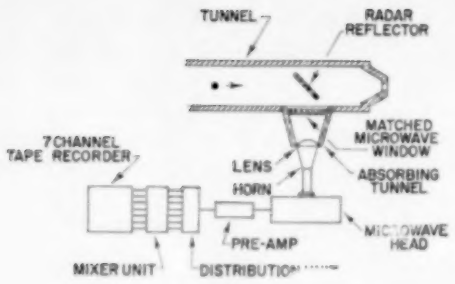

Fig. 5. 35 kMc/s Doppler radar.

the radiation of energy outside the range. The horn and microwave head produce the transmitted beam, receive the reflected energy and convert it to a low frequency Doppler signal. The latter is amplified in the pre-amplifier and is conveyed through the distribution unit to the multi-channel mixer. The outputs of the mixers are fed directly to a 7-channel tape recorder.

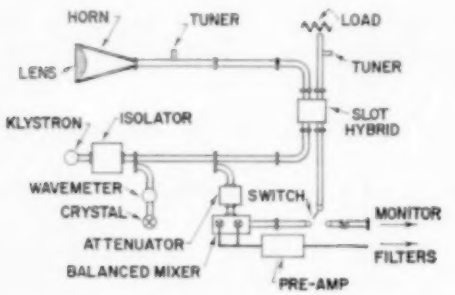

Fig. 6. 35 kMc/s Doppler radar microwave head.

The details of the microwave head are shown in Fig. 6. The antenna on the smaller range is a ten-wavelength aperture conical horn with lens correction. A similar horn with a twenty-wavelength aperture is used on the larger range. The gains are approximately 30 and 37 dB, respectively. Isolation of the received signal is obtained through the use of a short slot hybrid with suitable tuning in two arms. Although background reflections produce a signal at the frequency of the transmitter they can worsen the noise figure of the receiver since they enter the balanced mixer through the signal arm. Of course, if the unwanted signal is comparable to the mixing signal phase interference will take place in the mixer. In either case improved performance has been obtained by cancelling out unwanted background signals. This is done by tuning with the switch in the monitor position.

The radar on the smaller range has given satisfactory operation. Careful calibration has revealed a noise figure of approximately 20 dB (a free choice of IF would give a noise figure of about 12–13 dB), and a sensitivity of about −100 dBm. The latter performance, with a radiated power of 30 mW, enables the radar to detect an echoing area of less than 1 cm^2 at a range of 30 ft. The radar on the larger range is expected to give the same performance at a range of 80 ft.

The Doppler frequencies, after some amplification in the preamplifier, are conveyed at the right impedance level through a distribution network to a multi-channel mixer. The operation of this mixer can be understood by reference to Fig. 7. Three typical channels are shown. Each channel has a fixed local oscillator. The response

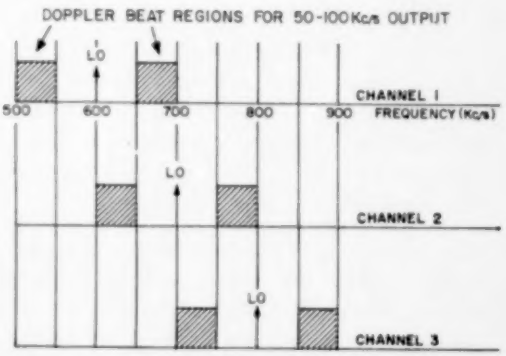

Fig. 7. Frequency diagram for channel response.

to an incoming Doppler signal will occur in a particular channel only if the signal falls within the two shaded regions indicated. If the signal falls outside these regions, it will cause some

other channel to respond. This system is ambiguous, but the ambiguity can be resolved easily by making use of the fact that the projectile must decelerate.

The mixer outputs in the 50–100 kc/s range, are passed to the individual channels of a tape recorder. There is an uncertainty in the number of channels to be used on any one firing which depends on the accuracy with which velocity can be predicted. Under the most favourable conditions three channels are sufficient but at times as many as six may have to be used.

5.2. *A 13·5 kMc/s radar*

At 13·5 kMc/s the Doppler frequencies as shown in Fig. 4 appear to be too low to use directly as the IF in a superheterodyne system. Consequently it was decided to use a separate LO with an IF of at least several megacycles. An equally important reason for an IF of this magnitude is that it is easier to filter the Doppler frequencies into their respective 50–100 kc/s channels. An IF of 4 Mc/s was chosen which was thought to be high enough to give a reasonably good noise figure and to make filtering relatively easy. The accuracy of the Doppler shift has been preserved by phase-locking the LO to the transmitter at the 4 Mc/s IF. The details of the microwave head are shown in Fig. 8. The transmitter klystron produces approximately 1·3 W. The sensitivity is approximately –110 dBm. The gain of the parabola is approximately 30 dB. A signal-to-noise ratio of at least 10 dB is obtained on an echoing area of 4 cm² at a range of 80 ft. Background reflections at the transmitter frequency are tuned to a minimum and the residual leakage signal at 4 Mc/s is eliminated in a filter located beyond the preamplifier. Otherwise it would produce spurious responses in the multi-channel mixers.

This radar will be used on the larger of the two ranges.

5.3. *A 70 kMc/s radar*

A 70 kMc/s radar is under consideration. It is very similar to the 35 kMc/s system. A 40 λ wavelength aperture conical horn with lens correction provides a gain of about 43 dB. An adequate signal-to-noise ratio on an echoing area of less than 1 cm² at a range of 80 ft is expected.

This radar will be used on the larger range.

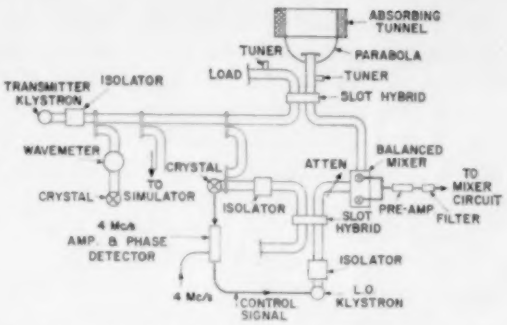

Fig. 8. 13·5 kMc/s Doppler radar microwave head.

6. RADAR CALIBRATION

The radar systems described above can provide accurate results only if the recorded signal can be calibrated accurately. The calibration has to include tunnel effects, insertion loss of the microwave head, etc. In other words a signal with known amplitude and Doppler shift has to be provided in the tunnel. The essential components of a system which can simulate the target in amplitude and velocity are shown in Fig. 9.

The simulator klystron is phase-locked, at a fixed IF, to the transmitter. When the IF is identical to the required Doppler shift, the latter is simulated to the accuracy of the low frequency

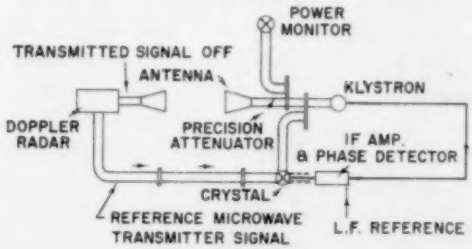

Fig. 9. Doppler simulator.

source. The power radiated by the simulator can be measured accurately and when this is made sufficiently high the insertion loss of the radar system up to the mixer crystals can be measured directly. The calibration of receiver sensitivity is of course carried out at much reduced power levels.

Two simulators have been built. One at 35 kMc/s, is now in routine use. The 13·5 kMc/s simulator will be available for use when the radar goes into operation.

7. TRANSVERSE BEAM EXPERIMENTS

The CW Doppler radar is able to measure the total scattered power arising from the target and significant portions of the associated plasma. It has no spatial resolution, unless different elements in the target area have different velocities. In order to achieve resolution we have turned to the use of a transverse beam, that is a beam directed normally to the line of flight in which both back and forward scatter measurements are made. The normal aspect with a given beam shape will produce maximum resolution.

7.1. *Broad antenna beams*

In our initial experiments we followed very closely ideas available from the large mass of publications concerning scattering from meteor trails. A recurring theme in that work is the use of a broad beam at low frequencies with very long trails which produce Doppler interference phenomena due to the relatively large curvature of the incident phase front in the vicinity of the trail. The interference phenomena, although strongly dependent on the parameters of the experiment, are nevertheless predictable and can be confirmed by experiment. It was immediately apparent in our experiments that the use of broad beams at microwave frequencies did not provide reproducible results. Careful study showed that this was to be expected and can be explained simply from the following diagram (Fig. 10).

Three tracks through the beam are shown. In

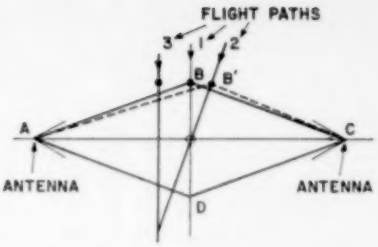

Fig. 10. Trajectories through a transverse beam.

back-scatter measurements it is almost impossible to eliminate transmitter leakage into the receiver. As a result of this, very low frequency Doppler beats or interference phenomena are predominant in the receiver output. The actual waveform is critically dependent on the distance AB, which of course varies as the projectile moves through the beam. This in itself is acceptable provided the same track is described on successive firings. However, different tracks of which 2 and 3 are typical are equally likely. This is mainly due to dispersion in firing. Consider a particular example. At 35 kMc/s the wavelength is approximately 0·34 in. If the difference in distances AB and AB^1 is 0·085 in., the unwanted phase change is 180° which can completely alter the received waveform. Results obtained from the forward scattered signal show a considerable improvement in that they are essentially reproducible. The reason is again apparent from the diagram (Fig. 10). The phase of the scattered signal depends on the properties of the target and the path length AB, BC. The phase of the reference is substantially constant and corresponds to the mean path $A0C$. As the projectile moves through the beam the path length AB, BC varies. This again is acceptable provided the variation is identical on successive firings. It can be seen that if AB changes to AB^1, BC will change to B^1C. These changes are in opposite directions and to the first order, they cancel. Consequently the forward scatter signal is much less susceptible to dispersion than the backscatter signal.

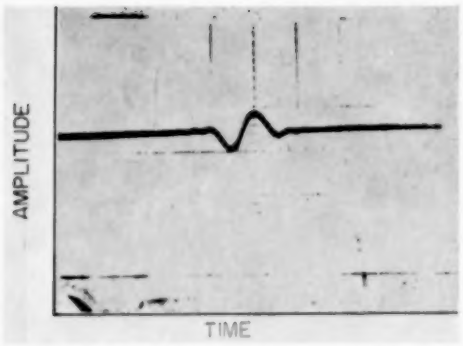

Fig. 12. Typical back-scatter signal.

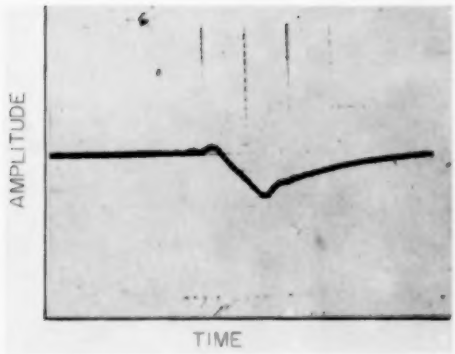

Fig. 13. Conditions as in Fig. 12; long decay possibly due to ionization.

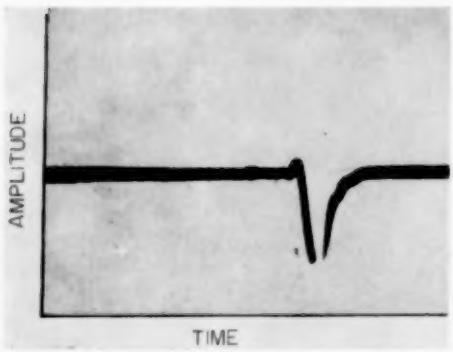

Fig. 14. Forward scatter signal on same beam as in Fig. 13; decay still evident.

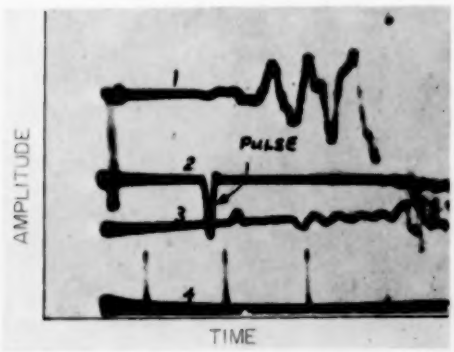

Fig. 15. Forward scatter signal on focused beam (channel 3).

Both situations are summarized in Fig. 11. Three typical backscatter signals are shown. The phase angles refer to the phase difference between the backscatter and leakage signals. Forward scatter signals resemble closely the curves labelled 0° or 180°. Patterns similar to these have been obtained in the laboratory. Some typical results are shown in Figs. 12–15.

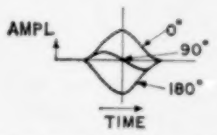

Fig. 11. Some received back-scatter signals.

A major improvement in the reliability and interpretation of results from both back and forward experiments can be obtained by narrowing the beamwidth until it is comparable to the projectile size. Under these conditions the passage of the projectile through the beam produces a clearly recognizable pulse.

It is fortunate that this improvement in reliability and interpretation with increased resolution is consistent with the main objective of probing the target area. With this in mind the main effort is now being devoted to achieving maximum resolution.

7.2. *Focused antenna beams*

The use of a focused lens is showing a great deal of promise.

If a lens of diameter a is focused at a distance R the resolution can be shown to be $S = 1/d$ where

$$d = \frac{R\lambda}{a} = f\lambda \qquad f = \frac{R}{a}$$

Alternatively d is the distance between the 3 dB points of the main lobe of the focused beam.

It is assumed that $a \geq 10\lambda$ and $R \geq a$.

For $R = a$, $d = \lambda$ which is the maximum resolution.

For a cosine squared amplitude distribution over the lens

$$d = 1{\cdot}45\frac{R}{a}\lambda = 1{\cdot}45f\lambda.$$

Applying these results to the 3-ft diameter range,

$R = 3/2$ ft

and for $R = a = 3/2$ ft

$d = 1{\cdot}45\lambda$

and for $\lambda = 0{\cdot}337$ in. (35 kMc/s)

$d = 1{\cdot}45 \times 0{\cdot}337 = 0{\cdot}49$ in.

for $\lambda = 0{\cdot}057$ in. (210 kMc/s)

$d = 1{\cdot}45 \times 0{\cdot}057$ in. $= 0{\cdot}082$ in.

On the 6-ft diameter range the same lens will produce half the resolution.

Experiments are being carried out on 13·86 in. diameter lens which is the largest that could be conveniently made. This lens has an f number of 1·3. It has been tested at 35 kMc/s. Typical patterns are shown in Fig. 16. This lens has $d = 1{\cdot}9\lambda = 0{\cdot}64$ in. The measured beamwidth is about 0·6 in. at the 6-dB points. The patterns were obtained by measuring the backscatter from a very small sphere (dia $= 1/3\lambda$) which involves two passes through the lens. Consequently the beamwidth is determined from the 6 dB and not the 3 dB points. This same lens at 210 kMc/s would have $d = 0{\cdot}1$ in.

The dispersion on typical firings would

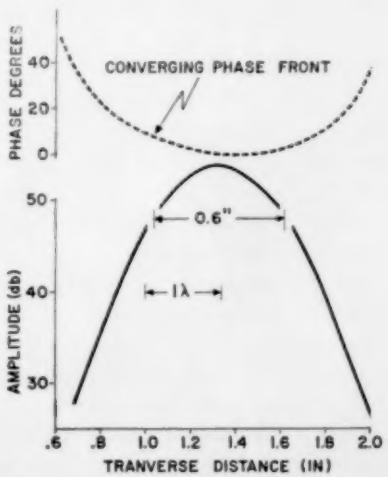

Fig. 16. Pattern of 40λ lens near focus.

prevent the focused spot from passing through the projectile on each shot. To overcome this difficulty a number of beams will be used. Each beam will be provided by the same lens but from a different feed horn which will be offset from the lens axis as shown in Fig. 17. In this way a number of focused spots in the vicinity of the axis will result and will ensure a response on each firing. In addition spots which do not intercept the projectile will probe the plasma in its vicinity. This scheme can also be applied to a forward scatter system.

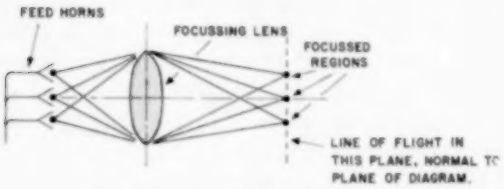

Fig. 17. Use of off-set feed horns.

8. APPLICATION OF BASIC TECHNIQUES

Previous sections have dealt with the design and development of two basic techniques. A brief outline will be given here of the ways in which these techniques can be applied to the measurement of plasma properties.

8.1. *CW Doppler radar*

The use of the CW Doppler radar is straightforward. It provides a continuous history of the projectile echoing area in flight and is most useful as a search instrument. In this latter role it can determine the conditions under which ionization is important at a given frequency.

An additional use is as a monitoring instrument. Some change in plasma conditions artificially induced or otherwise, would be recorded immediately. In one proposed experiment, a small corner reflector will be fired. Under static conditions this has an unusually large echoing area. However, if shock-front ionization is present then a large reduction in echoing area is expected. In a second experiment the plasma will be perturbed by the transverse beams and some interaction phenomena should be observed. This will be discussed later.

8.2. *Transverse beam experiment*

It is apparent from the development of the transverse beam that the interpretation of backscatter results is extremely difficult unless the resolution is high enough so that the projectile intercepts most of the beam. The change in signal level can be interpreted as a change in reflection from the stagnation region, the projectile and the ionized trail in turn. Under the same circumstances the transmitted beam results can be interpreted with the same ease.

It should be realized that the phase shift of a wave transmitted through a transparent plasma is a direct measure of the integrated electron density along the wave path. This measurement is normally beset by two difficulties. If the beam is wider than the plasma, diffraction effects introduce prohibitive errors. A varying amplitude signal will cause phase errors in the simplest form of microwave interferometer. This latter difficulty has been overcome in recent work by Wharton[7] and others[8] in the investigation of plasmas generated by fusion processes. The former difficulty can be overcome by the use of a focused beam as outlined previously. At present a "fringe" interferometer using focused beams is being considered at frequencies of 35, 70, 140 and 210 kMc/s. It is expected that accurate electron densities in the trail will be available and at the higher frequencies it should be possible to measure the electron density in the stagnation region.

Collisional processes in gases determine the absorption of a propagating wave. Consequently a measurement of absorption can be made to obtain the collision frequencies. The change in signal level due to absorption in a small volume of plasma is normally quite small and for this reason the interaction effect, which is discussed in the next section, is of great interest.

8.3. *The interaction effect*[9]

The propagation of an e.m. wave through a plasma is dependent on the power level of this wave. If sufficient power is available the wave will actually change the collision frequency by a measurable amount. In particular, if the wave is modulated the collisional frequency will tend to follow the modulation frequency. Since the absorption is determined by collision frequency a second wave propagating through the same plasma will suffer additional attenuation. Provided that the change is not too large it can be used as a measure of the collision frequency.[10]

This phenomena was first noticed in the broadcast band and is more commonly known as the Luxembourg effect.[10] In this connection it has been treated extensively. It appears that Goldstein[11] first applied this phenomena to the measurement of collision frequency at microwave frequencies. Using frequencies close to 9 kMc/s he demonstrated:

(a) The interaction effect as evidenced by a change in attenuation, is easily measurable.

(b) There is a finite time constant associated with the application of the disturbing wave and the resultant change in attenuation. For a small perturbation, the change in attenuation is exponential for a step-function change in the amplitude of the disturbing wave. The time constant can be made less than one microsecond.

It is proposed to use this phenomena in the following way. One of the focused transverse beams will be used to perturb the plasma as the projectile passes through the beam. With sufficient resolution it should be possible to probe the stagnation region and ionized trail successively. After short intervals these regions of plasma will successively attain new equilibrium conditions. It has been shown that these changes should be observable on the CW Doppler radar. Finally it should be possible to deduce the collision frequency in each region.

Acknowledgements—The course of this research is very much dependent on the co-operation of personnel at CARDE. The assistance of Drs G. V. Bull, C. J. Maiden and Mr G. H. Tidy has been particularly valuable. The experimental development of the microwave techniques is due to the combined Microwave Section at DRTE. Finally the author wishes to thank DRB for permission to publish this paper.

REFERENCES

1. D. Bershader, *Missile Aerophysics Phenomena of Electronic Import*, Inst. Radio Engrs. Wescon Convention Record, Pt. 8, p. 23 (1957).
2. S. G. Homic and R. L. Phillips, *Communicating with the Hypersonic Vehicle*, *Astronautics* **4**, p. 36 (1959).
3. *Ions Make Trouble at Mach 10*, p. 13 in *Electronics*, Business Edition McGraw-Hill, New York. (March 1958).
4. W. B. Sisco and J. M. Fiskin, *Shockwave Ionization and its effect on Space Communications* in *Inst. Radio Engrs. Nat. Symp. on Extended Range Communications, Oct. 6–7, 1958.*
5. C. J. Maiden and C. St. Pierre, *Some Measurements of the Physical Properties of the Plasma Sheath Around Hypervelocity Projectiles*, presented at this Symposium.
6. R. I. Primich, W. A. Pope, E. Atkins, W. Blore and A. L. Broadfoot, *A CW Doppler Radar for Observing Projectiles in Hypersonic Ballistic Ranges*, DRTE Rep. No. 1032 (Jan. 1960).
7. C. B. Wharton and D. M. Slager, *Trans. Inst. Radio Engrs. on Nuclear Sci.* **6**, 20 (1959).
8. M. A. Heald, *Trans. Inst. Radio Engrs. on Nuclear Sci.* **6**, 33 (1959).
9. The author has discussed this proposal at several conferences at which no formal record was kept. The first dates back to December 1957. In view of the interest being shown in this phenomena by people outside the ionosphere research field, a more detailed report is being prepared.
10. See for instance (a) V. A. Bailey and D. F. Martyn, *Nature, Lond.* **133**, 218 (1934); *Phil. Mag.* **18**, 369 (1934); *Nature, Lond.* **135**, 585 (1935).
(b) J. W. King, *J. Atmos. Terr. Phys.* **14**, 41 (1959) etc.
11. L. Goldstein, J. M. Anderson and G. L. Clark, *Phys. Rev.* **90**, 151 (1953).

SOME MEASUREMENTS OF THE PHYSICAL PROPERTIES OF THE PLASMA SHEATH AROUND HYPERSONIC PROJECTILES

C. J. MAIDEN and C. ST. PIERRE
Canadian Armament Research and Development Establishment, Quebec, Canada

Abstract—A brief description of the range facility is presented. Tests have been made in which 1/2 in. calibre models of various shapes are launched into a controlled atmosphere at velocities up to 16,000 ft/sec. The stagnation point conditions relevant to the velocities and range pressures used in these tests have been theoretically estimated. Such physical properties of the plasma as temperature, density, gas composition and electron density are given. It is found that stagnation point temperatures as high as 7,000 K may be obtained. The ablative effect of such high temperatures is discussed and results are presented showing meteor-like trails behind the models.

The paper also describes systems developed to measure the intensity of the radiation emitted by the plasma surrounding a hypervelocity projectile. Photomultipliers, infrared detectors, spectrographs and multiple-channel monochromaters have been utilized in the study. Results obtained are summarized and discussed.

1. INTRODUCTION

The experimental results presented in this paper have been obtained from the C.A.R.D.E. Hypersonic Range 1 facility. The purpose of this facility is to study hypersonic free-flight phenomena that are of interest to missile, anti-missile and space technology programmes. The properties of the plasma sheath surrounding a hypersonic body are of definite importance in these programmes. The advantages of a free-flight range for investigating such plasmas have been enumerated in Ref. (1) and will not be repeated here.

The study of the plasma surrounding a hypersonic body involves research in the fields of microwave physics, real gas dynamics, chemical kinetics and ablation physics. On the C.A.R.D.E. Range 1 facility the microwave research is a joint C.A.R.D.E.–D.R.T.E. programme and is described in Ref. (2). Experiments designed to measure ultraviolet, visible and infrared radiation generated by a hypersonic projectile are being conducted at the same time as the microwave research. The results of radiation experiments which have good spectral and spatial resolution can yield very useful information as to the chemical species in the plasma. Also, by comparing the experimentally measured radiation with theoretical predictions the validity of various theories concerning the properties of the plasma can be assessed.

2. DESCRIPTION OF FACILITY

The Range 1 facility is shown diagrammatically in Fig. 1. Basically the range consists of a dump tank to reduce gas contamination in the range proper, followed by a 50 ft long tank which can be evacuated to simulate altitude. At the moment a Kinney KDH mechanical rotary pump capable of evacuating the range to a pressure of 1 mm of mercury (155,000 ft) is used. An Edwards 18B3 oil booster pump capable of reducing the pressure to less than 10 μ ($>$265,000 ft) is being installed. To date the range atmosphere has not been controlled chemically, however, steps are being taken to install cold traps which should minimize oil and water vapour impurities. In addition provision is

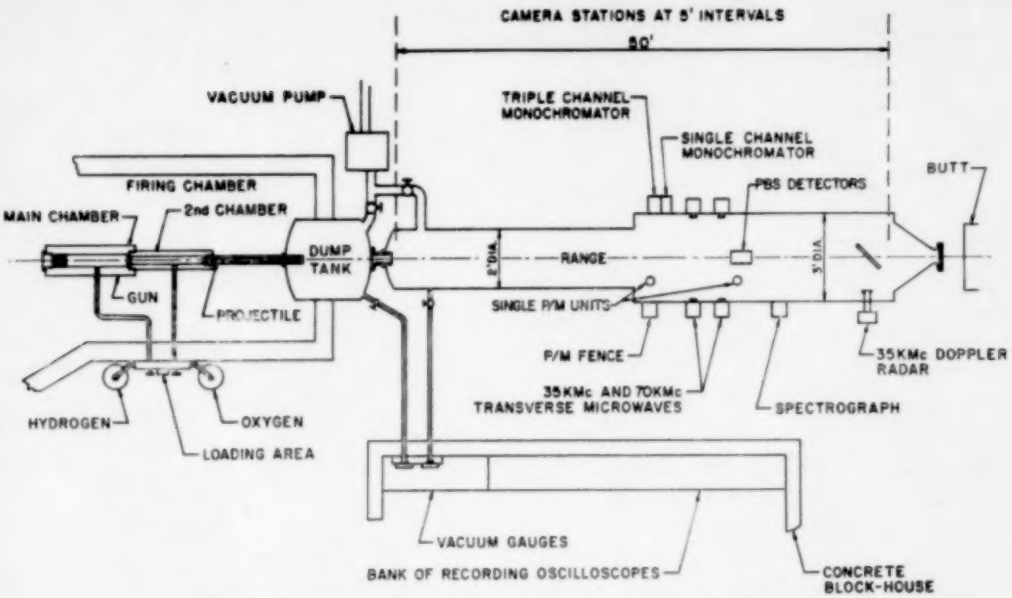

Fig. 1. A diagrammatic representation of the range No. 1 facility.

being made to sample and analyse the range atmosphere.

One half-in. diameter models of various shapes and materials are launched into the range at velocities as high as 16,100 ft/sec. To achieve these velocities a light gas gun has been used. Details of this gun are given in Ref. (3).

To measure the projectile velocity interruption-type light screens are used in conjunction with shadowgraph photographic stations. Fig. 1 shows a number of such stations at intervals down the range. At each station the projectile interrupts a narrow light beam which is focused on a photocell placed diametrically opposite the light source. The resulting amplified photocell output triggers the spark unit of the shadowgraph system. The spark discharge induces an output in a small low-inductance coil adjacent to the spark gap and the resulting signal is used to stop one electronic counter (chronograph) and start another. In this manner average velocities between each set of stations are measured. Velocities are confirmed if photographs are obtained.

This concludes the description of the C.A.R.D.E. Range 1 facility. A more comprehensive description of the range is contained in Ref. (3).

3. THEORETICAL EQUILIBRIUM CONDITIONS AT THE STAGNATION POINT OF A HYPERSONIC BODY

Before considering experimental results it is advisable to obtain some idea of the theoretical thermodynamic properties and gas composition at the stagnation region of a hypersonic body in a free-flight range. The stagnation point temperature and density can be obtained from Feldman's hypersonic gas dynamic charts for equilibrium air.[4] Table 1 presents these parameters for pressures of 760 mm (sea level), 1·65 mm (140,000 ft) and 0·13 mm (225,000 ft) at velocities from 8,000 to 18,000 ft/sec. The altitudes chosen are the altitudes from Ref. (4) that have free-stream temperatures

	VELOCITY FT/SEC	760 MM (SEA LEVEL)	1·65 MM (140,000 FT)	0·13 MM (225,000 FT)
RATIO OF STAGNATION POINT DENSITY TO SEA LEVEL DENSITY	8,000	6·70	$1·49 \times 10^{-2}$	$1·32 \times 10^{-3}$
	10,000	7·69	$1·85 \times 10^{-2}$	$1·64 \times 10^{-3}$
	12,000	8·62	$2·16 \times 10^{-2}$	$2·02 \times 10^{-3}$
	14,000	9·21	$2·24 \times 10^{-2}$	$2·02 \times 10^{-3}$
	16,000	9·50	$2·34 \times 10^{-2}$	$2·18 \times 10^{-3}$
	18,000	9·92	$2·56 \times 10^{-2}$	$2·42 \times 10^{-3}$
STAGNATION POINT TEMP. °K	8,000	2730	2580	2460
	10,000	3780	3060	2910
	12,000	4800	3630	3330
	14,000	5790	4560	4350
	16,000	7020	5460	5070
	18,000	8130	6000	5520

Table 1.

of 300°K, hence, direct simulation of flight conditions at these altitudes can be obtained in an evacuated range. From the table of results it can be seen that temperatures of several thousand degrees Kelvin can be obtained at the stagnation point. In deriving these figures it is assumed that the stagnation point gas is in thermodynamic equilibrium. This assumption is not always valid in practice. However, the greater the free-steam pressure the closer this condition is approached.

It is of interest to extend the results of Table 1 to investigate the gas properties behind the whole of the bow shock wave of a hypersonic sphere. Maslen and Moeckel[5] have presented a method to do this. In this method equilibrium gas conditions are assumed at every point, the flow is assumed to be inviscid and entropy changes along stream tubes behind the shock are taken to be negligible. In addition a Newtonian pressure distribution is assumed on the surface of the sphere. The most serious of these assumptions is the neglect of viscosity effects; however, these can perhaps be taken into account by altering the body shape to include an estimated boundary layer.

The method of Ref. (5) involves a tedious iterative process but has the advantage over other methods in that it considers the case of a real gas in dissociated equilibrium. For this paper four solutions have been calculated by hand; they are for spheres at 1·65 mm (140,000 ft) at velocities of 10,000, 12,000, 14,000 and 18,000 ft/sec. Full details of these solutions along with solutions for other flight conditions are presented in Ref. (6). Fig. 2 (a) and (b) shows the calculated bow shock wave shape, the streamline pattern, the temperature contours and the sonic line

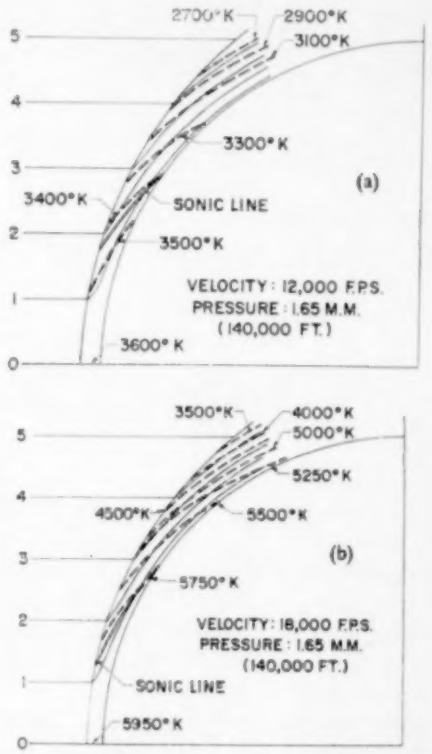

Fig. 2. Theoretical nose cap solutions by the method of Ref. (5), at a pressure of 1·65 mm. (a) Velocity: 12,000 ft/sec, (b) Velocity: 18,000 ft/sec.

for velocities of 12,000 and 18,000 ft/sec at a pressure of 1·65 mm. The four solutions calculated at 1·65 mm give rise to two main points of interest. The first is that the shock detachment distance is altered only slightly in the range of velocities considered and compares well with values given in Ref. (7) (3–4 per cent of the body diameter); and the second point is that the temperature contours curve in towards the body

keeping the gas next to the sphere comparatively hot. These solutions will be used later to calculate the theoretical radiation to be expected from the nose cap of a hypersonic sphere at 1·65 mm.

The theoretical gas composition at the stagnation point of a hypersonic body in air can readily be calculated from Ref. (8). This reference presents the composition of air in thermodynamic equilibrium as a function of temperature and density. Hence, for the cases considered in Table 1 the stagnation point particle concentration can be calculated. Tables 2 and 3 present the concentrations of e^-, O_2, O, O^+, O^-, NO_2, NO, NO^+, N^2, $N^{2+}N$, N^+, CO_2 and CO for several flight conditions. Table 2 considers a constant pressure of 1·65 mm and velocities of 10,000 to 18,000 ft/sec whereas Table 3 is for a constant velocity of 14,000 ft/sec and pressures of 760 mm, 1·65 mm and 0·13 mm, respectively. These tables consider the most significant particle concentrations and have been calculated for dry air. Particular points of interest from the tables are:

(i) The large concentrations of atomic oxygen, i.e. at 1·65 mm and 16,000 ft/sec there are approximately 1000 oxygen atoms per oxygen molecule.

(ii) The dissociation of N_2 is not nearly as complete as the dissociation of O_2, i.e. at 1·65 mm the projectile velocity must reach 18,000 ft/sec before the ratio of N–N_2 approaches one.

(iii) The relatively large concentrations of NO and the fact that the concentration of NO falls off slightly with increasing velocity in Table 2.

(iv) The relatively high concentrations of CO and, finally,

(v) the fact that the electron density is predominantly controlled by the ionization of NO and the formation of O^-.

The concentrations presented in Tables 2 and 3 are for limited flight conditions, however, the data presented will prove relevant to experimental measurements to be described later.

EQUILIBRIUM PARTICLE CONCENTRATION (NO/cm^3)

VEL (f.p.s.)	ALT. (ft.)	e^-	O_2	O	O^+	O^-	NO_2	NO
10,000	140,000	4.15^{10}	6.12^{16}	5.04^{16}	1.38^{4}	4.45^{8}	3.75^{12}	1.96^{16}
12,000	140,000	6.12^{11}	2.20^{15}	1.21^{17}	5.43^{6}	5.55^{9}	1.91^{12}	2.13^{16}
14,000	140,000	1.41^{13}	2.52^{13}	2.22^{17}	6.49^{9}	5.99^{10}	3.12^{11}	1.37^{16}
16,000	140,000	8.51^{13}	3.76^{14}	2.44^{17}	5.51^{11}	1.78^{11}	5.64^{10}	7.64^{15}
18,000	140,000	2.26^{14}	1.70^{14}	2.74^{17}	4.59^{13}	3.60^{11}	2.88^{10}	6.16^{15}

VEL (f.p.s.)	ALT. (ft.)	NO^+	N_2	N_2^+	N	N^+	CO_2	CO
10,000	140,000	4.25^{10}	3.80^{17}	3.21^{2}	1.76^{13}	6.42^{-1}	4.25^{13}	1.10^{16}
12,000	140,000	6.13^{11}	4.50^{17}	1.85^{3}	2.78^{14}	2.60^{3}	8.55^{12}	1.50^{16}
14,000	140,000	1.35^{13}	4.67^{17}	5.15^{4}	7.90^{15}	9.58^{7}	6.23^{11}	1.92^{16}
16,000	140,000	8.76^{13}	4.91^{17}	9.25^{10}	6.26^{16}	6.79^{13}	3.39^{10}	1.94^{16}
18,000	140,000	2.11^{14}	4.42^{17}	1.16^{12}	1.74^{17}	2.26^{12}	3.70^{10}	2.10^{16}

EQUILIBRIUM PARTICLE CONCENTRATION (NO/cm^3)

VEL. (f.p.s.)	ALT. (ft)	e^-	O_2	O	O^+	O^-	NO_2	NO
14,000	SEA LEVEL	8.40^{10}	9.63^{16}	5.43^{19}	7.70^{12}	2.66^{15}	3.31^{16}	2.76^{19}
14,000	140,000	1.41^{13}	2.52^{15}	2.22^{17}	6.49^{9}	5.99^{10}	3.12^{11}	1.37^{16}
14,000	225,000	1.20^{12}	2.53^{2}	1.70^{15}	8.47^{8}	5.06^{8}	8.30^{8}	3.20^{14}

VEL. (f.p.s.)	ALT. (ft)	NO^+	N_2	N_2^+	N	N^+	CO_2	CO
14,000	SEA LEVEL	1.14^{16}	1.73^{20}	3.16^{12}	2.47^{19}	1.92^{11}	4.10^{15}	7.40^{19}
14,000	140,000	1.35^{13}	4.67^{17}	5.15^{8}	7.90^{15}	9.58^{7}	6.23^{11}	1.92^{16}
14,000	225,000	1.16^{12}	3.11^{16}	5.81^{7}	1.15^{15}	2.82^{7}	5.98^{9}	1.29^{13}

Tables 2 and 3.

4. MACROSCOPIC RADIATION STUDIES

Theoretical estimates of the gas properties behind the bow shock wave of a hypervelocity body were presented in the previous section. A review of the phenomena that occur in the vicinity of a hypersonic sphere is relevant at this stage. As the air crosses the shock front it is strongly compressed and heated up to a temperature of several thousand degrees Kelvin (see Table 1). As the air heats up it tends towards thermodynamic equilibrium, in which state it is dissociated through one or two stage reactions into species whose concentrations have been estimated in Tables 2 and 3. At the high stagnation temperatures the air will radiate energy due to transitions between molecular and atomic levels of its constituents and by Bremsstrahlung produced by free electrons. In addition to air constituents other species are present in the wake. Material is ablated from the projectile

and may combine chemically with atmospheric constituents. Such ablation products can also contribute to the radiant energy.

As mentioned in the introduction to this paper the study of the ultraviolet, visible and infrared radiation emitted from the plasma surrounding a hypersonic projectile is of immediate interest. While macroscopic studies yield useful information for missile detection, microscopic studies can yield information about the plasma species, their rate of reaction and their temperature and density distribution. To obtain this information the ideal radiation detector would have perfect spectral, time and space resolution.

In a free-flight range it is possible to orientate a radiation detector to look side-on or head-on at the projectile. Looking head-on has the advantage that the results are more applicable to missile detection and also, for comparison purposes, theoretical intensity calculations are more easily performed since one has to deal with a symmetrical body. On the other hand in ballistic ranges it would be very difficult to distinguish the projectile from the flame of the gas gun. For this reason all radiation detection devices in the C.A.R.D.E. Range 1 facility view the projectile side-on.

4.1. *Photomultiplier fence*

Figure 3 shows details of this apparatus. There are six channels to provide spatial resolution, each channel consisting of a $\frac{3}{4}$ in. diameter–2 in. focal length lens, a slit focused on the trajectory plane and IP21 photomultiplier. This photomultiplier is sensitive in the wavelength region between 3,400 and 5,500Å. Each slit defines a $\frac{3}{16}$ in. $\times$ $1\frac{1}{4}$ in. field of view in the trajectory plane and thus the six channels cover a total area of $\frac{3}{16}$ in. $\times$ $7\frac{1}{2}$ in. Neutral filters are placed in front of the unit to keep the light flux on the photomultipliers within a given range defined at the lower limit by the background noise and at the higher limit by linearity considerations. Also, a shield extending 8 in. into the range is used to eliminate any extraneous radiation that would be scattered towards the detectors. Fig. 4 is a block diagram illustrating the presentation system and the oscilloscope triggering device. Since the sweep of the oscilloscope is intentionally relatively fast the pulse from the light screen has to be delayed prior to triggering the oscilloscopes. The output pulses on the three dual-beam Tektronix oscilloscopes are photographed with polaroid cameras.

Fig. 5 shows two sets of typical traces with the

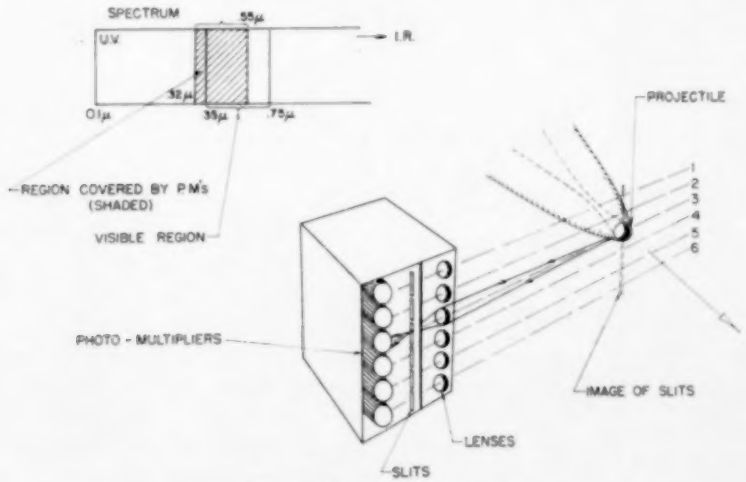

Fig. 3. Photomultiplier fence.

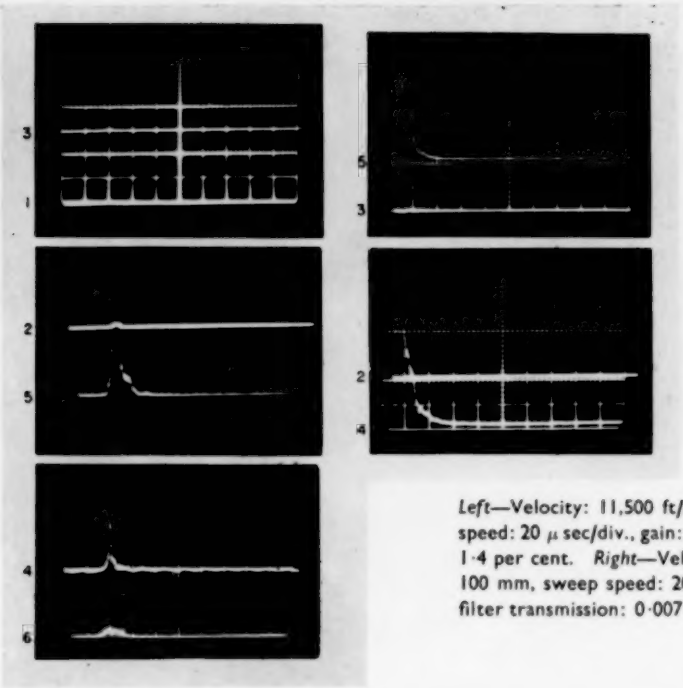

Fig. 5. Typical traces from the photomultiplier fence.

Left—Velocity: 11,500 ft/sec, pressure: 46 mm, sweep speed: 20 μ sec/div., gain: 0·2 V/div., filter transmission: 1·4 per cent. *Right*—Velocity: 13,000 ft/sec, pressure: 100 mm, sweep speed: 20 μ sec/div., gain: 0·2 V/div., filter transmission: 0·007 per cent.

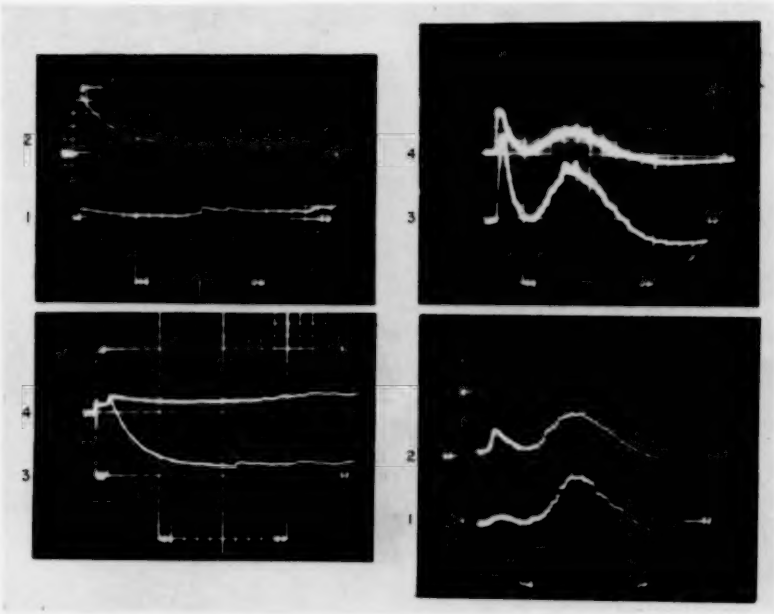

Fig. 9. Typical traces from the PbS fence.

Left—Velocity: 10,900 ft/sec, pressure: 26 mm, sweep speeb: 100 μ sec/div.
Right—Velocity: 7100 ft/sec, pressure: 52 mm, sweep speed: 1 m.sec/small div., gain: 0·5 V/div on channels 1, 2 anb 3; 1·0 V/div. on channel 4.

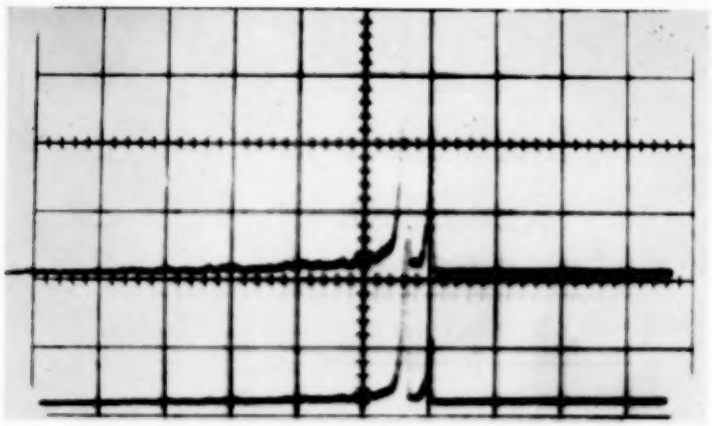

Fig. 10. Typical trace from a single photomultiplier unit. Velocity: 12,480 ft/sec, pressure: 1·9 mm, sweep speed: 20 μ sec/div., gain: upper beam: 2 V/div., lower beam: 1 V/div.

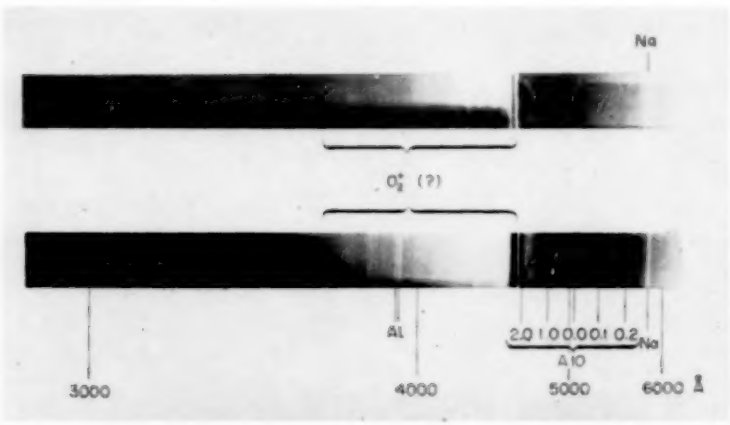

Fig. 12. Emission spectra from 1·5 in aluminium projectiles.

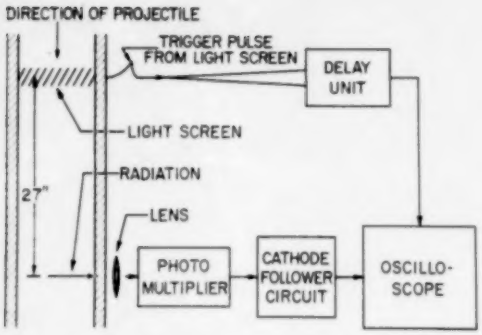

Fig. 4. Block diagram of the presentation circuit for the photomultiplier fence.

channel numbers shown on the left of the traces. The set on the left have a sweep speed of 20 μ sec/div and were obtained from an aluminium projectile travelling at 11,500 ft/sec in a range pressure of 46 mm. In this case the projectile passed between channels 4 and 5. For these channels the pulse duration is very short; in fact the width of the pulse at half peak is less than 4 μ sec. This means that there is a very high intensity region whose length is less than $\frac{3}{16}$ in. On many other shots this sharp pulse is seen in one channel only while no pulse is seen on the other channels. From the geometry of the detection system it can thus be deduced that this very intense region is less than $1\frac{1}{4}$ in. wide. One may also note in channels 4 and 5 the change in decay time of the pulse at an amplitude of approximately 1/6 of the peak value. The set of traces on the right of Fig. 5 was obtained with a projectile travelling at 13,000 ft/sec in a range pressure of 100 mm. In this case the projectile passed under channel 4 and the pulse goes off screen. On channel 5 the pulse was obtained from part of the gas behind the shock wave. This is seen by comparing the pulses from these two channels. If the pulse of channel 5 is superimposed on the pulse of channel 4 a good match is obtained except for the narrow peak on channel 4. The logical explanation is that the peak intensity originates from the stagnation region while the slowly decaying pulse is due to wake luminosity. Since the total duration of the pulse is 20 μ sec this region of lower intensity has a length of 2·5 in.

The first radiation programme in the C.A.R.D.E. Range 1 facility covered a two-month period in which 130 cylindrical aluminium pellets were fired at velocities from 7000 to 14,000 ft/sec in range pressures from 10 to 200 mm. Many of these shots were missed on the photomultiplier fence due to incorrectly timed oscilloscope triggers and also because too light or too dense neutral filters were used. Seventy photomultiplier traces were useful in some way. Three types of studies were made with the results.

The first study consisted in measuring the delay time between the trigger pulse from the light screen (see Fig. 4) and the pulse from the photomultiplier. This time was compared with the flight time between the light screen and the fence as deduced from the projectile velocity. Fig. 6 is a plot of the difference of these two-times against the flight time deduced from the

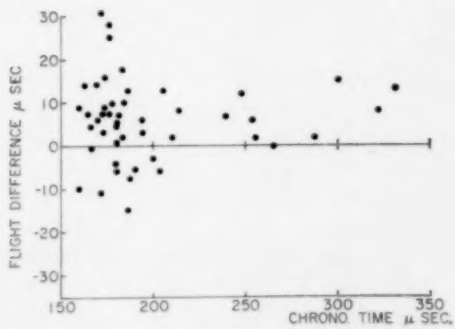

Fig. 6. Difference in flight time measured with the photomultiplier fence and with the chronographs.

velocity measurement. The average value of the difference is 6 μ sec. This value as well as most of the spread can be attributed to the light screen and in certain cases to the triggering of the oscilloscopes. The small average difference of 6 μ sec in Fig. 6 shows, however, that we are

definitely looking at the luminous gas surrounding the projectile. On the other hand this result does not permit localization of the origin of the radiation within the length of the projectile; however, the peak is almost certainly from the stagnation region.

The second study considered the time variation of intensity. The results can be stated in the following manner. If we look side-on through a $\frac{3}{16}$ in. wide slit at a $\frac{1}{2}$ in. projectile travelling at hypersonic velocity in a rarefied atmosphere we first see a very bright region surrounding the stagnation point. This is followed by a region whose intensity is nearly one order of magnitude lower and whose length is approximately 2 in. In many cases it has also been seen that this second region was followed by another region with still lower intensity which decayed exponentially to $1/e$ of its initial value in approximately 60 μ sec. This time corresponds to a length of 7 in., and the region was observed to extend more than $\frac{3}{4}$ in. on both sides of the projectile. Time resolved spectra would be necessary to find the mechanisms which would explain these features. The lengths of the three intensity regions have not yet been correlated with velocity and pressure, however, the lengths indicated above represent average values from which there was little departure for the flight conditions considered.

The object of the third study was to determine the relationship between peak intensities and velocity and pressure. The detectors have been calibrated against a tungsten ribbon filament. The signal from the photomultipliers were related to the detector power by taking into account the temperatures of the filament, the emissivity of tungsten and the wavelength response of the detector. Fig. 7 contains the experimental values of peak intensities for various velocities and pressures. The absolute radiant power from the projectile was determined from the pulse heights by assuming that the spectral intensity distribution has a constant value between 3400 Å and 5500 Å. The spread

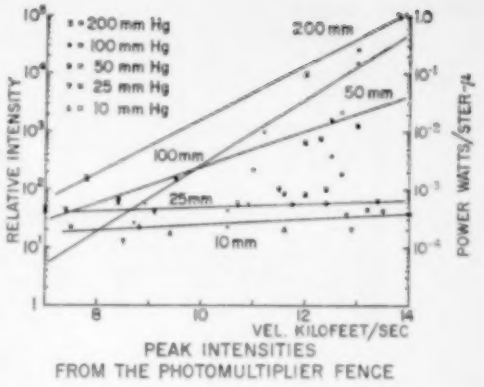

Fig. 7. Absolute peak intensities from the photomultiplier fence.

in the points can probably be accounted for by the impurities in the range, by the electronic drift, by the variation in the distance between the projectile and the detector and by the variable orientation of the projectile in the field of view. It was decided to draw tentatively straight lines through the maximum intensity points for each pressure. It will be later observed that the scatter in the results obtained from the second radiation programme using aluminium spheres is far less than in Fig. 7.

4.2. *Lead sulfide infrared fence*

This apparatus is illustrated in Fig. 8. There are four channels each having a field of view of

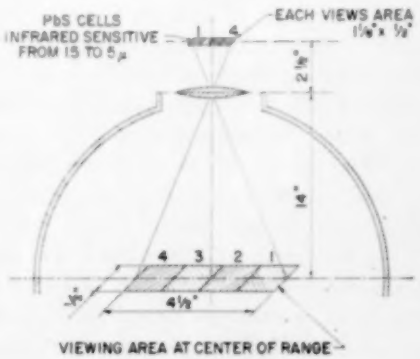

Fig. 8. Lead sulfide fence.

$\frac{1}{2}$ in. $\times$ 1 in. These detectors are sensitive in the wavelength region between 0·9 and 2·5 μ and their response time is 500 μ sec. Fig. 9 shows two sets of typical traces. For the set at left the velocity is 10,900 ft/sec, the pressure 26 mm and the sweep speed 100 μ sec per small division. The pulse is seen to rise sharply and decay to a tenth of its peak value in 1 m.sec. The set of traces at right was obtained for a velocity of 7100 ft/sec and a pressure of 52 mm. In this case, however, the sweep speed is 1 m.sec per small division. Here again the total duration of the pulse due to infrared radiation from the passage of the projectile is one millisec. The second large pulse is attributed to the flame from the gun.

Any correlation between peak values of the pulse or area under the pulse with velocity or pressure is impossible because of two factors. The first is the long response time of the detector compared to the fast onset of radiation. In addition, the area under the pulse is of little use because the total duration is neither much longer nor much shorter than the response time of the detector. The other complicating factor is that the radiating volume is not completely covered by the transverse 4 in. field of view.

A much better infrared system will be in operation in the next few months. This will consist of gold-doped germanium detectors with a response time of 1–2 μ sec. These detectors can be used in the 1·5–9·0 μ region and will be used with 0·15 μ filters.

4.3. *Single photomultiplier units*

These units consist essentially of two slits in front of an IP21 photomultiplier thus defining an $\frac{1}{8}$ in. $\times$ 7$\frac{1}{2}$ in. field of view at the centre of the range. Two such units are used at 10 ft intervals; the first unit is close to the photomultiplier fence and the second unit is adjacent to the lead sulfide fence. One of the purposes of these units is to compare the radiation intensities for various flight-times of the projectile. If the ratio of intensities is one, steady conditions have been reached after a flight of 25 ft (the distance of the first unit from the gun muzzle). It is to be noted that all the radiation detecting equipment is used at 25 ft or more from the gun muzzle.

The two single photomultiplier units have been used in the second radiation programme which commenced on November 12 and in which 0·4 in. aluminium spheres were launched into the range. These spheres were fired in an ethocell sabot which was permitted to follow the sphere down the range. A typical result from a unit is shown in Fig. 10, for a sphere at 12,400 ft/sec in a range pressure of 1·9 mm. The first signal on the right is the sphere and the second signal is the sabot. The two traces shown in the figure represent different oscilloscope gains and it can be seen from the top trace that the signal from the sabot has gone off screen.

Results obtained to date from these units at a range pressure of approximately 1·65 mm (140,000 ft) are presented in Fig. 11. The peak

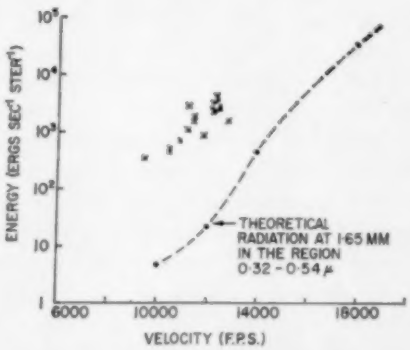

Fig. 11. Theoretical and experimental radiation results at 1·65 mm pressure. (Crosses represent experimental points.)

radiant energy in ergs sec^{-1} ster^{-1} is plotted against velocity. The units were calibrated using a tungsten lamp and the assumption made in obtaining the experimental points (crosses) in Fig. 11 was that the responsivity (R) of the photomultiplier is constant with wavelength between 3400 and 5500°A and is given by

$$R = \frac{1}{2100} \int_{3400}^{5500} R_\lambda d\lambda$$

where R_λ is the responsivity of the photomultiplier at wavelength λ, and λ is given in angstroms. This assumption is reasonably valid if the emission over the wavelength region considered is reasonably uniform. In all the measurements made at 1·65 mm the ratio of the peak intensity from the two units is close to one, thus indicating that steady conditions are obtained after a 25 ft flight. Also, shown in Fig. 11 is the theoretical radiation that would be emitted in the wavelength region 3400–5500 Å in a direction perpendicular to the trajectory of 0·4 in. spheres travelling at 10,000, 12,000, 14,000 and 18,000 ft/sec in a range pressure of 1·65 mm. These theoretical results can be adapted to any sphere size as the radiation is proportional to the cube of the diameter. The theoretical points in Fig. 11 were calculated using the nose cap solutions from Ref. (6), two of which solutions have been presented in Fig. 2. For each velocity considered the shock cap was partitioned into several hundred volume elements, each element having two faces parallel to each other and to the range axis. Each volume was assumed to be at constant temperature and density, and emissivity values were obtained from Ref. (9). The curves presented in Ref. (9) were extrapolated to cover the required range of temperature and density. Such extrapolations plus the fact that the temperature and density of the small volume elements were only constant to within ± 5 per cent must introduce errors into the analysis. It is considered that these factors could cause the points in Fig. 11 to be in error by up to ± 25 per cent; however, such errors will not significantly alter the shape of the theoretical radiation curve.

A comparison of the theoretical and experimental results in Fig. 11 indicates that the experimentally measured radiation is at least an order of magnitude greater than that predicted theoretically. The significance of this result is discussed later.

5. MICROSCOPIC RADIATION STUDIES

Apart from the very obvious limitations of the theory (Refs. 5 and 9) used to calculate the theoretical points in Fig. 11 there are a number of effects that could cause a discrepancy between theory and experiment. For instance, the presence of material ablated from the projectile and chemical reactions between ablated material and atmospheric constituents could contribute to the detected radiation. Experimental results have been obtained indicating that projectile ablation does occur during our tests. For example Fig. 12 shows typical emission spectra from aluminium alloy projectiles. The most predominant features that have been observed on such spectra are the second positive band system of nitrogen, the Schuman Runge band system of oxygen, AlO bands and Al, Mg and Na lines. Finally we can also observe a continuum which seems to disappear at 4500 Å, but this is due to the use of different photographic emulsions for the two parts of the spectrum.

The nitrogen and oxygen band systems are expected (see Tables 1–3), however, the Al, Mg and AlO characteristics could be due to material ablated off the projectile by the high temperature stagnation region gas. The projectile probably ablates in the form of macroscopic molten particles breaking away from the body; for at the comparatively high pressures (>1 mm) used in our experiments, ablation by sputtering would be negligible. It should be pointed out at this stage that these spectra are time integrated and could give erroneous results due to molten aluminium particles, eroded in the barrel, following the projectile down the range. An aluminium projectile will have a coating of Al_2O_3; thus it is considered that the ablated material could be both Al and Al_2O_3 with the Al_2O_3 being dissociated to Al, AlO and O by the high temperature stagnation gas. Any molten particles would break up into molecular and atomic form and the aluminium atoms would be slowed down by collisions with atmospheric constituents possibly reacting with monatomic oxygen to form AlO.

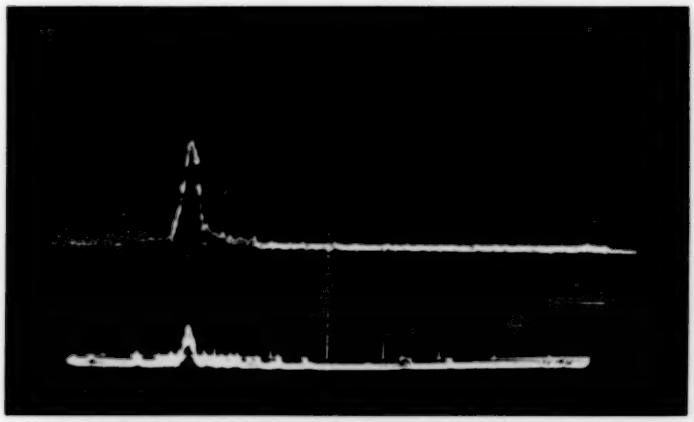

Fig. 14. Typical traces from the triple channel monochromator. Velocity: 12,600 ft/sec, pressure: 100 mm, sweep speed: 10 μ sec/div. Top trace corresponds to the Al lines, gain: 0·1 V/div. Lower trace corresponds to the AlO band, gain: 0·5 V/div.

This reaction is exothermic and the energy released would contribute to the luminous energy detected by the photomultipliers. We have endeavoured to investigate the existence of this reaction by using two monochromators to find the intensity versus time history of certain spectral characteristics shown in Fig. 12.

The first monochromator is a Perkin Elmer model 83 universal monochromator in which radiation covering the spectral region 4792 Å to 4892 Å is focused on an IP21 photomultiplier and the output displayed on an oscilloscope. The spectral region viewed with this unit thus includes the continuum and three strong AlO bands at 4842 Å, 4866 Å and 4888 Å. A typical trace from this monochromator is shown in Fig. 13; the sweep speed is 20 μ sec per division.

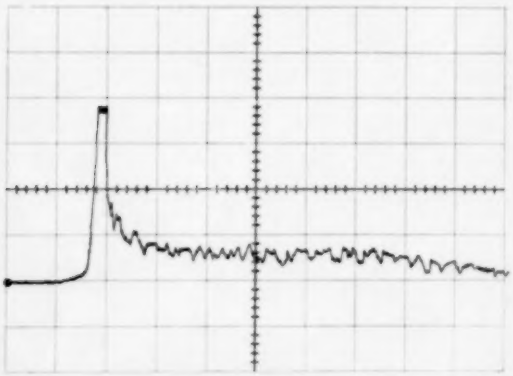

Fig. 13. Typical trace from single channel monochromator. Velocity: 11,600 ft/sec, pressure: 55 mm, sweep speed: 20 μ sec/div.

The pulse shape is significantly the same as those obtained from the photomultiplier units, and the image of the slit in the trajectory plane is nearly the same as for the photomultiplier fence. It may thus be concluded that the light emitted in this 100 Å wavelength band comes from the same region of space as the light in the whole range 3400 Å to 5500 Å.

The second unit is in effect a double channel monochromator. The dispersed light from a Hilger spectrograph has been partially blanked off so as to enable the light from two 20 Å wide bands to be separately viewed by IP21 photomultipliers. Fig. 14 shows a test result from a aluminium projectile at 12,600 ft/sec in a range pressure of 100 mm. The 20 Å regions viewed cover the AlO band at 4842 Å and the Al lines at 3944 Å and 3961 Å. There is a gain difference between channels such that the pulse height for the 20 Å bandwidth centred on the AlO band is ten times as great as that for the 20 Å covering the Al lines. Also the two peaks occur within 1 μ sec of each other which could indicate that the Al excitation closely follows the release of energy from the formation of AlO. Such a conclusion, however, is invalid if the radiation from the continuum in the two 20 Å bandwidths is greater than or comparable with the radiation produced by the relevant AlO band and Al lines. One also notes from Fig. 14 that the duration of the pulses measured at half peak is approximately 5 μ sec which is comparable to all the durations observed in the visible region of the spectrum. This result tends to support the theory that the radiation from the continuum in the 20 Å bandwidths used is at least comparable with the radiation produced by the AlO band and Al lines. Just how important ablation effects are on luminosity measurements will be seen in the near future when 0·4 in. spheres of various materials will be fired at a range pressure of 1·65 mm.

Finally some of the discrepancy between the theoretical and experimental curves in Fig. 11 could possibly be due to non-equilibrium effects. Luminosity measurements in shock tubes have shown that the radiation emitted from air during the non-equilibrium period after the passing of a shock is somewhat greater than equilibrium radiation.[10]

6. CONCLUSIONS

These studies have given preliminary answers regarding the type, the intensity and the duration of the radiative phenomena to expect from a hypersonic projectile at high altitude. Also the importance of ablation effects in seeding the plasma surrounding a hypervelocity body has been

indicated. It is considered that such spectrographic radiation experiments in conjunction with microwave measurements, yielding information concerning electron densities and collision frequencies, will eventually present a fairly complete picture of the plasma sheath surrounding a hypersonic body.

Acknowledgements—The assistance of Mr. W. H. Friend in carrying out the theoretical calculations in Section 3 of this paper is gratefully acknowledged. Also thanks are due to G. Brown, R. Wall, J. Audet and G. Gobeil for operating the C.A.R.D.E. Range 1 facility and associated research instrumentation. Finally, we wish to thank Dr. G. V. Bull for his encouragement and advice during the course of this investigation.

REFERENCES

1. G. V. Bull, *Re-entry Studies in Free-Flight Ranges*, IAS Paper No. 59–143, *7th Anglo-American Aeronautical Conference*, 1959.
2. R. Primich, this Symposium.
3. C. J. Maiden, *The C.A.R.D.E. Hypersonic Range One Facility and Associated Research Instrumentation*, C.A.R.D.E. TM–AB–49 (1959).
4. S. Feldman, *Hypersonic Gas Dynamic Charts for Equilibrium Air*, Avco Research Lab. Res. Note No. 25 (1957).
5. S. H. Maslen and W. E. Moeckel, *J. Aero. Sci.* **24**, 683 (1957).
6. C. J. Maiden and W. H. Friend, *Theoretical and Experimental Studies on Hypersonic Spheres at Low Pressures*, C.A.R.D.E. TM–AB–57 (1959).
7. A. R. Hochstim, *Air in Equilibrium for Normal Shocks at Hypersonic Velocities*, Convair Rept. No. Zph. 002 (1957).
8. F. R. Gilmore, *Equilibrium Composition and Thermodynamic Properties of Air to 24,000°K*, RAND RM–1543 (1955).
9. J. Keck, B. Kivel and T. Wentink, *Emissivity of High Temperature Air*, Avco Research Lab. Res. Rept. No. 8 (1957).
10. J. C. Keck, J. C. Camm, B. Kivel and T. Wentink, *Ann. Phys., New York*, **7**, 1 (1959).

TELECOMMUNICATIONS DURING RE-ENTRY

K. M. BALDWIN, O. E. BASSETT, E. I. HAWTHORNE
Avco Research and Advanced Development Division, Wilmington, Massachusetts, U.S.A.
and E. LANGBERG
Elcon Laboratory

Abstract—The problem of telemetering missile performance data to ground receiver stations from a re-entering ICBM is complicated by the presence of thermal plasma which completely envelopes the vehicle. The effects of the plasma on radio communications is briefly discussed.

The solution to the problem of communication blackout during re-entry is of immediate importance to the current Titan ICBM development programme. To obtain information during blackout, three approaches are considered together with their relative advantages and limitations. Briefly mentioned is the "record-re-transmit" system which relies upon transmitting data during the interval of time after blackout and prior to impact utilizing the VHF telemetry system. The second system involves a data cassette in which information is recorded during blackout. At a short time before impact, the cassette is ejected and must be recovered to obtain the recorded data.

The third system is the only one that attempts to directly solve the problem of telemetry blackout by propagating electromagnetic energy directly through the thermal plasma. This direct re-entry telemetry system operates in the K_a-band. Details of the system, component design and its expected operating parameters are discussed. Special problems arising from system design at this frequency such as signal acquisition, antenna design and tracking requirements are detailed.

1. INTRODUCTION

With the advent of man's entry into space, the requirements for constant communication with space vehicles are becoming increasingly more important. Typically, such communication capabilities are and will be required for telemetry of data from space vehicles, for voice communication with occupants of space vehicles, for guidance, tracking and control. One of the most difficult of all the communication problems arises during the terminal phases of flight of a space vehicle. During this portion of the flight trajectory, a communication blackout occurs as a result of absorption of electromagnetic waves over a wide frequency spectrum by highly ionized gas surrounding the re-entry vehicle. This paper is concerned with the nature of this problem.

2. PLASMA PARAMETERS

The word "plasma" was first used by Langmuir[1] to describe that region of an ionized gas where electrical neutrality exists, that is, where there are an equal number density of electrons and positive ions. Langmuir produced his plasma by the use of a d.c. electric field. In this type of plasma the gas is relatively cool whereas the plasma under discussion during re-entry is extremely hot. Furthermore, the composition of high temperature ionized air is neither as simple nor as well known as many of the monatomic gases. However, the same parameters can be used to characterize the electrical properties of either plasma.

One fundamental concept is the plasma frequency. The plasma frequency is proportional to the square root of the electron density. This term does not necessarily imply that plasma oscillations occur (although they may). Rather, as it enters into the expression for the electromagnetic wave propagation vector, it is simply a constant indicating the frequency above which the plasma is relatively transparent. Its value usually falls in the upper UHF or microwave region for the thermal plasmas associated with

re-entry. Another significant term is the electron collision frequency. This term relates to the dissipative loss of r.f. energy through collisions of electrons with neutral atoms and molecules and to a small extent with positive ions. At the high temperatures where thermal ionization occurs, the atmospheric constituents which are present in sufficient quantity and also contribute significantly to the number of collisions are O_2, O, N_2, N, NO and A. The two quantities, plasma frequency and collision frequency, have been determined from theoretical and experimental data as a function of temperature and air density.[2] For an electromagnetic wave propagating in a thermal plasma, the various electrical properties of the plasma are specified in terms of the above two frequencies and the signal frequency.

The temperature and density of the heated air determine the degree of ionization and the collision frequency. These parameters must be determined by the aerodynamicist as a function of missile geometry, velocity, re-entry angle and trajectory. However, certain general temperature distributions prevail in the enveloping shock layer around any missile and these will influence communication system design. The hottest region in the shock layer is around the stagnation point (the foremost point of the missile). Temperatures generally decrease towards the rear. If there is a flare in the rear of the missile, further compression and heating of the air takes place while if the diameter reduces, the shock layer becomes thicker and cooler.

On occasion it is necessary to predict plasma conditions on the basis of very limited aerodynamic data. The minimal data required is a knowledge of the velocity–altitude profile. From this, stagnation point temperatures and densities can be obtained.[3] The plasma conditions at the stagnation point are maximum values for a given altitude. If there is further aerodynamic information at a point towards the rear of the missile for a given altitude, this data may be extrapolated to other altitudes by the approximation that the temperature (or density) ratio between the stagnation point and the rearward point is constant for all re-entry altitudes. Temperature and density profiles along paths through the shock layer for altitudes differing from the reference altitude may also be determined from this approximation although the results are probably less valid as the distance from the missile increases.

In the event that the missile oscillates as it descends, it is to be expected that the temperature distribution in the shock layer will change. The exact nature of this change will depend upon vehicle configuration and amplitude of the oscillation. However, this can result in a sharply changing plasma density and can result in intermittent blackout.

The velocity at which a missile moves through the air at any altitude will, in general, determine the maximum air temperature in the shock layer. The velocity is dependent on the missile's ballistic coefficient. A high drag, light vehicle will slow down rapidly and peak heating will occur at higher altitudes than for the converse case, a low drag, heavy vehicle. In the altitude–velocity range of interest, electron densities and collision frequencies will be lower at high altitudes for any given velocity. Thus it is expected that missiles differing in performance, even though they re-enter with the same initial velocity, will suffer radio blackout over different altitude ranges.

Since the electrical properties of the plasma are dependent on signal frequency, this implies that although it may be difficult or impossible to control the plasma conditions around the vehicle, it might be possible to penetrate the plasma by proper selection of signal frequency. In general, if the signal frequency is made greater than the plasma frequency, attenuation drops to a low value. This is true for all values of collision frequency that might reasonably be encountered. An alternate approach is to resort to low frequencies. This approach is useful if the medium is sufficiently conductive, i.e. the collision frequency is relatively large. The propagation through the

plasma is somewhat analagous to "skin depth" penetration in this case. However, if the collision frequency is relatively low, no advantage is gained by resorting to low frequencies. Fig. 1 shows typical attenuation as a function of signal frequency at two altitudes illustrating the effect of collision frequency on signal attenuation.

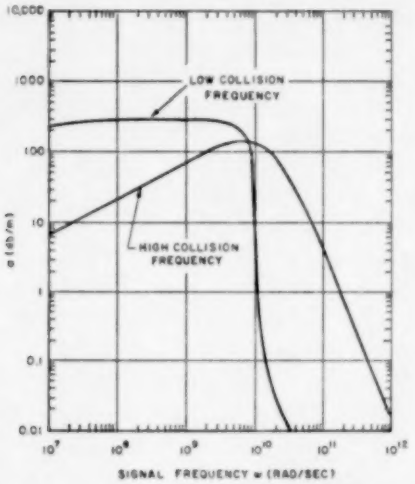

Fig. 1. Attenuation constant versus signal frequency for a plane wave propagating in a homogeneous plasma.

3. THE VHF–DATA CASSETTE SYSTEM

One approach to the problem of telecommunications during re-entry is a standard VHF telemetry system, supplemented by an ejectable data cassette in which information that could not be transmitted during the blackout phases of the flight is stored on magnetic tape for subsequent availability. A system, developed and constructed at AVCO RAD, will be briefly discussed first. This approach towards providing re-entry data is one solution to the blackout problem. Another technique, that of recording during blackout and re-transmitting after blackout, has been developed by AVCO RAD and reported elsewhere.[4]

The VHF system is a conventional PAM–FM–FM system operating in the standard (IRIG) telemetry band; herein lies its primary advantage of being a readily designable and producible system, completely within state-of-art capabilities. The system, furthermore, includes the ejectable data cassette, which is the only major novel addition to the more conventional components comprising it.

Fig. 2 is the block diagram of the system

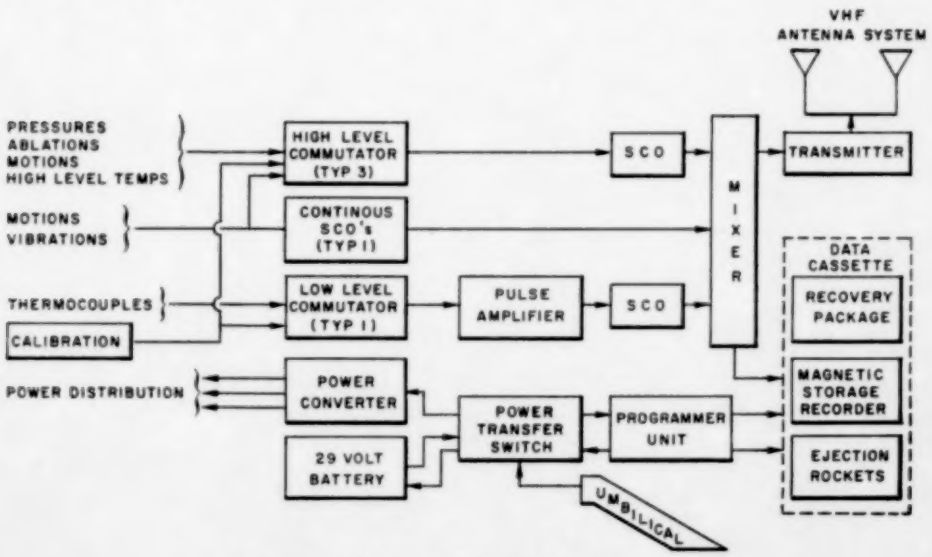

Fig. 2. Typical airborne PAM–FM–FM telemetry system.

showing its principal components and features. Inputs are derived from sensors required to measure the desired characteristics. These include high-level (0–4 V) inputs, as well as low-level (below 50 mV) inputs. Slowly varying inputs are commutated in the conventional fashion. Low-level inputs are amplified to a desired common level. Commutated data are made to modulate subcarrier oscillators. The entire complement of individually modulated inputs are then fed into a common mixer to subsequently modulate an FM transmitter. Figs. 3 and 4 show two views of the packaged canister, housing the VHF system less the data cassette. The system is rugged, miniaturized and transistorized.

The antenna system for this VHF telemetry system merits special mention. The obvious requirements of isotropic pattern, high efficiency, light weight and compatibility with environmental conditions presented a challenging design problem. The system described here includes a specially developed antenna consisting of two flush-mounted radiating elements. The two antennas are mounted diametrically opposite on the vehicle surface for special cross-polarization. The over-all pattern is shown in Fig. 5.

Fig. 6 shows the recoverable data cassette, which, in addition to the magnetic data storage recorder, includes a recovery package for aid in search and recovery. The recovery package includes an aerodynamic drag skirt, a rescue and search beacon, flashing lights, radar chaff, die-marker, shark repellent and all required power supplies (Fig. 7). The output of the mixer is fed to the data cassette for storage on the magnetic recorder during the period of telemetry blackout. A programmer performs the function of initiating this process at an appropriate time during the re-entry trajectory. Sufficient tape is provided to allow information storage during the entire blackout period. Following blackout it is ejected from the missile. It is slowed down by aerodynamic drag and impacts in the ocean from which it can be recovered.

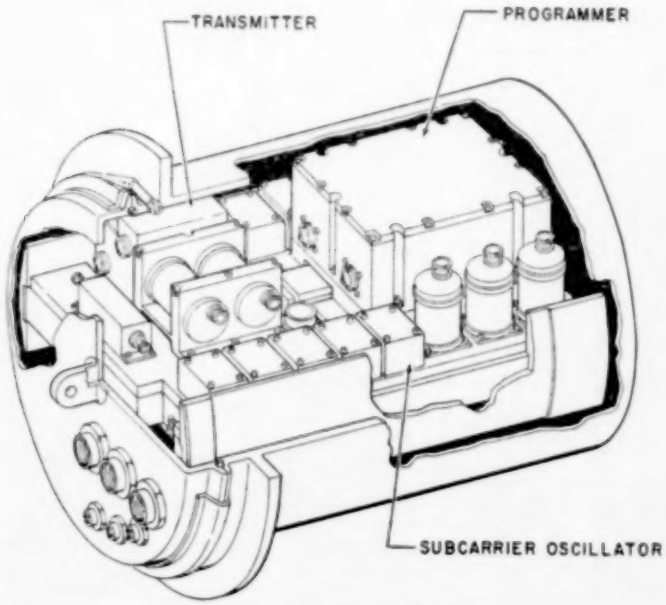

Fig. 3. Telemetry canister (top view).

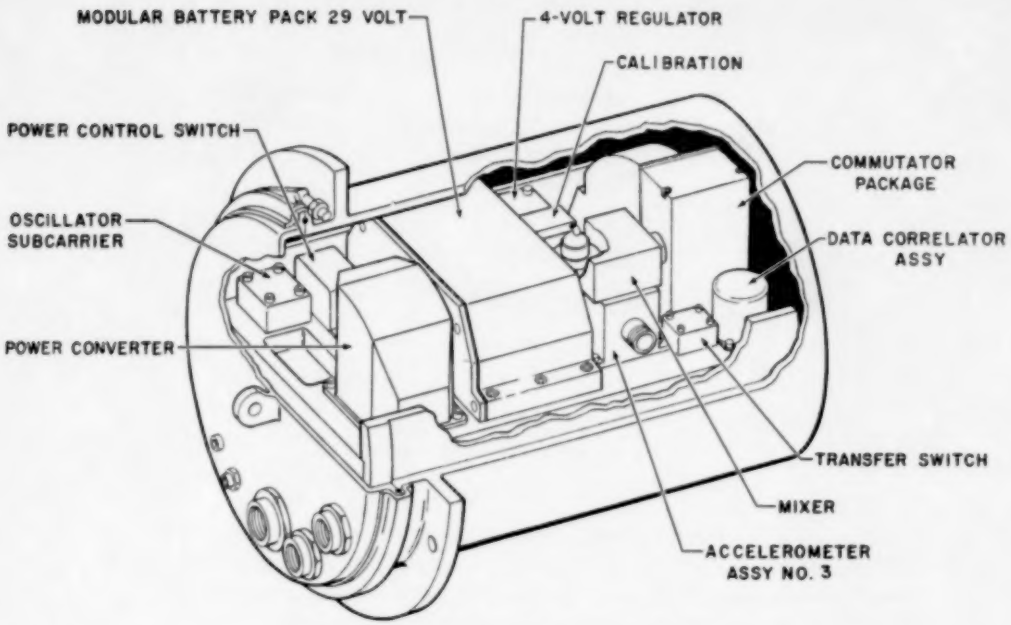

Fig. 4. Telemetry canister (bottom view).

The VHF–data cassette system described here, has many advantages, but also some very serious limitations. Its main advantages are the relative ease of design within state-of-art limitation, availability of hardware and compatibility with existing range installation. It has adequate range during the earliest phase of re-entry prior to blackout. The system provides for adequate data capacity, and is reasonably small and light. Further improvements in making the system smaller and lighter do not appear to be worthwhile since a point of diminishing returns is reached in this refinement process because of the basic requirements for batteries, power converters, programmers and data cassettes.

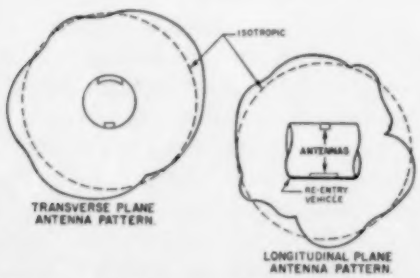

Fig. 5. Typical airborne VHF antenna patterns.

A major disadvantage of the VHF–data cassette system is the inability in this frequency range to communicate directly, in real time, during the plasma blackout phases of the re-entry trajectory. The use of the ejectable data cassette to cope with this problem adds to the weight, complexity and unreliability of this system, and at best these very important re-entry data are obtained on a non-real time basis. Another drawback of this system is the operational difficulty in recovering the data cassette—a problem so obvious and so severe that it requires no further elaboration here.

4. DIRECT RE-ENTRY TELEMETRY

(a) *System consideration*

The sharp attenuation cut-off characteristic

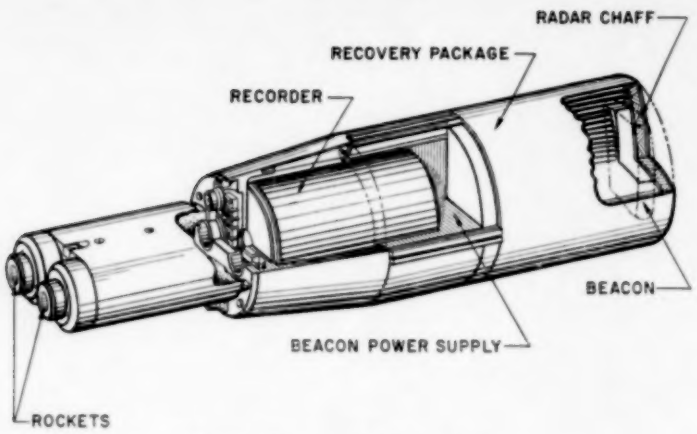

Fig. 6. Recoverable data cassette.

of a plasma allows a lower signal frequency limit to be specified by simply noting the maximum value of plasma frequency along any transmission path through the shock layer. When the signal frequency exceeds this maximum plasma frequency, attenuation drops to a very low level and even the integrated attenuation along transmission paths through typical shock-layer thicknesses will usually not prove prohibitive to system operation. Since the above plasma frequency generally falls in the microwave region, this dictates a microwave system.

The exact choice of frequency depends upon several practical considerations. Foremost is the availability of suitable equipment and components. This limitation becomes increasingly important in the upper microwave spectrum. Atmospheric propagation must also be considered. Strong attenuation due to water vapour and molecular oxygen absorption make many frequencies unsuitable. However, the situation is not quite as serious for missile-to-ground communication as for ground-to-ground communication due to the reduction of water vapour and oxygen density with altitude. Roughly 75 per cent of the water vapour is concentrated below an altitude of 20,000 ft while the oxygen density reduces exponentially with altitude. Depending upon where the system will be operated, cloud cover may be important in that the water vapour absorption is higher in clouds than for clear skies.

On the basis of plasma characteristics, equipment and atmospheric propagation, K_a-band was selected for DRET operation. Development of the complete system involved solving other basic problems associated with the operation of microwave equipment in a missile environment.

Highly directive, line-of-sight transmission paths and limited range characteristic of any microwave link placed one set of limitations on the receiver location. The possible transmission paths through the cooler, lower density plasma regions around the missile placed other restrictions on receiver locations. One solution is to fly the receiver in an aeroplane thereby allowing the best location for any particular trajectory to be chosen and at the same time significantly reducing atmospheric absorption. However, stabilization, necessary where narrow-beam antennas are used, requires a special servo system. On the other hand, a ground station can be more elaborate, and better performance may be expected. Both systems have been considered for DRET operation and the system is basically adaptable to either location.

Fig. 7. Data cassette assembly.

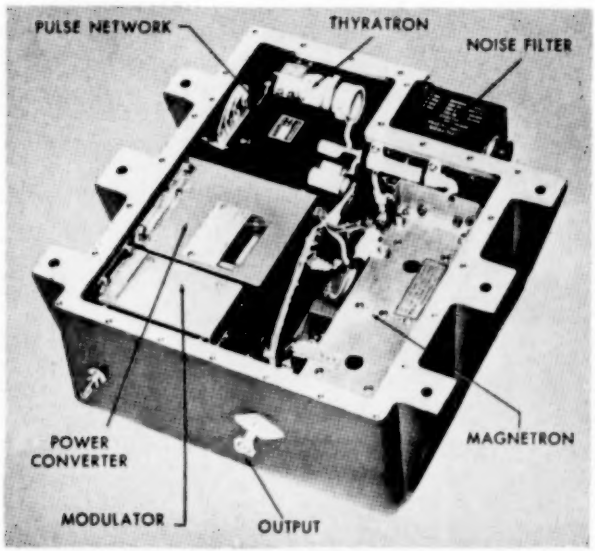

Fig. 9. DRET transmitter and components.

Signal acquisition as the vehicle begins re-entry presents a special problem. Limited range and the possibility of early vehicle orientation being such as to shadow the receiver in a null region of the antenna pattern limit the time available for acquisition. Vibration and temperature change can also result in a shift of frequency of the transmitted signal. Therefore, both spatial and frequency acquisition are required, although obviously spatial acquisition must precede frequency acquisition. This problem can be solved most conveniently by utilizing the VHF telemetry system prior to blackout. The DRETS antenna is oriented in the same direction as the VHF receiving antenna to achieve spatial acquisition. Automatic frequency scanning is then employed until the K_a-band signal is acquired. Spatial acquisition could also be accomplished by utilizing any other signal which may be transmitted from the missile in the same manner as the VHF system is employed.

As the missile moves along its trajectory, the highly directional microwave antenna must track the missile in order to continue receiving the signal. Temporary loss of signal due to momentary blackout resulting from missile oscillations or null regions in the antenna pattern can be allowed for by providing a memory unit which continues the tracking function at the same rate as when the signal was last received. To avoid fading due to changing polarization, the receiver utilizes polarity diversity reception.

(b) *Hardware consideration*

The block diagram of the airborne transmitter is shown in Fig. 8, while the construction of the transmitter package (less power supplies and switching chassis) is shown in Fig. 9. This initial design does not reflect any extensive effort towards miniaturization; it is anticipated that a reduction of the order of 50 per cent is feasible. The package is capable of withstanding missile environmental conditions similar to those met by the VHF telemetry system. The transmitter operates in the K_a-band and within the state-of-the-art could potentially be designed for peak pulse power of the order of 100 kW although only 40 kW has been used for DRETS. Because of magnetron duty cycle limitations and because more conventional modulation schemes such as FM or AM are not feasible for these applications, a pulse position modulation technique is best, and has been selected. In actual flight, the system may be actuated (such as by use of inertial sensors) at a convenient point during the trajectory for subsequent telemetering of data during re-entry portions of the flight. This is accomplished in a separate

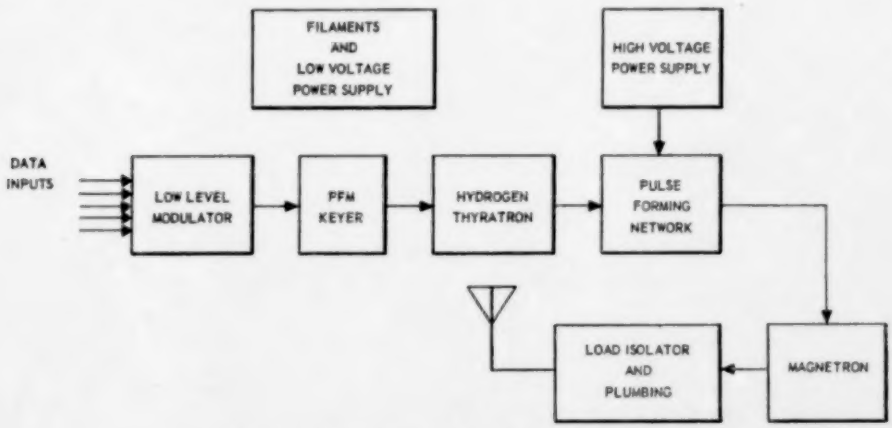

Fig. 8. Transmitter system block diagram.

switching chassis, not explicitly shown in these diagrams.

Development of a suitable missile-borne antenna system posed special developmental problems of antenna gain, pattern coverage and antenna window materials. These problems have been solved successfully. The antenna system consists of eight radiating elements, equally spaced around the re-entry vehicle at a suitable point on its surface (in a reasonably "cool" region, with adequate capability of forward-oriented radiation). Each element is a pyramidal horn, flush-terminated in a conductive ground plane, which eliminates wave trapping in the skin of the vehicle. The radiating apertures themselves are sufficiently large to limit the radiated power density at the surface of the antenna. An upper limit of allowable electromagnetic power density is necessitated so that ionization enhancement will not occur. A very adequate antenna pattern results, as shown in Fig. 10, with an acceptable interference pattern (scalloping) in the transverse plane between adjacent elements. The overall gain is of the order of 0 dB, except for small regions where 3–6 dB loss may be anticipated. However, this design results in an unusually wide beam pattern.

A block diagram of the receiving system is shown in Fig. 11. The receiving antenna is an 18-in. parabolic dish (gain of 41·5 dB) having a scanning beamwidth of 2·8 degrees (3 dB point) and a resolution and tracking error of the order of 0·5 degree. The receiving system itself is a superheterodyne, diversity reception type system, with a video base-band combiner. Major features of the system are self-evident from Fig. 11. The IF bandwidth of the receiver is 6 Mc/s, while the video bandwidth is only 3 Mc/s. The receiver noise figure is of the order of 13 dB. Theoretical results indicate that S/N requirements for the receiver are 10 dB for tracking and 12 dB for acquisition. It is important to point out that the directional characteristic of the K_a-band receiving system requires that an auxiliary means be available to aid in initial acquisition.

The system described here represents one of many possible versions of a K_a-band system for telecommunications with a re-entry vehicle. It was designed and constructed with the aid of Federal Telecommunications Laboratory (now ITTL), Crosley and Melpar, Inc. The system described may serve as a basis for many applications in addition to telemetering data from a re-entering ICBM nose cone.

(c) *Performance characteristics*

A wide variety of performance characteristics

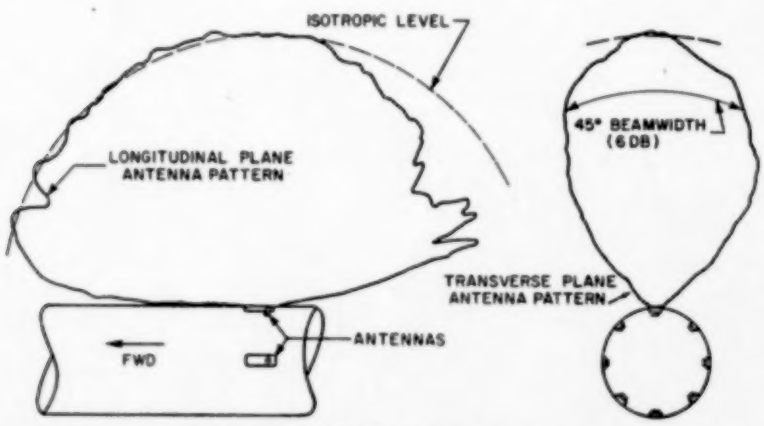

Fig. 10. Typical K_a-band antenna patterns.

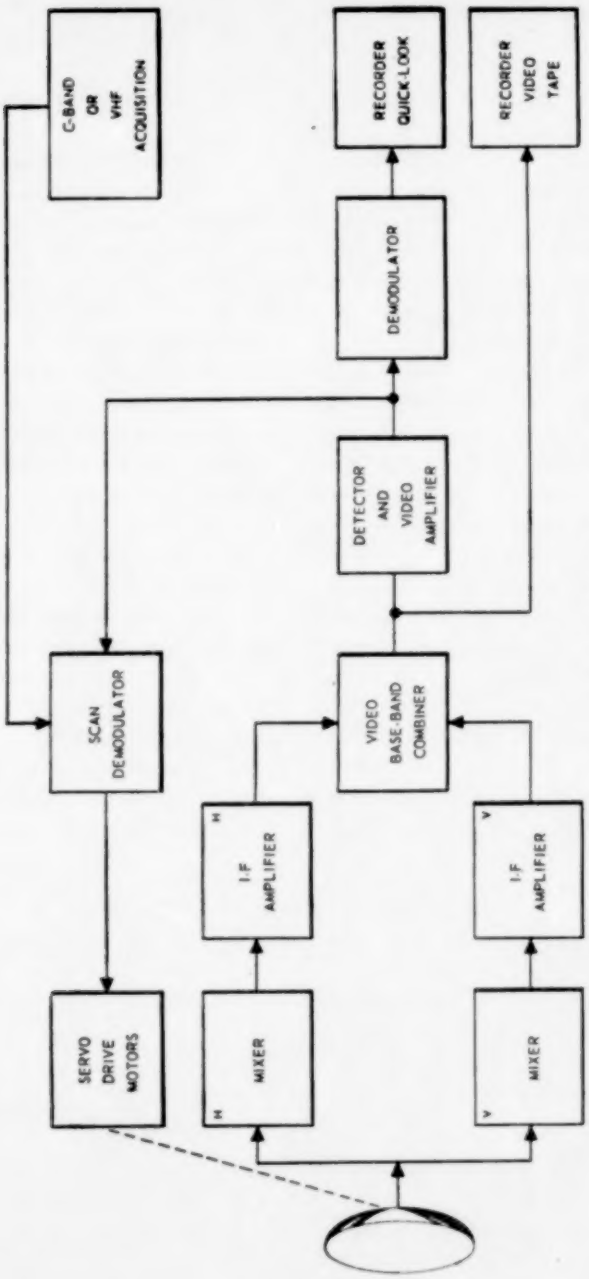

Fig. 11. Receiver system block diagram.

may be expected depending upon operating range, plasma conditions and weather conditions. In the future it is to be expected that state-of-the-art equipment improvements will result in even better performance than tabulated in Table 1.

Data capacity of the DRET system merits special mention. Because of magnetron limitations, PPM is best for maximum data capacity and minimum complexity, consistent with a required S/N. Furthermore, a simple PPM–PDM converter, readily available, enables the system to be compatible with existing range data processing systems. Comparison with VHF telemetry, limited by IRIG standards, readily reveals that the DRET system has a comparable or greater data capacity. If a common 2 per cent error criterion is adopted, then analysis indicates that a data rate of about 1000 samples/sec is easily attainable over a communication range of 500 miles with the resultant S/N ratio of 15 dB or better. Corresponding IRIG data rates can reach 1500 samples/sec or less. If a range of 300 nautical miles is adequate, then a 4000 sample/sec rate can be achieved by the DRET system. A more sophisticated design of a PPM modulator is possible with a corresponding increase in complexity of ground equipment. These rates are doubled by means of two-stage sub-division of the time period between pulses. The fundamental limitations on the data rate is imposed by the magnetron duty cycle (and peak power). With available magnetrons, the rates quoted above are achievable today with a promise of further improvement in the near future.

A typical PPM modulator for DRET is shown in Fig. 12 for the simplest of the above described systems. This has a 1000 samples/sec data rate with an error of 2 per cent or less. It will be noted that a suppression technique for the start-pulse is employed for transmission of each data sample in order to increase the data rate. Adequate accuracy is provided by the frame synchronization pulses as shown in Fig. 12. This modulator, furthermore, is lighter and smaller than a corresponding VHF FM/FM modulator. It is also worth observing, that in light of magnetron limitations on pulse rate, a corresponding PCM system would yield a much lower data capacity.

A study of the performance characteristics of DRET reveals that the system is not a cure-all for re-entry telecommunications. It has several drawbacks and limitations. A summary of major disadvantages includes directional characteristics; state-of-the-art limitations on magnetrons, hardware, component reliability and precision; dependence on atmospheric conditions; line of

Table 1. Typical DRET Signal-to-Noise Ratio

Signal		Noise	
Output of beacon	76 dbm	*kT* Power BW	–174 dbm c/s
Transmitter antenna gain	0 db	BW (6 M/cs)	68 db
Receiver antenna gain	41·5 db		
Polarization (loss)	–1·5 db	Receiver input noise	–106 dbm
Atmospheric absorption (loss)*	–3 db	Receiver noise figure	13 db
Scanning (loss)	–2 db		
R.F. plumbing (loss)	–5 db	Total noise power	–93 dbm

Distance	100 mi	200 mi
Free space	–159 db	–166 db
Total signal power	–53 db	–60 db
S/N	40 db	33 db

*Along typical upward slanting path through atmosphere.

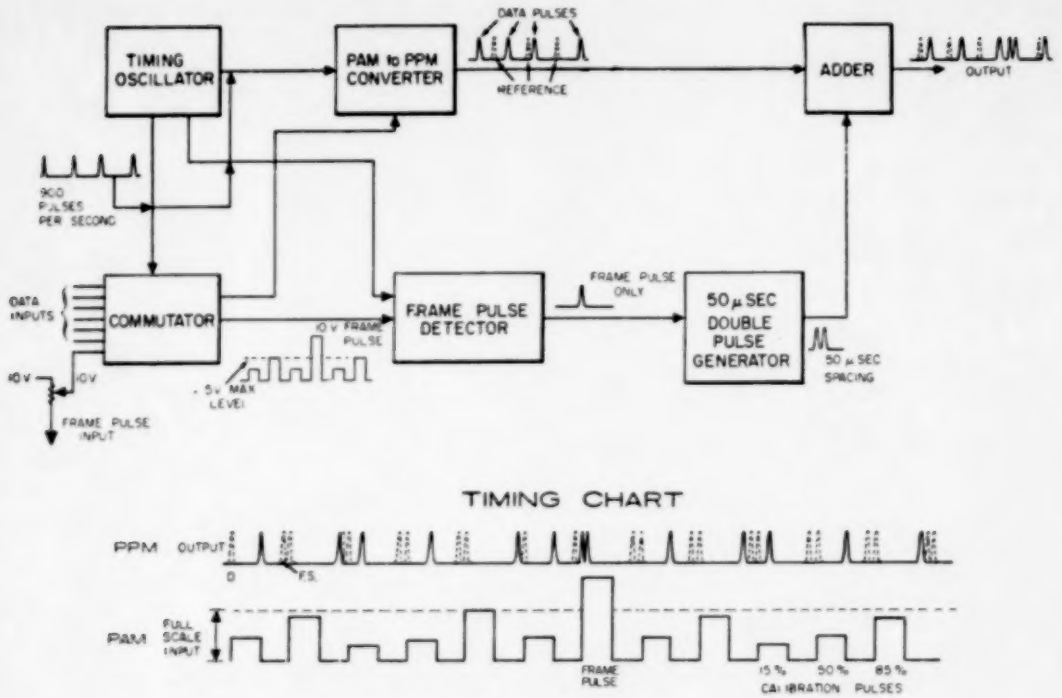

Fig. 12. PPM modulation unit.

sight limitations; ground equipment complexity and less flexible choice of modulation.

However, the DRET system possesses important advantages which make its consideration worthwhile for extended applications of telecommunications with re-entry vehicles of the future:

(1) penetration of ion sheath,
(2) small size and weight of transmitter,
(3) small and efficient antenna system,
(4) low power requirements,
(5) large data capacity,
(6) possible range measurement capability,
(7) small tracking error,
(8) no atmospheric, galactic or man-made noise interference.

The most important of these, by comparison with lower frequency telecommunication such as VHF is, of course, the ability to penetrate the ion sheath and the consequent avoidance of telecommunication blackout. As already indicated, this depends greatly on the aerodynamics of the vehicle under consideration. Under some re-entry conditions it may be necessary to go to still higher frequencies to exploit this advantage.

Of equal importance from the standpoint of potential application is the attractive possibility of extending the use of the DRET system to serve a wider variety of functions than merely telemetry of data from a re-entry vehicle. For instance, it is conceivable that the DRET system may be extended for voice transmission, two-way communications, range measurement by design and employment of a beacon transponder, and even for a combined radar-telecommunications system with re-entry vehicles or other space vehicles.

REFERENCES

1. I. LANGMUIR, *Phys. Rev.* **33**, 964 (1929).
2. E. LANGBERG, K. BALDWIN and J. YOS, *Radiation and Propagation of Telemetry Signals During Hypersonic Re-entry* in *IRE Proc. Nat. Symp. on Telemetering, September* 1958.
3. K. BALDWIN, *Transmission of Microwave Telemetry Signals from a Re-Entering Vehicle* in *Proc. Nat. Telemetering Conf., AIEE, May* 1959.
4. R. E. SCHMIDT, J. R. WHITE and R. A. PORTER, *A Time Redundancy Instrumentation System for an ICBM Re-Entry Vehicle*, presented at *IRE National Convention, New York City*, 25 *March* 1959.

ABSTRACTS OF PAPERS PRESENTED AT THE SYMPOSIUM BUT NOT INCLUDED IN THIS VOLUME

These abstracts pertain to papers presented at the Plasma Sheath Symposium, but whose texts will not be printed in this volume. Their complete texts are printed in an AFCRL publication, distributed free to all who attended the symposium. Requests for additional copies by Agencies of the Department of Defense, their contractors, and other government agencies should be directed to the: Armed Services Technical Information Agency, Arlington Hall Station, Arlington 12, Virginia. All other persons and organizations should apply to the: U.S. Department of Commerce, Office of Technical Services, Washington 25, D.C. In ordering, the AFCRL report number AFCRC-TR-60-108 (1) should be referenced.

METHODS FOR APPROXIMATING THE ION FIELD SURROUNDING ADVANCED MISSILES

R. L. DANIELS
North American Aviation

An extensive study of current aero and thermodynamic methods of calculating hypersonic flow fields has indicated techniques for evaluating problems of electromagnetic propagation from re-entry bodies and nuclear-propelled vehicles. The influence of thermal non-equilibrium, secondary radiations, boundary layer, ionization, dissociation and initial overshoot effects are considered. The general technique consists of determining free electron concentrations in the shock front and then determining changes that occur along streamlines due to electron attachment, detachment, recombination and temperature–density variations of the flow field. Error estimates are also discussed. The results of applying these methods to two specific vehicles, a hypersonic re-entry body and a supersonic nuclear missile, are presented in some detail.

RELAXATION PHENOMENA IN SHOCK FRONTS (A REVIEW)

I. P. SHKAROFSKY, T. W. JOHNSTON and M. P. BACHYNSKI
RCA, Montreal

For aerodynamic phenomena occurring at temperatures in excess of 1000 degrees K, a great number of collisions between the constituent particles of a gas are required in order that thermal equilibrium be established. Under these conditions, relaxation times can be associated with the distribution of the internal energy of the gas into the various energy states. This paper reviews the phenomena occurring in a shock front from the start of the shock to the point of thermal equilibrium behind the shock. Chemical reactions at high velocities, temperature variations across a shock front, mechanisms of energy transfer and effects of air flow rate on relaxation are considered. A comparison of a plasma set up by a hot gas and one created by a gas discharge is given. The distribution of energy into translational, rotational and electronic states as well as dissociation and ionization are discussed in detail. Some regard is given to relaxation rates, collision processes, ionization onset point and radiative relaxation.

RADIO FREQUENCY RADIATION FROM HYPERSONIC PLASMAS WITH IMPRESSED OSCILLATING ELECTRIC FIELDS

C. A. ROBERTS
Douglas Aircraft Company

The total (integrated frequency distribution) radiated power from a plasma with an impressed electric field ($E \cos \omega t$) is calculated taking into account only the semi-classical Bremsstrahlung due to electron ion encounters. The calculation is made by using the impulse approximation with

the lower limit on the impact parameter taken as the de Broglie wavelength of the electron. The electron velocities are then averaged by using the appropriate non-equilibrium velocity distribution. Results are given for various conditions that might be encountered in hypersonic plasmas.

The radiation frequency spectrum of the plasma in the radio frequency range for a zero field is then examined by a Fourier analysis of the acceleration using the impulse approximation. In order to determine the validity of the approximation, a comparison is made between the zero field radiation spectrum from an ionized gas calculated by using the impulse approximation with a cutoff at the de Broglie wavelength and the spectrum from the exact (dipole approximation) calculation for low (radio) frequencies.

Possible effects on electronic and detection equipment are briefly considered.

PROPAGATION OF ELECTROMAGNETIC WAVES IN A PLASMA WITH AN INHOMOGENEOUS ELECTRON DENSITY*

A. J. PENICO
Sylvania

A theoretical study was performed to determine the propagation characteristics of an electromagnetic wave in the presence of an isotropic, dissipative plasma whose electron density varies in the direction of propagation of the wave. In the analysis, various functional forms giving the electron density as a function of the position within the plasma were inserted into the wave equation for the medium, and exact solutions were obtained for the equation.

The above-mentioned solutions will be discussed from two points of view. First, their qualitative behaviour for all, or nearly all, of the values of the parameters will be discussed. Second, curves will be shown indicating the specific behaviour of the solutions for limited ranges of radio frequency, electron-neutral particle collision frequency, initial and final electron density and rate of variation of the electron density.

Criteria will be discussed for treating the electron density as "slowly-varying" or "rapidly varying". In particular, some "quarter-wavelength" and "half-wave-length" criteria of the medium will be exhibited. These criteria will be discussed in relation to the problems of reflection and absorption of the waves.

* This study was performed under Air Force Contract No. AF 30(602) – 1944.

PECULIAR WAVE PROPAGATION CHARACTERISTICS OF A PLASMA WITH CONSTANT MAGNETIC FIELD

H. POEVERLEIN
Air Force Cambridge Research Laboratories

A wave propagation theory based on a study of the conductivity of a plasma shows that with a sufficiently strong constant magnetic field the refractive indices are in the order of *one* and independent of the electron concentration.

The conductivity of a plasma with constant

magnetic field is an asymmetric tensor. There is no system of three principal directions for which the current density components would be proportional to the electric field strength components. This simple proportionality is however found in a coordinate system whose coordinates are a vector in the direction of the magnetic field and two vectors rotating in either sense around the magnetic field direction. The longitudinal conductivity, that is, the conductivity in the magnetic field direction, is predominant.

The transverse conductivities now will be assumed being suppressed by the magnetic field. The propagation characteristics then become independent of the electron concentration. The two magnetoionic modes in this case have refractive indices of or near 1, their attenuation is negligible, and one of them is perfectly guided along the magnetic field lines. This peculiar type of propagation requires a magnetic field of sufficient intensity, but no influence of ion motions or pressure gradients in the plasma.

NON-LINEAR MODELLING OF MAXWELL'S EQUATIONS

J. E. BELYEA and K. M. SIEGEL
University of Michigan

The basic stumbling block to carrying out many experiments in the laboratory is the reliance which is placed in the theory of linear modelling. In aerodynamics and electromagnetics one is seldom able to construct a precise linear model; one must appeal to physical reasoning to show that the model one is able to construct gives results in close agreement with those which would have been obtained from a precise one. For example, as long as good conductors are used, conductivity is not modelled.

Up until recent years the limitation on indoor radar cross-section ranges was simply the size of the model that could be handled and the magnitude of the frequency of the coherent source. No precise linear modelling experiments exist for bomber cross-sections at very high microwave frequencies.

With the growth of interest in ICBM programmes it becomes desirous (as measured in dollars) to determine the radar cross-sections of ablating warheads, and to determine attentuation effects and scattering effects in or by plasmas, by modelling. Linear modelling is of very limited utility for such experiments. One must model a lossy dielectric at high frequencies or not do the experiment in the laboratory. One must model some plasma parameters, or risk missing crucial first order effects.

Previous analysis predicted the feasibility of non-linear modelling. The first such modelling results are given in Ref. (1). In this paper many non-linear models of equations of mathematical physics are presented. *Maxwell's equations are non-linearly modelled.* Experiments making use of non-linear models are discussed.

1. R. K. RITT, *Trans. Inst. Radio Engrs. on Antennas and Propagation*, **4**, 216 (1956).

THE REGION BEHIND A BODY MOVING THROUGH A RAREFIED IONIZED ATMOSPHERE

E. T. KOROWSKI
General Electric Company

Physical arguments indicate that charge density gradients will exist some distance behind and possibly a short distance to the side of a body moving at high speed through the ionized layers of the upper atmosphere.

The medium is taken to be highly rarefied gas

composed of ions and electrons. An unsteady model is set up, wherein the ion and electron density profiles, which are obtained as a function of space and time, correspond to the profiles at a given cross-section aft of the body in the actual problem. The Boltzmann equation with electric effects taken into account is utilized and solutions are obtained numerically. Perturbations on the velocity distribution functions are calculated over small increments of time which then yield the magnitude of the electric effect over the next time increment.

Calculations indicate that the charge density gradients extend several body radii downstream. These gradients are inherent to the rarefied flow over any vehicle and can significantly alter its detectability by electromagnetic signals.

HIGH FREQUENCY WAVES IN IONIZED GASES

S. C. BROWN
Massachusetts Institute of Technology

A review will be given of the propagation of electromagnetic waves through an anisotropic ionized gas in order to elucidate the following studies presently under way in our laboratory:

(a) The emission of incoherent microwave radiation from plasmas (both with or without external magnetic fields) of various degrees of transparency.

(b) The contribution of ions to the radio-frequency of the plasma, with specific attention directed toward an investigation of various types of ion resonances.

EXPERIMENTAL INVESTIGATION OF PLASMA SHEATH PROPERTIES OF A RE-ENTRY VEHICLE

W. ROTMAN and G. MELTZ
Air Force Cambridge Research Laboratories

The effects of the plasma sheath, which surrounds a re-entry vehicle, upon the transmission and reception of radio signals will be investigated by means of an instrumented nonablative nose cone to be flown in a re-entry trajectory from Cape Canaveral in the latter part of 1960. The flight profile is such that an altitude of 100 miles and a maximum velocity of 18,000 ft/sec will be reached in a shallow (10–20 degrees) re-entry path. The instrumentation consists of five microwave transmitters, in the *L*, *S*, *C* and *X*-band frequency ranges, and *S* and *C* band receivers. The *S* and *C* band units also serve as the radar beacons while telemetry data is transmitted on the *X*-band frequencies. Parameters to be measured include signal attentuation and coherence, pulse deterioration, and plasma noise generation as a function of altitude and velocity. These results will be compared with estimated values from modified isentropic calculations and, also with results from the University of California's hypersonic wind tunnel tests. Subsequent to the flight test detailed nonequilibrium real gas calculations will be programmed to provide an exact theoretical comparison.

The radiation patterns of the antennas on the nose cone will be changed in shape by the plasma sheath. This effect is being simulated experimentally by the use of a lossy artificial dielectric which has the same propagation characteristics

as the plasma. The realization of an index of refraction of less than unity was achieved in this artificial dielectric by the use of a cubic lattice of closely spaced wires. The loss can be introduced either by loading the wires with lossy elements or by embedding the lattice in a lossy medium. These same techniques can also be used to simulate plasmas in radar reflection and diffraction problems.

SHOCK-LAYER ATTENTUATION DATA COLLECTED FROM MISSILE TESTS AT THE ATLANTIC MISSILE RANGE*

E. M. FETNER
RCA

The problem of propagating electromagnetic energy through shock-layer ionization has been a concern of theorists for the past several years. Theory on the subject has been fairly well explored. Also, some experimental data have come from laboratory shock tube tests. However, not until recently has this re-entry phenomenon been actually observed. During the past year, data at telemetry and *S*-band frequencies from several IRBM and ICBM tests have been collected. Samples of these data and other related information such as velocity and altitude are presented.

THE EFFECT OF DOPPLER BROADENING UPON RADAR CROSS-SECTION OF A PLASMA-SURROUNDED BODY*

R. E. KELL
Cornell Aeronautical Laboratory

The radar signal scattered from a plasma may be considered as the vector sum of the signals scattered from the individual electrons of the plasma. If the electrons have a component of motion radial with respect to the radar, the signal from each electron will possess a Doppler shift in accordance with its radial velocity, and an originally monochromatic illuminating electromagnetic wave will be scattered as a non-monochromatic spectrum of waves, where the spectral distribution represents the distribution of radial velocity for the electrons.

The effects of Doppler spectral broadening upon radar cross-section will be discussed, and experiments to determine the magnitude and shape of the broadened spectrum will be described.

THEORETICAL STUDIES AND DAMP FLIGHT-TEST RESULTS ON RADAR CROSS-SECTIONS*

W. O. CARLSON, A. J. SEID and C. BROWN
RCA

A solution for the interaction of an electromagnetic wave with the plasma sheath surrounding a hypersonic re-entry vehicle is presented. Flow fields around the body and in the wake are

* Papers classified.

set up and the electrical properties of the plasma sheath are determined by means of higher-order approximations.

Radar cross-sections obtained by means of ray-tracing techniques and the solution of the Maxwell equations referred to above are compared with flight-test data obtained by the Radio Corporation of America radar on the DAMP project. The numerical results are presented for a plane electromagnetic wave illuminating the re-entry body at various aspects.

Order-of-magnitude lengths and electric and thermodynamic properties at various stations are presented for wakes or trails of ballistic nose cones at trajectory points of interest. The interaction of electromagnetic waves of various frequences with these wakes is also considered.

END OF VOL.